The background of the image is a complex, interconnected network of grey, semi-transparent rods and spheres, representing a porous material's framework. In the lower right quadrant, a single molecule is highlighted in a vibrant orange and red color. This molecule has a central carbon atom (orange) bonded to several other atoms, including a red oxygen atom and a blue nitrogen atom. The blue nitrogen atom is further connected to a series of blue lines that fan out, suggesting a dynamic or simulated state. The overall composition is clean and scientific, with a focus on molecular simulation.

# Modelling and Molecular Simulation of Alcohols in Porous Materials

Rafael María Madero Castro







---

---

# MODELLING AND MOLECULAR SIMULATION OF ALCOHOLS IN POROUS MATERIALS

---

---

**RAFAEL MARÍA MADERO CASTRO**

Licenciado en Física



U N I V E R S I D A D  
**PABLO<sup>D</sup>  
OLAVIDE**  
S E V I L L A

Department of Physical, Chemical, and Natural Systems

UNIVERSITY PABLO DE OLAVIDE

SUPERVISORS

Prof. Sofía Calero

University Pablo de Olavide  
Eindhoven University of Technology

Dr. José Manuel Vicent-Luna  
Eindhoven University of Technology

Dissertation submitted to obtain the degree of Doctor with international mention.

SEVILLE, DECEMBER 2022

ISBN: 978-84-09-45592-8

Copyright © Rafael María Madero Castro

 0000-0002-2472-9854



Printed by: LLARdigital

---

---

■ **Doctoral Supervisors**

Prof. Sofía Calero

Dr. José Manuel Vicent Luna

■ **Examination Committee**

Chair: Dra. Conchi Ania

Secretary: Dr. Said Hamad Gómez

Member: Dr. Carlos Romero Muñiz

■ **External Committee**

Dr. David Dubbeldam

Dr. Juan Manuel Castillo Sánchez

---

---

The research reported in this thesis was carried out at the Department of Physical, Chemical, and Natural Systems in the University Pablo de Olavide (Seville, Spain)



## Table of Contents

	<b>Page</b>
<b>1 Introduction</b>	<b>1</b>
1.1 ADSORBATES (ALCOHOLS) . . . . .	2
1.2 POROUS MATERIALS . . . . .	3
1.2.1 Zeolites . . . . .	3
1.2.2 Metal Organic Frameworks (MOFs) . . . . .	4
1.2.3 Activated Carbons . . . . .	5
1.3 APPLICATIONS . . . . .	6
1.3.1 Gas Uptake . . . . .	6
1.3.2 Gas Separation . . . . .	6
1.3.3 Heat Transfer . . . . .	6
1.3.4 Heat Pumps and Chillers . . . . .	7
1.4 MODELING AND SIMULATION . . . . .	7
1.5 OUTLINE AND SCOPE OF THE THESIS . . . . .	8
1.6 BIBLIOGRAPHY . . . . .	8
<b>2 Methodology</b>	<b>13</b>
2.1 MONTE CARLO SIMULATION . . . . .	14
2.2 MOLECULAR DYNAMICS . . . . .	18
2.2.1 Pervaporation Membranes . . . . .	18
2.3 ENERGY MINIMIZATION . . . . .	19
2.4 PERIODIC BOUNDARY CONDITIONS . . . . .	19
2.5 SIMULATION DATA . . . . .	20
2.6 FORCE FIELDS AND MODELS . . . . .	24
2.6.1 Non-bonded potential . . . . .	24
2.6.2 Bonded potential . . . . .	25
2.6.3 Molecules . . . . .	26
2.6.4 Rigid and Flexible Structures . . . . .	26

2.7	THERMODYNAMICAL MODEL . . . . .	27
2.8	DEVELOPED HOMEMADE CODES . . . . .	29
2.9	BIBLIOGRAPHY . . . . .	32
<b>3</b>	<b>Adsorption of Light Alcohols in High Hydrophobic Metal Azolate Framework</b>	<b>33</b>
3.1	INTRODUCTION . . . . .	34
3.2	SIMULATION DETAILS . . . . .	36
3.3	RESULTS AND DISCUSSION . . . . .	38
3.4	CONCLUSIONS . . . . .	46
3.5	BIBLIOGRAPHY . . . . .	46
<b>4</b>	<b>The Role of Hydrogen Bonding in the Dehydration of Bioalcohols in Hydrophobic Pervaporation Membranes</b>	<b>49</b>
4.1	INTRODUCTION . . . . .	50
4.2	SIMULATION DETAILS . . . . .	52
4.3	RESULTS AND DISCUSSION . . . . .	54
4.3.1	Force field validation . . . . .	54
4.3.2	Single component permeation of methanol, ethanol and water in the MFI membrane . . . . .	54
4.3.3	Dehydration of binary alcohol-water mixtures in the MFI membrane	56
4.4	CONCLUSIONS . . . . .	59
4.5	BIBLIOGRAPHY . . . . .	59
<b>5</b>	<b>Adsorption of Linear Alcohols in Amorphous Activated Carbons: Implications for Energy Storage Applications</b>	<b>61</b>
5.1	INTRODUCTION . . . . .	62
5.2	SIMULATION DETAILS . . . . .	64
5.3	RESULTS AND DISCUSSION . . . . .	69
5.4	CONCLUSIONS . . . . .	78
5.5	BIBLIOGRAPHY . . . . .	79
<b>6</b>	<b>On the use of Water and Methanol with Zeolites for Heat Transfer</b>	<b>83</b>
6.1	INTRODUCTION . . . . .	84
6.2	METHODOLOGY . . . . .	86
6.2.1	Experimental Details . . . . .	86
6.2.2	Simulation Details . . . . .	86
6.2.3	Thermodynamical Model . . . . .	88

6.3	RESULTS AND DISCUSSION . . . . .	88
6.4	CONCLUSIONS . . . . .	98
6.5	BIBLIOGRAPHY . . . . .	98
<b>7</b>	<b>Alcohol-Based Adsorption Heat Pumps using Hydrophobic Metal-Organic Frameworks</b>	<b>101</b>
7.1	INTRODUCTION . . . . .	102
7.2	METHODOLOGY . . . . .	105
7.2.1	Adsorbents . . . . .	105
7.2.2	Simulation Details . . . . .	107
7.2.3	Thermodynamic Model . . . . .	108
7.2.4	Multistep Process . . . . .	109
7.3	RESULTS AND DISCUSSION . . . . .	111
7.4	CONCLUSIONS . . . . .	120
7.5	BIBLIOGRAPHY . . . . .	121
<b>8</b>	<b>CONCLUSIONS</b>	<b>125</b>
	<b>SUMMARY</b>	<b>129</b>
	<b>RESUMEN</b>	
	<b>(Summary in Spanish)</b>	<b>131</b>
<b>1</b>	<b>Appendix 1</b>	<b>133</b>
<b>2</b>	<b>Appendix 2</b>	<b>139</b>
2.1	Force field parameters for the MFI membrane atoms . . . . .	140
2.2	GCMC methodology . . . . .	142
2.3	CGD-MD parameters . . . . .	142
2.4	Supplementary results from CGD-MD simulations . . . . .	143
<b>3</b>	<b>Appendix 3</b>	<b>147</b>
3.1	Bibliography . . . . .	152
<b>4</b>	<b>Appendix 4</b>	<b>155</b>
4.1	Structural model for zeolites . . . . .	156
4.2	Parameterization of methanol-zeolite interactions . . . . .	156
4.3	Thermodynamical model . . . . .	158
4.4	Bibliography . . . . .	161

<b>5 Appendix 5</b>	<b>163</b>
5.1 Bibliography . . . . .	168
<b>List of publications</b>	<b>169</b>
<b>Acknowledgements/Agradecimientos</b>	<b>171</b>

## Introduction

---

Alcohols are organic chemical compounds that are found naturally. Since polar molecules are composed of hydroxyl groups that replace hydrogen atoms in an alkane, the number of accessible alcohols and their configurations are very high.

Because there are many alcohols, the systematic study of their properties is complex. With this in mind, the use of advanced techniques in simulation is an interesting and low cost alternative to experimental studies. In addition, molecular simulations provide valuable information about microscopic magnitudes, which are inaccessible by experiments. Monte Carlo methods, molecular dynamics and energy minimization algorithms are powerful tools to study the behaviour of alcohols in their pure state, in mixtures with other substances or interacting with solids.



This thesis studies the possibility of using molecules of alcohol, both pure and mixed with water, in combination with porous materials. These porous materials are diverse, each with particular characteristic: zeolites, metal organic frameworks (MOFs) and activated carbons, are the ones studied here.

---

## 1.1 ADSORBATES (ALCOHOLS)

Alcohols are organic molecules composed by hydroxyl groups ( $-OH$ ) attached to an aliphatic atom of carbon.<sup>1</sup> Alcohols contain two (diols), three (triols) or more (polyols) hydroxyl groups and also groups bonded to aromatic rings (phenols). Alcohols have many applications at industrial level, such as the creation of polymers and polycarbonates<sup>2-7</sup>, fuels<sup>2,5,8-10</sup> or solvents.<sup>11-14</sup> Linear alcohols are formed by a chain of  $CH_2$  groups linked to a methyl group ( $CH_3-$ ) and to a hydroxyl group. Branched alcohols have the  $-OH$  group bonded to a central carbon in the chain. Methanol ( $CH_3OH$ ) is the simplest alcohol, consisting solely of a methyl group attached to a hydroxyl group. Methanol is used to obtain hydrogen for fuel cells,<sup>15-18</sup> as working fluid in thermal machines<sup>19-25</sup> or as raw material to produce hydrocarbons.<sup>26-30</sup> Ethanol ( $C_2H_5OH$ ) is the most used alcohol due to its low toxicity and ease of obtaining from sugars fermentation.<sup>31-35</sup> Ethanol is used as biofuel,<sup>11,36-38</sup> in spirits,<sup>39,40</sup> as a solvent,<sup>11-14</sup> in the medical industry<sup>41-43</sup> and thermal reactors as heat transfer fluid.<sup>19,21,22,25</sup> Propanol ( $C_3H_7OH$ ) is used as an organic solvent<sup>11-14</sup> and a chemical intermediate in the production of amines and esters.<sup>44,45</sup> Propanol is also used as a biofuel because is less corrosive than ethanol,<sup>46</sup> but its primary use is as a propylene precursor, an important product for synthesising of some plastics.<sup>47</sup> Propanol can be obtained

from organic waste through microbial production.<sup>45,48</sup> Butanol ( $C_4H_9OH$ ) is considered one of the most promising biofuels due to its remarkable adaptability to various types of engines<sup>49,50</sup>. Linear alcohols with five or more atoms of carbon have higher heat capacity than short-chain alcohols.<sup>51,52</sup> In addition to the uses above, these alcohols are used as fuel or as additives for gasoline.<sup>53</sup>

Large-scale production of alcohols is carried out through chemical reactions.<sup>54,55</sup> Alcohols, used as cooling fluids and present in the petrochemical industry, are susceptible to being mixed with water.<sup>56,57</sup> Given the polar nature of both molecules and the presence of  $-OH$  groups, they can interact through hydrogen bonds and form clusters.<sup>57,58</sup> Dehydration of alcohol is a needed process for two reasons. First, ecological since the filtration of alcohols into rivers and seas can destroy flora and fauna of these areas.<sup>59</sup> Second, the economic reason since the recovery of raw materials lowers the costs of industrial applications. The main mechanism for alcohol-water separation is distillation.<sup>60</sup> However, this method has drawbacks, such as the high energy cost of heating the alcohol-water mixture and the impossibility of separating azeotropes.<sup>60</sup> For this reason, alternative techniques have been sought, such as pervaporation membranes (in liquid or gaseous state) or separation by adsorption in porous materials.<sup>61</sup>

This thesis aims to study the prop-

erties of molecules of alcohol and their physicochemical interactions, purification and use as working fluids in energetic processes such as energy transfer or heat pump applications.

## 1.2 POROUS MATERIALS

This section describes the porous materials that will be used to adsorb the molecules of alcohol. Zeolites, Metal Organic Frameworks (MOFs), Zeolitic Imidazole Frameworks (ZIFs) and activated carbon (ACs) have been studied. These frameworks have a periodic structure or can be studied using simplified models (ACs). When a molecule of gas interacts with the internal surface of the structure, it releases energy in the form of heat, making the system more stable.<sup>62</sup> The amount of energy released depends on the strength of the interaction of the molecule (guest) with the framework (host), which is given, among other factors, by the degree of hydrophobicity/hydrophilicity of the adsorbate-adsorbent pair.<sup>63</sup> The hydrophobicity of molecules of alcohol depends on the composition (number of carbon atoms and  $-OH$  groups) and geometry.<sup>64</sup> The hydrophobicity of the adsorbents depends on factors such as chemical composition, topology and other structural properties.<sup>24</sup>

### 1.2.1 Zeolites

Zeolites are microporous materials formed by silicon and oxygen tetrahedra, linked through covalent bonds. These tetrahedra are called Primary Building Units

(PBUs). PBU configurations generate the different topologies. Pure silica zeolites are highly hydrophobic materials due to the lack of unpaired electrons. However, they may contain impurities. Other metals, generally aluminium, can replace the atoms of silicon of some tetrahedra. Impurities introduce unpaired electrons into the tetrahedron, which are compensated with cations. These cations can be protons or heavier atoms such as sodium or calcium. The amount and type of cations change the degree of hydrophobicity of the zeolite.

Zeolites, as crystalline materials, have well-known symmetries and periodicity. They have specific topologies that can be studied through the unit cell. The unit cell represents the structure, and it can be replicated in space to generate an infinite crystal without edge effects. Figure 1 shows the PBU and some examples of zeolite topologies.

The first documented zeolites date from 1756 by Axel Fredrik Cronstedt. There are about 300 catalogued zeolites topologies, natural and from synthesis. Among others applications, zeolites are used for gas storage,<sup>65–67</sup> on catalysts<sup>26</sup> or as heat transfer devices<sup>67</sup>. The composition and topologies of the zeolites give pore sizes between 3 – 14 Å. Zeolites are structures with high stability and very low flexibility compared to other materials, so they can usually be considered rigid. This thesis studies zeolites for energy applications and for pervaporation membranes to

dehydrate methanol and ethanol.

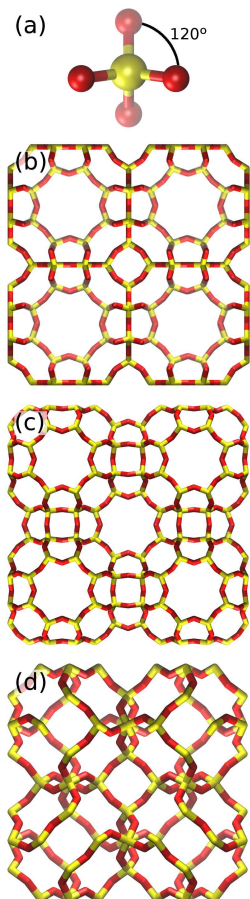


**Figure 1.** (a) PBU, (b) LTA, (c) RHO and (d) SOD topology. Yellow atoms represent atoms of silicon while red atoms represent atoms of oxygen.

For their relevance in industry, we emphasize the study of Faujasite (FAU) and MFI zeolites. FAU is the most used zeolite in catalysis and separation.<sup>66</sup> The unit cell is composed by 192 atoms of silicon and 384 atoms of oxygen. The composition can be modified by substituting some atoms of Si by atoms of Al and ex-

traframework cations. FAU has a topology formed by ten-membered rings linked through double rings that form big cages and small cavities named *sodalites*. There are several commercial zeolites with FAU topology but different chemical compositions and, therefore, different properties.

MFI is a zeolite formed by five-membered rings that creates a three-dimensional structure with straight and sinusoidal channels. MFI is industrially used in separation,<sup>68–70</sup> catalysis<sup>71,72</sup> and in the production of membranes.<sup>73</sup>

### 1.2.1.1 Membranes composed by zeolites

MFI is raw material to create membranes.<sup>73</sup> The process is non-trivial. It requires the control of the orientation in the growth of the crystal and the prevention of the twinning.<sup>73</sup> However, once manufactured, the membranes have sieves with straight channels and a very high degree of hydrophobicity.

Pure silica membranes are used for gas-gas or liquid-liquid separation<sup>73</sup> while membranes with impurities can be used in the catalytic reactions of organic compounds.<sup>73</sup>

### 1.2.2 Metal Organic Frameworks (MOFs)

MOFs are crystalline porous materials with metal clusters linked through organic ligands.<sup>58</sup> The characteristics of MOFs are similar to zeolites. They are periodic crystals capable of adsorbing gas molecules releasing energy in the process. However,

their chemistry is very diverse as chemical composition is not restricted to aluminosilicates. Thus, MOFs have many geometries and degrees of hydrophobicity, which entails pores of diverse sizes and shapes. MOFs are usually more flexible than zeolites. The flexibility is reflected in a vibration of the atoms of the structure, rotation of ligands or the variation of the angles of the crystalline cell.<sup>74</sup> Temperature is the main cause of vibration and affects the diffusion of molecules.<sup>75,76</sup> The structural changes are due to factors such as presence of adsorbed molecules,<sup>77</sup> change in PH or external agents.<sup>78</sup> These structural changes can alter the pore size, the window size that prevents or allows molecular diffusion, or changes in the geometry of the framework.<sup>78</sup>

MOFs have similar applications to zeolites.<sup>65</sup> However, they are usually bigger and are therefore optimal for gas adsorption and separation. However, MOFs have less stability than zeolites. This thesis analyses the use of MOFs for storage, separation and energy applications.

There is a subclass of MOF named Zeolitic Imidazole Frameworks (ZIFs). ZIFs are specific MOFs formed by metallic clusters linked by imidazolium ligands.<sup>65</sup> They have zeolite topology and MOF large capacity and variety of compositions.<sup>65</sup> This thesis studies the use of ZIFs in complex thermal machines such as heat pumps. Figure 2 shows a representation of MOF (MIL-140C) and ZIF with topology SOD (ZIF-8).

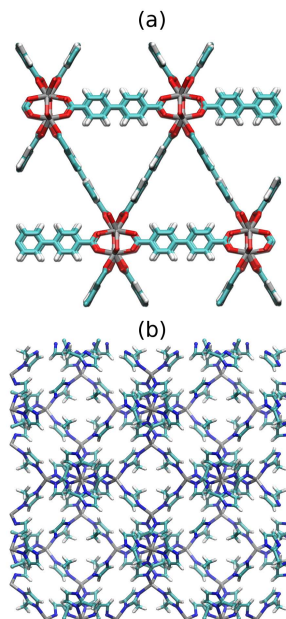


**Figure 2.** (a) MIL-140C and (b) ZIF-8. Gray, blue, red, teal and white atoms represent the atoms of the metal atoms, nitrogen, oxygen, carbon and hydrogen respectively.

For their big capacity and stability, we emphasize the study of MAF-6.<sup>58</sup> MAF-6 has a Zn-based metallic centre linked through an organic ligand of 2-ethylimidazole, forming a RHO topology (big cages linked by cylindrical channels). Its highly hydrophobic degree, low density ( $813.58 \text{ kg/m}^3$ ) and large pore volume ( $0.59 \text{ cm}^3/\text{g}$ ) make MAF-6 a promising candidate for capture, separation or energy applications. MAF-6 is used for fast adsorption removal of phthalic acid from aqueous solution<sup>79</sup> or separation of xylene isomers.<sup>80</sup>

### 1.2.3 Activated Carbons

Activated carbons (ACs) are porous adsorbents formed by atoms of carbon with

traces of oxygen and hydrogen.<sup>81</sup> ACs are obtained from burning organic materials such as wood or sugar cane residues,<sup>82</sup> or from mineral coals.<sup>81</sup> The activation process, determined by the pressure, temperature and composition of the atmosphere in which the pyrolysis occurs, determines the porosity of the samples.<sup>81</sup> ACs are not crystals since they do not have a periodic structure with symmetry, but their density is homogeneous. For this reason, models consider ACs as periodic materials with their atoms uniformly arranged and reproduce the porosity observed in experiments.<sup>81</sup>

ACs are used for gas storage,<sup>83–85</sup> separation, purification,<sup>86,87</sup> drug delivery,<sup>88</sup> photocatalysis<sup>89</sup> and heat transfer.<sup>67,90</sup> Here, we studied the use of ACs obtained from coke pyrolysis at several temperatures. These ACs have been subjected to activation processes to increase their pore volume and adsorption capacity. The cost and stability of ACs make them an attractive alternative to zeolites or MOFs for energy applications.

### 1.3 APPLICATIONS

There are many applications involving alcohol-porous material pairs. From the most straightforward, such as sequestration of molecules of gas,<sup>66,67</sup> to energetic applications,<sup>19,67</sup> separation or purification.<sup>73,86,87</sup> Here, we have studied all mentioned applications focusing on alcohols as fluid in combination with water or pure state, zeolites, MOFs, ZIFs and ACs.

#### 1.3.1 Gas Uptake

Gaseous molecules in the air should be removed for industrial applications<sup>65,83</sup> and also because they are dangerous to health.<sup>91</sup> However, discriminating particles of the size of a few angstroms is highly difficult. In this context, the aforementioned porous materials are desirable alternatives with endless possibilities due to their incredible diversity.<sup>58</sup> The study of the capture of organic and inorganic molecules, with industrial applications or dangerous for the health, has been widely studied in zeolites,<sup>65–67</sup> MOFs<sup>58,65,79</sup> or ACs.<sup>83,84</sup>

#### 1.3.2 Gas Separation

In many cases, chemical industry generates mixtures of water and alcohol as waste that can filter into rivers, generating dangerous contamination.<sup>59</sup> Dehydrating alcohol for ecological and industrial purposes (since it can be used as biofuel) is fundamental to maintaining our ecosystems.<sup>90</sup> The most widespread method is distillation,<sup>90</sup> however, this method uses a large amount of energy, and it is unable to separate azeotropes.<sup>90</sup> This thesis studies the use of membranes based on zeolite MFI to separate alcohols (methanol and ethanol) from water.

#### 1.3.3 Heat Transfer

Applications based on Heat Transfer phenomena intend to solve one of the main problems of renewable energies: their availability on demand.<sup>19</sup> Storing solar, wind or tidal energy and using it on demand is one of the keys to implementing

these technologies at industrial level. This thesis collects studies of energy stored in porous materials such as MOFs, Zeolites or ACs using alcohols as working fluid. These works are based on the fact that adsorption is an exothermic process and can use adsorption-desorption cycles to carry out energy exchange efficiently.

### 1.3.4 Heat Pumps and Chillers

Our planet is experiencing extreme temperatures. Heat Pumps and Chillers can help to mitigate the adverse effects of these extreme conditions.<sup>25</sup> Traditional climatic devices are based on the compression and decompression of a working fluid that, in many cases, is contaminant. Developing new, more environmentally safe and efficient devices is crucial to reduce the emission of greenhouse gases and thus stop a feedback process that ends with a higher global temperature. In this context, we studied the use of molecules of alcohol, both pure and hydrated, in combination with MOFs and ZIFs for the development of heat pumps and chillers with the desired characteristics.

## 1.4 MODELING AND SIMULATION

Given the significant progress in software and hardware that the world has experienced in recent years,<sup>92</sup> the study of physical and chemical systems through simulations is gaining importance. New and more optimized algorithms, large computer networks, artificial intelligence<sup>93</sup> or the still-in-development quantum comput-

ing prove that computational physics and chemistry are and will be very important in the development of science. Currently, Monte Carlo techniques are being used to calculate energy states for several systems,<sup>94–96</sup> to study the atmosphere<sup>97–99</sup> or in quantum calculations.<sup>100,101</sup> Another common simulation technique is molecular dynamics. It is used in many applications, such as to study the protein folding to gain insight into the mechanism of curating diseases.<sup>102</sup> It is also used for characterization of catalytic surfaces<sup>103</sup>, quantum mechanics studies,<sup>104</sup> etc.

Molecular simulations can describe a set of microscopic properties of physical and chemical systems at the molecular level that can be linked with macroscopic properties of the real systems. Through the movement of molecules and atoms of a few angstroms in size and the use of statistical mechanics, molecular mechanics and thermodynamics, we can learn about the world around us.

The use of correct models is a crucial factor in simulation. These models must be complex enough to reproduce the system correctly but simple enough to simulate them quickly. To be used, they have to be validated. Experiments help to validate models, and models and simulations provide extra information about the microscopic world. This way, simulation and experimentation maintain a symbiotic relationship that benefits science.

## 1.5 OUTLINE AND SCOPE OF THE THESIS

This thesis analyses the interaction of molecules of alcohol, both in the pure state and in mixtures with water, with porous materials such as MOFs, zeolites or activated carbons using advanced simulation techniques. The polarity of alcohols and their versatility make them promising adsorbents for numerous industrial processes. This thesis includes the study of the adsorption of alcohols in a hydrophobic MOF, separation and purification of alcohols using membranes and energetic applications of alcohols in several porous materials.

In Chapter 3, we studied how short-chain molecules of alcohol (4 atoms of carbon or less) interact with a highly hydrophobic and large-capacity adsorbent such as MAF-6. The adsorption capacity, the enthalpy of adsorption, or diffusion coefficients of the alcohols inside MAF-6 have been obtained through the data analysis carried out by Monte Carlo simulations and molecular dynamics.

Chapter 4 discusses the performance of a MFI zeolite membrane to separate and purify water and alcohol. Using molecular dynamics, it is shown that the purification cannot be perfect since the mutual interactions between the molecules of alcohol and water play an essential role in the diffusion through the membrane.

Chapters 5-7 focus on studying energy storage applications using alcohol-porous

materials working pairs. For this purpose, we combine Monte Carlo simulations with thermodynamic models of adsorption. Chapter 5 explores the use of porous carbons with molecules of alcohol for thermal energy storage. Chapter 6 shows the development of a set of parameters that describes the interaction of molecules of alcohol and water with zeolites. Using these parameters, we studied the adsorption of alcohols in zeolites with different ratios of cations and the possibility of using this to store thermal energy. Chapter 7 goes a little further and describes the use of alcohols as the working fluid in devices such as heat pumps or chillers based on adsorption-desorption processes in MOFs. Finally, chapter 8 presents the conclusions obtained throughout this thesis.

## 1.6 BIBLIOGRAPHY

- [1] Moss, G. P.; Smith, P. A.; Tavernier, D. *Pure and Applied Chemistry* **1995**, *67*, 1307–1375.
- [2] Sun, D.; Sato, S.; Ueda, W.; Primo, A.; Garcia, H.; Corma, A. *Green Chemistry* **2016**, *18*, 2579–2597.
- [3] Kindermann, N.; Jose, T.; Kleij, A. W. *Topics in Current Chemistry* **2017**, *375*, 1–28.
- [4] Bellamy, L. J.; Pace, R. J. *Spectrochimica Acta* **1966**, *22*, 525–533.
- [5] Lagaron, J. M.; Powell, A. K.; Bonner, G. *Polymer Testing* **2001**, *20*, 569–577.
- [6] Besson, M.; Gallezot, P.; Pinel, C. *Chemical Reviews* **2014**, *114*, 1827–1870.
- [7] Gallezot, P. *Chemical Society Reviews* **2012**, *41*, 1538–1558.
- [8] Liu, X.; Wang, H.; Zheng, Z.; Liu, J.; Reitz, R. D.; Yao, M. *Energy* **2016**, *114*, 542–558.
- [9] Turner, J. W.; Pearson, R. J.; Holland, B.; Peck, R. *SAE Technical Papers* **2007**, *116*, 55–69.
- [10] Cairns, A.; Stansfield, P.; Fraser, N.; Blaxill, H.; Gold, M.; Goodfellow, C.; Sae, S.; Journal, I.; Cairns, A.; Stansfield, P.; Fraser, N.; Blaxill, H.; Gold, M.; Rogerson, J.; Goodfellow, C. *SAE International Journal of Fuels and Lubricants* **2009**, *2*, 41–57.

- [11] Clarke, C. J.; Tu, W. C.; Levers, O.; Bröhl, A.; Hallett, J. P. *Chemical Reviews* **2018**, *118*, 747–800.
- [12] Hoogenboom, R.; Becer, C. R.; Guerrero-Sanchez, C.; Hoepfener, S.; Schubert, U. S. *Australian Journal of Chemistry* **2010**, *63*, 1173–1178.
- [13] Seth, S.; Agrawal, Y. C.; Ghosh, P. K.; Jayas, D. S.; Singh, B. P. *Biosystems Engineering* **2007**, *97*, 209–217.
- [14] Jiang, X.; Wang, Y.; Li, M. *Scientific Reports* **2014**, *4*, 15–18.
- [15] Breen, J. P.; Ross, J. R. *Catalysis Today* **1999**, *51*, 521–533.
- [16] De Wild, P. J.; Verhaak, M. J. *Catalysis Today* **2000**, *60*, 3–10.
- [17] Ulejczyk, B.; Nogal, L.; Mlotek, M.; Krawczyk, K. *Energy Reports* **2022**, *8*, 183–191.
- [18] Qing, S.; Hou, X.; Liu, Y.; Li, L.; Wang, X.; Gao, Z.; Fan, W. *Chemical Communications* **2018**, *54*, 12242–12245.
- [19] Madero-Castro, R. M.; Vicent-Luna, J. M.; Peng, X.; Calero, S. *ACS Sustainable Chemistry Engineering* **2022**, *10*, 6509–6520.
- [20] Shi, Z.; Liang, H.; Yang, W.; Liu, J.; Liu, Z.; Qiao, Z. *Chemical Engineering Science* **2020**, *214*, 115430.
- [21] Chauhan, P. R.; Kaushik, S. C.; Tyagi, S. K. *Energy Conversion and Management: X* **2022**, *14*, 100225.
- [22] Moreno, D.; Ferro, V. R.; de Riva, J.; Santiago, R.; Moya, C.; Larriba, M.; Palomar, J. *Applied Energy* **2018**, *213*, 179–194.
- [23] Edin Hamrahi, S.; Goudarzi, K.; Yaghoubi, M. *Solar Energy* **2018**, *173*, 920–927.
- [24] Sun, T.; Hao, S.; Fan, R.; Qin, M.; Chen, W.; Wang, P.; Yang, Y. *ACS Applied Materials and Interfaces* **2020**, *12*, 56435–56444.
- [25] De Lange, M. F.; Verouden, K. J.; Vlught, T. J.; Gascon, J.; Kapteijn, F. *Chemical Reviews* **2015**, *115*, 12205–12250.
- [26] Chang, C. D. *Catalysis Reviews: Science and Engineering* **1983**, *25*, 1–118.
- [27] Tan, K. B.; Zhan, G.; Sun, D.; Huang, J.; Li, Q. *Journal of Materials Chemistry A* **2021**, *9*, 5197–5231.
- [28] Liu, Y.; Kirchberger, F. M.; Müller, S.; Eder, M.; Tonigold, M.; Sanchez-Sanchez, M.; Lercher, J. A. *Nature Communications* **2019**, *10*, 1–9.
- [29] Zhang, W.; Zhi, Y.; Huang, J.; Wu, X.; Zeng, S.; Xu, S.; Zheng, A.; Wei, Y.; Liu, Z. *ACS Catalysis* **2019**, *9*, 7373–7379.
- [30] Yarulina, I.; Chowdhury, A. D.; Meirer, F.; Weckhuyssen, B. M.; Gascon, J. *Nature Catalysis* **2018**, *1*, 398–411.
- [31] Chen, S.; Xu, Z.; Li, X.; Yu, J.; Cai, M.; Jin, M. *Biorenewable Technology* **2018**, *258*, 18–25.
- [32] da Conceição Gomes, A.; Rodrigues, M. I.; de França Passos, D.; Machado de Castro, A.; Maria Mello Santa Anna, L.; Pereira, N. *Electronic Journal of Biotechnology* **2019**, *42*, 16–22.
- [33] Wang, L.; York, S. W.; Ingram, L. O.; Shanmugam, K. T. *Biorenewable Technology* **2019**, *273*, 269–276.
- [34] Galbe, M.; Zacchi, G. *Applied Microbiology and Biotechnology* **2002**, *59*, 618–628.
- [35] Lian, J.; Chen, S.; Zhou, S.; Wang, Z.; O’Fallon, J.; Li, C. Z.; Garcia-Perez, M. *Biorenewable Technology* **2010**, *101*, 9688–9699.
- [36] Franco, J. H.; Minter, S. D.; de Andrade, A. R. *Journal of The Electrochemical Society* **2018**, *165*, H575–H579.
- [37] Zhou, Y.; Chen, Y.; Li, M.; Hu, C. *Renewable Energy* **2020**, *147*, 293–301.
- [38] Zabed, H.; Sahu, J. N.; Suely, A.; Boyce, A. N.; Faruq, G. *Renewable and Sustainable Energy Reviews* **2017**, *71*, 475–501.
- [39] Martinez, P.; Kerr, W. C.; Subbaraman, M. S.; Roberts, S. C. *Alcoholism: Clinical and Experimental Research* **2019**, *43*, 509–521.
- [40] Rochte, J. D.; Berglund, K. A. *Beverages* **2019**, *5*, 1–8.
- [41] Karahanian, E.; Quintanilla, M. E.; Tampier, L.; Rivera-Meza, M.; Bustamante, D.; Gonzalez-Lira, V.; Morales, P.; Herrera-Marschitz, M.; Israel, Y. *Alcoholism: Clinical and Experimental Research* **2011**, *35*, 606–612.
- [42] Le Daré, B.; Gicquel, T. *Journal of pharmacy pharmaceutical sciences* **2019**, *22*, 525–535.
- [43] Sadakane, K.; Ichinose, T. *International Journal of Medical Sciences* **2015**, *12*, 116–125.
- [44] Ho, C. R.; Defalque, V.; Zheng, S.; Bell, A. T. *ACS Catalysis* **2019**, *9*, 2931–2939.
- [45] Walther, T.; François, J. M. *Biotechnology Advances* **2016**, *34*, 984–996.
- [46] Fernando, S.; Adhikari, S.; Kota, K.; Bandi, R. *Fuel* **2007**, *86*, 2806–2809.
- [47] Kibby, C. L.; Hall, W. K. *Journal of Catalysis* **1973**, *29*, 144–159.
- [48] Cho, C.; Choi, S. Y.; Luo, Z. W.; Lee, S. Y. *Biotechnology Advances* **2015**, *33*, 1455–1466.
- [49] Zhen, X.; Wang, Y.; Liu, D. *Renewable Energy* **2020**, *147*, 2494–2521.
- [50] Jin, C.; Yao, M.; Liu, H.; Lee, C. F. F.; Ji, J. *Renewable and Sustainable Energy Reviews* **2011**, *15*, 4080–4106.
- [51] Perez-Casas, S.; Castillo, R.; Costas, M. *Journal of Physical Chemistry B* **1997**, *101*, 7043–7054.
- [52] Ashrafi, F.; Saadati, R.; Amlashi, A. B.; Ave, F.; St, K. *Afr. J. Pure Appl. Chem.* **2008**, *2*, 116–120.
- [53] Graciaa, A.; Lachaise, J.; Cucuphat, C.; Bourrel, M.; Salager, J. L. *Langmuir* **1993**, *9*, 3371–3374.
- [54] Scully, S. M.; Orlygsson, J. *Advanced Bioprocessing for Alternative Fuels, Biobased Chemicals, and Bioproducts: Technologies and Approaches for Scale-Up and Commercialization*; Elsevier Inc., 2019; pp 83–108.
- [55] Torres, G. M.; Frauenlob, R.; Franke, R.; Börner, A. *Catalysis Science and Technology* **2015**, *5*, 34–54.
- [56] Wensink, E. J.; Hoffmann, A. C.; Van Maaren, P. J.; Van Der Spoel, D. *Journal of Chemical Physics* **2003**, *119*, 7308–7317.
- [57] Onori, G.; Santucci, A. *Journal of Molecular Liquids* **1996**, *69*, 161–181.

- [58] Madero-Castro, R.; Vicent-Luna, J.; Calero, S. *The Journal of Physical Chemistry C* **2019**, *123*, 23987–23994.
- [59] Dewey, H. M.; Jones, J. M.; Keating, M. R.; Budhathoki-Uprety, J. *ACS Chemical Health Safety* **2022**, *29*, 27–38.
- [60] Haider, J.; Harvianto, G. R.; Qyyum, M. A.; Lee, M. *ACS Sustainable Chemistry and Engineering* **2018**, *6*, 14901–14910.
- [61] Zohreh Raeisia\*, Laleh Hosseinzadeha, A. M.; Sadeghi, M. *Iranian Chemical Society* **2021**,
- [62] Teker, M.; Imamoglu, M.; Saltabas, Ö. *Turkish Journal of Chemistry* **1999**, *23*, 185–191.
- [63] Nuhnén, A.; Janiak, C. *Dalton Transactions* **2020**, *49*, 10295–10307.
- [64] Ballal, D.; Chapman, W. G. *Journal of Chemical Physics* **2013**, *139*.
- [65] Azam, T.; Pervaiz, E.; Javed, S.; Amina, S. J.; Khalid, M. S. *Chemical Physics Impact* **2020**, *1*, 100001.
- [66] Calero, S.; Dubbeldam, D.; Krishna, R.; Smit, B.; Vlught, T. J.; Denayer, J. F.; Martens, J. A.; Maesen, T. L. *Journal of the American Chemical Society* **2004**, *126*, 11377–11386.
- [67] Kohler, T.; Müller, K. *Energy Science and Engineering* **2017**, *5*, 21–29.
- [68] Masuda, T.; Asanuma, T.; Shouji, M.; Mukai, S. R.; Kawase, M.; Hashimoto, K. *Chemical Engineering Science* **2003**, *58*, 649–656.
- [69] Lin, X.; Kita, H.; Okamoto, K. I. *Industrial and Engineering Chemistry Research* **2001**, *40*, 4069–4078.
- [70] Shu, X.; Wang, X.; Kong, Q.; Gu, X.; Xu, N. *Industrial and Engineering Chemistry Research* **2012**, *51*, 12073–12080.
- [71] Yan, Y.; Jiang, S.; Zhang, H.; Zhang, X. *Chemical Engineering Journal* **2015**, *259*, 243–251.
- [72] Chen, H.; Zhang, H.; Yan, Y. *Chemical Engineering Journal* **2014**, *254*, 133–142.
- [73] Li, Y.; Zhu, G.; Wang, Y.; Chai, Y.; Liu, C. *Microporous and Mesoporous Materials* **2021**, *312*, 110790.
- [74] Sussardi, A.; Hobday, C. L.; Marshall, R. J.; Forgan, R. S.; Jones, A. C.; Moggach, S. A. *Angewandte Chemie* **2020**, *132*, 8195–8199.
- [75] Balestra, S. R.; Bueno-Perez, R.; Hamad, S.; Dubbeldam, D.; Ruiz-Salvador, A. R.; Calero, S. *Chemistry of Materials* **2016**, *28*, 8296–8304.
- [76] Vicent-Luna, J. M.; Idígoras, J.; Hamad, S.; Calero, S.; Anta, J. A. *Journal of Physical Chemistry C* **2014**, *118*, 28448–28455.
- [77] Slawek, A.; Vicent-Luna, J. M.; Marszalek, B.; Gil, B.; Morris, R. E.; Makowski, W.; Calero, S. *Chemistry of Materials* **2018**, *30*, 5116–5127.
- [78] Namsani, S.; Yazaydin, A. O. *Molecular Systems Design and Engineering* **2018**, *3*, 951–958.
- [79] Wang, C.; Yan, X.; Hu, X.; Zhou, M.; Ni, Z. *Journal of Molecular Liquids* **2016**, *223*, 427–430.
- [80] He, C.-t.; Jiang, L.; Ye, Z.-m.; Krishna, R.; Zhong, Z.-s.; Liao, P.-q.; Xu, J.; Ouyang, G.; Zhang, J.-p.; Chen, X.-m. *Journal of the American Chemical Society* **2015**, *137*, 7217–7223.
- [81] Jain, S. K.; Pellenq, R. J.; Pkunic, J. P.; Gubbins, K. E. *Langmuir* **2006**, *22*, 9942–9948.
- [82] Pollard, S. J. T.; Fowler, G. D.; Sollars, C. J.; Perry, R. *The Science of the Total Environment* **1992**, *116*, 31–52.
- [83] Plaza, M. G.; Pevida, C.; Arenillas, A.; Rubiera, F.; Pis, J. J. *Fuel* **2007**, *86*, 2204–2212.
- [84] Plaza, M. G.; García, S.; Rubiera, F.; Pis, J. J.; Pevida, C. *Chemical Engineering Journal* **2010**, *163*, 41–47.
- [85] García, S.; Pis, J. J.; Rubiera, F.; Pevida, C. *Langmuir* **2013**, *29*, 6042–652.
- [86] Peng, X.; Wang, W.; Xue, R.; Shen, Z. *AIChE Journal* **2006**, *52*, 994–1003.
- [87] Lopes, F. V. S.; Grande, C. A.; Rodrigues, A. E. *Chemical Engineering Science* **2011**, *66*, 303–317.
- [88] Miriyala, N.; Ouyang, D.; Perrie, Y.; Lowry, D.; Kirby, D. J. *European Journal of Pharmaceutics and Biopharmaceutics*; 2017; Vol. 115; pp 197–205.
- [89] Ahmad, A.; Jini, D.; Aravind, M.; Parvathiraja, C.; Ali, R.; Kiyani, M. Z.; Alothman, A. *Arabian Journal of Chemistry* **2020**, *13*, 8717–8722.
- [90] Madero-Castro, R. M.; Calero, S.; Yazaydin, A. O. *Journal of Molecular Liquids* **2021**, *340*, 117297.
- [91] Matito-Martos, I.; Moghadam, P. Z.; Li, A.; Colombo, V.; Navarro, J. A.; Calero, S.; Fairen-Jimenez, D. *Chemistry of Materials* **2018**, *30*, 4571–4579.
- [92] Mollick, E. *IEEE Annals of the History of Computing* **2006**, *28*, 62–75.
- [93] Ramesh, A.; Pavlov, M.; Goh, G.; Gray, S.; Voss, C.; Radford, A.; Chen, M.; Sutskever, I. Zero-Shot Text-to-Image Generation. 2021; <https://arxiv.org/abs/2102.12092>.
- [94] Buendía, E.; Gálvez, F. J.; Maldonado, P.; Sarsa, A. *Chemical Physics Letters* **2014**, *615*, 21–25.
- [95] Blume, D.; Greene, C. H. *Physical Review A - Atomic, Molecular, and Optical Physics* **2001**, *63*, 063601.
- [96] Deustua, J. E.; Yuwono, S. H.; Shen, J.; Piecuch, P. *Journal of Chemical Physics* **2019**, *150*, 111101.
- [97] Gao, M.; Yin, L.; Ning, J. *Atmospheric Environment* **2018**, *184*, 129–139.
- [98] Antanasijević, D.; Pocažt, V.; Perić-Grujić, A.; Ristić, M. *Journal of Hydrology* **2014**, *519*, 1895–1907.
- [99] Dehghani, M.; Saghafian, B.; Nasiri Saleh, F.; Farokhnia, A.; Noori, R. *International Journal of Climatology* **2014**, *34*, 1169–1180.
- [100] Tews, I. *Frontiers in Physics* **2020**, *8*, 1–19.
- [101] Lynn, J. E.; Tews, I.; Gandolfi, S.; Lovato, A. *Annual Review of Nuclear and Particle Science* **2019**, *69*, 279–305.
- [102] Staples, M.; Chan, L.; Si, D.; Johnson, K.; Whyte, C.; Cao, R. Artificial Intelligence for Bioinformatics: Applications in Protein Folding Prediction. 2019 IEEE Technology Engineering Management Conference (TEMSCON). 2019; pp 1–8.

[103] Liu, W.; Zhu, Y.; Wu, Y.; Chen, C.; Hong, Y.; Yue, Y.; Zhang, J.; Hou, B. *Catalysts* **2021**, *11*.

[104] Shen, L.; Yang, W. *Journal of Chemical Theory and Computation* **2018**, *14*, 1442–1455, PMID: 29438614.

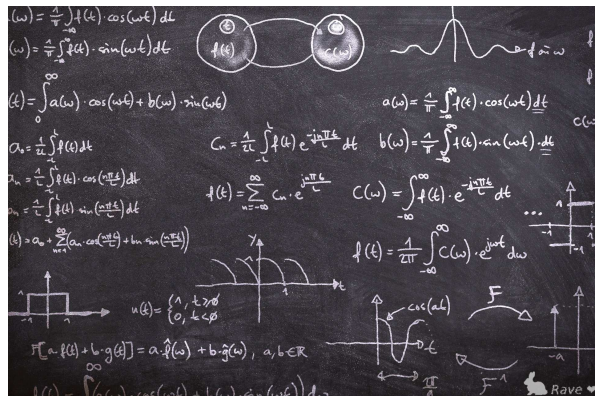


## Methodology

This chapter summarizes the methods and models developed and used in this thesis. Monte Carlo (MC), Molecular Dynamics (MD) and Energy Minimization (EM) are the main methods. Using molecular simulation, we have calculated properties such as adsorption capacity or diffusion coefficients.

Data obtained from simulations together with thermodynamical models are used to study the enthalpy of adsorption ( $\Delta H$ ), the average number of hydrogen bonds (nHB) or storage density (SD) of the working pair.

In this thesis, we have combined molecular simulations with thermodynamical models to study energetic applications. To bridge the gap between the results obtained from the simulations and the computation of properties needed to describe the targeted applications, we have developed a set of homemade codes. These codes combine the FORTRAN programming language with BASH shell scripts. The working principle of the most representative codes will be briefly described at the end of this chapter.



Simulation techniques provide knowledge on macroscopic magnitudes such as internal energy, temperature or entropy from microscopic variables such as the positions and momentum of the particles in the system. To connect microscopic and macroscopic properties, it resorts to statistical mechanics, a part of physics responsible for relating macroscopic magnitudes, measurable in a laboratory, with the behaviour of the individual particles that compose the system. All simulations in this thesis are performed using the RASPA code (for Monte Carlo and Energy Minimization),<sup>1</sup> LAMMPS<sup>2</sup> and GROMACS<sup>3</sup> (for Molecular Dynamics).

## 2.1 MONTE CARLO SIMULATION

The Monte Carlo (MC) method is based on solving problems by generating random numbers.<sup>4</sup> MC is especially useful for solving probabilistic equations such as those in statistical mechanics. Based on the law of large numbers, MC simulation used in this thesis follows the Monte Carlo Markov Chain (MCMC) method.<sup>5</sup> MCMC provides a “random” value within the possibilities given by the equations that govern statistical mechanics. That is, it generates microstates accessible to the system according to a certain probability. When the number of trials is large enough, the average value obtained, which is the most probable (assuming normal distribution), is the observed in the experiments. The measured error can be estimated from the

expression  $e = \sqrt{\mathbf{N}}$  by the Central Limit Theorem, where  $\mathbf{N}$  is the number of data evaluated.<sup>4</sup>

If we suppose a vector  $X_i^j(\vec{r}_i, \vec{p}_i)$  that represents  $i = 1, \dots, N$  particles for  $j = 1, \dots, J$  different configurations using their phase space variables (position,  $\vec{r}_i$  and momentum,  $\vec{p}_i$ ), the probability that any particle  $i$  evolves from a state  $j$  to a state  $j + 1$  will be given by the expression

$$P_{j,j+1} = P\{X_i^{j+1} | X_i^j\} \quad (2.1)$$

This transition probability depends exclusively on the immediately previous state, that is, on state  $j$ . To generate the  $j + 1$  state, MCMC uses the generation of random numbers that configure this new state. The probability of accepting this new state will be higher the more favourable the new configuration is. A random number,  $a$ , is created and the move is accepted if  $a < P_{j,j+1}$ . For this reason, the method is also called “random walk”.<sup>6</sup> It simulates a walker who moves randomly through accessible states, but there is a convergence towards the most probable states. MCMC is an algorithm used to solve many problems. In this thesis, the probability of each accessible state is represented by a function that depends on the group (ensemble) in which the calculations are performed.<sup>7</sup> The ensembles used here are:

### Micro Canonical Ensemble (NVE)

This ensemble imposes the number of particles, the volume and the energy of the system. An analogy with the micro-

canonical ensemble is given by a gas with specific internal energy enclosed in a rigid box with adiabatic walls. The probability of finding the gas in a micro-state “ $j$ ” will be given by a constant probability function, that is, all accessible microstates (resulting in  $\mathbf{N}$  particles in a volume  $\mathbf{V}$  with an energy  $\mathbf{E}$ ) will be equally probable. Figure 1a shows an example of a gas in a microcanonical ensemble.

**Canonical Ensemble (NVT)** This ensemble imposes the number of particles, the volume and the temperature of the system. The canonical ensemble can be represented by a rigid box that contains a gas at certain temperature. The system can exchange heat with the environment (Figure 1b). The probability of finding the gas in a micro-state “ $j$ ” is no longer equiprobable. This probability function is proportional to the Boltzmann factor  $\left(e^{-\frac{E}{k_B T}} = e^{-\beta E}\right)$ , where  $E$  is the energy of the system,  $T$  is the temperature and  $k_B$  is the Boltzmann constant.  $\beta = \frac{1}{k_B T}$  is called “Boltzmann factor”. The probability density function is

$$f(\vec{r}_i, \vec{p}_i) \propto e^{-\beta E} \quad (2.2)$$

where  $\vec{r}_i$  and  $\vec{p}_i$  represents the position and momentum of the particle “ $i$ ”. The proportionality constant is the inverse of the partition function,  $Z$

$$f(\vec{r}_i, \vec{p}_i) = \frac{1}{Z} e^{-\frac{E}{k_B T}} \quad (2.3)$$

The energy of the system is represented by the Hamiltonian of the system that depends on its phase state variables

$$E = H(\vec{r}_i, \vec{p}_i) \quad (2.4)$$

And the partition function is determined in a way that normalizes the probability

$$1 = \int_R \int_P f(\vec{r}_i, \vec{p}_i) d\vec{r}_i d\vec{p}_i = \int_R \int_P \frac{1}{Z} e^{-\frac{H(\vec{r}_i, \vec{p}_i)}{k_B T}} d\vec{r}_i d\vec{p}_i \quad (2.5)$$

$$Z = \int_R \int_P e^{-\frac{H(\vec{r}_i, \vec{p}_i)}{k_B T}} d\vec{r}_i d\vec{p}_i \quad (2.6)$$

The probability of finding any microstate “ $A(\vec{r}_i, \vec{p}_i)$ ” is given by the expression

$$\langle A \rangle = \frac{\int_R \int_P e^{-\frac{H(\vec{r}_i, \vec{p}_i)}{k_B T}} A(\vec{r}_i, \vec{p}_i) d\vec{r}_i d\vec{p}_i}{\int_R \int_P e^{-\frac{H(\vec{r}_i, \vec{p}_i)}{k_B T}} d\vec{r}_i d\vec{p}_i} \quad (2.7)$$

This ensemble allows the search for the most stable configuration of a system with a specific temperature. It is used to validate density models, study the most stable configurations for molecules within structures, calculate host-guest interactions and calculate the adsorption enthalpy of the molecules in the material.

### **Grand Canonical Ensemble ( $\mu$ VT)**

This ensemble imposes the volume of the system but allows the exchange of particles and energy by fitting the chemical potential and temperature. The Grand Canonical ensemble can be represented by a rigid box with permeable walls that allow on the exchange of particles and heat with the environment (Figure 1c).

As in the canonical ensemble, the probability density depends on the Boltzmann factor, but it also depends on the chemical potential,  $\mu$ .<sup>8</sup> This parameter represents the change of internal energy when introducing an infinitesimal mass (in our case, a particle) in a homogeneous system without changing entropy or volume. So the probability distribution is

$$f(\vec{r}_i, \vec{p}_i) = \frac{1}{Q} e^{-\frac{H(\vec{r}_i, \vec{p}_i) - \mu N}{k_B T}} \quad (2.8)$$

where “ $Q$ ” is the grand partition function or the partition function for the macrocanonical ensemble. This function allows accessible microstates to have different number of particles. Using this ensemble, it is possible to calculate the adsorption/desorption of molecules of gas in the adsorbent.

Simulations were performed using the MCMC method with the probability distributions mentioned above. The microstates “ $j + 1$ ” generated from the “ $j$ ” were built through programmed movements and executed according to variable weights. These movements are:

**Insertion/Deletion Move.** This movement allows the insertion or elimination of molecules within the simulation box. However, the insertion of molecules, especially long chain molecules, is not trivial. Configurational Bias Monte Carlo (CBMC)<sup>9</sup> helps to improve the probability of acceptance in the insertion of molecules. CBMC is an equiprobable insertion/deletion movement based on the

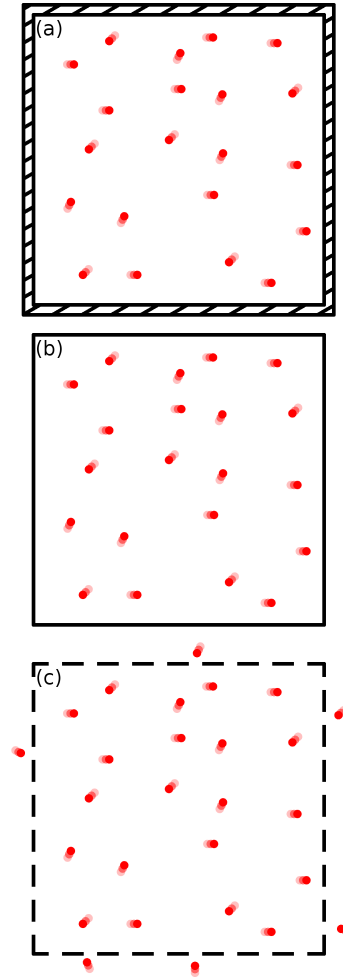


**Figure 1.** Representation of systems in (a) NVE, (b) NVT and (c)  $\mu$ VT ensembles.

insertion of molecules by parts. A position is randomly chosen, and the molecule is grown according to its internal energy, minimizing the total energy of the system. For a molecule composed of  $i = 1, \dots, n$  segments,  $j = 1, \dots, k$  different orientations are generated for each segment  $i$  according to the energy of interaction with the system. Probability is expressed as

$$P_i(j) = \frac{e^{-\frac{U_i(j)}{k_B T}}}{\sum_{j'=1}^k e^{-\frac{U_i(j')}{k_B T}}} = \frac{e^{-\frac{U_i(j)}{k_B T}}}{\omega_i} \quad (2.9)$$

where  $U_i(j)$  represents the energy of the particle “ $i$ ” in configuration “ $j$ ”.  $\omega_i$  is defined like  $\omega_i = \sum_{j'=1}^k e^{-\frac{U_i(j')}{k_B T}}$ . Once the position of segment “ $i$ ” is accepted, the position of segment “ $i + 1$ ” is calculated until the molecule is completely constructed. The Rosenbluth factor is defined as

$$W = \prod_{i=1}^n \omega_i \quad (2.10)$$

The Rosenbluth factor<sup>10</sup> provides information on the flexibility of the molecule and allows to define the probability of acceptance ( $P_{acc}$ ) of this movement from the equation

$$P_{acc}(o \rightarrow n) = \min\left(1, \frac{W(n)}{W(o)}\right) \quad (2.11)$$

where the states “ $o$ ” and “ $n$ ” belong to the old and new configurations, respectively. To insert (or delete) a particle within a system with  $N$  existing particles, the probability will be proportional to the Rosenbluth factor but also to the volume of the system, number of existing particles and chemical potential, which is related to fugacity and therefore to the external pressure. Probabilities of acceptance/removal are:

$$P_{acc}(N \rightarrow N + 1) = \min\left(1, \frac{W^{N+1} V}{k_B T (N + 1) \langle W^{ideal} \rangle} f\right) \quad (2.12)$$

$$P_{acc}(N \rightarrow N - 1) = \min\left(1, \frac{k_B T N \langle W^{ideal} \rangle}{W^{N-1} V} f\right) \quad (2.13)$$

where  $W^\pm$  and  $W^{ideal}$  are the Rosenbluth factor of the new state and the ideal gas, and  $f$  the fugacity. Fugacity can be related to external pressure ( $p$ ) from the fugacity coefficient  $\phi$  by the expression  $f = \phi p$ .

**Translation Move.** This move displaces the molecule randomly through the accessible volume of the simulation box. This movement can be equiprobable or set with different probability in the three directions of the space. The orientation of the molecule is not affected by this movement. The probability for this movement to be accepted is given by

$$P_{acc}(o \rightarrow n) = \min\left(1, e^{\frac{1}{k_B T}(U_i(n) - U_i(o))}\right) \quad (2.14)$$

**Rotation Move.** As for translation, this move allows random rotation of a molecule. The probability of acceptance is the same as that for equation 2.14. The position of the centre of mass of the molecule is not affected by this movement.

**Identity Change Move.** This movement is restricted to mixtures. It changes a molecule “ $i$ ” by another “ $j$ ”. The probability of acceptance is

$$P_{acc}(i \rightarrow j) = \min\left(1, \frac{W_j^i f_j \langle W_i^{ideal} \rangle N_i}{W_i^j f_i \langle W_j^{ideal} \rangle (N_j + 1)}\right) \quad (2.15)$$

## 2.2 MOLECULAR DYNAMICS

MD relies on solving the equations of mechanics (Newton's or Hamilton's equations) to reconstruct the path that particles follow.<sup>7</sup> MD is a deterministic method that calculates positions and velocities at an instant of time “ $t + \Delta t$ ” from the configuration at time “ $t$ ”. The velocity-Verlet algorithm is the most widespread for MD. It is a Cauchy problem, a second-order method with initial variables. The equations that govern this method are:

$$\begin{aligned}\vec{r}_i(t + \Delta t) &= \vec{r}_i(t) + \vec{v}_i(t)\Delta t + \frac{\vec{f}_i(t)}{2m}\Delta t^2 + \\ &\quad + \Theta(\Delta t^3) \\ \vec{v}_i(t + \Delta t) &= \vec{v}_i(t) + \frac{\vec{f}_i(t) + \vec{f}_i(t + \Delta t)}{m}\Delta t + \\ &\quad + \Theta(\Delta t^3)\end{aligned}\quad (2.16)$$

where  $\vec{r}_i(t)$ ,  $\vec{v}_i(t)$  and  $\vec{f}_i(t)$  represent the position, velocity and forces exerted on the particle “ $i$ ” at the time “ $t$ ”. “ $m$ ” is the mass of the particle, and “ $\Delta t$ ” is the simulation time step. The choice of this timestep is crucial element in simulation. Very small timesteps increase the calculation time and the accumulation error, while large timesteps lead to non-reliable values.<sup>11</sup> This algorithm introduces a control element based on the energy change in each step. If the change in energy exceeds a typical value “ $\delta$ ” after “ $\lambda$ ” integration steps according to equation 2.17, the method fails and indicates that the timestep is too large.

$$\sum_{i=1}^{\lambda} \left| 1 - \frac{E(i \cdot \Delta t)}{E(0)} \right| < \delta \lambda \quad (2.17)$$

MD allows to average in time a property  $\langle A \rangle$ , that is, in thermodynamic equilibrium.

$$\langle A \rangle = \lim_{t \rightarrow +\infty} \frac{1}{t} \int_0^t A(\vec{r}_i, t') dt' \quad (2.18)$$

### 2.2.1 Pervaporation Membranes

GROMACS plugin “*Plumed*”<sup>12</sup> can create regions in the simulation box with specific molecule densities. *Plumed* defines three regions in the simulation box, Control Region (CR), Transition Region (TR) and Force Region (FR). Counting the number of molecules in CR, *Plumed* performs a force over the molecules in the FR push or pull up to the TR to obtain the target density. This method allows different densities on both sides of a membrane to simulate a pervaporation membrane. Fixing the liquid density on an edge and vacuum on the other side, the molecules cross the membrane by density gradient.<sup>13</sup> The flux ( $J_z$ ) of particles through the membrane is given by the difference on the particles that cross a perpendicular surface inside the membrane with positive direction ( $N_i^+$ ) and negative direction ( $N_i^-$ ) divided by the surface area ( $A_{xy}$ ) and time ( $t$ ).

$$J_z = \frac{N_i^+ - N_i^-}{t \cdot A_{xy}} \quad (2.19)$$

The pervaporation membrane is created by replicating the unit cell in the  $z$  axis and truncating it perpendicularly by

the most stable plane. Hydrogen atoms are added to maintain charge neutrality.

### 2.3 ENERGY MINIMIZATION

EM searches for the state of the system with the lowest internal energy. Starting from any state decreases the energy to the minimum energy. Various algorithms seek to minimize energy.<sup>14</sup> The simplest is the *Steepest Descent Method*.<sup>14</sup> This method calculates the internal energy of the system on the phase space variables and modifies the coordinates to reach a minimum. Since the potential energy only depends on the position of the particles in the system, only the position of the particles influences the calculation of energy. The minimum energy is reached when the forces exerted on the particles are minimum (zero in an ideal situation) because the (conservative) force is related to the potential energy through the gradient. Thus, we can calculate the minimum energy positions through the equation:

$$\vec{r}_i^n = \vec{r}_i^0 - k_i \vec{\nabla} f(\vec{r}_i^0) \quad (2.20)$$

where  $k_i$  is a dynamical parameter. This method is a good approximation for systems with energies for which the second derivative varies monotonously. However, the possibility of falling into a local minimum is high for more complex functions. For this reason, more complex algorithms such as the *Conjugated Gradient*<sup>15</sup> or *Baker*<sup>16</sup> algorithm are used. These algorithms reduce computation time and find non-local minima more frequently. In this

thesis, EM simulations have been carried out to calculate the position of the binding sites and the most stable configuration of a molecule in a structure.

### 2.4 PERIODIC BOUNDARY CONDITIONS

The systems researched in this thesis are (infinite) crystals and fluids with particles of the order of the Avogadro's number. Since it is impossible to simulate such large systems, we need to apply constraints that reduce the number of degrees of freedom. The aforementioned unit cells represent each crystal with a finite number of degrees of freedom. We can use this fact and reduce the number of degrees of freedom to a computable number just by applying symmetries to the system. This method is called *Periodic Boundary Conditions (PBC)*<sup>7</sup> and allows to define the simulation box as a representative system region with which to obtain all the information through the spatial repetition of the simulation box.

The simulation box must be large enough to represent the system correctly but to a certain level to prevent ample calculation time. The minimum size adopted by the scientific community is at least twice the cutoff of the van der Waals interactions ( $12\text{\AA} < r_{VDW} < 14\text{\AA}$ ).

The simulation box is replicated in all directions according to the cell parameters. It generally assumes a triclinic system composed of three lengths ( $a \neq b \neq c$ ) and angles ( $\alpha \neq \beta \neq \gamma$ ) where side  $a$  coincides

with the x-axis, and  $b$  is in the xy-plane (see Figure 2a). The normalized positions of the triclinic system ( $R'$ ) are related to the Cartesian positions ( $R$ ) through the following transformation matrix  $M$ :

$$M = \begin{pmatrix} a & b \cos \gamma & c \cos \gamma \\ 0 & b \sin \gamma & \frac{c(\cos \alpha - \cos \beta \cos \gamma)}{\sin \gamma} \\ 0 & 0 & \frac{V}{ab \sin \gamma} \end{pmatrix} \quad (2.21)$$

with  $V$

$$V = \frac{abc}{\sin \gamma} \cdot \sqrt{1 - \cos^2 \alpha - \cos^2 \beta - \cos^2 \gamma + 2 \cos \alpha \cos \beta \cos \gamma}$$

so that

$$R = M \times R' \quad (2.22)$$

The matrix  $M$  is used to reproduce the unit cell and to calculate the shortest distance between two points using PBC (Figure 2b).

## 2.5 SIMULATION DATA

This section describes the simulation properties obtained in the thesis. Data and properties were calculated using RASPA,<sup>1</sup> LAMMPS<sup>2</sup> and GROMACS,<sup>3</sup> as well as own codes.

**Helium void fraction (HVF)** defines the accessible space by a helium molecule within a structure divided by the total space it occupies. That is, it is the percentage of available space that molecules of helium can occupy.

**Pore volume (PV)** is closely related to HVF. HVF represents the fraction of occupiable space, and PV represents the accessible volume in the porous material. ( $PV = HVF \times UnitCellVolume$ ).

**Internal surface area (SA)** is calculated by "rolling" a probe molecule, commonly argon or nitrogen, on the internal surface of the structure. This method is implemented by placing spheres centred on each atom of the structure of various radii and eliminating overlaps. The sum of all these surfaces results in the internal surface of the structure.

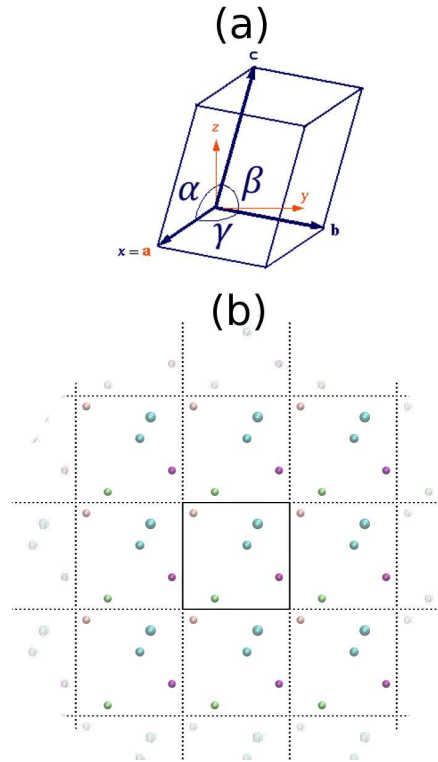


**Figure 2.** Representation of (a) triclinic simulation box and (b) PBC.

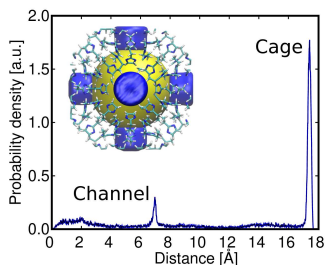


**Figure 3.** Example of PSD of a crystalline material containing channels (blue cylinders) and cages (yellow spheres).

**Pore size distribution (PSD)** is defined as a histogram showing the frequency at which a sphere can be inserted into the various cavities of the structure based on its size. The width of the peaks and their intensity depend on the topology of the structures. Figure 3 shows an example of PSD with its corresponding MOF. In the example, we found two peaks corresponding to a channel (7Å) and a cage (17.5Å). Channels depicted as blue cylinders and the cage as a yellow sphere.

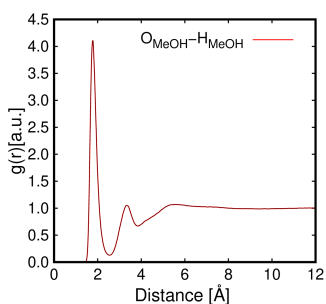


**Figure 4.** Example of the RDF between atoms of oxygen and hydrogen of a sample of methanol in the bulk.

**Radial Distribution Function (RDF)** shows the variation in particle

density “ $i$ ” as a function of the distance to another reference particle “ $j$ ” (see Figure 4). The RDF is calculated by counting the number of particles between a distance  $r$  and  $r + dr$ . The integration of RDF between 0 and  $R$  provides the number of particles at a distance  $R$  from the reference particle.

**Movies** are representations of the microstates of the system. They show the position of the particles in a specific state (MC simulation) or in time (MD). By chaining several Movies, we can represent the trajectory of the particles as a function of time (MD) or a succession of states in equilibrium in the ensemble (MC). Visualization programs give *Snapshot* of the different microstates. Figure 5 shows an example of molecules of methanol adsorbed in MAF-6. Visualization can be done using programs like GDIS, iRASP or Visual Molecular Dynamics (VMD).

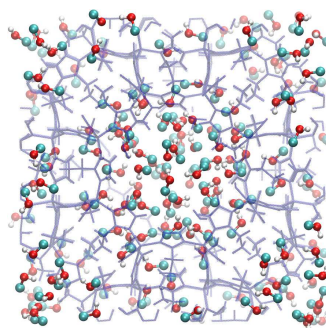


**Figure 5.** Snapshot of trajectory (Movie) of methanol inside MAF-6. Teal, red and white spheres represent the carbon, oxygen and hydrogen atoms respectively. The blue lines represent the crystallographic positions of the MAF-6 structure.

### Mean Square Displacement (MSD)

gives an idea of the distance travelled by an average particle or atom/pseudo atom within a system as a function of time. MSD is a quadratic function, so it will always be positive and is usually represented on a double logarithmic scale to more easily differentiate three regions: the ballistic region, the region dominated by collisions and the diffusive region. The ballistic regime occurs at very short times, less than the average collision time between particles. The particle behaves like a free particle in this region, and its MSD is proportional to  $t^2$ . As time progresses, the particles begin to interact and collide. At this point, the MSD does not show a defined trend, reaching a flat shape in some cases. The second region is a transitive regime that evolves to the diffusive regime where the particle continues the interaction with other particles, but the MSD becomes linear, proportional to  $t$ . This regimen may not be reached depending on whether the molecules diffuse or not. Figure 6 shows an example of the MSD of methanol in MAF-6.

**The Self-diffusion Coefficient ( $D_s$ )** can be extracted from the MSD slope in a diffusive regime through the Einstein equation.

$$D_s = \frac{1}{2N} \lim_{t \rightarrow \infty} \frac{d}{dt} \left\langle \sum_{i=1}^N (\vec{r}_i(t) - \vec{r}_i(0))^2 \right\rangle \quad (2.23)$$

where  $N$  is the total number of particles and  $\vec{r}_i(t)$  is the position of the particle “ $i$ ”

at time  $t$ .

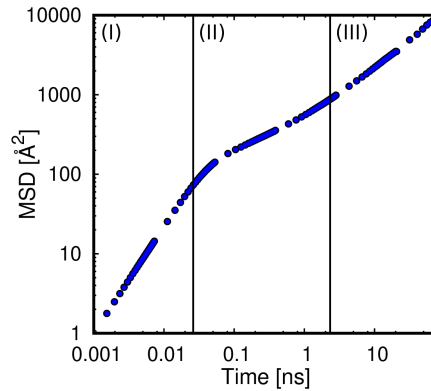


**Figure 6.** MSD (in log-log-scale) of methanol confined within the pores of MAF-6. Vertical lines delimit 3 different regions: (I) Ballistic, (II) collision and (III) diffusive.

**The Adsorption Capacity** of a material depends on factors such as the composition and geometry of the adsorbent, external temperature and pressure. Isotherms and isobars are obtained by setting others temperatures or pressures. These isotherms and isobars provide the number of particles that are adsorbed or desorbed in a pore as a function of pressure or temperature, respectively.

**Enthalpy of Adsorption** is the energy released in the form of heat when a structure adsorbs molecules. Information on the adsorption enthalpy is crucial for energy applications using porous materials. Two extreme cases are adsorption at infinite dilution and adsorption at saturation. In the first case, the interaction of the molecule is governed by the interactions with the surface of the adsorbent and in

the second case, by mutual interactions between adsorbed molecules. To perform this calculation, we can rely on models such as those developed by Dubinin-Polanyi, using the Clausius-Clapeyron equation or taking the interaction energies obtained with RASPA, performing a Legendre transformation to obtain the heat.

**Average Number of Hydrogen Bonds per Molecule (nHB).** Molecules like water or alcohol can create hydrogen bonds (HB). HB are forces exerted between electronegative atoms such as fluorine, oxygen or nitrogen with hydrogen linked by a covalent bond to another electronegative atom. These forces are not especially strong, so their half-life time is bare short ( $\sim 1\mu s$ ). HB are evaluated with a geometric criterion based on three maximum distances (*cutoffs*) between the atoms involved. nHB denotes the number of HB between the molecules of a substance or mixture. The arrangement of the molecules (within an adsorbent or in bulk), the number of hydroxyl groups or the temperature are evaluated through this parameter. nHB is calculated from the positions (Movies) of the particles.

**Spatial Distribution Function (SDF)** shows the distribution of molecules that can form bonds (in this case, HB) with a reference molecule. Figure 7 shows the SDF of water where the red surface represents the possible positions of the atoms of oxygen of all the water molecules capable of forming an HB with the reference molecule.

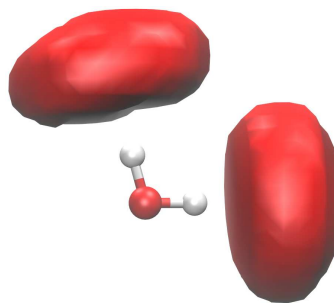


**Figure 7.** SDF of water. Red shape corresponds to atoms of oxygen of molecules of water able to bond with the reference molecule of water through HB.

**Electrostatic Field Lines** near the internal surface of the porous material are calculated from the crystallographic positions of the atoms in the structure and their partial charges. This form provides a view of the electrostatic field near the internal surface of a material. This representation shows the sinks (negative charges) and the sources (positive charges) position of field lines, and how the electrostatic field flows within a material. In addition, it can expand our knowledge about binding sites and adsorption mechanisms. Figure 8 shows an example of the electrostatic field lines near the MAF-6 ligand.

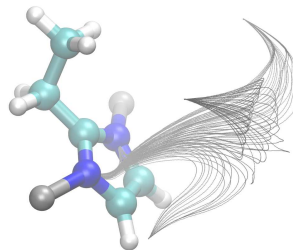


**Figure 8.** Representation of electrostatic field lines near to the organic ligand of MAF-6.

## 2.6 FORCE FIELDS AND MODELS

The force field is a compendium of models of atoms, molecules and adsorbents and their mutual interactions.<sup>17–20</sup> It has to be a trade-off between accuracy of the model and computational cost. The interaction of the molecules with other molecules and the structure is carried out by calculating the interaction potential energy. The interaction energy is taken into account through non-bonded and bonded potentials:

$$U_{system} = U_{non-bonded} + U_{bonded} \quad (2.24)$$

### 2.6.1 Non-bonded potential

Non-bonded energy has two contributions. Long-range interactions, governed by electrostatic contribution ( $U^{Coul}$ ) and short-range interaction described by the van der Waals contribution ( $U^{vdW}$ ). The following equation gives the contribution to the energy by electrostatic interactions

$$\begin{aligned} U^{Coul} &= \sum_i \sum_{j \neq i} \frac{1}{4\pi\epsilon} \frac{q_i q_j}{|\vec{r}_i - \vec{r}_j|} = \\ &= \frac{1}{2} \sum_i \sum_j \frac{1}{4\pi\epsilon} \frac{q_i q_j}{|\vec{r}_{ij}|} \quad (2.25) \end{aligned}$$

where  $q_x$  are the partial charges of the atoms,  $\vec{r}_{ij} = |\vec{r}_i - \vec{r}_j|$  the distance between pairs of atoms and  $\epsilon$  the electrical permittivity. Partial charges are obtained either from quantum calculations or using the

charge-equilibration method.<sup>21</sup> Calculation of electrostatic energy becomes complicated for periodic structures since summations would extend to infinity. Assuming a cubic system of cell length  $L$ , the energy will be

$$U^{Coul} = \frac{1}{2} \frac{1}{4\pi\epsilon} \sum_{\vec{n}} \sum_{i=1}^N \sum_{j=1}^N \frac{q_i q_j}{|\vec{r}_{ij} + \vec{n} \cdot L|} \quad (2.26)$$

where  $\vec{n}$  represents the reproducibility in each of the coordinate axes. This expression converges very slowly, requiring methods such as Ewald summation.<sup>22</sup> The Ewald summation method replaces the (infinite) sum of interaction energies in real space with its equivalent in Fourier space, which converges quickly. The application of the Ewald summation method at discrete systems is described by the Particle Mesh Ewald method (PME).

PME separates the energy contribution into short-range and long-range contributions. The short-range contribution is calculated in the real space, and the long-range contribution using the Fourier transform. In the case of the Coulomb interaction, the electrostatic contribution of the nearby points (unit cell) is calculated through the direct sum and the furthest points (periodically reproduced, called images) through the Fourier transform.

The contribution to the energy from the van der Waals interactions can be obtained with several potentials (e.g. Morse,<sup>23</sup> Buckingham<sup>24</sup>, or Lennard Jones<sup>25</sup>). These potentials have attractive and repulsive terms that generate an equi-

librium region. The most used potential to describe the van der Waals interactions is the Lennard-Jones potential (LJ) (Eq. 2.27)

$$V_{ij}(r) = 4\varepsilon_{ij} \left[ \left( \frac{\sigma_{ij}}{r_{ij}} \right)^{12} - \left( \frac{\sigma_{ij}}{r_{ij}} \right)^6 \right] \quad (2.27)$$

where  $\varepsilon$  and  $\sigma$  are parameters that describe the interaction between atoms “ $i$ ”, “ $j$ ”. The potential depends only on the distance between atoms ( $r_{ij}$ ), that is, it is isotropic, so it generates a central (conservative) force. Figure 9 shows the shape of this potential as a function of distance  $r_{ij}$ .

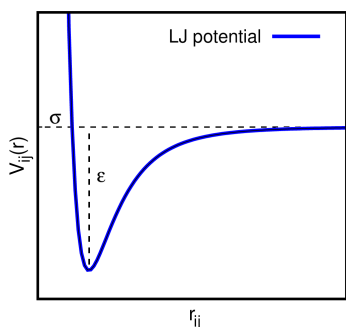


**Figure 9.** Representation of Lennard-Jones potential as a function of distance between particles.

Many force fields reproduce the adsorption and diffusion of different molecules in various materials. It is important to develop transferable force fields since this increases applicability. In this thesis, we use Universal Force Field (UFF)<sup>18</sup> for the parameters ( $\varepsilon, \sigma$ ) of the metallic clusters in the MOFs and Dreading for the organic ligands.<sup>17</sup> These set of parameters

do not take into account cross terms. We use Lorentz-Berthelot Mixing rules to describe the cross interaction (Eq. 2.28).<sup>26</sup>

$$\varepsilon_{ij} = \sqrt{\varepsilon_{ii} \cdot \varepsilon_{jj}}; \sigma_{ij} = \frac{\sigma_{ii} + \sigma_{jj}}{2} \quad (2.28)$$

Although mixing rules are not always accurate. In the case of MOFs, they are a good approximation but in the case of zeolites, mixing rules are not good enough. So searching for interaction parameters between the atoms of the structure and the molecule becomes crucial for describing adsorption and diffusion properties there.

## 2.6.2 Bonded potential

Rigid molecules are formed by atoms that can have an electric charge and with fixed internal distances. These atoms do not have (variable) internal energy. For flexible molecules, the internal energy can be described as

$$U_{bonded} = U_{bonds} + U_{bends} + U_{torsion} \quad (2.29)$$

$U_{bonds}$  is the vibration energy of the bonded atoms with respect to the equilibrium point ( $r_0$ ). These potentials can take various forms. The most widely used is the harmonic potential (Eq. 2.30). The parameter  $k_r$  is the force constant while  $r_{ij}$  shows the distance between particles “ $i$ ” and “ $j$ ”. Figure 10a shows a bond between two atoms

$$U_{ij} = \frac{1}{2} k_r (r_{ij} - r_0)^2 \quad (2.30)$$

$U_{bends}$  is the potential energy generated by three consecutive atoms that oscillate with an equilibrium angle  $\theta_0$ . Like for bonds, this potential can be represented by several functions, being the harmonic potential (Eq.2.31) the most widely used. Figure 10b shows  $U_{bends}$  between atoms  $i, j, k$

$$U_{ijk} = \frac{1}{2}k_{\theta}(\theta_{ijk} - \theta_0)^2 \quad (2.31)$$

$U_{torsion}$  energy is generated by four consecutive (proper) or non-consecutive (improper) atoms that form two planes that rotate concerning each other. Several potentials describe  $U_{torsion}$ . (Eq.2.32) shows an example of proper torsion potential.

$$U_{ijkl} = p_0 + p_1 [1 + \cos(\phi_{ijkl})] + p_2 [1 - \cos(2\phi_{ijkl})] + p_3 [1 + \cos(3\phi_{ijkl})] \quad (2.32)$$

$p_x$  are the parameters which define the potential, and  $\phi_{ijkl}$  are the angle formed by the planes which contain atoms  $i, j, k$  and  $l$ . Figures 10c and 10d show an example of proper and improper torsion potential.

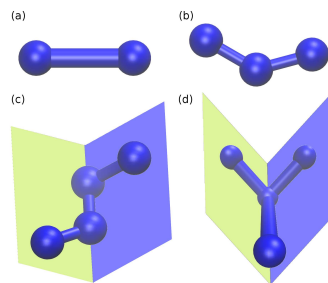


**Figure 10.** Example of (a) bond, (b) bend, (c) proper torsion and (d) improper torsion. Spheres represent atoms, cylinders bonds and green and blue shapes represent the planes that contain the atoms.

### 2.6.3 Molecules

To model the molecules of alcohol, we use the Transferable Potentials for Phase Equilibria Model (TraPPE)<sup>27</sup>. TraPPE is a pseudo-atom model that considers groups of atoms as simple points of charge with assigned LJ parameters. In the case of alcohol,  $CH_x$  groups are treated as spheres with the mass of all constituent atoms and a partial charge corresponding to the group. TraPPE assumes rigid bonds but allows angles to vary. This simplification, together with a suitable choice of interaction parameters, gives accurate results adjusted to experimental values. For water, we use the SPC/E model.<sup>28</sup> SPC/E is a 3-body model for water with charges on the three atoms. This model is fully flexible.

### 2.6.4 Rigid and Flexible Structures

Zeolites, MOFs and ACs, can be modelled rigid or flexible. The choice depends on

the level of detail needed. For example, zeolites are generally more rigid than MOFs, and they can be modelled as rigid in adsorption calculations. The interaction of the molecule with the structure and position of the binding sites are hardly altered by the vibration of the framework, but it can affect the transport of molecules. This will be reflected in the values of the diffusion coefficient.

In rigid structures, the atoms are fixed at their crystallographic positions. Flexible structures allow vibration of atoms. The flexibility of the structures is modelled with non-bonded and bonded potentials described by the same functions used for molecules. The flexibility of structures can be reflected in the vibration of the network and the rotation of the ligands. This flexibility can lead to gate opening or breathing phenomena.

## 2.7 THERMODYNAMICAL MODEL

This section summarizes all the thermodynamic models used in this thesis.

### 2.7.0.1 Dubinin-Polanyi Theory

Dubinin and Polanyi provided a theory to calculate adsorption enthalpies. This requires adsorption isotherms and isobars, and models for density ( $\rho$ ), saturation pressure ( $P_{sat}$ ) and heat of vaporization ( $\Delta H_{vap}$ ).<sup>29</sup> This method of calculating adsorption enthalpies is based on loading,

temperature and pressure related through a function

$$f(q, T, p) = 0 \quad (2.33)$$

The characteristic curve is defined as a function  $W = W(A)$ , where  $W$  is the volumetric capacity and  $A$  is the Gibbs free energy:

$$W = \frac{q(T, p)}{\rho(T)} \quad (2.34)$$

$$A = RT \ln \left( \frac{P_{sat}(T)}{p} \right) \quad (2.35)$$

The characteristic curve is independent on temperature and pressure and contains all information related to the adsorption of the adsorbate-adsorbent pair. To estimate the value of density we used the model developed by Hauer *et al.*<sup>30</sup> (Eq.2.36)

$$\rho(T) = \rho_0(T_0) \cdot [1 - \alpha_T(T - T_0)] \quad (2.36)$$

$T_0$  is a reference temperature (usually, 298K) and  $\rho_0(T_0)$ , the experimental density at this temperature. This model considers that density follows a linear trend with temperature. The slope of the line is the thermal expansion coefficient ( $\alpha_T$ ), described as

$$\alpha_T = \frac{1}{\rho(T)} \frac{\partial \rho(T)}{\partial T} \quad (2.37)$$

$\alpha_T$  is obtained from the experimental density of the substance at high pressure ( $\sim 100MPa$ ). This value is very low, so this

model considers that the density of the adsorbate inside the structure is quite similar to the density in the bulk at room temperature. Saturation pressure is calculated using the Peng-Robinson equation of state.<sup>31</sup>

Dubinin-Polanyi defines the adsorption enthalpy ( $\Delta H$ ) such as

$$\Delta H = \Delta H_{vap} + A - T\Delta S \quad (2.38)$$

where  $\Delta H_{vap}$  is the heat of vaporization,  $A$  is the Gibbs free energy,  $T$  is the temperature, and  $\Delta S$  is the change of entropy produced in the system when adsorption undergoes. This change in entropy is related to the inverse derivative of the characteristic curve at constant temperature:

$$\Delta S = \alpha_{Ads} W \left. \frac{\partial A}{\partial W} \right|_T \quad (2.39)$$

Since a derivative appears in the equation (2.39), the characteristic curve must have a smooth value in the first derivative.  $\alpha_{Ads}$  is the thermal expansion coefficient, defined as:

$$\alpha_{Ads} = - \frac{1}{\rho(T)} \frac{\partial \rho(T)}{\partial T} \quad (2.40)$$

The method is robust and allows calculating the enthalpy of adsorption using simulation and experimental data. However, the method cannot be applied to extreme conditions for the difficulty of finding tabulated data (vaporization enthalpy or density) and for the limitations of the saturation pressure.

### 2.7.0.2 Adsorption-Based Heat Pumps and Desiccant Cooling System

Porous materials can be used as heat pumps or chillers.<sup>32</sup> The porous material adsorbs the working fluid, which releases energy to the outside. Once the adsorbent is full, it adsorbs thermal energy to desorb the fluid and the latter, in turn, expels it to condense. This fact can exchange surrounding energy and pump heat from one place to another. This process generates very efficient thermal devices called Adsorption-Based Heat Pumps (AHP) if used as heat pumps and Desiccant Cooling Systems (DCS) if used as coolers. The process consists of four stages represented in Figure 11.

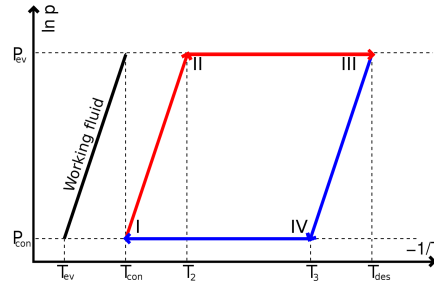


**Figure 11.** Schematic representation of the isosteric cycle of AHP.

The cycle starts by placing the fluid next to the dry adsorbent. The fluid takes energy from the environment ( $Q_{ev}$ ), which is at a temperature  $T_{ev}$  lower than that of the fluid ( $T_1$ ). The fluid evaporates and adsorbs, emitting energy ( $Q_{ads}$ ) to the en-

vironment. This point is stage I, where the cycle starts.

The system needs to be regenerated when the adsorbent is entirely saturated. To regenerate the system, the fluid is heated from temperature  $T_1$  to temperature  $T_2$ , increasing pressure in the same way so that, ideally, the adsorbent remains fully saturated (II). Next, the heating process continues isobarically up to a temperature  $T_{des}$ . This is possible since the system is in contact with the condenser and is capable of heating up without changing pressure. Temperature must be high enough to desorb as much fluid as possible without overheating the system. To do this, it has to provide heat ( $Q_{reg}$ ) to the system (III). The desorbed fluid becomes liquid in the condenser, releasing energy in the process ( $Q_{con}$ ). At this point, the adsorbent is empty, and it can reload. It first carries out an isosteric cooling to a temperature  $T_3$  to place the system at a pressure  $P_{ev}$ . As before, this process does not load the adsorbent (IV). Finally, the system continues to cool down to temperature  $T_1$ . The fluid takes heat from the environment ( $Q_{ev}$ ) that is at a lower temperature ( $T_{ev}$ ) so that the fluid evaporates and the adsorbent is loaded reaching the starting point (stage I).

The values of  $P_{ev}$  and  $P_{con}$  are related to the saturation pressure of the fluid at these temperatures since they are in the liquid state. The choice of temperatures is essential to achieve adequate efficiencies. Temperatures  $T_2$  and  $T_3$  are chosen

as a function of the other temperatures so that the adsorbent remains full or empty, respectively.

To use the system as a heat pump, the evaporator temperature must be slightly lower than the ambient temperature while  $T_1 = T_{ads}$  (usually taken equal to that of the condenser  $T_{con} = T_{ads}$ ) must be higher than the evaporation temperature and lower than the desorption temperature.

To use the system as a chiller, the evaporator temperature has to be lower than ambient temperature,  $T_{ads} = T_{con}$ , slightly higher than room temperature.  $T_{des}$  must be high but not much for AHP.

The performance of these devices are measured by the Coefficient of Performance (COP):

$$COP_H = \frac{-(Q_{ads} + Q_{con})}{Q_{reg}} \quad (2.41)$$

$$COP_C = \frac{Q_{ev}}{Q_{reg}} \quad (2.42)$$

where  $COP_H$  and  $COP_C$  are the COP of the device using as AHP and DSC, respectively.

## 2.8 DEVELOPED HOMEMADE CODES

### 2.8.0.1 BondCalc

BondCalc software computes the average number of hydrogen bonds per molecule using a predefined geometric criterion. It is applicable to pure compounds or binary mixtures. The latest version of this code

operates with pure water and all types of alcohols, both in their pure state and mixtures. It also calculates  $\pi$ -bonds of aromatic molecules. To evaluate all kinds of bonds between generic molecules, the positions of the molecules in the “.pdb” format are taken as input. BondCalc identifies each molecule as an entity and calculates the distances and relative positions (angles) of each molecule with the others. Based on the established criteria, both preset and modifiable, it evaluates the number of bonds for each configuration. Finally, the number of configurations (Movies) and molecules are averaged.

BondCalc can also calculate the average number of molecules with 0,1,2,3... bonds. It also calculates the clusters of grouped molecules that are in the system following the network of linked molecules.

Finally, BondCalc can calculate the spatial distribution function (SDF). If BondCalc detects a bond between a molecule  $i$  and another  $j$ , it translates the system so that molecule  $i$  is located at the origin of coordinates. BondCalc reorients the system so that molecule  $i$  is always at the same position and notes the position of molecule  $j$  that forms the bond. Performing this calculation with many molecules, BondCalc generates the point cloud seen in Figure 7. BondCalc needs a minimum of 3 atoms per molecule to establish an orientation criterion. Furthermore, these molecules must be rigid (or not very flexible) to obtain accurate SDFs.

BondCalc is available for download

and use at “[www.github.com/rmmadcas/BondCalc](http://www.github.com/rmmadcas/BondCalc)”.

### 2.8.0.2 Electrostatic Field Lines Calculator (EosFiLiC)

EosFiLiC code provides the electrostatic field lines generated by the partial charges of the atoms of a structure. This program uses the superposition principle to calculate the electrostatic field through the Coulomb equation at a point  $r$  generated by the contribution of the atoms in the structure. The crystal is infinite because it replicates in all directions to eliminate edge effects, so only atoms within a sphere of radius  $R$  are taken. This way, the contribution of the farthest atoms has a negligible value with the total field. That is

$$\frac{|\vec{E}(R) - \vec{E}(R + dr)|}{|\vec{E}(R)|} < \delta \quad (2.43)$$

Once the value of the field at point  $r$  has been calculated, the program saves the value for that point and moves a small distance  $dl \cdot \hat{u}_l$ . Where  $\hat{u}_l = \frac{\vec{E}(r)}{|\vec{E}(r)|}$  it is a unit vector in the direction of the electrostatic field. Upon reaching the new point  $\vec{r}' = \vec{r} + dl \cdot \hat{u}_l$ , the process is performed again to obtain a series of points in which the electrostatic field is always tangent, that is, a field line.

EosFiLiC is available for download and use at “<https://github.com/rmmadcas/EosFiLiC>”.

### 2.8.0.3 Characteristic curves

Dubinin Polanyi's theory defines the characteristic curve through one or several adsorption isotherms/isobars. We have developed a code that reads the loading of an isotherm or isobar and uses density data (with the Hauer model) and saturation pressure (from the Peng-Robinson equation of state) to obtain  $W(q, T, p)$  and  $A(q, T, p)$ . With all data collected from the simulations, a point cloud is generated in which all points converge to the same curve. Many functions resemble a characteristic curve, such as an arc tangent. We decided to fit the values to the most probable curve using splines through the open source code *Gnuplot*. This method generates a table of values that fit the characteristic curve.

The characteristic curve only depends on the adsorbate-adsorbent pair and is non-dependent on conditions. The curve calculated above it can be used for inverse calculations to generate isotherms or isobars at conditions that have not been simulated.<sup>33</sup>

### 2.8.0.4 Storage Density Calculator

Dubinin Polanyi's theory also defines a way to calculate adsorption enthalpy through the characteristic curve and tabulated data. From equations (2.38), (2.39) and (2.40) we can calculate the adsorption enthalpy. Equations (2.39) and (2.40) contains derivatives. A numerical derivative is needed for (2.39). To perform a cor-

rect numerical derivative, the characteristic curve must have correct point spacing and smoothness to prevent the presence of peaks in the function. This is why using splines, and a good fit to the characteristic curve is crucial. Density follows a linear behaviour, and its derivate is analytical.

Adsorption enthalpy is obtained as a function of loading. Storage energy is defined by Storage Density (*SD*). *SD* can be calculated through numerical integration of adsorption enthalpy over temperature. The relationship between loading and temperature is given by the pressure at which the adsorption takes place (isobar).

$$SD = \int_{q(T_f)}^{q(T_0)} \Delta H(q) dq \quad (2.44)$$

### 2.8.0.5 Heat Pumps Calculator

Thermodynamic models to describe Adsorption-Based Heat Pumps and Chillers are complex. Temperatures of the evaporator, condenser (which coincides with that of adsorption) and desorption are input parameters, together with the characteristic curve of the adsorbate-adsorbent pair. These temperatures set the minimum and maximum values of the volumetric capacity ( $W_{min}$  and  $W_{max}$  respectively). As the cycle consists of two stages of isosteric adsorption and desorption, temperatures  $T_2$  and  $T_3$  are calculated so that the values of  $W_{min}$  and  $W_{max}$  are not altered. The code generates the isobars a pressures  $P_{ev}$  and  $P_{con}$  from characteristic curves and calculates

$T_2$  and  $T_3$  through numerical resolution. Once temperatures have been calculated, the heats described by the thermodynamic model are calculated using numerical integrals.  $Q_{sorp}$ , defined as the heat that the structure releases/adsorbs when adsorbing/desorbing, is calculated by integrating the adsorption enthalpy. This calculation is the most sensitive. It depends on the model and not on tabulated values such as the specific heat ( $C_p$ ). This heat is calculated through the numerical integration of the enthalpy of adsorption described by DP.

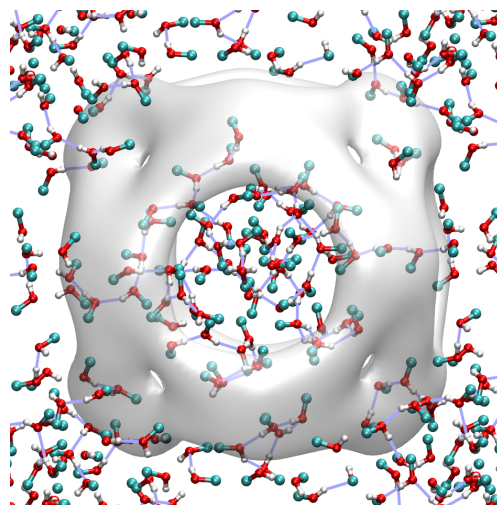
## 2.9 BIBLIOGRAPHY

- [1] Dubbeldam, D.; Calero, S.; Ellis, D. E.; Snurr, R. Q. *Molecular Simulation* **2016**, *42*, 81–101.
- [2] Plimpton, S. *Journal of Computational Physics* **1995**, *117*, 1–19.
- [3] Bekker, H.; Dijkstra, E. J.; Renardus, M. K.; Berendsen, H. J. *Molecular Simulation* **1995**, *14*, 137–151.
- [4] Robert, C. P. *Wiley StatsRef: Statistics Reference Online*; 2016; pp 1–13.
- [5] Metropolis, N.; Rosenbluth, A. W.; Rosenbluth, M. N.; Teller, A. H.; Teller, E. *The Journal of Chemical Physics* **1953**, *21*, 1087–1092.
- [6] Yang, J.; Roberts, G. O.; Rosenthal, J. S. *Stochastic Processes and their Applications* **2020**, *130*, 6094–6132.
- [7] Frenkel, D.; Smit, B. In *Understanding Molecular Simulations from Algorithms to Applications*; Diego, A. P. S., Ed.; 2002.
- [8] Adams, D. *Molecular Physics* **1974**, *28*, 1241–1252.
- [9] Siepmann, J. I.; Frenkel, D. *Molecular Physics* **1992**, *75*, 59–70.
- [10] Rosenbluth, M. N.; Rosenbluth, A. W. *The Journal of Chemical Physics* **1955**, *23*, 356–359.
- [11] Mazur, A. K. *Journal of Computational Physics* **1997**, *136*, 354–365.
- [12] PLUMED Consortium, T. *Nature Methods* **2019**, *16*, 667–673.
- [13] Ozcan, A.; Perego, C.; Salvalaglio, M.; Parrinello, M.; Yazaydin, O. *Chemical Science* **2017**, *8*, 3858–3865.
- [14] Meza, J. C. *Wiley Interdisciplinary Reviews: Computational Statistics* **2010**, *2*, 719–722.
- [15] Nazareth, J. L. *Wiley Interdisciplinary Reviews: Computational Statistics* **2009**, *1*, 348–353.
- [16] Baker, J. *Journal of Computational Chemistry* **1986**, *7*, 385–395.
- [17] Mayo, S. L.; Olafson, B. D.; Iii, W. a. G.; Eb, E.; El, E. a. E. T. *Journal of Physical chemistry* **1990**, *101*, 8897–8909.
- [18] Rappé, A. K.; Casewit, C. J.; Colwell, K. S.; Goddard III, W.; Skiff, W. J. *Am. Chem. Soc.* **1992**, *114*, 10024–10035.
- [19] Jorgensen, W. L.; Maxwell, D. S.; Tirado-Rives, J. *Journal of the American Chemical Society* **1996**, *118*, 11225–11236.
- [20] Jorgensen, W. L.; Mcdonald, N. a. *Journal of Molecular Structure (Theochem)* **1998**, *424*, 145–155.
- [21] Wilmer, C. E.; Kim, K. C.; Snurr, R. Q. *Journal of Physical Chemistry Letters* **2012**, *3*, 2506–2511.
- [22] Essmann, U.; Perera, L.; Berkowitz, M. L.; Darden, T.; Lee, H.; Pedersen, L. G. *The Journal of Chemical Physics* **1995**, *103*, 8577–8593.
- [23] Morse, P. M. *Phys. Rev.* **1929**, *34*, 57–64.
- [24] Buckingham, R. A. *Proceedings of the Royal Society of London* **1938**, *168*, 264–283.
- [25] Jones, J. E. *Proceedings of the Royal Society of London* **1924**, *106*, 463–477.
- [26] Boda, D.; Henderson, D. *Molecular Physics* **2008**, *106*, 2367–2370.
- [27] Stubbs, J. M.; Potoff, J. J.; Siepmann, J. I. *Journal of Physical Chemistry B* **2004**, *108*, 17596–17605.
- [28] Mark, P.; Nilsson, L. *Journal of Physical Chemistry A* **2001**, *105*, 9954–9960.
- [29] Lehmann, C.; Beckert, S.; Gläser, R.; Kolditz, O.; Nagel, T. *Applied Energy* **2015**, *185*, 1965–1970.
- [30] Nagel, T.; Beckert, S.; Büttcher, N.; Gläser, R.; Kolditz, O. *Energy Procedia* **2015**, *75*, 2106–2112.
- [31] Peng, D.-Y.; Robinson, D. B. *Ind. Eng. Chem.. Fundam* **1976**, *15*, 59–64.
- [32] De Lange, M. F.; Verouden, K. J.; Vlugt, T. J.; Gascon, J.; Kapteijn, F. *Chemical Reviews* **2015**, *115*, 12205–12250.
- [33] Madero-Castro, R. M.; Vicent-Luna, J. M.; Peng, X.; Calero, S. *ACS Sustainable Chemistry Engineering* **2022**, *10*, 6509–6520.

## Adsorption of Light Alcohols in High Hydrophobic Metal Azolate Framework

Rafael María Madero-Castro, José Manuel Vicent-Luna, and Sofía Calero

As an alternative option to conventional fuels, biofuels based on light alcohols are receiving great attention. In this context, we investigate the adsorption mechanism of light alcohols in the hydrophobic metal-organic framework MAF-6. To study the effect of the conformation of molecules in the adsorption process, we evaluate the effect of the length of the alkyl chain of linear alcohols (methanol, ethanol, propanol, and butanol) and branched alcohols (2-propanol, 2-butanol, and tert-butanol). We perform Monte Carlo simulations in the grand-canonical ensemble



to study the adsorption and energetic properties of the systems. We analyze the structural organization and the nucleation mechanism of the molecules of alcohol and the dynamics of the adsorbed molecules within the big cavities of MAF-6. We found that the initial step of adsorption is governed by the interaction of the adsorbates with the structure, while in saturation, the adsorbate-adsorbate gain importance.

### 3.1 INTRODUCTION

To mitigate global warming, one possibility is the utilization of alternative fuels that are nonbased in fossils, such as biofuels.<sup>1</sup> The interest in new biofuels based on light alcohols has increased in recent years, making necessary the storage and purification of these compounds.<sup>2</sup> Methanol, ethanol, propanol, and butanol have industrial interest since they can be used in internal combustion engines as biofuels.<sup>3–5</sup> In this regard, the biofuels obtained from organic residues such as sugarcane<sup>6</sup> or crops<sup>4</sup> are a more ecofriendly alternative to fossil fuels.<sup>7–9</sup> The capture, purification, and separation of these alcohols are crucial for industrial processes.<sup>10–12</sup> Methods like distillation<sup>13</sup> or pervaporation<sup>11</sup> are used in the industry. Distillation is the most extended method to obtain and purify bioethanol.<sup>14</sup> However, the elevated cost of this process and the negative repercussion on the environment<sup>15</sup> encourage the search for alternatives. Here, we consider metal-organic frameworks (MOFs) as potential materials to improve the storage of light alcohols. MOFs are crystalline structures formed by metallic centers with organic ligands connected to them. The combination of a large variety of metallic centers and organic linkers makes the number of MOFs almost unlimited and hinders the possibility of finding the adequate structure for each purpose.<sup>16</sup> Characteristics of MOFs such as high pore volumes and large surface areas make them

good candidates for storage, separation, or catalysis. The use of MOFs also opens a new world of possibilities for their capacity of storage and separation. A number of studies have investigated the adsorption of alcohols in MOFs.<sup>17–32</sup> de Lima *et al.*<sup>23</sup> studied the separation of water and alcohol mixture using  $Zn_2(BDC)_2(TED)$  MOF [BDC: benzene-1,4-dicarboxylate; TED:triethylenedi-amine]. This was proposed as a suitable material for the separation and purification of bioethanol. Cousin-saintremi *et al.*<sup>30</sup> also studied the separation of several bioalcohols using zeolite imidazolate framework (ZIFs-8). They found that this material can purify butanol from a liquid mixture containing ethanol, acetone, and water. Li *et al.*<sup>24</sup> synthesized a robust cobalt-based MOF with a high capacity and affinity for water and for linear and branched alcohols from methanol to pentanol. Zhang *et al.*<sup>25</sup> investigated the potential of ZIF-8, ZIF-71, and ZIF-90 to capture light alcohols from methanol to butanol, and they predicted the separation of alcohol/water mixtures with the ideal adsorbed solution theory. de Lange *et al.*<sup>26</sup> selected 18 MOFs for methanol and ethanol adsorption for energy-storage applications. They discussed the MOF/alcohol working pair behavior for heat pumps and chillers based on adsorption measurements and thermodynamic models. In addition to the experimental investigations, several theoretical studies have been reported, showing the potential of molecular simulations to describe the adsorption of alcohols in

MOFs. Zhang *et al.*<sup>27</sup> reported a molecular simulation study of the adsorption of linear alcohols in ZIF-8. They analyzed the adsorption mechanisms in this hydrophobic material and the ability of different force fields to reproduce the experimental observations. They showed that the DREIDING<sup>28</sup> force field provides the best prediction of the adsorption isotherms, while the isotherms are not affected by the atomic charges of the structure and the framework flexibility. Jiang *et al.*<sup>33</sup> performed molecular simulations of ethanol and water in six ZIFs with different imidazole linkers. They discussed the differences found in the adsorption isotherms and in the microscopic structure of the confined adsorbates and proposed ZIF-8 as a potential candidate for biofuel purification. Nalaparaju *et al.*<sup>29</sup> identified different adsorption mechanisms of water, methanol, and ethanol in the hydrophilic Na-rho-ZMOF and in the hydrophobic ZIF-71 using molecular simulations. Even though the two structures have identical topology and a similar pore size, the hydrophobicity/hydrophilicity of the adsorbent is crucial for the adsorption of these polar molecules. Sławek *et al.*<sup>32</sup> investigated the effect of adsorption of water and linear alcohols in the flexibility of a hydrophobic/hydrophilic MOF with open metal sites. They found that polar molecules induce a “gate opening” in STAM-1 MOF.

The adsorption of light alcohols in hydrophobic materials with large cavities is of industrial interest. However, the mech-

anisms that govern the adsorption process are still not understood. This work sheds light into these molecular mechanisms, providing valuable information to find/predict new materials for the storage of light alcohols. In this paper, we evaluate the ability of metal azolate framework 6 (MAF-6) to store alcohols. MAF-6 is reported as a stable material<sup>34–36</sup> with high storage capacity and hydrophobicity, which makes it an interesting candidate for the separation of water and alcohols.<sup>36</sup> MAF-6 is a ZIF, that is, a MOF with a zeolite topology. It has an RHO topology,<sup>37–39</sup> and it is formed by a zinc-based metallic center and the organic ligand 2-ethylimidazole. This MOF exhibits a big central pore connected by cylindrical channels. Wang *et al.*<sup>34</sup> studied the fast adsorption of phthalic acid from aqueous solution in MAF-6. These authors found that the adsorption capacity of MAF-6 is better than other MOFs.<sup>29</sup> The hydrophobic character of MAF-6 makes it a perfect candidate for adsorption of light alcohols. We investigate the adsorption capabilities of MAF-6 for the storage of  $C_1 - C_4$  linear alcohols and the adsorption of branched alcohols (2-propanol, 2-butanol, and tert-butanol) for comparison. We also include ethylene glycol to explore the effect exerted by the number of hydroxyl groups on the adsorption mechanism. We will show that adsorption is governed by the nucleation of the molecules of alcohol, that is, the first adsorbed molecules act as seeds allowing other molecules to cluster around

them, filling the pores of the MOF completely below the saturation conditions of each compound. The microscopic structure of the adsorbed alcohols is similar to their structure in the bulk liquid phase. We described the aggregation of the molecules by means of the analysis of hydrogen bonds (HBs) and adsorption energies.

### 3.2 SIMULATION DETAILS

Monte Carlo (MC) simulations in the grand-canonical ensemble (GCMC) were carried out at room temperature using RASPA simulation software.<sup>40,41</sup> These simulations consist of  $2 \cdot 10^5$  MC cycles of initial equilibration followed by  $5 \cdot 10^5$  MC cycles to adequately average the adsorption properties. The adsorption of alcohols in hydrophobic materials at some values of pressure is tricky and requires additional MC cycles. These can be up to  $5 \cdot 10^6$  additional MC cycles for the values of pressure that are close to the onset pressure. This will be discussed in-depth in the results section. We impose fugacity to be equal to pressure, that is, the fugacity coefficient is equal to unity. In addition, we calculated the saturation pressure of each compound using the Peng–Robinson equation of state. These calculations also provide the fugacity coefficient. This value is equal to unity at pressures lower than the saturation pressure of each compound (Table A1.1). If we refer the adsorption isotherms to fugacity instead of pressure, the last value of each isotherm should correspond to the loading at the saturation

pressure of the alcohol. We also performed MC simulations in the NVT ensemble to obtain the surface area and pore volume of MAF-6. We calculated the surface area by rolling a helium molecule over the surface of the framework and the pore volume by computing the void space in the structure using the Widom particle insertion method.<sup>42</sup> The dynamical properties of the system were calculated with molecular dynamics (MD) simulations in the NVT ensemble. We computed the self-diffusion coefficients of the adsorbates through the slope of the mean squared displacement in the diffusive regime. MD simulations were carried out with the loading corresponding to saturation conditions provided by the MC simulations. These simulations consist of  $10^8$  MD steps giving a total of 100 ns and an integration time step of 1 fs. The self-diffusion coefficients were extracted in the time interval from 10 to 80 ns of the production run. MD simulations were performed with the MD simulation software LAMMPS.<sup>43</sup>

The complete set of interaction parameters for the molecules of alcohol were taken from the TraPPE force field.<sup>44</sup> This force field considers flexible pseudo-atom models where the  $CH_x$  groups are described by single interaction centers attached to the hydroxyl group. The force field includes Lennard-Jones (LJ) parameters for each atom and point charges for the oxygen, hydrogen, and carbon atom attached to the hydroxyl group. Bonds, bends, and torsion terms are also included

for a full flexible description of the adsorbates.

We calculated the average number of HBs per molecule ( $n_{\text{HB}}$ ) by averaging 250 MC configurations recorded during the GCMC simulations to obtain the adsorption isotherms using the geometrical criterion described by Padró *et al.*<sup>45</sup> This criterion is based on three conditions: (i) a maximum distance between the oxygen atoms of two nearest molecules, ( $d_{\text{OO}}$ ), (ii) a cutoff for the oxygen-hydrogen distance ( $d_{\text{OH}}$ ) of different molecules, and (iii) the angle formed between the atom of oxygen of the acceptor molecule and the atoms of oxygen and hydrogen of the donor molecule ( $\phi_{\text{OOH}}$ ) that must be less than a specific value. Figure A1.1 shows a schematic representation of the HB criterion. For water, Martí *et al.*<sup>46</sup> reported the following cutoff values:  $d_{\text{OO}} = 3.6 \text{ \AA}$ ,  $d_{\text{OH}} = 2.45 \text{ \AA}$ , and  $\phi_{\text{OOH}} = 30^\circ$ . The values reported by Padró *et al.*<sup>45</sup> for alcohols are  $d_{\text{OO}} = 3.5 \text{ \AA}$ ,  $d_{\text{OH}} = 2.6 \text{ \AA}$ , and  $\phi_{\text{OOH}} = 30^\circ$ . The cutoff distances were determined by the position of the first minimum of the corresponding radial distribution functions (RDFs) in the liquid system (Figure A1.2). We used the same HB definition for the molecules of alcohol confined in the pores of MAF-6. Figure A1.2 also shows the spatial distribution function of the possible HBs with respect to a molecule of alcohol using the described criterion. We defined a similar criterion to evaluate the molecules of alcohol occupying the binding sites of MAF-6. We consider a molecule in a binding site when

the distance between the atom of oxygen of the alcohol and the geometric center of the imidazolium ring is lower than  $4.3 \text{ \AA}$  ~ and the distance between the atom of hydrogen of the same molecule and the geometric center of the ring is lower than  $3.9 \text{ \AA}$ . These cutoff values match with the minimum of RDFs (Figure A1.3). The values of  $n_{\text{HB}}$  in the bulk are included for comparison. We used the same models and force field parameters to carry out MD simulations for each alcohol in the bulk. These simulations consist of  $10^6$  MD steps in the NVT ensemble at room temperature in a cubic box of  $25 \text{ \AA}$  length. The number of molecules is adjusted to reproduce the experimental density of each adsorbate.

MAF-6 is considered rigid in GCMC simulations and flexible in MD simulations. LJ parameters for the imidazole link are taken from DREIDING<sup>28</sup> and those for zinc atoms are taken from UFF.<sup>47</sup> For the cross LJ interaction parameters, we used Lorentz-Berthelot mixing rules. We assigned partial charges to each atom of the structure according to the work of Gutiérrez-Sevillano *et al.*<sup>48</sup> The simulation box consists of a cubic cell of  $29.258 \text{ \AA}$ , which surpasses twice the spherical cutoff of  $12 \text{ \AA}$  used for nonbonded potentials. The atomic positions of the MAF-6 structure were provided by Huang *et al.*<sup>49</sup> and are available in the Cambridge Crystallographic Data Centre.<sup>50</sup> For MD simulations, we take into account the vibrations of the atoms during the dynamic process. To do so, we used a bonded potential for

the adsorbent to mimic the flexibility of the material. Because of the similarity of the adsorbents, we use the intramolecular force field parameters provided by Wu *et al.*<sup>51</sup> developed for ZIF-8.

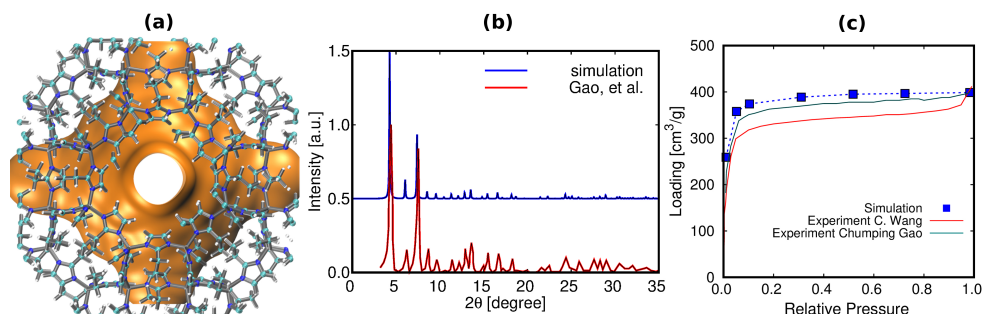


**Figure 1.** (a) Representation of the structure and accessible surface area of MAF-6. (b) Powder XRD of MAF-6 calculated and compared with the experiment. (c) Adsorption isotherm of nitrogen at 77K in MAF-6.

### 3.3 RESULTS AND DISCUSSION

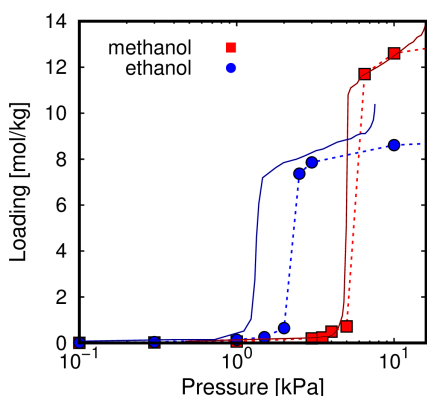
Figure 1a shows a representation of MAF-6 and the internal surface area of the structure. The potential parameters are accurate enough to describe the adsorption properties of the MOF. As shown in Figure 1b, the X-ray diffraction pattern (XRD) obtained with simulation is in agreement with the experiment.<sup>36</sup> Figure 1c compares the calculated and the experimental isotherms of nitrogen<sup>34,36</sup> at 77 K in MAF-6. The calculated values of the surface area and the pore volume as well as those reported in the literature<sup>35,36</sup> are collected in Table 1.

Figure 2 shows the adsorption isotherm of methanol and ethanol at room temperature. The calculated values are in agreement with the experimental data reported by He *et al.*<sup>35</sup> In particular, the

shape of the adsorption isotherms of the two components is in line with the experiments, showing a sudden increase of the adsorption loading at a given pressure below the saturation pressure of the adsorbates (16.78 kPa for methanol and 7.77 kPa for ethanol). Our values also agree with the reported saturation loading and with the onset pressures of methanol. This validates the force field used, though there is a tiny deviation in the onset pressure value of the adsorption isotherm of ethanol (about 2 kPa).

**Table 1.** Surface Area and Pore Volume of MAF-6

exp.	this work	exp.	this work
surface area (m <sup>2</sup> /g)		pore volume (cm <sup>3</sup> /g)	
1622 <sup>36</sup>	1664.48	0.63 <sup>36</sup>	0.59
1695 <sup>35</sup>		0.61 <sup>35</sup>	



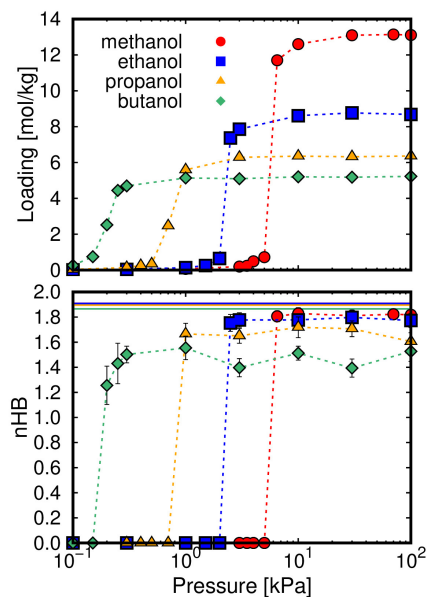
**Figure 2.** Comparison between the experimental 35 (solid lines) and calculated (symbols) adsorption isotherms of methanol and ethanol in MAF-6 at 298 K. Dashed lines are a guide to the eye.

Figure 3 (top) shows the adsorption isotherm of the linear alcohols in MAF-6 at 298 K. The saturation loading and the onset pressure decrease with the increase of the alkyl chain length of the alcohol since the structure exhibits high pores, and there are not specific adsorption sites for each molecule as for other structures with a more complex distribution of the pore/channel system. We observed similar shapes of isotherms for all alcohols. The onset values of pressure are lower than the saturation pressure of the compounds. Table A1.1 shows the values of saturation pressure of the molecules calculated with the Antoine equation and with the Peng Robinson equation of state. However, an increase of the alkyl chain length smoothens the sharp step of the isotherm. The adsorption of one molecule of alcohol in the pore of MAF-6 allows

other molecules to interact with it. HBs play an important role here, as shown by the average of HBs per molecule ( $n_{HB}$ ) as a function of pressure (Figure 3 bottom). The evolution of the  $n_{HB}$  follows the same trend as the adsorption isotherm, meaning that the adsorption of molecules of alcohol in a high hydrophobic structure is mainly due to HB interactions. The  $n_{HB}$  at saturation loading is similar to the bulk for methanol and ethanol. Table A1.2 shows the computed values of  $n_{HB}$  in bulk for all adsorbates. However, the confinement within the pores affects the HB network for the longest molecules and especially for butanol. The internal surface of the framework is highly hydrophobic, and because of the repulsion with the surface, in saturation, the molecules of alcohol are strongly coordinated in the middle of the structure. This is evidenced by the increase in the intensity of the first peak of the RDF between the molecules of alcohol in confinement (Figure A1.4). In general, we observed lower values of  $n_{HB}$  in confinement as compared with the bulk (a reduction of about 10-20% depending on the alcohol) because of the confinement effect. The size of the adsorbate also plays an important role since, due to steric effects, the smallest alcohols exhibit the largest number of  $n_{HB}$ s.

Figure 4 compares the adsorption isotherm and  $n_{HB}$  of linear C3 and C4 alcohols with their branched forms. All isotherms exhibit a similar trend, and the isomers reach almost the same sat-

uration loading, with the variation of the onset value of pressure. Molecules with the hydroxyl group in the second position (2-propanol and 2-butanol) adsorb slightly later than those with the hydroxyl group in the first position (propanol and butanol). The bulkiest alcohol selected for this study, tert-butanol, adsorbs at lower values of pressure than its isomers. This is related to the binding geometries of the first molecules adsorbed in the cavities, as will be explained later.



**Figure 3.** Adsorption isotherms of linear alcohols in MAF-6 at room temperature (top). Average number of HBs per molecule ( $n_{\text{HB}}$ ) as a function of pressure (bottom). Solid lines show the value of  $n_{\text{HB}}$  in the bulk. Dashed lines are a guide to the eye.

To analyze the effect of increasing number of hydroxyl groups in a molecule, we calculated the adsorption isotherm and

$n_{\text{HB}}$  of ethylene glycol (Figure 5). The onset value of pressure of this molecule is the lowest of all studied alcohols because the two hydroxyl groups favor the clusterization via HBs. Therefore, the  $n_{\text{HB}}$  of this molecule in the bulk is larger than those for the rest of alcohols. As for the other alcohols of long chain, the value of  $n_{\text{HB}}$  is larger in the bulk than in confinement because of the steric effect with the surface of the MOF.

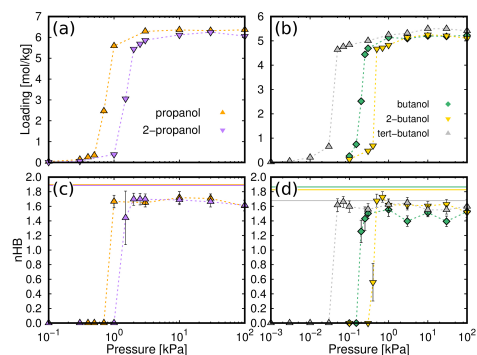


**Figure 4.** Adsorption isotherms of linear and branched C3 (a) and C4 (b) alcohols in MAF-6 at room temperature. Average number of HBs per molecule ( $n_{\text{HB}}$ ) as a function of pressure (c,d). Solid lines show the value of  $n_{\text{HB}}$  in the bulk. Dashed lines are a guide to the eye.

To analyze in-depth the HB network of molecules of alcohol confined in MAF-6, we calculated the distribution of HBs per hydroxyl group. Figure 6 shows the percentage of hydroxyl groups with  $n$  HBs ( $n = 0-4$ ). About 60-80% of all molecules are connected via two HBs, and about 20% of the molecules are connected via one HB. The remaining molecules mainly form monomers. The number of monomers for

methanol and ethanol is lower than 5%, whereas for the other molecules they can be up to 15%. Ethylene glycol has two hydroxyl groups and can form HB with the two extremes, and so we referenced to the hydroxyl groups instead of to the whole molecule.

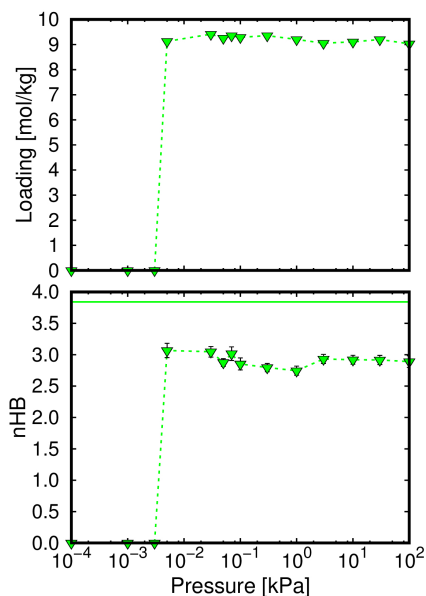


**Figure 5.** Adsorption isotherms of ethylene glycol in MAF-6 at room temperature (top). Average number of HBs per molecule ( $n_{HB}$ ) as a function of pressure (bottom). Solid lines show the value of  $n_{HB}$  in the bulk, and dashed lines are a guide to the eye.

The energetic adsorbent-adsorbate interactions also play an important role during the adsorption process. To analyze these interactions, we calculated the adsorption energy, focusing on the isosteric heat of adsorption ( $Q_{st}$ ). Figure 7a shows the absolute value of  $Q_{st}$  of linear alcohols in MAF-6 at infinite dilution, which gives

an idea of the energy involved in the adsorption process. To study the effect of the alkyl chain length, we extended the study up to molecules with 12 carbon atoms. We observed a linear increase in the heat of adsorption with the number of carbon atoms in the range from 4 to 12. This is also the normal behavior of the alkyl chain when increasing the chain length. However, the heat of adsorption obtained for methanol, ethanol, and propanol is almost the same. The contribution of each term of the heat of adsorption shown in Figure 7b allows elucidating the origin of this anomalous effect. To calculate  $Q_{st}$ , we used a Legendre transformation for the conversion of the internal energy between the adsorbent and the adsorbates to enthalpy of adsorption or heat of adsorption:  $Q_{st} = \Delta U - RT$  and  $\Delta U = \Delta U_{HG} - \Delta U_G$ . In these expressions,  $\Delta U$  is the total potential energy,  $R$  is the ideal gas constant, and  $T$  is the temperature.  $\Delta U_{HG}$  represents the host-guest energy, and  $\Delta U_G$  is the internal energy of a single molecule. There is no contribution of the host energy involved in the calculations since the structure is considered as a rigid crystal.  $RT$  is a constant quantity, and  $\Delta U_G$  increases linearly with the number of carbon atoms of the alkyl chain of the molecule. According to this, the interaction responsible for the unusual behavior of  $Q_{st}$  is the term for the host-guest interaction. We observed in Figure 7b that  $\Delta U_{HG}$  is  $36\text{kJ/mol}$  for methanol and decreases to 33 and  $28 - 29\text{kJ/mol}$  for ethanol, propanol, and butanol, respec-

tively. This value increases by  $1-2\text{kJ/mol}$  with each additional atom of carbon, being  $38\text{kJ/mol}$  for dodecanol. The initial decrease of  $\Delta U_{HG}$  from methanol to propanol causes the unusual behavior depicted in Figure 7a.

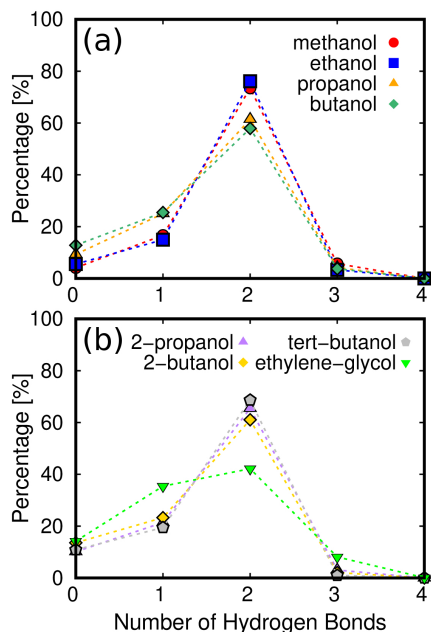


**Figure 6.** Percentage of hydroxyl groups in linear alcohols (a) and branched alcohols and ethylene glycol (b) with  $n$  HBs. Dashed lines are a guide to the eye.

Figure 8 shows the heat of adsorption of all alcohols at low coverage and saturation conditions. The heat of adsorption under saturation conditions were averaged over all simulations, that is, after the onset value of pressure of each alcohol. This improves the statistic of the values obtained with the fluctuation method. We compared the heat of adsorption at infinite dilution, computed using the Widom

particle insertion method for one single molecule,<sup>42</sup> with the heat of adsorption from an average of three molecules per unit cell, computed using a fluctuation method.<sup>52</sup> These values are similar for all molecules but ethylene glycol. In the particular case of linear molecules, the heat of adsorption calculated from one or from the average of three molecules do not change the trend found in Figure 7a. On the other hand, as shown in Figure 8, the heat of adsorption is higher at saturation than at the low coverage regime. This is due to the energy involved in the process of aggregation of the molecules of alcohol and indicates that the contribution of the HB to the nucleation of the molecules plays an important role in the adsorption process and in the energetic behavior. Focusing on linear alcohols, the heat of adsorption increases linearly, and the almost constant trend found at low coverage disappears. Therefore, the anomalous host-guest interaction shown in Figure 7 only takes place at low coverage.

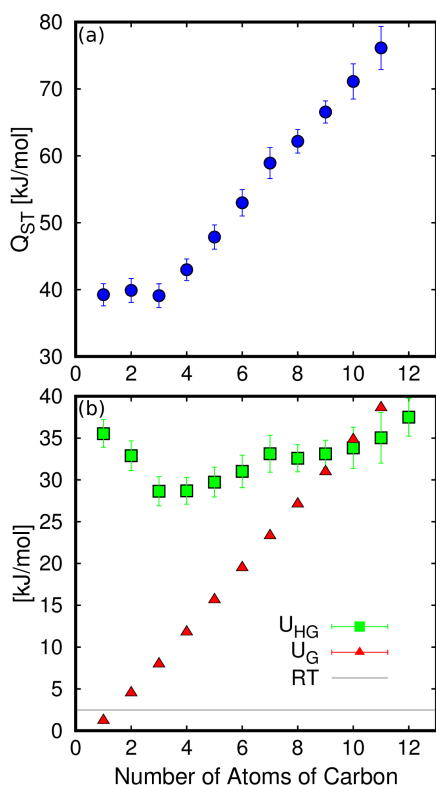


**Figure 7.** Absolute value of the isosteric heat of adsorption of linear alcohols at infinite dilution in MAF-6. (b) Terms of energy contributing to the isosteric heat of adsorption.

To analyze the binding of the molecules of alcohol with the structure, we performed energy minimization simulations of a single molecule of each alcohol. The most stable configuration of the molecules of alcohol in the pores of MAF-6 is with the hydroxyl group facing the center of the imidazole ring. This is due to the electrostatic interactions of the aromatic ring of the ligand with the dipole formed by the oxygen and hydrogen atoms of the light alcohols. Figure 9a shows the computed

electrostatic field lines in the region of the most probable location of the molecules, that is, around the imidazole ring. The hydroxyl group of methanol is aligned to the field lines facing the center of the ring. We also found the same behavior for the other molecules. Therefore, the location and distribution of the imidazole rings inside the cavities are the key factors for the adsorption of the first molecule. All imidazolium rings of the structure are accessible to the molecules of alcohol. Figure 9b shows the accessible surface of the cavities of MAF-6. The surface exhibits homogeneous distribution of pockets, which allows the molecules of alcohol to access the imidazole rings. These pockets act as binding sites for the first molecule adsorbed in the structure. In the case of short molecules (methanol, ethanol, and propanol), the hydroxyl group binds to MAF-6 through the imidazole rings. However, these molecules are more rigid than the long alcohols, and if the hydroxyl group is located in the pocket site, the tail of the molecule cannot interact with the rest of the structure. Long alcohols are more flexible so the hydroxyl group binds to the ring, and simultaneously, the tail could interact with the surroundings. This explains the constant values of  $Q_{st}$  for methanol, ethanol, and propanol shown in Figure 7a.

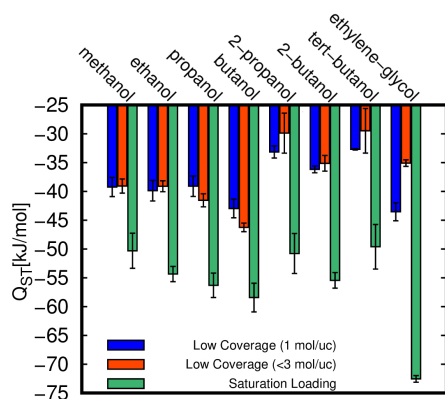


**Figure 8.** Heat of adsorption of methanol, ethanol, propanol, butanol, 2-propanol, 2-butanol, tert-butanol, and ethylene-glycol in MAF-6.

Figure 9c shows the percentage of the binding sites occupied by molecules of alcohol at low coverage and saturation conditions. We consider a molecule in a binding site when the distance between the oxygen atom of the alcohol and the geometric center of the imidazolium ring is lower than a certain value (see simulation details). The occupation of binding sites increases with the chain length of linear alcohols at low coverage and decreases at high coverage. Therefore, the longest molecules interact stronger with the structure at low coverage. At high coverage, the shortest molecules can fill more binding sites because of steric effects. The distance between two consecutive binding sites is about  $5\text{\AA}$ . Then, when the structure is saturated with molecules, the tail of the longest molecules reduces the possibility of accessing to consecutive binding sites. These binding sites are narrow pock-

ets and therefore favor the adsorption of linear alcohols.

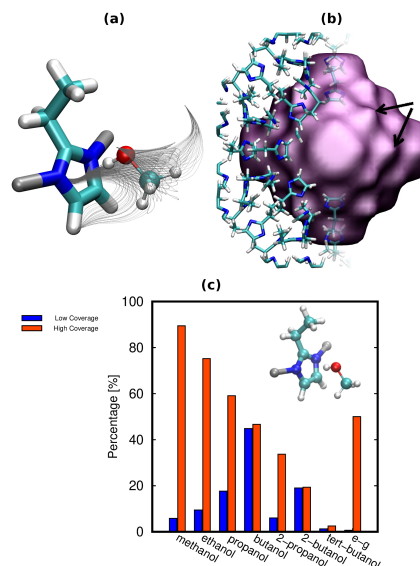


**Figure 9.** Electrostatic field lines near organic ligand binding of a single molecule of methanol. (b) Representation of the accessible surface of MAF-6. Black arrows pointing to the binding sites of MAF-6. (c) Percentage of 2-ethylimidazole rings of the structure (binding site) occupied by molecules of alcohol, oriented as shown in the inset figure (binding geometry).

Figure 10 shows the average occupation profiles of ethanol at saturation. These profiles are similar for all alcohols. The average occupation profiles were computed by averaging the entire trajectory recorded during the GCMC simulations. We observe that methanol fulfills the cavities of MAF-6, supporting a previous discussion and proving that the pocket sites defined above are accessible to the molecules of alcohol.

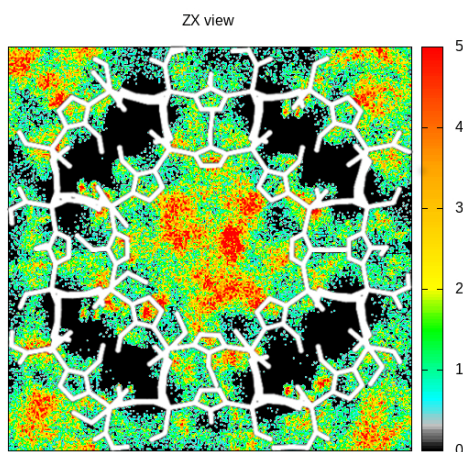


**Figure 10.** ZX view of the average occupation profile of ethanol at saturation loading.

Finally, we calculated the diffusion of the adsorbed molecules within the cavities of MAF-6 under saturation conditions. Figure 11a,b shows the mean squared displacement of the linear alcohols, while

Figure 11c depicts the self-diffusion coefficients of the linear and branched alcohols. The increase in the chain length of linear alcohols leads to the decrease of the self-diffusion coefficients. This is consistent with the trend observed for the heat of adsorption at high coverage and the onset values of pressure of the adsorption isotherms. As expected for a system with large pores, where the diffusion is not limited by confinement, the structure exhibits more affinity for the longest molecules that have the lowest diffusion coefficients. In this case, the diffusion of propanol is of the same order of magnitude as the diffusion of 2-propanol. Likewise, the diffusion of butanol is of the same order of magnitude as the diffusion of 2-butanol and tert-butanol.

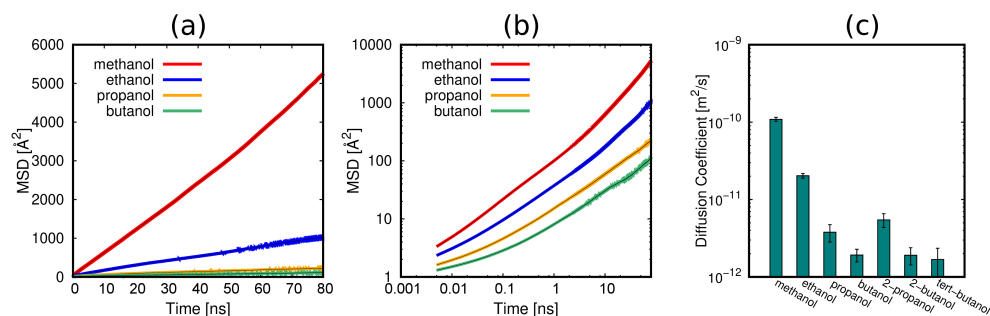


**Figure 11.** (a) Mean squared displacement of linear alcohols: (a) linear scale and (b) logarithmic scale. Self-diffusion coefficients of linear and branched alcohols (c).

As discussed here, the adsorption of light alcohols in hydrophobic MAF-6 is governed by the clusterization of molecules inside the big cavities by the formation

of a strong HB network. This aggregation starts in the pocket sites of the structure where the hydroxyl group of the molecules points to the center of the imidazolium

ring of the organic linker. It is important to mention that these binding sites are the place where the first molecules adsorb in the pores. However they do not act as active sites which favor the adsorption at lower values of pressure, preserving the hydrophobic nature of the adsorbent. In this regard, the energy exchange involved in the process is related to the nucleation too. As a result of this, the dynamics of the system is driven by the host-guest interactions.

### 3.4 CONCLUSIONS

We studied the adsorption of light alcohols in the hydrophobic metal azolate framework MAF-6. We analyzed the effect of the alkyl chain length and the conformation of the molecules in the adsorption process. Steeped adsorption isotherms are optimal for the capture of light alcohols by pressure swing adsorption since the structure does not require high pressure changes to adsorb and release the adsorbates. We identified that the clusterization of the molecules after values of pressure that are below the saturation pressure of each adsorbate is the key factor governing the adsorption mechanism. This clusterization involves a large exchange of energy between the low concentration regime and the saturation loading. We found that the specific binding sites of the structure are the aromatic rings of the 2-ethylimidazole organic linker. These sites are pockets where the hydroxyl group of the molecules of alcohol point to the cen-

ter of the aromatic ring. This is because the dipole of the hydroxyl group is oriented by the electrostatic field around the binding sites. The lack of diffusion limitations of light alcohols in the structure was demonstrated too. The self-diffusion coefficients decrease with increase in the chain length of the molecules, whereas they remain similar for each isomer. In summary, MAF-6 shows a very high adsorption capacity, steeped adsorption behavior, and high energy exchange during the adsorption process and allows the diffusion of the adsorbates. On the basis of these findings, MAF-6 seems a promising structure for the capture of light alcohols. The main conclusions of this work could also be applied to other hydrophobic MOFs.

### 3.5 BIBLIOGRAPHY

- [1] Hill, J.; Nelson, E.; Tilman, D.; Polasky, S.; Tiffany, D. *Proceedings of the National Academy of Sciences* **2006**, *103*, 11206–11210.
- [2] Searchinger, T.; Heimlich, R.; Houghton, R. A.; Dong, F.; Elobeid, A.; Fabiosa, J.; Tokgoz, S.; Hayes, D.; Yu, T. H. *Science* **2008**, *319*, 1238–1240.
- [3] Shamsul, N. S.; Kamarudin, S. K.; Rahman, N. A.; Kofli, N. T. *Renewable and Sustainable Energy Reviews* **2014**, *33*, 578–588.
- [4] Kim, S.; Dale, B. E. *Biomass and Bioenergy* **2004**, *26*, 361–375.
- [5] Kameoka, A.; Nagai, K.; Sugiyama, G.; Seko, T. *SAE Technical Paper Series* **2010**, *1*.
- [6] Dias, M. O.; Junqueira, T. L.; Rossell, C. E. V.; MacIel Filho, R.; Bonomi, A. *Fuel Processing Technology* **2013**, *109*, 84–89.
- [7] Bessa, L. C.; Batista, F. R.; Meirelles, A. J. *Energy* **2012**, *45*, 603–612.
- [8] Bessa, L. C.; Ferreira, M. C.; Batista, E. A.; Meirelles, A. J. *Energy* **2013**, *63*, 1–9.
- [9] Vorayos, N.; Kiatsiriroat, T.; Vorayos, N. *Renewable Energy* **2006**, *31*, 2543–2554.
- [10] Atadashi, I. M. *Alexandria Engineering Journal* **2015**, *54*, 1265–1272.

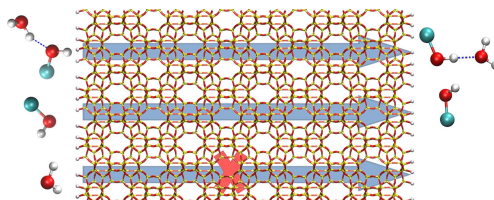
- [11] Jonquières, A.; Clément, R.; Lochon, P.; Néel, J.; Dresch, M.; Chrétien, B. *Journal of Membrane Science* **2002**, *206*, 87–117.
- [12] Berg, L.; Ratanapupech, P. Separation of Ethyl Acetate from Ethanol and Water by Extractive Distillation. 1983.
- [13] Wang, C.; Guang, C.; Cui, Y.; Wang, C.; Zhang, Z. *Chemical Engineering Research and Design* **2018**, *136*, 513–528.
- [14] Kiran, B.; Jana, A. K.; Samanta, A. N. *Energy* **2012**, *41*, 443–453.
- [15] Tgarguifa, A.; Abderafi, S. *Proceedings of 2016 International Renewable and Sustainable Energy Conference, IRSEC 2016*; 2016; pp 884–889.
- [16] Matito-Martos, I.; Moghadam, P. Z.; Li, A.; Colombo, V.; Navarro, J. A.; Calero, S.; Fairen-Jimenez, D. *Chemistry of Materials* **2018**, *30*, 4571–4579.
- [17] Claessens, B.; Martin-Calvo, A.; Gutiérrez-Sevillano, J. J.; Dubois, N.; Denayer, J. F.; Cousin-Saint-Remi, J. *Langmuir* **2019**, *35*, 3887–3896.
- [18] Bueno-Perez, R.; Merklung, P. J.; Gómez, P.; Calero, S. *Chemistry - A European Journal* **2017**, *23*, 874–885.
- [19] Bueno-perez, R.; Gutierrez-Sevillano, J. J.; Dubbeldam, D.; Merklung, P. J.; Calero, S. *ChemPhysChem* **2015**, *16*, 2735–2738.
- [20] Gutierrez-Sevillano, J. J.; Calero, S.; Krishna, R. *The Journal of Physical Chemistry C* **2015**, *119*, 3658–3666.
- [21] Calero, S.; Gómez-álvarez, P. *The Journal of Physical Chemistry C* **2015**, *119*, 467–472.
- [22] Gutierrez-Sevillano, J. J.; Dubbeldam, D.; Belarosa, L.; López, N.; Liu, X.; Vlucht, T. J.; Calero, S. *The Journal of Physical Chemistry C* **2013**, *117*, 20706–20714.
- [23] de Lima, G. F.; Mavrandonakis, A.; de Abreu, H. a.; Duarte, H. a.; Heine, T. *J. Phys. Chem. C* **2013**, *117*, 4124–4130.
- [24] Li, H.; Shi, W.; Zhao, K.; Niu, Z.; Chen, X.; Cheng, P. *Chemistry - A European Journal* **2012**, *18*, 5715–5723.
- [25] Zhang, K.; Lively, R. P.; Dose, M. E.; Brown, A. J.; Zhang, C.; Chung, J.; Nair, S.; Koros, J.; Chance, R. R. *Chem. Soc. Rev.* **2013**, *49*, 3245–3247.
- [26] De Lange, M. F.; Verouden, K. J.; Vlucht, T. J.; Gascon, J.; Kapteijn, F. *Chemical Reviews* **2015**, *115*, 12205–12250.
- [27] Zhang, K.; Zhang, L.; Jiang, J. *Journal of Physical Chemistry C* **2013**, *117*, 25628–25635.
- [28] Mayo, S. L.; Olafson, B. D.; Iii, W. a. G.; Eb, E.; El, E. a. E. T. *Journal of Physical chemistry* **1990**, *101*, 8897–8909.
- [29] Nalaparaju, A.; Zhao, X. S.; Jiang, J. W. *The Journal of Physical Chemistry C* **2010**, *114*, 11542–11550.
- [30] Cousin Saint Remi, J.; Rémy, T.; Vanhunskerken, V.; Vandeperre, S.; Duerinck, T.; Maes, M.; Devos, D.; Gobchiya, E.; Kirschhock, C. E.; Baron, G. V.; Denayer, J. F. *ChemSusChem* **2011**, *4*, 1074–1077.
- [31] De Lange, M. F.; Van Velzen, B. L.; Ottevanger, C. P.; Verouden, K. J.; Lin, L. C.; Vlucht, T. J.; Gascon, J.; Kapteijn, F. *Langmuir* **2015**, *31*, 12783–12796.
- [32] Sławek, A.; Vicent-Luna, J. M.; Marszałek, B.; Gil, B.; Morris, R. E.; Makowski, J.; Calero, S. *Chemistry of Materials* **2018**, *30*, 5116–5127.
- [33] Zhang, K.; Nalaparaju, A.; Chen, Y.; Jian, J. *Physical Chemistry Chemical Physics* **2014**, *16*, 9643–9655.
- [34] Wang, C.; Yan, X.; Hu, X.; Zhou, M.; Ni, Z. *Journal of Molecular Liquids* **2016**, *223*, 427–430.
- [35] He, C.-t.; Jiang, L.; Ye, Z.-m.; Krishna, R.; Zhong, Z.-s.; Liao, P.-q.; Xu, J.; Ouyang, G.; Zhang, J.-p.; Chen, X.-m. *Journal of the American Chemical Society* **2015**, *137*, 7217–7223.
- [36] Gao, C.; Shi, Q.; Dong, J. *CrystEngComm* **2016**, *18*, 3842–3849.
- [37] Wu, T.; Zhang, J.; Zhou, C.; Wang, L.; Bu, X.; Feng, P. *Journal of the American Chemical Society* **2009**, *131*, 6111–6113.
- [38] Johnson, G. M.; Tripathi, A.; Parise, J. B. *Microporous and Mesoporous Materials* **1999**, *28*, 139–154.
- [39] Liu, Y.; Kravtsov, V. C.; Larsen, R.; Eddaoudi, M. *Chemical Communications* **2006**, 1488–1490.
- [40] Dubbeldam, D.; Calero, S.; Ellis, D. E.; Snurr, R. Q. *Molecular Simulation* **2015**, *42*, 81–101.
- [41] Dubbeldam, D.; Torres-Knoop, A.; Walton, K. S. *Molecular Simulation* **2013**, *39*, 1253–1292.
- [42] Widom, B. *The Journal of Chemical Physics* **1963**, *39*, 2808–2812.
- [43] Plimpton, S. *Journal of Computational Physics* **1995**, *117*, 1–19.
- [44] Stubbs, J. M.; Potoff, J. J.; Siepmann, J. I. *Journal of Physical Chemistry B* **2004**, *108*, 17596–17605.
- [45] Padró, J. A.; Saiz, L.; Guàrdia, E. *Journal of Molecular Structure* **1997**, *416*, 243–248.
- [46] Martí, J.; Padró, J. A.; Guàrdia, E. *The Journal of Chemical Physics* **1996**, *105*, 639–649.
- [47] Rappé, A. K.; Casewit, C. J.; Colwell, K. S.; Goddard III, W.; Skiff, W. *J. Am. Chem. Soc.* **1992**, *114*, 10024–10035.
- [48] Gutierrez-Sevillano, J. J.; Calero, S.; Ania, C. O.; Parra, J. B.; Kapteijn, F.; Gascon, J.; Hamad, S. *Journal of Physical Chemistry C* **2013**, *117*, 466–471.
- [49] Huang, X. C.; Lin, Y. Y.; Zhang, J. P.; Chen, X. M. *Angewandte Chemie* **2006**, *45*, 1557–1559.
- [50] Cambridge Crystallographic Data Centre. 2019.
- [51] Wu, X.; Huang, J.; Cai, W.; Jaroniec, M. *RSC Advances* **2014**, *4*, 16503–16511.
- [52] Karavias, F.; Myers, A. L. *Langmuir* **1991**, *7*, 3118–3126.



## The Role of Hydrogen Bonding in the Dehydration of Bioalcohols in Hydrophobic Pervaporation Membranes

Rafael María Madero-Castro, Sofía Calero, and Ozgur Yazaydin

The dehydration of bioalcohols is considered one of the major factors contributing to the cost of biofuel production. In this study, liquid phase separation of water from methanol and ethanol in a siliceous MFI pervaporation membrane was studied by performing concentration gradient driven molecular dynamic (CGD-MD) simulations. CGD-MD simulations work by imposing a higher concentration in the feed side and a lower concentration in the permeate side of the membrane. This creates a concentration gradient across the membrane that facilitates the diffusion of molecules from the feed to the permeate side, mimicking the experimental pervaporation membrane set up. Fluxes of methanol, ethanol and water were calculated in single component permeation simulations and in equimolar methanol-water and ethanol-water mixture separation simulations. It was found that water formed hydrogen bonds with the silanol (Si-OH) groups on the external surface of the MFI and did not enter the membrane in the single component permeation simulation. While this may suggest that MFI can be used to effectively dehydrate bioalcohols, our simulations showed that water permeated through the MFI membrane when it was in a mixture with either methanol or ethanol. Furthermore, in the alcohol-water mixture simulations, the fluxes of methanol and ethanol were significantly lower than that of expected based on their single component fluxes. A detailed analysis of hydrogen bonding in the alcohol-water mixture separation simulations revealed that water preferred making hydrogen bonds with methanol and ethanol rather than with the silanol groups. This resulted in drifting of water molecules along with permeating alcohol molecules in to the MFI membrane in mixture simulations, while slowing the permeation of methanol and ethanol fluxes. The hydrogen



bonding between water and alcohol molecules indicates that it may not be possible to achieve complete alcohol selectivity even if defect-free membranes were manufactured; however, our findings also hint at the possibility of functionalizing membrane surfaces with chemical groups that will overcome water-alcohol hydrogen bonding and retain water molecules in order to approach complete selectivity.

---

## 4.1 INTRODUCTION

The warming of our planet has been closely linked to the anthropogenic release of greenhouse gases to the atmosphere.<sup>1</sup> To prevent further increase of Earth's temperature, substitution of fossil fuel based energy with that of generated from renewable resources, such as solar,<sup>2,3</sup> wind<sup>4,5</sup> and biomass,<sup>6,7</sup> has been considered essential. However, the effectiveness of these alternative energy resources in the fight against climate change has not been without controversy.<sup>8</sup> In the case of biofuels in particular, there has been an ongoing debate about how environmentally friendly they are in reality.<sup>9</sup> For instance, some studies suggest that production of biofuels consume more energy than they produce.<sup>10,11</sup> One of the major factors contributing to the cost of biofuel production is the dehydration of bioalcohols. This process has traditionally employed distillation, which requires large amounts of energy to achieve sufficient purity for alcohol to be used as fuel. Furthermore, ethanol, for instance, makes an azeotrope with water. Therefore, it is not possible to obtain more than 95 wt% purity ethanol with distillation only. Such difficulties have led to the development of alternative meth-

ods for dehydration of bioalcohols, such as, extractive distillation, adsorption and membrane separation, as well as, hybrid methods which incorporate membrane separation and distillation.<sup>12-14</sup>

Membrane pervaporation has been considered as one of the most effective and energy-saving processes for separation of alcohol-water mixtures, in particular, for the azeotropic ones.<sup>15-17</sup> Hydrophobic and hydrophilic membranes have been developed for the separation of alcohol and water,<sup>12</sup> although making reliable and economical membranes is challenging.<sup>18</sup> For the fabrication of hydrophobic pervaporation membranes, MFI, a hydrophobic zeolite, has been widely used, either in the form of a thin film membrane deposited on a porous support,<sup>19,20</sup> or by dispersing MFI crystals in a polymer matrix,<sup>21,22</sup> exhibiting high flux and separation factors. Furthermore, several molecular simulation studies investigated the adsorption, diffusion and separation of alcohol and water systems in MFI zeolite.<sup>23-27</sup>

By carrying out configurational bias grand canonical Monte Carlo (CB-GCMC) simulations Xiong *et al.*<sup>23</sup> reported that the adsorption of water in MFI is negligible due to its hydrophobicity and

that larger alcohols are adsorbed at relatively lower pressures compared to the smaller alcohols. Krishna *et al.*<sup>24</sup> employed CB-GCMC and molecular dynamics (MD) methods to show that it is not possible to accurately estimate adsorption and diffusion characteristics of alcohol-water mixture based on single component data due to the effect of hydrogen bonding between water and alcohol molecules. Gómez-Álvarez *et al.*<sup>25</sup> performed GCMC and MD simulations in MFI and showed that the diffusion coefficients of water, methanol and ethanol in the adsorbed alcohol-water mixtures were greater than their diffusion coefficients in the adsorbed single component. Studies cited in references 23 to 25 were conducted in periodic MFI structures and as such were not representative of pervaporative membrane separation experiments. Working with periodic structures also meant that these studies did not consider the effect of functional groups; i.e. silanol groups, that are present on the external surface on the separation of alcohol-water mixtures, which can be an important factor as we show later in this paper. Jia *et al.*,<sup>26</sup> on the other hand, carried out MD simulations to study the diffusion of alcohol-water mixtures through MFI slabs in a simulation setup that mimicked pervaporation separation experiments. They emphasized that the behaviour of mixtures differed considerably from that of for the single component systems. For example, they reported that water diffused through the MFI membrane

when it was in a mixture with ethanol but not in the single component phase, which they attributed to the strong hydration energy of ethanol; however, they did not elaborate on the origins of this effect at the molecular level. Furthermore; the MFI model they used did not have any partial atomic charges; i.e. the interaction between the MFI and alcohol and water molecules were purely based on van der Waals forces, and that there were no silanol groups on the external surface of the MFI slabs they used, which are both important for an accurate modelling of the system. Additionally, the method they used did not allow computing the steady-state fluxes. Takaba *et al.*,<sup>27</sup> investigated the pervaporation of an ethanol/water binary mixture in silicalite membrane with dual ensemble Monte Carlo simulations. However, they modelled the ethanol and water molecules as Lennard-Jones fluids, i.e. single spheres, which is a very crude approximation that prevents exploring the role of specific interactions on the separation mechanism.

In this work, we investigate the dehydration of bioalcohols in an MFI membrane by carrying out concentration gradient driven molecular dynamics simulations (CGD-MD).<sup>28</sup> CGD-MD is a non-equilibrium molecular dynamics simulation method which works by applying bidirectional bias forces to maintain the concentration of molecules in designated control volumes. By maintaining a higher concentration at the inlet of a membrane

(feed), and lower concentration at the outlet of a membrane (permeate) the CGD-MD method creates a concentration gradient which drives the diffusion of molecules through the membrane. This method was previously used to study multicomponent gas transport and separation in porous membranes.<sup>28–30</sup> Using the CGD-MD approach allows computing the steady-state flux of molecules and membrane selectivity directly, which is important, because some of us previously showed that at conditions where fluid molecules strongly associate, selectivity of a membrane may not always be computed accurately based on predictions of single component transport properties.<sup>28</sup> Here, we consider the separation of methanol and ethanol from water in an MFI pervaporation membrane setting; i.e., vacuum on the permeate side. The simulations are carried out in the liquid phase and at ambient conditions, and thus useful to understand the potential of porous membranes for the dehydration of bioalcohols with minimum energy consumption; i.e. without heating of the feed. Most importantly, our study reveals that water molecules prefers forming hydrogen bonds with alcohol molecules over the silanol groups that exist on the external surfaces of the MFI membrane. This leads to a diminishing effect on the alcohol-water selectivity and lower than expected alcohol fluxes.

## 4.2 SIMULATION DETAILS

Methanol and ethanol molecules were modelled with the TraPPE-UA force field.<sup>31</sup> In this force field, bonds are rigid but angles are flexible, and  $CH_x$  groups are treated as united atoms, i.e., single interaction centres. For the water molecule, a flexible variant of the SPC/E model was used.<sup>32,33</sup> An MFI membrane was constructed by using the “Computation-ready 2D Zeolitic Slabs Database” of Knio *et al.*<sup>34</sup> This database consists of DFT optimized unit cells of zeolites and their model surfaces for different crystallographic planes terminated with -OH groups. The dimensions of the MFI membrane used in our simulations were 60.49, 53.17 and 110.83 Å in the x, y and z direction, respectively, and the external surfaces were perpendicular to the straight channels [010]. The membrane was treated as a flexible structure using the force field developed by Sastre *et al.*<sup>35–37</sup> Lorentz-Berthelot mixing rules were used to calculate the cross term parameters between different atom types for Lennard-Jones (LJ) potential, which was used to model short range non-bonded interactions. Long range electrostatic interactions were computed using the Ewald summation method.<sup>38</sup> The cut-off distance for the LJ potential and the real part of the Ewald sum was set to 12 Å. Further details on the force field used and all parameters are provided in Table A2.1.

As mentioned in the introduction, we used the CGD-MD method to study the

liquid phase transport of water, methanol and ethanol, and the separation of equimolar methanol-water and ethanol-water mixtures. The CGD-MD simulation setup is illustrated in Figure 1 and CGD-MD specific parameters are provided in Table A2.2. A detailed explanation of how CGD-MD method works can be found in Ozcan *et al.*<sup>28</sup> and Perego *et al.*<sup>39</sup> In our CGD-MD simulations, the MFI membrane was placed in the centre of the simulation box, which was 311.0 Å in the z direction (Figure 1). During the CGD-MD simulations, the concentration of the water, methanol and ethanol molecules were maintained at their target densities in the feed control region (FCR) and the permeate control region (PCR), to mimic a pervaporation membrane separation setup; i.e. higher concentration in FCR (feed) and vacuum in PCR (permeate). This is achieved by applying bi-directional bias forces on fluid

molecules in the feed force region (FFR) and the permeate force region (PFR). The bias force works in such a way that if the instantaneous concentration in the control region is less than the target concentration then the bias force acts in the direction to move more molecules to the control region; and if the instantaneous concentration in the control region is more than the target concentration then the bias force acts in the direction to remove molecules from the control region. We emphasize that it is the concentration gradient that is established across the membrane which facilitates the transport of the molecules, not the bias forces. Molecules which cross the membrane return to the feed side through the periodic boundary (see blue arrows in Figure 1). This ensures that there are always molecules in the feed side and that the transport of the molecules through the membrane can reach to steady state.

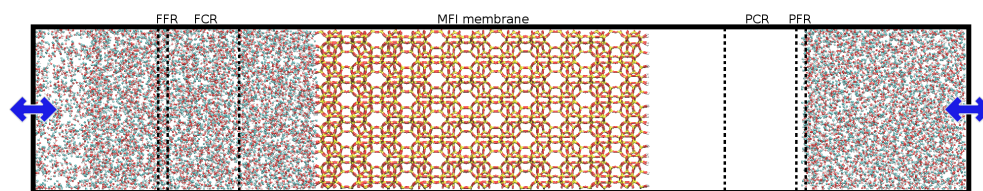


**Figure 1.** CGD-MD simulation setup.

All CGD-MD simulations were carried out using the GROMACS MD simulation package (version 2019.2) patched with an in-house modified version of Plumed 2.4.2. The patch is freely available for download.<sup>40</sup> Simulations were run in the NVT

ensemble and the temperature was kept at 300 K using a Nose-Hoover thermostat. Leapfrog algorithm<sup>38</sup> was used for integrating the Newton's equations of motion with a timestep of 1 fs. A small number of Si atoms (less than 2%) were restrained to

their initial positions in order to avoid the MFI membrane drifting under the concentration gradient. To ensure that the flux of the molecules through the MFI membrane has achieved steady state, CGD-MD simulations were first run for 200 million steps, followed by 200 million steps of production runs, during which fluxes, z-density profiles and hydrogen bonding characteristics of water, methanol and ethanol were calculated in single component and mixture settings.

### 4.3 RESULTS AND DISCUSSION

#### 4.3.1 Force field validation

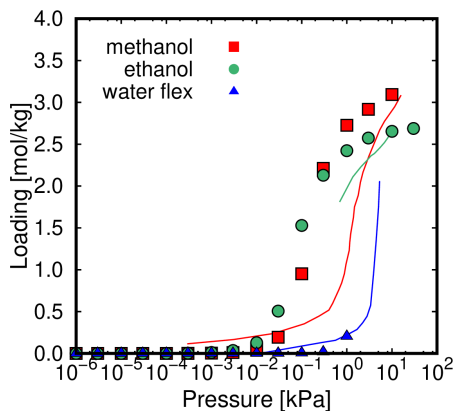


**Figure 2.** Comparison of the experimental (solid lines) and simulated (symbols) adsorption isotherms of methanol (303K), ethanol (308K) and water (308K) in MFI.

We first validated the force field by computing the adsorption isotherms of methanol, ethanol and water in MFI and comparing them against experimental data. For this purpose, we performed grand canon-

ical Monte Carlo (GCMC) simulation using the RASPA molecular simulation package.<sup>41</sup> Further details of the GCMC simulations are provided in the Appendix 2. Figure 2 shows the comparison between simulated and experimental adsorption isotherms of methanol, ethanol and water in MFI.<sup>23,42</sup> The agreement between the simulated and experimental data is very good, and it is particularly important that simulated isotherms reproduce the fact that methanol and ethanol are adsorbed at a lower pressure compared to water. It should also be noted that the amount of water adsorbed within the pressure range investigated is much lower compared to the amount of water that condenses in the pores of all-silica MFI at very high pressures; i.e.  $> 75 MPa$ .<sup>43,44</sup>

#### 4.3.2 Single component permeation of methanol, ethanol and water in the MFI membrane

After validating the force field, we studied the single component permeation of methanol, ethanol and water in the MFI membrane by carrying out CGD-MD simulations. Target concentrations of methanol, ethanol and water in the feed control region were set to their liquid molar densities at 300 K. in the permeate control region, the target concentrations were set to vacuum to mimic pervaporation conditions (Table A2.3). Instantaneous concentrations (Figure A2.1) and the average concentrations of methanol, ethanol and wa-

ter (Table A2.3) in the control regions in single component simulations show that the concentration of the molecules were maintained very close to the target values during the production runs.

Figure 3 shows the z-density profiles of methanol, ethanol and water in the MFI membrane. While both methanol and

ethanol enter the MFI membrane, water does not enter because of the hydrophobicity of the MFI zeolite. The z-density profiles of methanol and ethanol reflect the structure of MFI, i.e., the z-densities peak at the intersection of the zig-zag and straight channels.

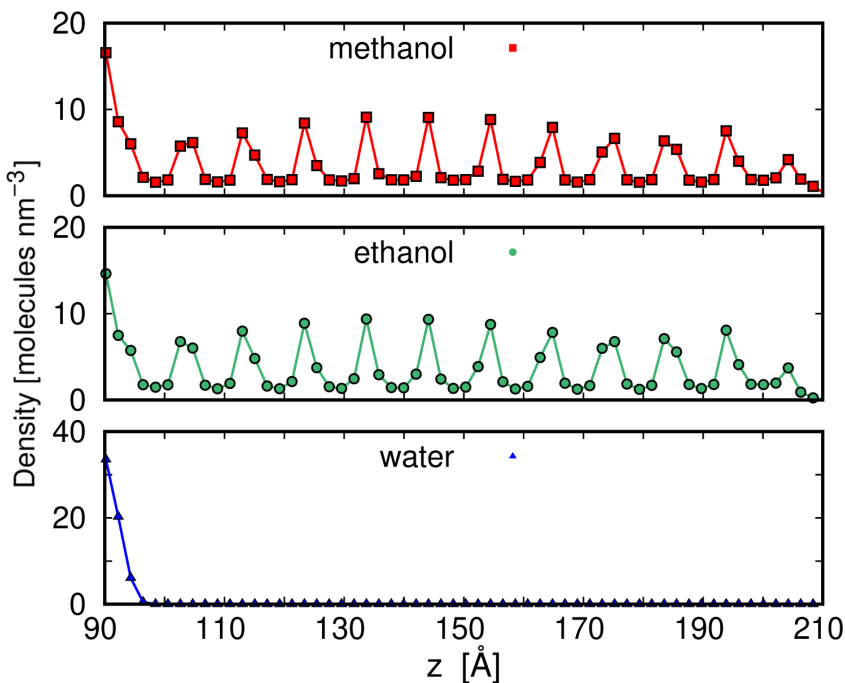


**Figure 3.** Z-density profiles of a) methanol, b) ethanol and c) water in the MFI membrane in single component CGD-MD simulations. The MFI membrane is located between  $z \approx 93 \text{ \AA}$  and  $204 \text{ \AA}$ .

The fluxes of methanol, ethanol and water in the MFI membrane were calculated by using the following formula<sup>28</sup>

$$J_z = \frac{N_i^+ - N_i^-}{t \cdot A_{xy}}$$

where  $J_z$  is the flux in the direction of the flow,  $N^+$  and  $N^-$  are the number of

molecules that cross a geometric plane located at the centre of the membrane in the positive and negative z-directions, respectively,  $A_{xy}$  is the cross sectional area of the membrane, and  $t$  is the simulation time. In the single component simulations, methanol flux is about twice that of

ethanol, and water has a zero flux (Table 1) since it does not enter the MFI membrane, which is in agreement with the experimental findings that water only enters all-silica MFI at very high pressures.<sup>43,44</sup>

This may suggest that MFI can demonstrate complete selectivity for methanol and ethanol over water; however, as we show in the mixture simulations below this is not the case.

**Table 1.** Methanol, ethanol and water fluxes, expressed in *molecules/nm<sup>2</sup>ns*, in MFI from single component and mixture simulations.

	Methanol	Ethanol	Water
Single component	$0.20 \pm 0.01$	$0.09 \pm 0.02$	0*
Methanol-water mixture	$0.013 \pm 0.008$	-	$0.002 \pm 0.004$
Ethanol-water mixture	-	$0.03 \pm 0.01$	$0.0005 \pm 0.0004$

\*Water does not enter the MFI membrane in the single component simulation.

### 4.3.3 Dehydration of binary alcohol-water mixtures in the MFI membrane

To study the dehydration of binary alcohol-water mixtures in the MFI membrane, we considered equimolar mixtures of methanol-water and ethanol-water. For both mixtures, target concentrations of the components in feed control region were set to reproduce the molar density of equimolar mixtures at 300 K assuming ideal mixing, and the target concentrations were set to zero in the permeate control region to mimic pervaporation conditions (Table A2.4). Instantaneous concentrations (Figure A2.2) and the average concentrations of methanol, ethanol and water (Table A2.4) in the control regions in mixture simulations show that the concentration of the molecules were maintained very close to the target values during the production

runs. Figure 4 shows the z-density profiles of methanol, ethanol and water in the MFI membrane in the mixture simulations. Unlike the case in the single component simulation of water, the density of water within the membrane, although very small, is non-zero in both mixture simulations. That is, water enters the membrane when it is in a mixture with methanol or ethanol. Indeed, there is a quantifiable water flux in MFI in the mixture simulations, although it is very small compared to the fluxes of methanol and ethanol (Table 1). Furthermore, the presence of water appears to be slowing down the permeation of methanol and ethanol in alcohol-water mixtures (Table 1). One can argue that the slower fluxes of methanol and ethanol in alcohol-water mixtures compared to their fluxes in the single component simulations is due to their relatively lower feed concentrations in the mixture simulation com-

pared to their feed concentrations in the single component simulations. However, the lower feed concentrations of alcohols in the mixture simulations do not alone account for the slower fluxes of methanol and ethanol in the mixture simulations. For instance, the feed concentration of methanol in the mixture simulations is about 45% lower than that of its feed concentration in the single component simulation; i.e. 10.43 vs 14.99 [ $\text{molecules}/\text{nm}^3$ ], respectively (Tables A2.3 and A2.4). The

flux of methanol in the mixture simulation is about an order of magnitude smaller than its single component flux (Table 1). Likewise, the flux of ethanol in the mixture is three times smaller than its single component flux (Table 1), but the ethanol feed concentration in the mixture simulation is only  $\approx 30\%$  lower than that of in the single component; i.e. 7.92 vs 10.16 [ $\text{molecules}/\text{nm}^3$ ], respectively (Tables A2.3 and A2.4).

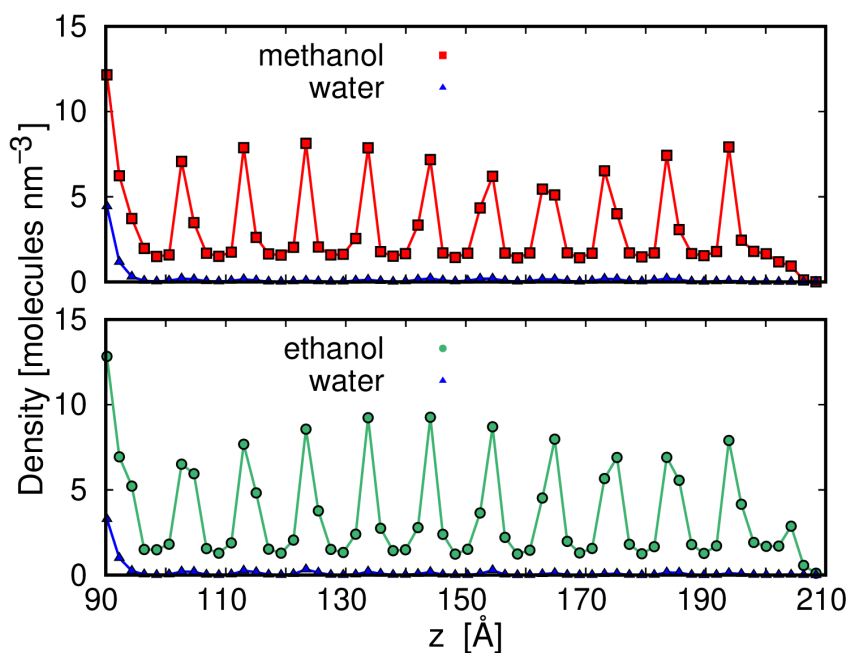


**Figure 4.** Z-density profiles of methanol, ethanol and water as a function of  $z$  coordinate in mixture CGD-MD simulations. The MFI membrane is located between  $z \approx 93\text{\AA}$  and  $204\text{\AA}$ .

To understand why water enters the MFI membrane in the alcohol-water mixture simulations but not in the single com-

ponent water simulation, we analysed the number of hydrogen bonds that form between the silanol groups located on the

feed side of the MFI surface and the methanol, ethanol and water molecules (Table 2). In single component simulations water molecules form about five times more hydrogen bonds with the surface silanol groups compared to methanol and ethanol. This may be due to two reasons; first, water has two  $-OH$  groups whereas methanol and ethanol has only one, and second, the molecular density of water is larger compared to methanol and ethanol, that is, there are relatively more water molecules present per unit volume in comparison to methanol and ethanol. However, in the mixture simulations there is a very different scenario. The number of hydrogen bonds that methanol or ethanol form with the silanol groups are more than the number of hydrogen bonds that form between the water molecules and silanol groups. The number of hydrogen bonds that water forms with silanol groups when it is in a mixture with methanol is about 10 times smaller compared to that of in the single component simulation, and it is 14 times smaller when it is in a mixture with ethanol. This cannot be explained only by the lower concentration of water in the mixture simu-

lations (10.39 and 7.88 [ $molecules/nm^3$ ] for methanol and ethanol mixtures, respectively (Table A2.4)), compared to its concentration in the single component simulation, ( $33.7 molecules/nm^3$ ) (Table A2.3)). It is clear that, water molecules interact more strongly with the alcohol molecules; i.e. through hydrogen bonding, compared to the surface silanols. This in turn facilitates the diffusion of water in the MFI membrane, because thanks to the hydrogen bonding that forms between the water and alcohol molecules, water molecules are carried in to the MFI with the diffusing methanol and ethanol molecules. The preferred hydrogen bonding of water with alcohol molecules also explains the lower than expected fluxes of methanol and ethanol in their mixtures with water. While water enters MFI thanks to the hydrogen bonds that it forms with alcohol molecules, it slows down the permeation of methanol and ethanol. It is also noteworthy that the hydrogen bonding is relatively weaker between alcohol molecules in the membrane compared to the feed (see Table A2.5 and the pertinent discussion in the Appendix 2).<sup>45</sup>

**Table 2.** Number of hydrogen bonds that methanol, ethanol and water molecules form with the MFI surface at the feed side in single component and mixture simulations.

	Methanol	Ethanol	Water
Single component	$17 \pm 4$	$17 \pm 3$	$76 \pm 7$
Methanol-water mixture	$12 \pm 3$	-	$8 \pm 3$
Ethanol-water mixture	-	$9 \pm 3$	$5 \pm 2$

The reason for the preference of water molecules for making hydrogen bonding with alcohols rather than with surface silanols can be due to the difference in the polarity of  $-OH$  groups in the silanol groups and those of in the methanol and ethanol molecules. Partial charges of oxygen atoms in the  $-OH$  groups of alcohol and the silanol are very similar (i.e.,  $q_{O_{alc}} = -0.7e$  and  $q_{O_{sil}} = -0.725e$ ). However, the partial charge of the hydrogen atom of the  $-OH$  group of alcohol is more than twice that of for the hydrogen atom of the  $-OH$  group of the silanol (i.e.;  $q_{H_{alc}} = 0.435e$  and  $q_{H_{sil}} = 0.2e$ , respectively). The larger hydrogen partial charge on the alcohol  $-OH$  group leads to a stronger interaction with water compared to the interaction between the silanol group and water. This suggest that even if defect free membranes can be manufactured, the hydrogen bonding between water and alcohol molecules will always result in diffusion of water molecules along with alcohols, thus eliminating the possibility of complete dehydration of biofuels. Nevertheless, the ethanol/water selectivity based on the ethanol and water fluxes from the ethanol-water mixture simulation, i.e.  $0.03/0.0005 = 60$ , can still be considered very high.

#### 4.4 CONCLUSIONS

The purification of bioalcohols using pervaporation membranes based on hydrophobic zeolites potentially has several advantages in comparison to distillation, includ-

ing and most importantly, lower energy requirements. All silica MFI zeolite allows the diffusion of pure methanol and ethanol and prevents the diffusion of pure water due to its hydrophobic character. Pure water hydrogen bonds strongly with the silanol groups on the external surface of the MFI. On the other hand, when water is in a mixture with alcohol, the hydrogen bonding of water with silanol groups reduces due to its preferred hydrogen bonding with alcohols and this leads to water permeating through the MFI membrane along with alcohol molecules. The strong hydrogen bonding between water and alcohol molecules may suggest that total selectivity of alcohol over water in a hydrophobic pervaporation membrane, such as MFI, cannot be achieved. However, our findings also hint at the possibility of modifying surfaces with functional groups that will overcome the interaction between water and alcohol molecules and retain water outside the membrane as a new strategy for manufacturing membranes with improved separation performance for the dehydration of bioalcohols.

#### 4.5 BIBLIOGRAPHY

- [1] Lüthi, D.; Le Floch, M.; Bereiter, B.; Blunier, T.; Barnola, J. M.; Siegenthaler, U.; Raynaud, D.; Jouzel, J.; Fischer, H.; Kawamura, K.; Stocker, T. F. *Nature* **2008**, *453*, 379–382.
- [2] Lewis, N. S.; Nocera, D. G. *Proceedings of the National Academy of Sciences of the United States of America* **2006**, *104*, 20142.
- [3] Lewis, N. S. *Science* **2007**, *315*, 798–801.
- [4] Joselin Herbert, G. M.; Iniyar, S.; Sreevalsan, E.; Rajapandian, S. *Renewable and Sustainable Energy Reviews* **2007**, *11*, 1117–1145.

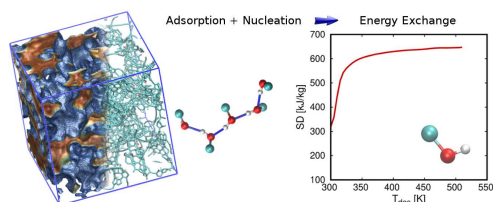
- [5] Saidur, R.; Rahim, N. A.; Islam, M. R.; Solangi, K. H. *Renewable and Sustainable Energy Reviews* **2011**, *15*, 2423–2430.
- [6] Nigam, P. S.; Singh, A. *Progress in Energy and Combustion Science* **2011**, *37*, 52–68.
- [7] Somerville, C.; Youngs, H.; Taylor, C.; Davis, S. C.; Long, S. P. *Science* **2010**, *329*, 790–792.
- [8] Jacobson, M. Z. *Review of Solutions to Global Warming, Air Pollution, and Energy Security*. 2009.
- [9] Scharlemann, J. P.; Laurance, W. F. *Science* **2008**, *319*, 43–44.
- [10] Pimentel, D.; Patzek, T.; Cecil, G. *Reviews of Environmental Contamination and Toxicology*; 2007; Vol. 189; pp 25–41.
- [11] Ulgiati, S.; Hall, C. A. S. *Critical Reviews in Plant Sciences* **2001**, *20*, 71–106.
- [12] Claessens, B.; Cousin-Saint-Remi, J.; Denayer, J. F. *Structure and Bonding* **2020**, *184*, 85–119.
- [13] Frolkova, A. K.; Raeva, V. M. *Theoretical Foundations of Chemical Engineering* **2010**, *44*, 545–556.
- [14] Huang, H. J.; Ramaswamy, S.; Tschirner, U. W.; Ramarao, B. V. *Separation and Purification Technology* **2008**, *62*, 1–21.
- [15] Mulder, M.; Hendrikman, J. O.; Hegeman, H.; Smolders, C. A. *J. Membrane Sci.* **1983**, *16*, 269–284.
- [16] Ong, Y. K.; Shi, G. M.; Le, N. L.; Tang, Y. P.; Zuo, J.; Nunes, S. P.; Chung, T. S. *Progress in Polymer Science* **2016**, *57*, 1–31.
- [17] Wei, P.; Cheng, L. H.; Zhang, L.; Xu, X. H.; Chen, H. L.; Gao, C. *J. Renewable and Sustainable Energy Reviews* **2014**, *30*, 388–400.
- [18] Huang, Y.; Baker, R. W.; Vane, L. M. *Industrial Engineering Chemistry Research* **2010**, *49*, 3760–3768.
- [19] Korelskiy, D.; Leppäjärvi, T.; Zhou, H.; Grahn, M.; Tanskanen, J.; Hedlund, J. *Journal of Membrane Science* **2013**, *427*, 381–389.
- [20] Shu, X.; Wang, X.; Kong, Q.; Gu, X.; Xu, N. *Industrial and Engineering Chemistry Research* **2012**, *51*, 12073–12080.
- [21] Bowen, T. C.; Meier, R. G.; Vane, L. M. *Journal of Membrane Science* **2007**, *298*, 117–125.
- [22] Kamelian, F. S.; Mohammadi, T.; Naeimpoor, F. *Separation and Purification Technology* **2019**, *229*, 115820.
- [23] Xiong, R.; Sandler, S. I.; Vlachos, D. G. *Langmuir* **2012**, *28*, 4491–4499.
- [24] Krishna, R.; Van Baten, J. M. *Langmuir* **2010**, *26*, 10854–10867.
- [25] Gómez-Álvarez, P.; Noya, E. G.; Lomba, E.; Valencia, S.; Pires, J. *Study of Short-Chain Alcohol and Alcohol Water Adsorption in MEL and MFI Zeolites*. 2018.
- [26] Jia, W.; Murad, S. *Molecular Physics* **2006**, *104*, 3033–3043.
- [27] Takaba, H.; Koyama, A.; Nakao, S. I. *Journal of Physical Chemistry B* **2000**, *104*, 6353–6359.
- [28] Ozcan, A.; Perego, C.; Salvalaglio, M.; Parrinello, M.; Yazaydin, O. *Chemical Science* **2017**, *8*, 3858–3865.
- [29] Namsani, S.; Ozcan, A.; YazaydĀšn, A. Ö. *Advanced Theory and Simulations* **2019**, *2*, 1900120.
- [30] Ozcan, A.; Semino, R.; Maurin, G.; Yazaydin, A. O. *Chemistry of Materials* **2020**, *32*, 1288–1296.
- [31] Chen, B.; Potoff, J. J.; Siepmann, J. I. *Journal of Physical Chemistry B* **2001**, *105*, 3093–3104.
- [32] Mark, P.; Nilsson, L. *Journal of Physical Chemistry A* **2001**, *105*, 9954–9960.
- [33] Schmid, N.; Eichenberger, A. P.; Choutko, A.; Riniker, S.; Winger, M.; Mark, A. E.; Van Gunsteren, W. F. *European Biophysics Journal* **2011**, *40*, 843–856.
- [34] Knio, O.; Medford, A. J.; Nair, S.; Sholl, D. S. *Chemistry of Materials* **2019**, *31*, 353–364.
- [35] Sastre, G.; Kärger, J.; Ruthven, D. M. *Journal of Physical Chemistry C* **2018**, *122*, 7217–7225.
- [36] Ghysels, A.; Moors, S. L.; Hemelsoet, K.; De Wispelaere, K.; Waroquier, M.; Sastre, G.; Van Speybroeck, V. *Journal of Physical Chemistry C* **2015**, *119*, 23721–23734.
- [37] Ghysels, A.; Moors, S. L.; Hemelsoet, K.; De Wispelaere, K.; Waroquier, M.; Sastre, G.; Van Speybroeck, V. *Journal of Physical Chemistry C* **2017**, *119*, 23721–23734.
- [38] Allen, T. D., M and *Computer simulation of liquids*; 1987.
- [39] Perego, C.; Salvalaglio, M.; Parrinello, M. *Journal of Chemical Physics* **2015**, *142*, 144113–144120.
- [40] CmuMD. <https://github.com/mme-uc1/CmuMD>.
- [41] Dubbeldam, D.; Calero, S.; Ellis, D. E.; Snurr, R. Q. *Molecular Simulation* **2016**, *42*, 81–101.
- [42] Zhang, K.; Lively, R. P.; Noel, J. D.; Dose, M. E.; McCool, B. A.; Chance, R. R.; Koros, W. J. *Langmuir* **2012**, *28*, 8664–8673.
- [43] Trzpit, M.; Soulard, M.; Patarin, J. *Microporous and Mesoporous Materials* **2009**, *117*, 627–634.
- [44] Trzpit, M.; Soulard, M.; Patarin, J.; Desbiens, N.; Cailiez, F.; Boutin, A.; Demachy, I.; Fuchs, A. H. *Langmuir* **2007**, *23*, 10131–10139.
- [45] Madero-Castro, R. M.; Vicent-Luna, J. M.; Calero, S. *The Journal of Physical Chemistry C* **2019**, *123*, 23987–23994.

## Adsorption of Linear Alcohols in Amorphous Activated Carbons: Implications for Energy Storage Applications

Rafael María Madero-Castro, José Manuel Vicent-Luna, Xuan Peng, and  
Sofía Calero

**T**hermal energy storage using porous materials has become a key technology for improving efficiency and sustainability of heat storage applications to reduce the carbon dioxide emissions. Choosing the adsorbent-fluid working pairs that im-

prove the performance of an energy storage process is a challenge due to the large number of possible combinations. The use of activated carbons for adsorption, purification, and energy applications as an alternative to other porous materials such as zeolites or silica gel is a promising strategy due to its low production cost combined to a good thermochemical energy storage performance. In this work, we have explored the use of activated carbons derived from the pyrolysis of saccharose coke (CS1000a) for thermal energy storage. For this, we have considered the first four n-alcohols (methanol, ethanol, 1-propanol, and 1-butanol) as working fluids because their large enthalpy of vaporization. We carried out Monte Carlo simulations combined with the thermodynamical model based on the Dubinin-Polanyi theory to evaluate adsorption, interaction energies, microscopic structure, and thermal energy storage density of CS1000a-alcohol pairs. We compared these properties with the performance of other commercial activated carbon, such as BPL. We employed a realistic model containing functional groups in the internal surface and a simplified model without these functional groups. The role of these functional groups and their consequences on the targeted properties is discussed. CS1000a shows excellent performance to store thermal energy and considerably reduces the operational temperatures, being a good alternative to those on the market.



## 5.1 INTRODUCTION

Thermal energy storage is one of the main current technologies leading the transition towards more efficient energy systems.<sup>1</sup> In this context, one of the technologies that are gaining attention within the field of thermo-chemical heat storage is the adsorption heat storage.<sup>2,3</sup> This is based on the energy released upon the interactions of working pairs composed by a porous solid adsorbent and a liquid adsorbate. Therefore, the efficiency of the heat storage process is highly dependent on the adsorbent-adsorbate interactions.<sup>4–6</sup> Being a promising technology, it still needs further development and research to end up on the market as a competitive alternative. Understanding the fundamental mechanisms that trigger the adsorption heat storage process is key to boost the performance and reduce cost of this emerging technology. The adsorption of gases or liquids (working fluids) in porous materials (solid adsorbents) is an exothermic process<sup>7</sup> commonly used for heat storage applications.<sup>4,8</sup> The interactions between the molecules of the working fluid and the solid adsorbent generate a decrease in the total energy of the system, which releases heat to the outside. This heat exchange is the basis of thermal energy storage using porous materials.<sup>4,8</sup> A large number of existing porous materials, together with the wide variety of working fluids, make challenging the search for the most appropriate adsorbate-adsorbent pair for each application. Within porous

materials, the most common adsorbents for adsorption energy storage are silica gels,<sup>5,9–11</sup> zeolites,<sup>3,4,12–14</sup> Metal-Organic Frameworks,<sup>4,15–17</sup> and activated carbons (ACs).<sup>18–20</sup> Many of these works have suggested porous materials as great candidates for thermal energy-related applications. However, most of the adsorbents have been studied in laboratories, and they are still not ready for large-scale development at industrial scale. In this sense, activated carbons exhibit a competitive production cost and wide commercial availability, which is essential to end in the market.

The reference example of industrial application is the well-known and commercial 13X zeolite with water working pairs.<sup>21,22</sup> This pair shows high efficiencies, but it also needs high desorption temperatures (over 500 K).<sup>23</sup> The desorption temperature is affected by the adsorbate-adsorbent interactions, which in the case of 13X/water, are strong due to the high hydrophilic nature of this zeolite. The goal is to achieve high efficiencies but lowering desorption temperatures of the process. For this condition, a steeped isotherm is desired, where the adsorption increases substantially in a small range of pressure/temperature lifts. One strategy can be the use of other adsorbates replacing water. The most common fluids used in thermal energy storage devices are water, methanol, ethanol, and ammonia.<sup>24</sup> Here, we investigate the use of activated carbons with the first four n-alcohols working pairs.

ACs have been used in heat transfer applications using different adsorbates.<sup>18–20</sup> Its big storage capacity, together with a low production cost, is desirable to be a promising candidate for heat transfer applications using light alcohols as working fluids.<sup>23,25,26</sup> Authors such as Kanamori *et al.*<sup>26</sup> and Cacciola *et al.*<sup>27</sup> have studied the use of activated carbons for refrigerating machines with satisfactory results. The activation process of the adsorbent and the correct choice of the working fluid are critical aspects for the efficiency of an adsorption energy storage process.

Porous carbons are amorphous materials formed by atoms of carbon and traces of other atoms such as oxygen or hydrogen. These materials are produced from organic waste, such as wood, sugar or rice residues, or fossils, such as coal or oil, among many others.<sup>28</sup> This makes them low cost materials.<sup>29</sup> ACs are porous carbons subjected to a physicochemical process to adapt their characteristics<sup>30</sup> to specific needs.<sup>30</sup> Pyrolysis is one of the forms used to eliminate moisture and volatile compounds within the samples. Subjecting the carbon to this process alters its internal surface area, pore size, and physicochemical properties.<sup>31</sup> There is currently a large industry based on activated carbons. There are type F commercial activated carbons obtained from coconut shell<sup>32</sup> or carbon nanofibers, sintered by chemical vapor deposition.<sup>33</sup> ACs are used for gas storage,<sup>34–37</sup> separation and purification,<sup>38–40</sup> as catalytic agents,<sup>41,42</sup> or in the pharma-

ceutical industry.<sup>43,44</sup> This is due to its large surface area and chemical surface.<sup>45</sup> At the industrial level, ACs are also used to capture and purify molecules of alcohol.<sup>46–50</sup> Adsorption of polar molecules, such as molecules of alcohol, is closely related to the surface chemistry of the adsorbent, e.g., it is strongly affected by the functional groups.<sup>31</sup>

Delgado *et al.*<sup>50</sup> used activated carbon BPL to separate water-ethanol mixtures with a cyclic adsorption-desorption system until the ethanol was purified. Ravi *et al.*<sup>47</sup> used ACs from M/S. Silica Versahrenstechnik, Germany to adsorb phenol and benzyl alcohol, among other aqueous solutions showing irreversible phenol desorption because it alters the surface chemistry of activated carbon. Critoph<sup>19</sup> studied the possibility of using ACs as heat pumps with ammonia and methanol as working fluids. Similarly, Wang *et al.*<sup>25</sup> studied the same two adsorbates in different materials by changing the form (powders, micro-porous, granular, molecular sieves, and carbon fibers). They obtained higher performances when solidifying the samples than in their granular form. They also found that the channels formed when processing the material are a crucial aspect of the performance of the process. Finally, Kohler *et al.*<sup>23</sup> studied the influence of the carbon chain on n-alcohols, temperature, and desorption time on maximum efficiency for thermal energy, concluding that short-chain alcohols are an excellent alternative to water

as working fluid. These authors observed that methanol, ethanol, and propanol are good candidates for that purpose. Nevertheless, they found that butanol is not an appropriate candidate to substitute water.

In this work, we study CS400, CS1000, and CS1000a carbon materials as candidates for heat storage applications using light alcohols. These structures are synthesized by pyrolyzing pure saccharose coke under a nitrogen flow at 400 °C and 1000 °C~ for CS400 and CS1000 structures. CS1000a is also activated by keeping it at 1000 °C~ in a  $CO_2$  atmosphere for 20 h.<sup>51</sup> At industrial level, these materials have been used previously to capture and separate light gases like nitrogen, methane, or carbon dioxide.<sup>52</sup> The activation of these structures produces a big internal surface area and activated binding sites, making the pore environment appropriate for the adsorption of polar molecules like light alcohols.<sup>51</sup> At the computational level, the structural models of CS400, CS1000, and CS1000a have been developed using Hybrid Reverse Monte Carlo (HRMC) techniques by Jain *et al.*<sup>53</sup> This method introduces variations in the acceptance probabilities and provides advantages over other Monte Carlo methods. These carbons have been generated to reproduce the radial distribution functions (RDF) between atoms of carbon and the porosity of the material. Porosity is described as the accessible surface divided by the total surface. CS1000a has undergone an activation process to

increase its porosity and presents higher porosity value than the other two carbons ( $\phi_{CS1000a} = 0.659$  versus  $\phi_{CS1000} = 0.342$  and  $\phi_{CS400} = 0.466$ ).<sup>52</sup> For the first time, we combine molecular simulations with a thermodynamical model of adsorption to study the performance of the ACs-alcohol working pairs for energy storage applications. For this purpose, we carried out Monte Carlo simulations to obtain the adsorption and interaction energies of the first four n-alcohols in three ACs samples. This allows us to connect the physicochemical properties of the adsorbent fluid at the molecular level with the energy released from an adsorption heat storage process.

## 5.2 SIMULATION DETAILS

We combined molecular simulations with a mathematical model based on the Dubinin-Polanyi theory of adsorption to assess the performance of microporous ACs for heat storage applications. First, we used Monte Carlo simulations to obtain the adsorption properties of light alcohols (methanol, ethanol, 1-propanol and 1-butanol). We computed the adsorption isotherms with the Configurational-Bias Monte Carlo (GCMC) method in the Grand Canonical ensemble, using RASPA molecular simulation software.<sup>54,55</sup> The simulations consist of  $1.2 \cdot 10^6$  cycles of production run. We used the last  $2 \cdot 10^5$  cycles to average the computed properties. This number of cycles guarantees the equilibration of the simulation. The average number of hydrogen bonds per molecule (nHB)

was obtained using a geometrical criterion defining three cut offs including: distances between atoms of oxygen of donor and acceptor molecule and between atom of hydrogen of the donor molecule and atom of oxygen of the acceptor molecule and the angle between atom of oxygen of acceptor molecule and atoms of oxygen and hydrogen of donor molecule. More details about the computation of nHB and the definition of the cut offs can be found in our previous work.<sup>56</sup>

We used a classical force field with Lennard-Jones and Coulombic potentials to describe the van der Waals and electrostatic interactions, respectively. The crossed terms of the Lennard-Jones parameters have been estimated using Lorentz-Berthelot mixing rules,<sup>57</sup> while the electrostatic interactions are calculated using the Ewald summation method.<sup>58</sup> We used the values for the Lennard-Jones parameters and point charges reported by Peng *et al.*<sup>52</sup> to describe the adsorbents, and the Transferable Potentials for Phase Equilibria (TraPPE) force field<sup>59,60</sup> to model the molecules of alcohol. These parameters are listed in Table A3.1 of the Appendix 3. The TraPPE force field for alcohols employs a flexible united atom model where the  $CH_3$  and  $CH_2$  groups are described as single effective interaction centres attached to an -OH group. The bonded interactions are described by a fixed bond, harmonic bending, and a dihedral potential.<sup>61</sup> These models for the alcohols molecules

have proven to be suitable for reproducing their physicochemical properties<sup>58</sup> and adsorption in porous materials.<sup>56,62,63</sup>

The structural models of the adsorbents were developed to describe the textural properties of the real samples. ACs are amorphous materials that do not have an ordered structure that can be deduced from experimental measurements, which makes the development of atomistic models difficult. In this context, we used the realistic structures developed by Jain *et al.*<sup>53</sup> following the Hybrid Reverse Monte Carlo (HRMC) method. This method is based on Monte Carlo insertions to produce atomic configurations that reproduce a targeted property measured experimentally. In this case, the RDFs of the ACs samples obtained from the measured structure factor. The HRMC method also includes an energy penalty to avoid unfavorable configurations. This way, the differences between the reference and the simulated RDF and the energy of the developed system are minimized simultaneously, where the resulting structures fit the experimental data and are physically realistic. The adsorbents are considered as rigid frameworks. The systems consist of a side length 50Å cubic unit cell, ensuring RDF and porosity match with actual ACs samples.<sup>64</sup> In addition to the structural properties, another factor that we need to consider is the chemical composition. It is well known that activated carbons contain functional groups, which are crucial for the adsorption of po-

lar molecules. To model the most realistic conditions, the carbon models used in this work have a certain amount of carboxylic acid ( $-COOH$ ) and alcohol ( $-OH$ ) functional groups to reproduce the experimental  $O/C$  and  $H/C$  ratio.<sup>53</sup> Based on the chemical composition of each material, a certain amount of ( $-COOH$ ) and ( $-OH$ ) functional groups are randomly placed on the internal surface of the ACs samples. The process ensures that the addition of the functional groups does not overlap with other existing atoms. Once the functional groups are attached, the system is relaxed to minimize the energy of the functionalized structures. During the optimization, the carbon atoms of the matrices are fixed and only the functional groups are allowed to move. Table A3.2 collects the structural properties of the three ACs. We analyzed the effect of functional groups on the adsorption and energetic properties and compare them with the bare structures. Due to their accuracy in describing the actual samples, these models have been extensively used in literature for diverse applications.<sup>52,53,64–69</sup> To reinforce the validity of these structural models and the selected force field, we performed additional simulations aimed at comparing with the available experimental data for adsorption in these ACs.

Figure A3.1 shows the comparison between computed and experimental adsorption isotherms of argon<sup>65</sup> and nitrogen<sup>65</sup> at 77 K in CS400 and CS1000 ACs. The low temperature adsorption of these probe

molecules is used in experiments to obtain the textural properties of porous materials. Figure A3.2 shows the isosteric heat of adsorption at infinite dilution of linear hydrocarbons in CS1000a and the corresponding adsorption isotherms of methane, ethane, and propane at 423 K. The computed data was obtained using the Widom test particle insertion method<sup>70,71</sup> in the NVT ensemble. We compared to the data reported by Falk *et al.*<sup>66</sup> obtained with MC simulations in CS1000a used as a kerogen models and with the experimental data for carbon black.<sup>72</sup> We found a good agreement between the experimental and computed isotherms and the heat of adsorption in the three ACs (Figures A3.1 and A3.2), indicating that the force field used to describe the ACs is suitable to describe the adsorption properties for a variety of adsorbates and in a wide range of temperatures.

Despite the lack of adsorption data for alcohols in CS400, CS1000, and CS1000a in the literature, we can compare with other existing similar ACs. This strategy is not new. As mentioned above, Falk *et al.*<sup>66</sup> used the same CS1000 and CS1000a models to simulate the adsorption of alkanes in kerogens. They argue that this approach is consistent because of the similar features of kerogens and CS1000/CS1000a ACs, such as pore size distribution and morphological and topological disorders. They selected CS1000 and CS1000a models because of the realistic representation of the carbon matrices. Moreover, Zeng *et*

*al.*<sup>73</sup> used the same models for the AC and methanol than in this work, to investigate the methanol adsorption in two activated carbons, namely A5 and Carbopack F. They used a simple model for the adsorbent consisting in finite graphene surfaces containing functional groups. They used the Henry constants for methanol in the AC to estimate the concentration of functional groups in each AC. Moreover, Myronyuk *et al.*<sup>74</sup> demonstrated that ACs with analogous structural properties also show similar adsorption properties. They studied the structural features of ACs produced using glucose, lactose, and saccharose precursors at different temperatures. They found that a few of the resulting carbons, activated at high temperatures, have analogous textural properties, such as surface area, pore volume, or pore size distribution. These similarities give rise to similar nitrogen adsorption isotherms, independently of the used precursor. In the same way, we can compare the CS1000a AC, obtained from the pyrolysis saccharose coke with other commercial AC (WS-480) based on the carbonization of coconut shell at high temperature. WS-480 and CS1000a exhibit an analogous pore size distribution where the main peak is around 10 Å.<sup>67,75</sup> Both adsorbents also have comparable pore volume, 0.77 cm<sup>3</sup>/g and 0.66 cm<sup>3</sup>/g and porosity 0.65 and 0.62 for CS1000a<sup>52</sup> and WS-480,<sup>67</sup> respectively. This makes this AC a suitable reference sample to validate the GCMC simulations for alcohols

in CS1000a. In this regard, Figure A3.3 shows the adsorption isotherm and the loading dependence of the enthalpy of adsorption for methanol in CS1000a at room temperature. We found good agreement compared to the experimental data for WS-480 sample reported by Wu *et al.*<sup>67</sup> Due to the similarities of the two ACs, both isotherms have a similar shape and a comparable saturation capacity. Furthermore, the nucleation of methanol within the pores takes place in the same pressure range. Despite the values in the low coverage regime, the enthalpy of adsorption as a function of the loading shows the same trend as the reported experimental curve. The experimental values were evaluated by the Clausius-Clapeyron equation, using the adsorption isotherms at three values of temperature.<sup>67</sup> Disagreements at very low loading in the experimental data can be due to uncertainties in the experimental measures, which are very difficult to equilibrate at very low pressures. However, at finite loading, experiments and simulation predict very similar behavior where the absolute values are consistently close to the enthalpy of vaporization of the fluid at room temperature.<sup>76,77</sup> We use two approaches to calculate the dependence with loading of the adsorption enthalpy, 1) from the GCMC simulations using the fluctuation method<sup>78</sup> and 2) from the characteristic curve, using the mathematical model described below (see Figure A3.3b). The good agreement between the two approaches reinforces the consistency

of the force fields used in this work and the mathematical description to obtain the heat storage properties. As detailed below, the adsorption enthalpy is used to obtain storage densities by integrating the area under the curve. In this case, a continuous or discrete function with a small step size is desirable for proper numerical integration. In this regard, the discretization of the curve and the error bars associated with the fluctuation method make more convenient the use of the mathematical model to obtain the adsorption enthalpy as a function of the alcohol loading.

In addition to the GCMC simulations, we used the mathematical model based on the Dubinin-Polanyi theory<sup>6,79</sup> to calculate the heat storage properties of the studied ACs. Using this theory, we first convert the adsorption isotherms from the GCMC simulations into their corresponding characteristic curves,<sup>6</sup> which only depend on the adsorbate-adsorbent pair. Another advantage of the characteristic curve is that it can be reverted to obtain the adsorption isotherms at other conditions, as well as the adsorption isobars. The characteristic curve relates the volumetric uptake  $W$  (volume of fluid in the adsorbed phase in ml/g) with the adsorption potential  $A$  (in  $kJ/mol$ ).

$$A = RT \log \left( \frac{p_{sat}}{p} \right) \quad (5.1)$$

$$W = q(p, T) / \rho(T) \quad (5.2)$$

where  $q(p, T)$ ,  $\rho(T)$ , and  $p_{sat}$  the loading (mass adsorbed of fluid per mass of ad-

sorbent, g/g), density within the micropores (density of the fluids in the adsorbed phase, g/ml), and saturation pressure of the working fluid, respectively. We have calculated the saturation pressure of each alcohol using the Peng-Robinson equation of state.<sup>80</sup> Lehmann *et al.*<sup>6</sup> studied the influence of the density model for numerical simulations for heat storage applications. Among others, they tested the model of Hauer<sup>81,82</sup> and recommended its use for simplicity and good performance. According to the model of Hauer, the adsorbate density of a confined fluid in the micropores of an adsorbent decreases linearly with temperature:

$$\rho(T) = \rho_0(T_0) \cdot [1 - \alpha_T(T - T_0)] \quad (5.3)$$

where  $\rho_0$  and  $T_0$  are the reference temperature and the free liquid density at the same temperature. In this work we used 298 K as reference temperature for all alcohols.  $\alpha_T$  is the thermal expansion coefficient of each working fluid at ambient temperature and high pressure. Table A3.3 collects the thermal expansion coefficient of each alcohol used in the density model of Hauer. The values were computed using the experimental liquid density of the light alcohols at high pressure.<sup>83–88</sup>

The Dubinin-Polanyi theory<sup>3</sup> also allows determining the adsorption enthalpy, which is defined as:

$$\Delta H = \Delta H_{vap} + A - T\Delta S \quad (5.4)$$

where  $\Delta H_{vap}$ ,  $A$ , and  $\Delta S$  are the enthalpy of vaporization, the adsorption po-

tential (Gibbs free energy), and the entropy changes, respectively. The enthalpy of vaporization has been taken from literature,<sup>89</sup> while the entropy term is<sup>90</sup>

$$\Delta S = \alpha_{Ads} W \left. \frac{\partial A}{\partial W} \right|_T \quad (5.5)$$

where  $\alpha_{Ads}$  is the thermal expansion coefficient of the adsorbate obtained from the density model.<sup>90</sup> Finally, we followed the methodology reported by Lehmann *et al.*<sup>3</sup> to calculate the thermochemical storage density of each working pair by integrating the enthalpy curves:

$$SD = \int_{q(T_{ads})}^{q(T_{des})} \Delta H(q) dq \quad (5.6)$$

In summary, the mathematical model based on the Dubinin-Polanyi theory allows obtaining the storages densities of a given adsorbent-fluid working pairs, just having an adsorption isotherm or isobar and some physicochemical properties of the fluids. Those properties are the enthalpy of vaporization, the bulk liquid density, the thermal expansion coefficient, and the saturation pressure. To check the validity of this model in computing the storage densities, we compared to the data reported by Kohler *et al.*<sup>23</sup> (see Figure A3.4). They computed the storages densities of light alcohols in commercial BPL AC and water in 13X zeolite using a dynamic simulation process. We found a reasonable agreement between the curves predicted with the mathematical model used in this work and those reported by them. We used the method described above and the experimental adsorption isotherms reported by

Taqvi *et al.*<sup>68</sup> to calculate the storage densities presented in Figure A3.4. For water in 13X, we used the adsorption isotherms reported in previous work.<sup>91</sup>

### 5.3 RESULTS AND DISCUSSION

To analyze the energy transfer produced by the adsorption of alcohols in activated carbons is convenient to understand the adsorption mechanisms. Figure 1 shows the adsorption isotherms of methanol, ethanol, 1-propanol, and 1-butanol in the three porous carbons at 298 K. Figures 1 and A3.5 also show the atomistic representation of the three AC models. CS400 and CS1000 adsorb a significantly lower amount of alcohol than CS1000a. The adsorbed amount in saturation conditions is related to the surface area and porosity of the adsorbent. The computed surface area is 485.95, 306.94, and 3022.76 m<sup>2</sup>/g for CS400, CS1000, and CS1000a, respectively, and their helium void fractions<sup>92</sup> are 0.153, 0.145, and 0.603. The activation process to create CS1000a is crucial to obtain an adsorbent with a large surface area and porosity. In addition to the adsorption capacity, we found an abrupt increase in the adsorption loading for all molecules in CS1000a after a certain value of pressure. This is desirable for energy storage applications since tiny modifications of the working conditions could maximize the energy release. On the other hand, CS400 and CS1000 show a linear isotherm for all the molecules in a wide range of pressure values. This type of

isotherms is not appropriate for energy transfer applications since the mass transfer during adsorption/desorption cycles is

minimal. For this reason, we focus our attention on the performance of CS1000a.

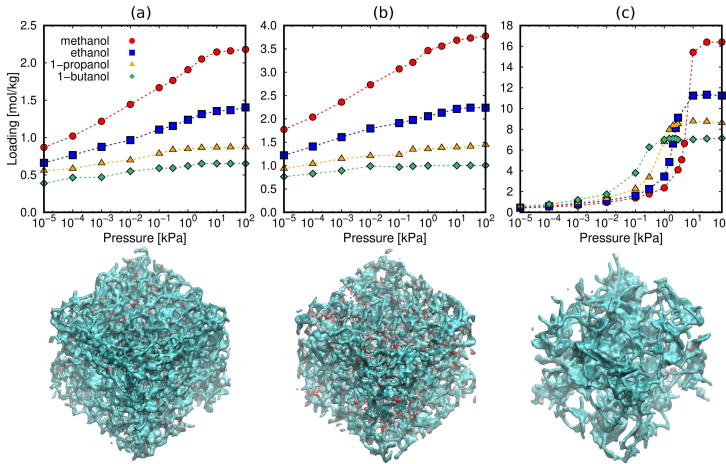


**Figure 1.** Computed adsorption isotherms of light alcohols in (a) CS1000, (b) CS400 and (c) CS1000a at 298 K with the corresponding visualization of each structure. The visualization represents the isosurface taking into account a volumetric density map of a Gaussian density computed from each atom. The full atomistic representation of the ACs is depicted in Figure A3.5.

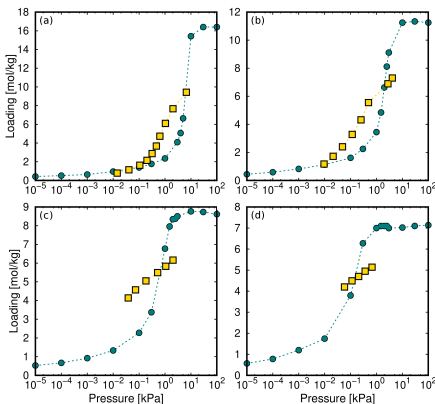


**Figure 2.** Adsorption isotherms of (a) methanol, (b) ethanol, (c) 1-propanol, and (d) 1-butanol in BPL activated carbon (experimental) and CS1000a (computed). Vertical lines indicate the saturation pressure of each adsorbate at 298K. The error bars are in the order of the size of the symbols.

We compare the adsorption, energetic, and heat transfer properties of CS1000a with the values obtained for other commercial activated carbon, namely BPL. The porosity of BPL is  $\phi_{BPL} = 0.45$ ,<sup>93</sup> which is slightly lower than the porosity of CS1000a ( $\phi_{CS1000a} = 0.659$ ). This is reflected in the saturation capacity of each alcohol in the two adsorbents (Figure 2). Experimental data for BPL have been taken from Taqvi *et al.*<sup>68</sup> The porosity of CS1000a is 1.45 times higher than the porosity of BPL. On average, the ratio between the adsorbed amount of each alcohol in the two adsorbents at saturation conditions

( $\theta(P_{sat}) = q_{CS1000a}/q_{BPL}$ ) is in the range of 1.4-1.6, which is in concordance with the mentioned differences in the porosity. Even taking these differences into account, we can see that the adsorption of these polar molecules follows a similar trend in CS1000a and BPL. It is worth mentioning that the adsorption of these light alcohols in CS1000a reaches saturation conditions at their corresponding vapor pressure.

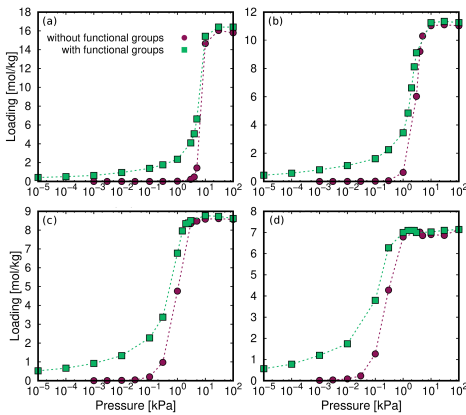


**Figure 3.** Computed adsorption isotherms of (a) methanol, (b) ethanol, (c) 1-propanol, and (d) 1-butanol in CS1000a without and with functional groups. The error bars are in the order of the size of the symbols.

To describe the most realistic conditions, the models that we use for the adsorbents contain functional groups on the internal surface. To analyze the role exerted by the functional groups on the adsorption of the alcohols, we also calculated the adsorption isotherms in the same structure, but without functional groups. Figure 3 shows the adsorption isotherms of the four aliphatic alcohols in CS1000a with

and without functional groups at room temperature. The loading at saturation conditions is essentially the same for the two samples. This is because removing the functional groups does not alter the porosity or the internal surface area of the structure, so the adsorption capacity does not change. The differences are noticeable for the onset pressure of adsorption and at low coverage regime. Differences become larger as the alkyl chain of the light alcohols increases. At low pressure values, the molecules are mainly adsorbed on the exposed functional groups. The absence of these active adsorption sites in the bare model causes a lack of adsorption in the low-pressure range and a more pronounced increase in loading. This is the typical behavior of highly hydrophobic materials.

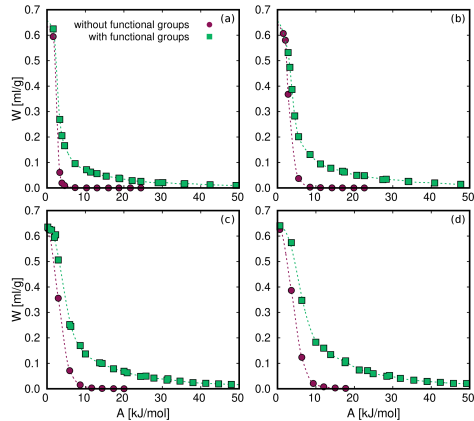


**Figure 4.** Comparison of adsorption characteristic curves in CS1000a without and with functional groups of (a) methanol, (b) ethanol, (c) 1-propanol, and (d) 1-butanol obtained using the Dubinin-Polanyi theory. Dotted lines correspond to an interpolation curve using splines.

The stored energy in an adsorption-based heat transfer process is related to the loading (mass) and enthalpy of adsorption (energy). After studying the adsorption isotherms described before, it is interesting to investigate the energetic properties related to the adsorption trend. We calculated the enthalpy of adsorption through the characteristic curve using the Dubinin-Polanyi theory. The characteristic curve of adsorption is related to the volume of the adsorbed fluid and its adsorption potential. Figure A3.6 confirms the invariance of the characteristic curve with temperature and pressure where two adsorption isotherms and one isobar of methanol in CS1000a converge to the same low coverage regime of the characteristic curve. Since these simulations are computationally expensive, we are interested in the low coverage region of the characteristic curve, i.e. where adsorbent-fluid interactions are dominant. Figure 4 compares the characteristic curves of the two CS1000a activated carbon models. We combined the values of the adsorption isotherms (Figures 1-3) and the values of the low coverage regime from additional adsorption isobars (see Figure A3.6) to construct the characteristic curves. Interestingly, we observe that contrary to the molar adsorption shown in Figure 3, the volumetric adsorption of all alcohols converges to approximately the same value, around 0.63 ml of alcohol per gram of adsorbent. The saturation loading in the representation of the characteristic curve takes

place when the adsorption potential  $A$  approaches to zero, that is, at the saturation pressure of each working fluid.

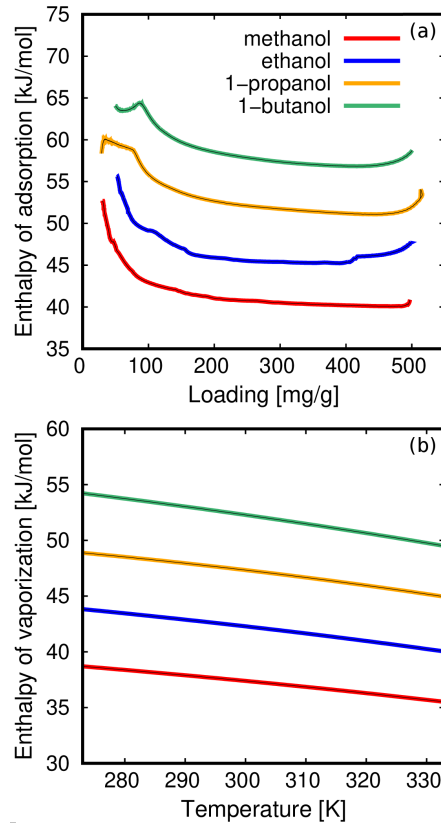


**Figure 5.** Enthalpy of adsorption in CS1000a with functional groups obtained from the characteristic curve using the Dubinin-Polanyi theory (a) and experimental enthalpy of vaporization as a function of temperature (b) of  $n$ -alcohols.

We compared the loading dependence on the adsorption enthalpy for increasing the chain length of the alcohol molecules (Figure 5a). We found similar behavior for the four adsorbates but shifted to higher energies as the alcohol length increases.

At intermediate and high loadings, the values of the enthalpy of adsorption range from 40 to 55  $\text{kJ/mol}$  and equally spaced. Increasing the alkyl chain by one  $\text{CH}_2$  increases its enthalpy of adsorption by approximately 5  $\text{kJ/mol}$ . These values are close to the enthalpy of vaporization of each molecule, which also changes by about 5  $\text{kJ/mol}$  per  $\text{CH}_2$  group (Figure 5b). This indicates that the fluid properties of the alcohols influence their interaction with the carbon adsorbent, but also determine the behavior of the loading depending on the enthalpy of adsorption.

Figure 6 depicts the calculated enthalpy of adsorption for the activated carbons without functional groups and the experimental results for BPL carbon.<sup>68</sup> At high loading, the enthalpy of adsorption in CS1000a, without and with functional groups, converges to a similar value. It is in the low coverage regime where we see the greatest differences. The most hydrophilic structure, i.e., CS1000a with functional groups, shows a rise in the enthalpy of adsorption when decreasing the loading. This shape is similar to that found for BPL carbon in the low coverage regime. This evidences the need to use realistic models to describe the adsorption mechanism adequately. As the loading increases, the enthalpy of adsorption in BPL carbon shows a small plateau before decreasing again. It is necessary to reach the highest loading to get close to the enthalpy of vaporization of each fluid. This is because the pores of BPL are too narrow compared

to the pores of CS1000a, and therefore the interactions with the internal surface of BPL are larger than those of CS1000a.

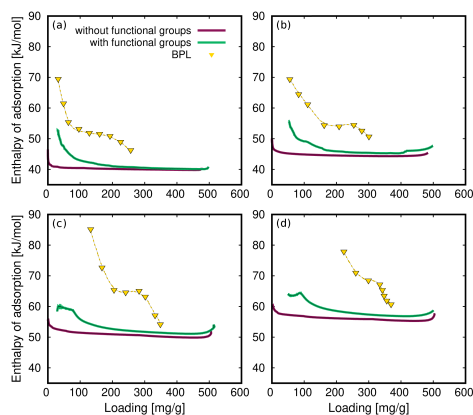


**Figure 6.** Enthalpy of adsorption of (a) methanol, (b) ethanol, (c) 1-propanol, and (d) 1-butanol in CS1000a with and without functional groups (obtained using the Dubinin-Polanyi theory) and BPL (experimental).

The enthalpy of adsorption is a combination of the energy exchanged between the adsorbent and the fluid and the mutual interactions of the fluid molecules. Figure 7 shows the separate contributions of host-guest and guest-guest internal energy per molecule. As expected from previous results, at low loading the host-guest energy in the structure with functional groups is much higher, due to its hydrophilic nature. As the adsorption loading increases and the active adsorption sites are filled, the host-guest interactions decrease rapidly. Consequently, guest-guest energies follow the reverse trend; increasing the number of adsorbed molecules increases the energy

per molecule. We found that the guest-guest energies are almost independent of the alkyl chain of the alcohol, showing small differences between methanol and 1-butanol. However, the host-guest energies increase as increasing the length of the molecules. At higher loadings, the energy shift per  $CH_2$  group is about  $5\text{kJ/mol}$ . This suggests that the behavior of the enthalpy of adsorption shown in Figure 5 is a direct consequence of host-guest interactions. As these differences seem to be correlated with the length of the alcohol molecules, we calculated the energy of the isolated adsorbates. Hence, the internal energy of a single molecule is 1.2, 4.5, 8.0, and  $11.8\text{kJ/mol}$  for methanol, ethanol, 1-propanol, and 1-butanol, respectively. On average, these are about  $3.5\text{kJ/mol}$  of difference per  $-CH_2$  added. This value is slightly lower but of the same order that the shift in energies found for the enthalpy of adsorption, enthalpy of vaporization, and host-guest internal energies. The addition of each  $-CH_2$  increases the internal energy of the isolated molecule. This clearly entails an increase in the size of the molecules, which have a larger surface to interact with the walls of the adsorbent.

Mutual interactions between molecules are a key aspect in the nucleation of alcohol molecules within the large pores of CS1000a. These polar molecules are known to interact strongly with each other through hydrogen bonds. Figure 8 shows the loading and pressure dependence on the nHB of the four fluids in

CS1000a. We can see how molecules nucleate faster at low loading through hydrogen bonds, and then, the aggregates grow slowly from intermediate to saturation conditions. Figure 8a exhibits the same behavior that the guest-guest energies represented in Figure 7d. On the other hand, the similarity between the evolution of the nHB with the pressure (Figure 8b) is perfectly correlated with the adsorption isotherms of Figure 1c. This relationship between adsorption isotherms, interaction energies, and adsorbates aggregation indicates that the nucleation of the molecules via hydrogen bonds primarily drives the adsorption of alcohols in this activated carbon.

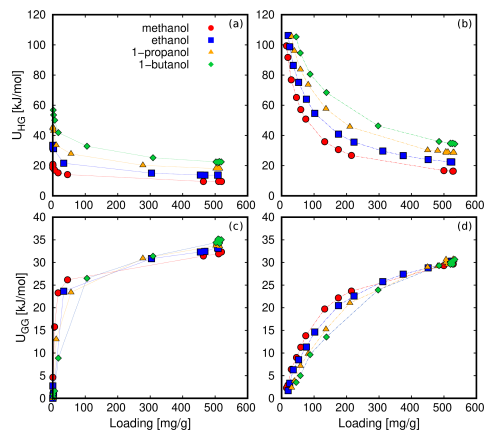


**Figure 7.** Host-guest (Top; a,b) and guest-guest (Bottom; c,d) internal energy of n-alcohols in CS1000a without (Left; a,c) and with functional (Right; b,d). The error bars are in the order of the size of the symbols.

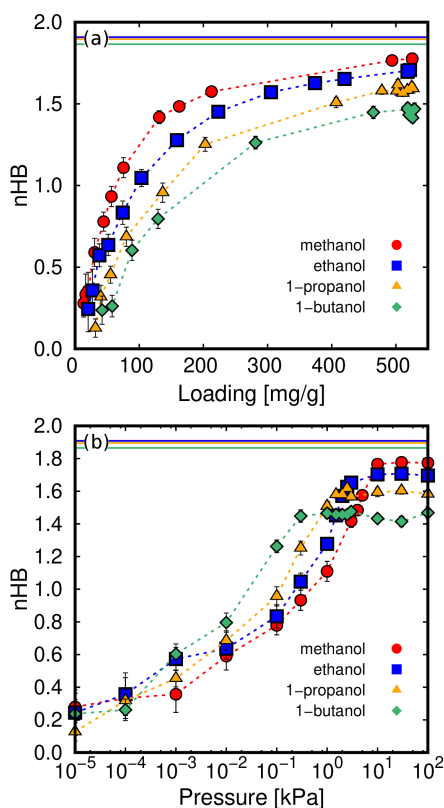


**Figure 8.** Average number of hydrogen bonds per molecule (nHB) of light alcohols as a function of loading (a) and pressure (b) in CS1000a with functional groups. Solid lines represent the nHB value in the bulk.

To illustrate and summarize these findings, Figure 9 shows a representative snapshot of high and low coverage adsorption of methanol on CS1000a. We can see how the molecules of methanol are initially adsorbed on the active adsorption sites of the activated carbon, giving rise to the high host-guest energies depicted in Figure 7b. This initial adsorption is the starting point of the nucleation

of molecules forming a uniform hydrogen bond network similar to that found in the bulk, as indicated in Figure 8. On average, we found that less than 5% of the molecules are not connected through hydrogen bonds, while more than 70% of them are bonded to other two molecules.

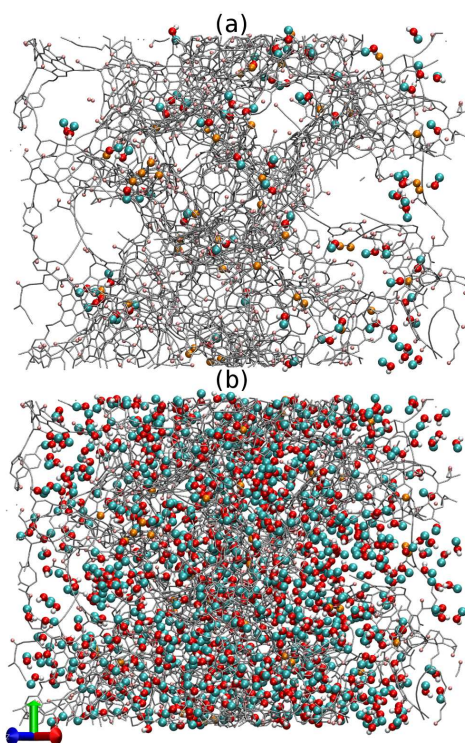


**Figure 9.** Representative snapshots of (a) low coverage adsorption and (b) high concentration of methanol in CS1000a with functional groups. Orange spheres represent the oxygen atoms of the functional groups of the adsorbent.

We calculated the energy exchange upon the adsorption of these fluids, that is, the storage density, integrating the enthalpy of adsorption over the loading at

the adsorption and desorption temperatures. To do this, we need to relate the amount adsorbed and the temperature of the process. In other words, we need to calculate the adsorption isobars of the working fluids. We selected the external pressure values for each molecule based on the behavior of the adsorption isotherm at room temperature. These values should be lower than the saturation pressure of the fluid, but large enough to ensure that the pores are nearly full. This will provide the maximum performance of the process.

We used the characteristic curves in Figure 4 to obtain the adsorption isobars. This provides the relation between loading and temperature needed for the numerical integration of the storage densities (see Simulation Details section). Figure 10 shows the results for methanol at  $10\text{kPa}$ , ethanol at  $5\text{kPa}$ , 1-propanol at  $1.5\text{kPa}$ , and 1-butanol at  $0.7\text{kPa}$ , obtained from the characteristic curve and compared to the simulated adsorption isobars. These results confirm the potential of the characteristic curve to predict the adsorption properties of these alcohols in CS1000a with and without functional groups under different conditions. According to these adsorption isobars, CS1000a desorbs most molecules in the 300-400 K range of temperatures. These desorption temperatures are much lower than those typically found in more hydrophilic materials such as aluminosilicates. An example of this is the adsorption of water in 13X zeolite, commonly used in industrial processes.<sup>23</sup> Re-

ducing the desorption temperatures while maintaining high storage densities is one of the challenges for industrial applications. With this in mind, we calculated the storage densities for the targeted working pairs.

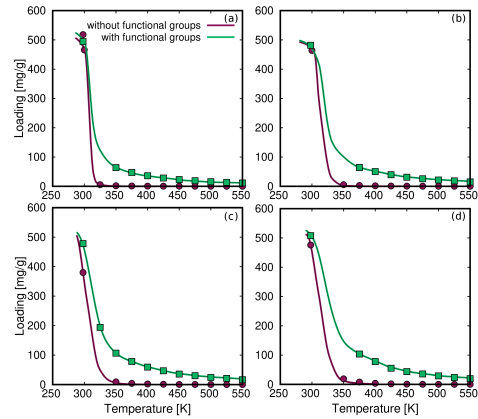


**Figure 10.** Adsorption isobars of (a) methanol, (b) ethanol, (c) 1-propanol, and (d) 1-butanol in CS1000a without and with functional groups. Lines represent the data obtained from the characteristic curves while dots are the values obtained from the GCMC simulations. The error bars are in the order of the size of the symbols.

Figure 11 shows the storage densities of the CS1000a-alcohols working pairs and compared to the experimental data taken from the work of Kohler *et al.*<sup>23</sup> for BPL activated carbon. CS1000a and BPL show very similar behavior for the storage densities when changing the alcohol molecules. The ordered trend from high to low values is for methanol > ethanol > 1-propanol > 1-butanol, in both adsorbents. However, CS1000a exhibits considerably higher storage densities than BPL and they shift at

lower desorption temperatures. Similar to the difference between the alcohols saturation capacity described above, (see Figure 2), we can relate the difference between the storage densities in the two ACs with their porosity. The maximum storage densities of methanol and ethanol are approximately 1.5-1.6 times higher for CS1000a than for BPL, while the same values reach 1.3 for 1-propanol and 1-butanol. In all cases, these factors are close to 1.45, which is the ratio between the porosity of the

two adsorbents. Regarding the influence of CS1000a functional groups on the predicted storage densities, we can deduce that there are no significant differences in overall performance. The structure with functional groups shows a slight increase in the storage densities than the structure without functional groups, reaching maximum efficiencies below 350 K in both cases. Above this temperature, the storage density shows an almost constant value.

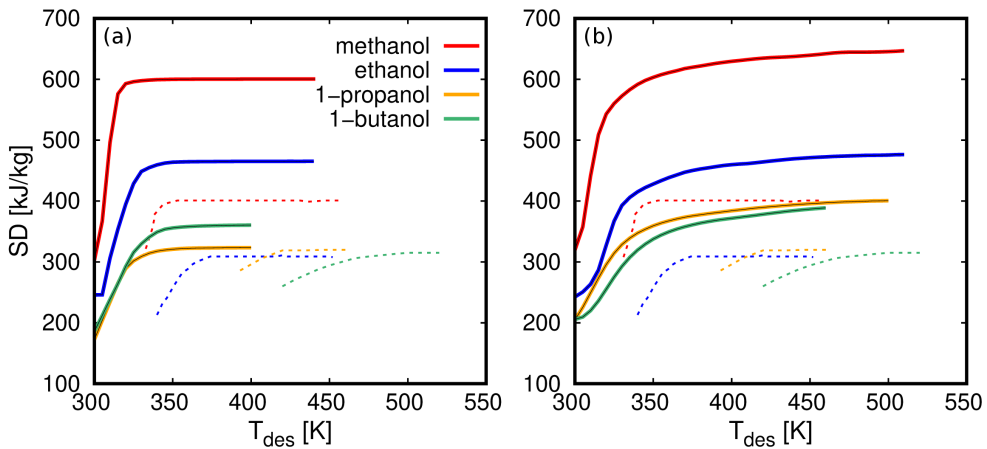


**Figure 11.** Storage densities (SD) of n-alcohols in CS1000a (a) without and (b) with functional groups. Dashed lines correspond to experimental data of BPL activated carbon reported by Kohler *et al.*

Although the incorporation of functional groups in the activated carbon model plays an essential role in accurately describing the adsorption behavior, it is possible to predict reliable storage densities with the simplified models. Our results show that CS1000a with methanol as working fluid reach maximum efficiency

in the range of 600 – 650 kJ/kg, slightly lower than the 850 kJ/kg demonstrated by the working pair water-13X.<sup>23</sup> However, this loss of efficiency is compensated for by reducing the desorption temperature from 500 K to less 350 K. Molecular simulations performed in this work predict that CS1000a outperforms commercial ac-

tivated carbon BPL for energy transfer using alcohols.

Through this study we have shown that there are a few factors that influence the performance of an adsorption heat storage process. These factors include the physicochemical properties of the working fluids, such as density in the adsorbed phase, thermal expansion, saturation pressures, and enthalpy of vaporization and the interaction properties between the adsorbent and the fluid, such as the adsorption isotherms or isobars and the adsorption enthalpy and entropy. It is known that the adsorption enthalpy is one of the important factors for the application, but it is a combination of factors that drives the adsorption heat storage processes. The storage density can be obtained by integrating the enthalpy of adsorption over a range of temperatures (varying the loading). Then, the variation of the loading over the temperature range is crucial for the outcome of the process. At the same time, each adsorbent-fluid working pair maximizes their performance in a different range of working conditions, such as different adsorption/desorption temperatures. Thus, the adsorbent-fluid working pair must have a balance between adsorption/desorption amount and adsorption enthalpy to maximize the operation of an adsorption heat storage process in a given range of working conditions.

#### 5.4 CONCLUSIONS

We have investigated the performance of porous carbons obtained from organic

waste to capture light alcohols for thermochemical energy storage applications. We used molecular simulation to calculate the adsorption, energetic and structural properties of methanol, ethanol, 1-propanol, and 1-butanol on the CS1000a activated carbon. Aided by a thermodynamical model, we obtained the heat transfer properties of these working pairs. Activation of the adsorbent at high temperatures is a vital step to ensure adequate porosity. Therefore, we used a realistic model of the CS1000a activated carbon, including functional groups on the inner surface, and it was compared to the pristine model. These groups regulate the degree of hydrophobicity/hydrophilicity of CS1000a. We found that the results obtained using the model with functional groups are in line with the experimental results of the commercial BPL activated carbon. This highlights the importance of using realistic models to describe the adsorption properties of these polar adsorbates appropriately. Computational modeling of amorphous materials is challenging due to the lack of a well-defined crystallographic structure. In this regard, the insights presented in this work can help in further developments of materials modeling. We also found that the simplified model can correctly predict the energy storage densities obtained from the adsorption of these fluids. However, the simplified model fails to accurately describe the adsorption mechanisms due to its high hydrophobicity compared to real adsorbents. The combination

of atomistic simulations with a mathematical analysis based on the thermodynamical model of adsorption is a promising method to connect the performance of an energy storage process with the physico-chemical properties at the molecular level.

The interactions of light alcohols with the structure dominate the low coverage adsorption, while the mutual interactions are essential for the nucleation that fills the pore until saturation. This results in a steeped isotherm that, together with a large amount of adsorbed mass, causes CS1000a to outperform BPL activated carbon. This is confirmed by the enhancement of the energy released upon adsorption shown by CS1000a for calculated storage densities compared to BPL. Based on these results, we can conclude that CS1000a carbon is an excellent candidate for the storage of light alcohols and for use in thermal energy applications. The results derived from this work could serve as a guide for a future design of new and efficient adsorbents for low-cost energy storage applications.

## 5.5 BIBLIOGRAPHY

- [1] Ibrahim, H.; Ilinca, A.; Perron, J. *Energy Storage Systems-Characteristics and Comparisons*. 2008.
- [2] Ristić, A.; Fischer, F.; Hauer, A.; Zabukovec Logar, N. *Journal of Materials Chemistry A* **2018**, *6*, 11521–11530.
- [3] Lehmann, C.; Beckert, S.; Nonnen, T.; Möllmer, J.; Gläser, R.; Kolditz, O.; Nagel, T. *Energy Procedia* **2017**, *105*, 4334–4339.
- [4] Vasta, S.; Brancato, V.; La Rosa, D.; Palomba, V.; Restuccia, G.; Sapienza, A.; Frazzica, A. *Adsorption Heat Storage: State-of-the-Art and Future Perspectives*. 2018.
- [5] Deshmukh, H.; Maiya, M. P.; Srinivasa Murthy, S. *Applied Thermal Engineering* **2017**, *111*, 1640–1646.
- [6] Lehmann, C.; Beckert, S.; Gläser, R.; Kolditz, O.; Nagel, T. *Applied Energy* **2017**, *185*, 1965–1970.
- [7] Teker, M.; Imamoğlu, M.; Saltabaş, Ö. *Turkish Journal of Chemistry* **1999**, *23*, 185–191.
- [8] Semprini, S.; Asenbeck, S.; Kerskes, H.; Drück, H. *Energy Procedia* **2017**, *135*, 513–521.
- [9] Sun, J.; Besant, R. W. *International Journal of Heat and Mass Transfer* **2005**, *48*, 4953–4962.
- [10] Mebarki, B.; Solmus, I.; Gomri, R. *Journal of Thermal Science and Technology* **2016**, *36*, 107–118.
- [11] Alam, K. C. A.; Saha, B. B.; Kang, Y. T.; Akisawa, A.; Kashiwagi, T. *International Journal of Heat and Mass Transfer* **2000**, *43*, 4419–4431.
- [12] Tatsidjoudoug, P.; Le Pierrès, N.; Heintz, J.; Lagre, D.; Luo, L.; Durier, F. *Energy Conversion and Management* **2016**, *108*, 488–500.
- [13] Du, S. W.; Li, X. H.; Yuan, Z. X.; Du, C. X.; Wang, W. C.; Liu, Z. B. *Solar Energy* **2016**, *138*, 98–104.
- [14] Wang, L.; Gandorfer, M.; Selvam, T.; Schwieger, W. *Materials Letters* **2018**, *221*, 322–325.
- [15] Babaei, H.; Wilmer, C. E. *Physical Review Letters* **2016**, *116*, 1–6.
- [16] Solovyeva, M. V.; Gordeeva, L. G.; Krieger, T. A.; Aris-tov, Y. I. *Energy Conversion and Management* **2018**, *174*, 356–363.
- [17] Jenks, J. J.; Motkuri, R. K.; Tegrotenhuis, W.; Paul, B. K.; McGrail, B. P. *Heat Transfer Engineering* **2017**, *38*, 1305–1315.
- [18] Critoph, R. E.; Turner, L. *Int. J. Heat Mass Transfer* **1995**, *38*, 1577–1585.
- [19] Critoph, R. E. *Carbon* **1989**, *27*, 63–70.
- [20] Xiao, J.; Tong, L.; Deng, C.; Bénard, P.; Chahine, R. *International Journal of Hydrogen Energy* **2010**, *35*, 8106–8116.
- [21] Hauer, A. *Adsorption* **2007**, *13*, 399–405.
- [22] Jänchen, J.; Stach, H. *Energy Procedia* **2012**, *30*, 289–293.
- [23] Kohler, T.; Müller, K. *Energy Science and Engineering* **2017**, *5*, 21–29.
- [24] De Lange, M. F.; Verouden, K. J.; Vlugt, T. J.; Gascon, J.; Kapteijn, F. *Chemical Reviews* **2015**, *115*, 12205–12250.
- [25] Wang, L. W.; Wu, J. Y.; Wang, R. Z.; Xu, Y. X.; Wang, S. G.; Li, X. R. *Applied Thermal Engineering* **2003**, *23*, 1605–1617.
- [26] Kanamori, M.; Hiramatsu, M.; Katsurayama, K.; Watanabe, F.; Matsuda, H.; Hasatani, M. *Journal of Chemical Engineering of Japan* **1997**, *30*, 434–439.
- [27] Cacciola, G.; Restuccia, G.; Mercadante, L. *Carbon* **1995**, *33*, 1205–1210.
- [28] Pollard, S. J. T.; Fowler, G. D.; Sollars, C. J.; Perry, R. *The Science of the Total Environment* **1992**, *116*, 31–52.
- [29] Mohan, D.; Pittman, C. U. *Journal of Hazardous Materials* **2006**, *137*, 762–811.
- [30] Adentorun Shalaby, Ç.; Uçak-Astarlioglu, M. G.; Ar-tok, L.; Sarici, Ç. *Microporous and Mesoporous Materials* **2006**, *88*, 126–134.

- [31] Ioannidou, O.; Zabanitout, A. *Renewable and Sustainable Energy Reviews* **2007**, *11*, 1966–2005.
- [32] Moral-Rodríguez, A. I.; Leyva-Ramos, R.; Ania, C. O.; Ocampo-Pérez, R.; Isaacs-Pérez, E. D.; Carrales-Alvarado, D. H.; Parra, J. B. *Environmental Science and Pollution Research* **2019**, *26*, 6141–6152.
- [33] Chen, X.-w.; Timpe, O.; Hamid, S. B. A.; Schlögl, R.; Sheng, D. *Carbon* **2009**, *47*, 340–343.
- [34] Pevida, C.; Plaza, M. G.; Arias, B.; Feroso, J.; Rubiera, F.; Pis, J. J. *Applied Surface Science* **2008**, *254*, 7165–7172.
- [35] Plaza, M. G.; García, S.; Rubiera, F.; Pis, J. J.; Pevida, C. *Chemical Engineering Journal* **2010**, *163*, 41–47.
- [36] García, S.; Pis, J. J.; Rubiera, F.; Pevida, C. *Langmuir* **2013**, *29*, 6042–652.
- [37] Plaza, M. G.; Pevida, C.; Arenillas, A.; Rubiera, F.; Pis, J. J. *Fuel* **2007**, *86*, 2204–2212.
- [38] Peng, X.; Wang, W.; Xue, R.; Shen, Z. *AIChE Journal* **2006**, *52*, 994–1003.
- [39] Lopes, F. V. S.; Grande, C. A. *Chemical Engineering Science* **2011**, *66*, 303–317.
- [40] Sarkisov, L.; Centineo, A.; Brandani, S. *Carbon* **2017**, *118*, 127–138.
- [41] Adapa, S.; Gaur, V.; Verma, N. *Chemical Engineering Journal* **2006**, *116*, 25–37.
- [42] Li, H.; Yu, D.; Hu, Y.; Sun, P.; Xia, J.; Huang, H. *Carbon* **2010**, *48*, 4547–4555.
- [43] Andersen, A. H. *Acta Pharmacologica et Toxicologica* **1946**, *2*, 69–78.
- [44] Bailey, B. *Clinical Pediatric Emergency Medicine* **2008**, *9*, 17–23.
- [45] Figueiredo, J. L.; Pereira, M. F.; Freitas, M. M.; Ór-fão, J. J. *Carbon* **1999**, *37*, 1379–1389.
- [46] Bouzid, M.; Sellaoui, L.; Khalfaoui, M.; Belmabrouk, H.; Lamine, A. B. *Physica A: Statistical Mechanics and its Applications*; Elsevier B.V., 2016; Vol. 444; pp 853–869.
- [47] Ravi, V. P.; Jasra, R. V.; Bhat, T. S. *Journal of Chemical Technology and Biotechnology* **1998**, *71*, 173–179.
- [48] Saha, B. B.; El-Sharkawy, I. I.; Chakraborty, A.; Koyama, S.; Yoon, S. H.; Ng, K. C. *Journal of Chemical and Engineering Data* **2006**, *51*, 1587–1592.
- [49] Chern, J. M.; Wu, C. Y. *Water Research* **2001**, *35*, 4159–4165.
- [50] Delgado, J. A.; Águeda, V. I.; Uguina, M. A.; Sotelo, J. L.; García-Sanz, A.; García, A. *Separation and Purification Technology* **2015**, *149*, 370–380.
- [51] Jain, S. K.; Pikunic, J. P.; Pellenq, R. J.; Gubbins, K. E. *Adsorption* **2005**, *11*, 355–360.
- [52] Peng, X.; Jain, S. K.; Singh, J. K. *Journal of Physical Chemistry C* **2017**, *121*, 13457–13473.
- [53] Jain, S. K.; Pellenq, R. J.; Pikunic, J. P.; Gubbins, K. E. *Langmuir* **2006**, *22*, 9942–9948.
- [54] Dubbeldam, D.; Calero, S.; Ellis, D. E.; Snurr, R. Q. *Molecular Simulation* **2016**, *42*, 81–101.
- [55] Dubbeldam, D.; Torres-Knoop, A.; Walton, K. S. On the inner workings of monte carlo codes. 2013; <http://dx.doi.org/10.1080/08927022.2013.819102>.
- [56] Madero-Castro, R. M.; Vicent-Luna, J. M.; Calero, S. *The Journal of Physical Chemistry C* **2019**, *123*, 23987–23994.
- [57] Boda, D.; Henderson, D. *Molecular Physics* **2008**, *106*, 2367–2370.
- [58] Darden, T.; York, D.; Pedersen, L. *The Journal of Chemical Physics* **1993**, *98*, 10089–10092.
- [59] Stubbs, J. M.; Potoff, J. J.; Siepmann, J. I. *Journal of Physical Chemistry B* **2004**, *108*, 17596–17605.
- [60] Chen, B.; Potoff, J. J.; Siepmann, J. I. *Journal of Physical Chemistry B* **2001**, *105*, 3093–3104.
- [61] Transferable Potentials for Phase Equilibria. <http://trappe.oit.umn.edu>.
- [62] Slawek, A.; Vicent-Luna, J. M.; Marszalek, B.; Gil, B.; Morris, R. E.; Makowski, W.; Calero, S. *Chemistry of Materials* **2018**, *30*, 5116–5127.
- [63] Zhang, K.; Zhang, L.; Jiang, J. *Journal of Physical Chemistry* **2013**,
- [64] Pikunic, J.; Clinard, C.; Cohaut, N.; Gubbins, K. E.; Guet, J. M.; Pellenq, R. J.; Rannou, I.; Rouzaud, J. N. *Langmuir* **2003**, *19*, 8565–8582.
- [65] Pikunic, J.; Llewellyn, P.; Pellenq, R.; Gubbins, K. E. *Langmuir* **2005**, *21*, 4431–4440.
- [66] Falk, K.; Pellenq, R.; Ulm, F. J.; Coasne, B. *Energy and Fuels* **2015**, *29*, 7889–7896.
- [67] Wu, J. W.; Madani, S. H.; Biggs, M. J.; Phillip, P.; Lei, C.; Hu, E. J. *Journal of Chemical and Engineering Data* **2015**, *60*, 1727–1731.
- [68] Taqvi, S. M.; Appel, W. S.; LeVan, M. D. *Industrial & Engineering Chemistry Research* **1999**, *38*, 240–250.
- [69] Brochard, L.; Vandamme, M.; Pellenq, R. J.; Fen-Chong, T. *Langmuir* **2012**, *28*, 2659–2670.
- [70] Widom, B. *The Journal of Chemical Physics* **1963**, *39*, 2808–2812.
- [71] Luna-Triguero, A.; Vicent-Luna, J. M.; Dubbeldam, D.; Gómez-Álvarez, P.; Calero, S. *Journal of Physical Chemistry C* **2015**, *119*, 19236–19243.
- [72] Carrott, P. Characterization of Porous Solids. In Proceedings of the IUPAC Symposium. 1988; pp 77–87.
- [73] Zeng, Y.; Prasetyo, L.; Nguyen, V.; Horikawa, T.; Do, D.; Ncholson, D. *Carbon* **2015**, *81*, 447–457.
- [74] Myronyuk, I. F.; Mandzyuk, V. I.; Sachko, V. M.; Gun'ko, V. M. *Nanoscale Research Letters* **2016**, *11*, 508.
- [75] Coasne, B.; Jain, S. K.; Naamar, L.; Gubbins, K. E. *Physical Review B* **2007**, *76*, 085416.
- [76] De Lange, M. F.; Van Velzen, B. L.; Ottewanger, C. P.; Verouden, K. J.; Lin, L. C.; Vlugt, T. J.; Gascon, J.; Kapteijn, F. *Langmuir* **2015**, *31*, 12783–12796.
- [77] Thommes, M.; Morell, J.; Cychosz, K. A.; Fröba, M. *Langmuir* **2013**, *29*, 14893–14902.
- [78] Vlugt, T. J.; García-Pérez, E.; Dubbeldam, D.; Ban, S.; Calero, S. *Journal of Chemical Theory and Computation*

- 2008, 4, 1107–1118.
- [79] Dubinin, M. M. *Russian Chemical Bulletin* **1960**, 9, 1072–1078.
- [80] Peng, D.-Y.; Robinson, D. B. *Ind. Eng. Chem., Fundam* **1976**, 15, 59–64.
- [81] Nagel, T.; Beckert, S.; Böttcher, N.; Gläser, R.; Kolditz, O. *Energy Procedia* **2015**, 75, 2106–2112.
- [82] Hauer, A. Classification of solid adsorbents in open sorption systems for energetic applications. Ph.D. thesis, Technische Universität Berlin, Fakultät III - Prozesswissenschaften, 2002.
- [83] K.M. de Reuck, R. C. *International Thermodynamic Tables of the Fluid State*; 1993.
- [84] Takiguchi, Y.; Uematsu, M. *International Journal of Thermophysics* **1995**, 16, 205–214.
- [85] Takiguchi, Y.; Uematsu, M. *Journal of Chemical Thermodynamics* **1996**, 28, 7–16.
- [86] Sun, T. F.; Schouten, J. A.; Biswas, S. N. *International Journal of Thermophysics* **1991**, 12, 381–395.
- [87] Kubota, H.; Tanaka, Y.; Makita, T. *International Journal of Thermophysics* **1987**, 8, 47–70.
- [88] Alaoui, F.; Montero, E.; Bazile, J. P.; Comuñas, M. J.; Galliero, G.; Boned, C. *Fluid Phase Equilibria* **2011**, 301, 131–136.
- [89] V. Majer, V. S. *Enthalpies of vaporization of organic compounds: a critical review and data compilation*; 1986.
- [90] Bering, B. P.; Dubinin, M. M.; Serpinsky, V. V. *Journal of Colloid and Interface Science* **1966**, 21, 378–393.
- [91] Luna-Triguero, A.; Ślawek, A.; Huinink, H. P.; Vlugt, T. J.; Poursaeidesfahani, A.; Vicent-Luna, J. M.; Calero, S. *ACS Applied Nano Materials* **2019**, 2, 3050–3059.
- [92] Ongari, D.; Boyd, P. G.; Barthel, S.; Witman, M.; Haranczyk, M.; Smit, B. *Langmuir* **2017**, 33, 14529–14538.
- [93] Stach, H.; Mugele, J.; Jänchen, J.; Weiler, E. *Adsorption* **2005**, 11, 393–404.

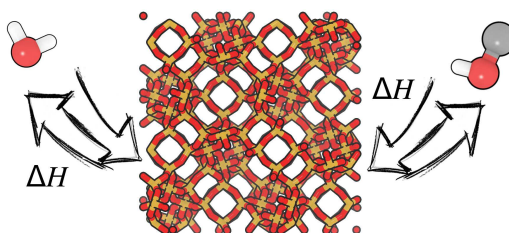


## On the use of Water and Methanol with Zeolites for Heat Transfer

Rafael María Madero-Castro, Azahara Luna-Triguero, Andrzej Sławek, José Manuel Vicent-Luna and Sofía Calero

**R**educing carbon dioxide emissions has become a must in society, being crucial to find alternatives to supply the energy demand. Adsorption-based cooling and heating technologies are receiving attention for thermal energy storage applications.

In this paper, we study the adsorption of polar working fluids in hydrophobic and hydrophilic zeolites by means of experimental quasi-equilibrated temperature-programmed desorption and adsorption combined with Monte Carlo simulations. We measured and computed water and methanol adsorption isobars in high-silica HS-FAU, NaY, and NaX zeolites. We use the experimental adsorption isobars to develop a set of parameters to model the interaction between methanol and the zeolite and cations. Once having the adsorption of these polar molecules, we use a mathematical model based on the adsorption potential theory of Dubinin-Polanyi to assess the performance of the adsorbate-working fluids for heat storage applications. We found that molecular simulations are an excellent tool for investigating energy storage applications since we can reproduce, complement, and extend experimental observations. Our results highlight the importance of controlling the hydrophilic/hydrophobic nature of the zeolites by changing the Al content to maximize the working conditions of the heat storage device.



## 6.1 INTRODUCTION

A considerable decrease in energy consumption is essential for the mitigation of global warming.<sup>1–3</sup> The use of renewable energies along with the reduction of fossil fuels is important here.<sup>4,5</sup> To mitigate this problem, solar, wind energy, or biofuels are promising candidates, but the intermittent nature of renewable energies limits their application for society consumption. This is motivating researchers to work on new approaches for the storage of renewable energy.<sup>6–8</sup>

There are many methods for energy storage at industrial level based on converting renewable energy into potential energy. One of the most used is Pumped-Storage Hydroelectricity (PSH) or Pumped Hydro Energy Storage (PHES). PSH uses the surplus energy obtained in hydroelectric dams in low power demand hours to elevate water from lower to higher levels. That converts the surplus energy into potential energy, which can be used in high power demand periods.<sup>9–15</sup> However, hydroelectric dams have an impact on the environment.<sup>16</sup> Another method is the Compressed Air Energy Storage (CAES).<sup>6,17–20</sup> CAES uses renewable energies, mainly wind, to compress air at high pressure and generate electricity.<sup>21</sup> Based on the same principle of stored mechanical energy, Flywheel Energy Storage (FES) uses inertia for the storage.<sup>22</sup> The operation of the system consists of a rotor that is driven and keeps spinning to store kinetic energy.<sup>19,23–26</sup> The best known storage

method is electrochemical storage, specifically lithium-ion batteries.<sup>27–30</sup> The current expansion of cell phones or hybrid cars<sup>31</sup> has increased the need of developing the technological market in this field.<sup>32</sup> The main limitations of batteries are the loss of capacity<sup>33</sup> and the risk of thermal runaways or explosions.<sup>29</sup>

In the context of finding alternative methods, Thermal Energy Storage (TES) in three variants (using sensible, latent, or thermochemical heat) has been proposed.<sup>8</sup> Adsorption-based energy storage belongs to thermochemical heat storage. This technology is based on the adsorption of (gas-liquid) adsorbates with solid adsorbents, storing energy in the desorption phase (charging) and releasing energy in the adsorption phase (discharging). Thus, the efficiency of the heat storage process strongly depends on the adsorbent-adsorbate interactions. Porous materials such as Metal-Organic Frameworks (MOFs),<sup>34–36</sup> silica gels,<sup>37–39</sup> activated carbons<sup>40–42</sup>, or zeolites<sup>43–46</sup> have proven to be promising candidates for this application. The most common adsorbates are water,<sup>47,48</sup> ammonia<sup>34,49</sup> and light alcohols<sup>50,51</sup> being water the most studied molecule for storing energy in diverse porous materials.<sup>51–53</sup>

Because adsorption-based energy storage is a promising alternative, the number of experimental and simulation studies is rising. In this context, numerical modeling and molecular simulations are excellent tools to complement experiments. Tatsid-

jodoung *et al.*<sup>44</sup> studied the water-NaX zeolite pair to store thermal energy from the sun. This work concluded that, although there are slight discrepancies between experiments and numerical calculations, simulation is an excellent method for making feasible predictions. Semprini *et al.*<sup>52</sup> studied the energy transfer between the 13XBF zeolite and water and its orientation towards the construction of refrigerants, finding a good agreement between simulations and experiments. Lehmann *et al.*<sup>53</sup> studied the influence of the cation (sodium or calcium) in the NaX zeolite and water working pairs for energy storage applications. They revealed the importance of working conditions, such as vapor pressure, in the thermochemical energy properties such as the energy storage density or simply the storage density (SD), which is defined by the quantity of heat which can be stored in a unit mass or volume of adsorbent. Similarly, Kohler *et al.*<sup>51</sup> studied the energy stored in zeolite NaX using water as a working fluid showing the influence of the desorption temperature in the storage density. They compared their values with the energy stored by activated carbons with alcohols as working fluids and noted that the adsorption capacity is as important as the interactions with the adsorbent. Stach *et al.*<sup>54</sup> studied the influence of Na and Mg cations and their ratio in zeolites and silica gels using water. Most studies in the literature involve NaX zeolite (with FAU topology) as it is one of the most popular commercial ze-

olites. It is worth mentioning that NaX usually operates at very high desorption temperatures, typically over 500 K. This is due to the high hydrophilicity of the structure caused by the high content of sodium cations. However, other FAU-type zeolites are proposed as interesting alternatives. Ristic *et al.*<sup>48</sup> highlighted the significance of decreasing the desorption temperature to optimize the low-temperature heat storage density. To this end, they used NaY zeolite, which is equivalent to NaX but with a slightly higher Si/Al ratio, to study the adsorption heat storage with water as working fluid. To reduce the desorption temperature of the water they proposed six post-synthesis modified samples from chemical treatment of NaY. The modified adsorbents reduced the desorption temperature up to 300 K, showing a maximum performance at temperatures circa 400 K. This is an improvement compared to the operating conditions of the NaX zeolite as discussed above. However, for low-temperature applications a working pair that lower the desorption temperature near room conditions is preferred. In this regard, we propose to regulate the hydrophilic degree of the adsorbent by controlling the Si/Al ratio of the zeolite. This way, the performance of a low-temperature process can be maximized while avoiding the post-synthesis treatment step, which may reduce the production costs.

This work combines experimental techniques, molecular simulation, and thermodynamical modeling for the study of wa-

ter and methanol adsorption-based energy storage in FAU-type zeolites (FAU)<sup>55,56</sup> with different Si/Al ratio.<sup>57</sup> We have chosen methanol as an alternative to water as the conventional working fluid. Our previous publication investigated the adsorption-driven heat transfer of the four first aliphatic alcohols for heat storage applications using activated carbons.<sup>58</sup> We concluded that methanol exhibits the best performance among the other alcohols for heat storage applications in large pore nanoporous materials. We analyze the effect of the hydrophobic/hydrophilic nature of the adsorbent in the adsorption behavior, external operating conditions, and energy storage. We used quasi-equilibrated temperature-programmed desorption and adsorption (QE-TPDA) experiments to measure the adsorption isobars of the working pairs. Molecular simulation was used to shed light on the adsorption mechanism from the atomistic level. To this aim, we developed a set of Lennard-Jones parameters that defines the FAU-methanol interactions independently of the ratio of cations in high-silica (HS) FAU, NaY, and NaX structures. Finally, we are using a thermodynamical model to correlate the adsorption properties with the energy storage of each particular working fluid-zeolite pair.

## 6.2 METHODOLOGY

### 6.2.1 Experimental Details

Three samples of FAU were used for the adsorption experiments. HS-FAU is  $Na^+$

exchanged dealuminated high-silica faujasite with  $Si/Al > 100$ , NaY is  $Na^+$  exchanged faujasite with  $Si/Al \approx 2.61$ , while NaX is  $Na^+$  exchanged faujasite with  $Si/Al \approx 1.06$ . The characteristics of these materials, i.e., low-temperature nitrogen adsorption and powder X-ray diffraction, were reported in our previous works.<sup>59,60</sup>

Adsorption measurements were performed using quasi-equilibrated temperature-programmed desorption and adsorption (QE-TPDA) technique. This instrument is a homemade modified setup for temperature-programed desorption (TPD), which was described in detail in previous works.<sup>61,62</sup> The samples of 7–10 mg were placed in a quartz tube and activated by heating in He flow ( $6.75 \text{ cm}^3 \cdot \text{min}^{-1}$ ) up to 400 °C (HS-FAU, NaY) or 500 °C (NaX) with a  $10 \text{ }^\circ\text{Cmin}^{-1}$  ramp and cooling it down to  $RT$ . Adsorption was measured in flow of He containing a water steam (saturated) or methanol vapors ( $\frac{p}{p_0} < 0.05$ ). The samples were heated to induce desorption and cooled to induce adsorption. Each profile was averaged over 3 desorption-adsorption cycles. For methanol we used  $4 \text{ }^\circ\text{Cmin}^{-1}$  ramp for all materials, while for water  $2 \text{ }^\circ\text{Cmin}^{-1}$  for NaY and NaX and  $1 \text{ }^\circ\text{Cmin}^{-1}$  for HS-FAU. Between each cycle, they were kept at  $RT$  for 2 hours. More details on data reduction and methodology are available in the literature.<sup>63</sup>

### 6.2.2 Simulation Details

We carried out Monte Carlo simulation in the Grand Canonical ensemble (GCMC) to

obtain the adsorption properties of water and methanol in the three selected zeolites. We performed a minimum of  $5 \cdot 10^5$  MC cycles to ensure the adsorption data is fluctuating around equilibrium values. After the equilibration procedure, we conducted additional  $2 \cdot 10^5$  cycles for the final production runs. All simulations were performed using the RASPA simulation software.<sup>64</sup> Adsorbent-adsorbate, adsorbate-adsorbate, and adsorbate-cation interactions were defined with van der Waals and electrostatic interactions via the Lennard-Jones and Coulombic potentials, respectively, while we use a Coulombic potential to model the adsorbent-cation interaction. We truncated the potential with an effective cut off of  $12 \text{ \AA}$  and we used the Ewald summation method<sup>65</sup> to compute the long range electrostatic interactions.

The adsorbents are zeolites with FAU topology; NaX, NaY, and HS-FAU with Si/Al ratio of 1.06, 2.61, and 100, respectively. These structures contain 88, 56, and 2 Al in the unit cell, respectively, and the same number of Na cations to compensate the net negative charge of the system. The structural models were reported in previous works,<sup>59,60,66,67</sup> which were created following the methodology developed by Balestra *et al.*<sup>68</sup>; (i) random distribution of Si atoms following Lowenstein's rules (ii) extra framework-cations initially located at their crystallographic positions and (iii) structural minimization using Baker's<sup>69</sup> method with full-flexible core-shell potential.<sup>70,71</sup> More details about the

assembly of the structures can be found in the Appendix 4 (Section A4.1).

To describe the molecules of water we used the flexible SPC/E model<sup>72,73</sup> and for methanol, the TraPPE model.<sup>74</sup> Force fields to model the water and methanol adsorption curves in zeolites can be found in literature.<sup>75–78</sup> Xiong, R.<sup>76</sup> studied the interaction between molecules of water and alcohol with pure silica type MFI-zeolite, but without extra framework cations in the system. Di Lella *et al.*<sup>75</sup> provided a set of parameters to reproduce water adsorption in FAU-topology zeolites. However, the parameters and charges of each zeolite-water pair are dependent of the composition of the adsorbent, making this set highly specific and non-transferable. In this work, we used a transferable set of Lennard-Jones parameters and zeolite and cation point charges<sup>79</sup> that are independent of the Si/Al ratio. Specific Lennard-Jones parameters for the pair interactions for water-zeolite were taken from our previous work,<sup>60</sup> while for methanol-zeolite they were unavailable. To sort this out, we parameterized these host-guest interactions by fitting to the experimental adsorption isobars measured with QE-TPDA experiments. Additional details about the parameterization procedure and final set parameters can be found in the Appendix 4 (Section A4.2 and Tables A4.1 and A4.2). For the crossed interactions, we used Lorentz-Berthelot mixing rules.<sup>80</sup> The sodalites cages in FAU zeolites, accessible to water molecules, were

artificially blocked for the molecules of methanol.

### 6.2.3 Thermodynamical Model

QE-TPDA experiments and GCMC simulation provided the adsorption properties of zeolites-fluids working pairs. Using these results and a mathematical model based on the adsorption theory of Dubinin-Polanyi<sup>81</sup> we predicted the adsorption-based energy storage. The complete description of the thermodynamical model can be found in the Appendix 4 and is also available in the literature.<sup>82</sup> In short, we first used the adsorption isobars and isotherms to calculate the adsorption characteristic curve.<sup>83</sup> This reduces the two-dimensional relation between loading ( $q(p, T)$ ), temperature ( $T$ ), and pressure ( $p$ ), to the temperature-pressure invariant characteristic curve ( $W(A)$ ). This curve describes the relation between the specific volume of the adsorbed fluid ( $W$ ) with the adsorption potential ( $A$ ) or Gibbs free energy. Using the characteristic curve, we can determine the loading dependence of the adsorption enthalpy ( $\Delta H$ ), which depends on the vaporization enthalpy of the fluid ( $\Delta H_{vap}$ ), the slope of the characteristic curve, and the entropy changes ( $\Delta S$ ). Finally, we obtained the thermochemical storage density ( $SD$ ) of each working fluid from the numerical integration of the adsorption enthalpy as a function of the loading within the adsorption and desorption temperature range (see Section A4.3 of the Appendix 4 for specific details).

## 6.3 RESULTS AND DISCUSSION

Figure 1 shows the QE-TPDA profiles in the studied faujasites, where the profile above the baseline ( $ssr = 0$ ) reflects the desorption process and the profile below the baseline reflects the adsorption process. The intensity of the profiles corresponds to the instantaneous concentration of adsorbate desorbed or adsorbed in the material at a given temperature.

The profiles reveal differences in the adsorption of water and methanol. For HS-FAU we found very sharp profiles both for water and methanol. This means that adsorption occurs abruptly in a narrow temperature range. For NaY and NaX, the low-temperature adsorption at 300–350 K corresponds to high density states where the guest-guest interactions are of great importance. Figure 1a shows that most water is adsorbed in NaY and NaX between 375–475 K. A long tail at higher temperatures is most likely due to the interactions of the water molecules with the cations. This effect is more pronounced for NaX, which has more cations than NaY. The profiles for methanol (Figure 1b) are similar than for water. Desorption maxima and adsorption minima for NaY and NaX are shifted towards higher temperatures than for water, up to circa 530 K. Also, the broad high-temperature tail for NaX is extraordinarily intensive. Generally, the QE-TPDA profiles show that adsorption is stronger for methanol than for water in NaY and NaX. The interactions between methanol and NaX cations are particularly strong.

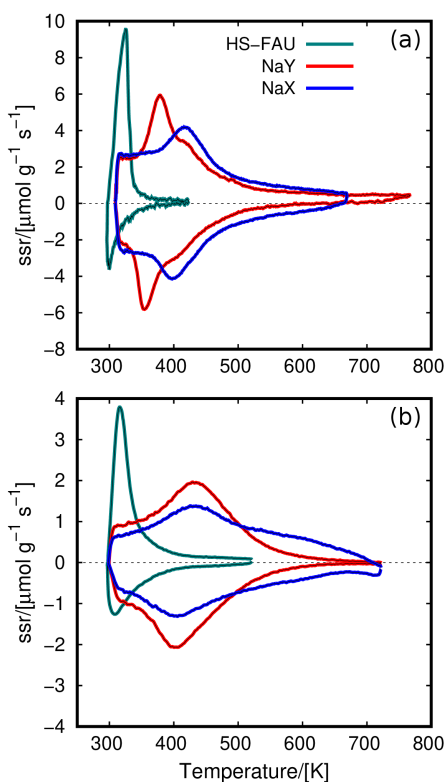


**Figure 1.** QE-TPDA profiles of (a) water and (b) methanol in FAU zeolites. *ssr* stands for specific sorption rate, which is proportional to the change of concentration of the adsorptive in helium stream flowing through the sample. Positive values correspond to desorption branches, while negative values correspond to adsorption cycles. The values of partial pressure for water and methanol in HS-FAU, NaY, and NaX are 1.98, 2.8, and 3.1 kPa, respectively (water) and 0.7 kPa (methanol).

The adsorption isobars can be obtained by integrating the QE-TPDA profiles.<sup>63</sup> We used the adsorption isobars of methanol for the parameterization of the force field required for molecular simulation (Table A4.2). Figure 2 compares the experimental and computed adsorp-

tion isobars under the same working conditions (see Figure 1). Considering that we are using the same set of (transferable) parameters and partial charges for all the systems, we found good agreement with the experimental results.

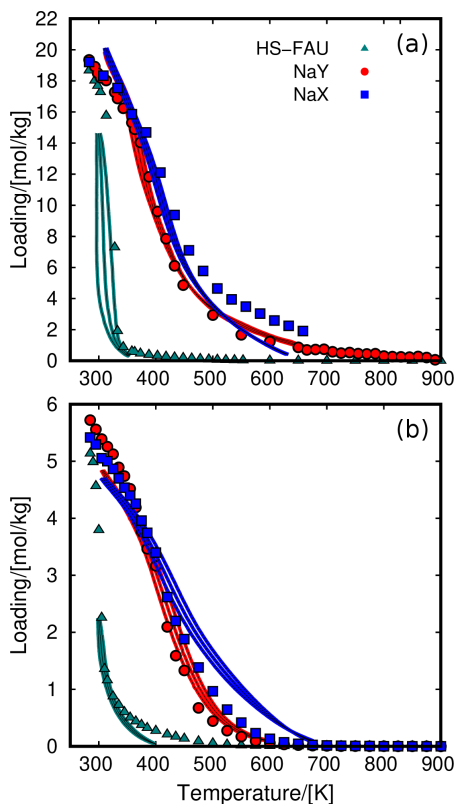


**Figure 2.** Experimental (lines) and calculated (symbols) adsorption isobars for (a) water and (b) methanol in FAU zeolites. Each experimental isobar is divided into three curves corresponding to adsorption and desorption cycles (obtained from the QE-TPDA profiles) and the average of them. The values of partial pressure for water and methanol in HS-FAU, NaY, and NaX are 1.98, 2.8, and 3.1 kPa (water) and 0.7, 0.7, and 0.7 kPa (methanol), respectively.

The behavior of the adsorption isobars is similar for water and methanol, since both fluids are polar. The hydrophobicity of HS-FAU, due to the low content of Na cations, leads to a steeped isobar at low values of temperature. As increasing the cations content in the zeolites, the shape of the isobar shows a smooth loading decrease reaching desorption temperatures at about 600 K. This proves the high affinity of polar fluids for the extra framework cations of the zeolites. The adsorption of methanol in the Na-FAU zeolites shows a minor hysteresis loop, a displacement between adsorption and desorption. Similarly, the adsorption isobar of water in HS-FAU shows a tiny hysteresis loop, which is lower for the zeolites with higher cation content. The set of parameters was then fitted to the intermediate curve, which is the average of adsorption/desorption from experimental measurements (Figure 2).

Since partial pressures of methanol and water adsorption are different, it is not possible to directly compare saturation loadings of the two fluids from the adsorption isobars. However, we can convert each adsorption isobar to their corresponding characteristic curve, which only depends on the fluid-zeolite working pairs. Figure 3 shows the characteristic curves of water and methanol obtained from the adsorption data. For the GCMC curve, we used the adsorption isobar from Figure 2 and additional adsorption isotherms (Figure A4.1) to complete the characteristic curve ranging from zero-coverage to sat-

uration conditions. The data from independent adsorption isobars and isotherms fall into the same characteristic curve. We found that the volumetric adsorption is considerably higher for water (about 0.35 ml of fluid per gram of adsorbent) than for methanol (0.25 ml/g). This is due to the smaller size of water that can connect through four hydrogen bonds per molecule.<sup>84</sup> Methanol can connect through two,<sup>85,86</sup> leading to a worse molecular packaging. Another relevant factor for the higher adsorption of water compared to methanol is that, contrary to methanol,<sup>87</sup> the water molecules can enter the small sodalite cages of FAU zeolites.<sup>88</sup> For this reason, the free volume for the adsorbents is larger for water than for methanol. To increase the limited number of points obtained from the GCMC simulation, we use splines. It is important to use smooth functions that fit the data well to minimize the noise in the calculations involving the characteristic curves. The fitting for the experimental characteristic curve is more straightforward since it contains more points resulting from the measurements for small temperature increments. The characteristic curves were complemented with adsorption at high temperatures to reach the low coverage regime.

The presence of cations in the FAU zeolites does not alter their pore volume significantly.<sup>59</sup> This is why adsorption isobars and characteristic curves have similar saturation values, independently of the cation content. However, the con-

centration of cations influences the hydrophilic/hydrophobic nature of the zeolites. The adsorption trend of both fluids in NaY and NaX is very similar despite the differences in the number of cations. The curves in NaY are slightly shifted to lower values of temperature (Figure 2) or lower adsorption potential (Figure 3). This effect is not as strong as for the n-alkanes.<sup>59</sup> As discussed earlier, Ristic *et al.*<sup>48</sup> proposed a post-synthesis chemical treatment of NaY to control the desorption temperatures of water. However, all modified samples contained a similar Si/Al ratio, and they found a decrease of the desorption temperatures of about 30 K compared to the original NaY zeolite. To control the desorption temperatures over a wider range of working conditions, we suggest to reduce the cation content to values between HS-FAU (Si/Al ratio = 100) and NaY (Si/Al ratio = 2.61).

Reported adsorption studies for heat storage applications typically measure adsorption isotherms at a wide range of temperatures. Then, the adsorption isotherms are reduced to a common characteristic curve. Instead of doing this, here we measure and compute a single adsorption isobar to obtain the temperature dependence of the loading needed for further calculations of the storage density. To validate this approach, we compared the characteristic curves for water obtained in this work from QE-TPDA and GCMC simulation

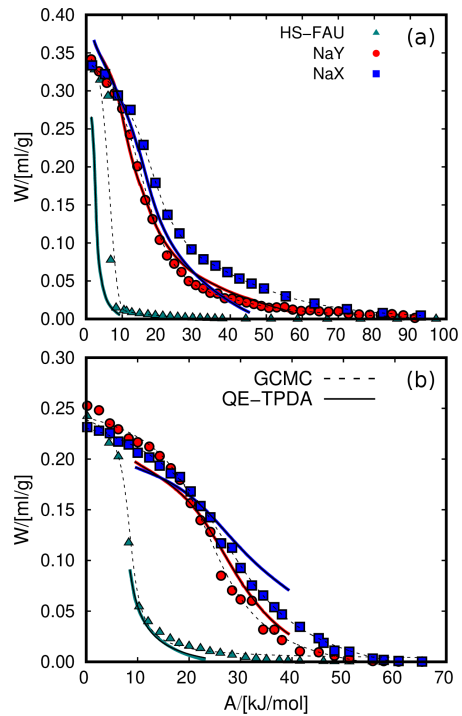


**Figure 3.** Characteristic curves of (a) water and (b) methanol in FAU zeolites using data from QE-TPDA (solid lines) and CGMC (dashed lines). The dashed lines represent the fitted curve using splines.  $W$  represents the volume of fluid adsorbed in the micropores and  $A$  is the adsorption potential.

with those reported by Lehmann *et al.*<sup>53</sup> and Stach *et al.*<sup>54</sup> (Figure 4). Our results are in line with those reported in the literature, with slight deviations mainly due to the use of different commercial samples. In all cases, we observe that the saturation loading (corresponding to  $A \rightarrow 0 \text{ kJ/mol}$ ) converges to similar values, i.e., about  $0.35 \text{ ml/g}$ , which is the saturation value for water in all FAU zeolites (Figure 3). The results shown in Figures 3 and 4 reveal the invariance of the characteris-

tic curves with the adsorption conditions, thus giving consistency to the use of the DP theory for the working pairs of this work.

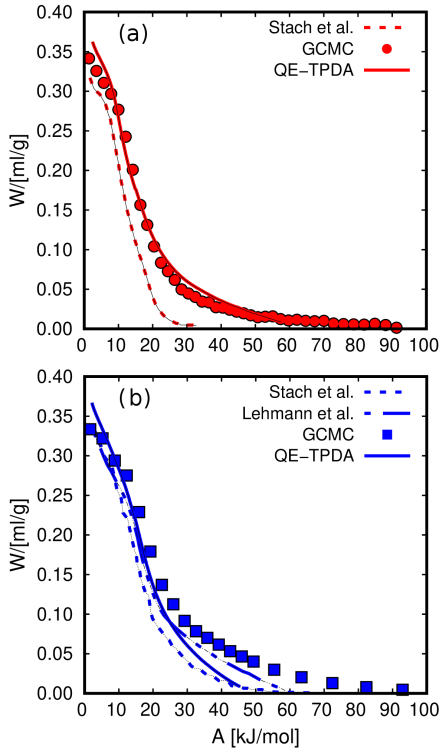


**Figure 4.** Characteristic curves of water in (a) NaY and (b) NaX obtained from GCMC (symbols) and experiments (lines). The experimental values are from QE-TPDA and reported by Stach *et al.*<sup>54</sup> and Lehmann *et al.*<sup>53</sup>  $W$  represents the volume of fluid adsorbed in the micropores and  $A$  is the adsorption potential

The performance of a working pair for adsorption-based heat storage depends on two thermodynamical quantities; the adsorption capacity and the adsorption enthalpy at the working conditions. However, these two quantities are not independent,

and the adsorption enthalpy can be obtained from the adsorption data and the physicochemical properties of the working fluid. We take the data from the characteristic curves (Figure 3) to obtain the adsorption enthalpy of water and methanol in the three zeolites (Figures 5 and 6) using the DP theory as described in the methodology. The results obtained from the QE-TPDA experiments and GCMC simulation, depicted in Figures 5 and 6, are in agreement, showing similar differences to those found in Figures 2 and 3. Differences between the measured and the computed adsorption isobars shown in Figure 3 entail a deviation of less than  $3\text{ kJ/mol}$  in the adsorption enthalpy, except for methanol in NaX, where the differences are about  $10\text{ kJ/mol}$ .

The adsorption enthalpy depends on the adsorption behavior and on the physicochemical properties of the working fluid. The properties used in the DP formulation are the vaporization enthalpy, thermal expansion coefficients, liquid density, and saturation pressure. Although Figures 2 and 3 indicate similar behavior for water and methanol adsorption, we found variations in the adsorption enthalpy for these two fluids. These discrepancies are related to the physicochemical properties of water and methanol. Figure 5 shows the loading dependence on the adsorption enthalpy of water in the three zeolites. There is correlation between the number of cations (degree of hydrophilicity) and the adsorption enthalpy. At low coverage, the abso-

lute value of the adsorption enthalpy is about  $80\text{ kJ/mol}$  for the three structures, but the behavior is differentiable at intermediate and higher loadings. For HS-FAU, the adsorption enthalpy shows an abrupt decrease with loading after the low coverage regime. This phenomenon is related to the low concentration of cations that act as strong interaction centers. Once the first molecules of water are adsorbed near the cations at low coverage regime, they quickly nucleate and occupy the rest of the adsorption sites in the structure. Similar findings have been described in the literature<sup>89,90</sup> for water and methanol adsorption in other sodium-based materials. The decrease in adsorption enthalpy in NaY and NaX is less pronounced than in HS-FAU due to the higher sodium content. At saturation, the adsorption enthalpy is about  $50\text{--}55\text{ kJ/mol}$  because adsorbate-adsorbate interactions prevail over the interactions with the zeolite.

Figure 6 shows the adsorption enthalpy using methanol as working fluid. The general trend differs from the values for water shown in Figure 5. The curve corresponding to the adsorption of methanol in HS-FAU is like that found for water. The values reach  $80\text{ kJ/mol}$  at low coverage and immediately decrease to  $50\text{ kJ/mol}$ . However, the sudden decrease of adsorption enthalpy at low coverage is less pronounced for methanol than for water, and the trend shifts slightly at high loading. The most remarkable differences

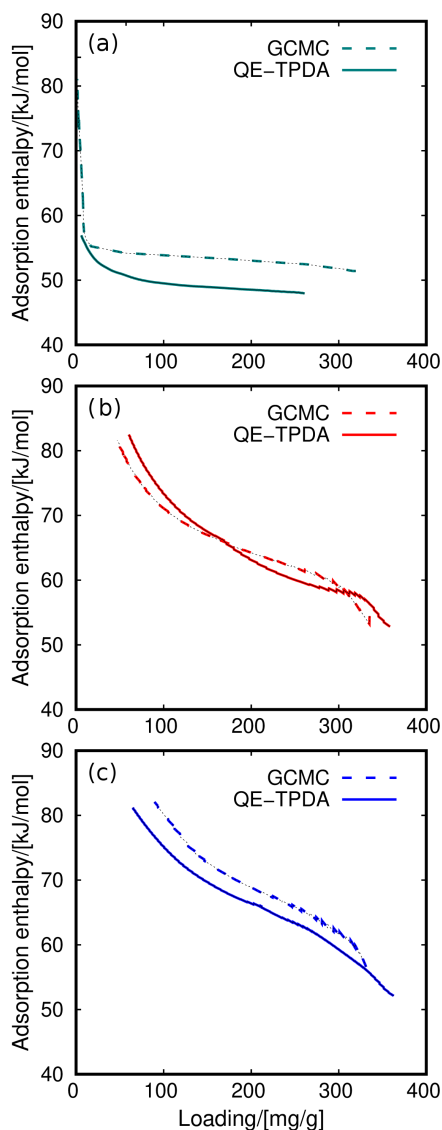


**Figure 5.** Adsorption enthalpy of water as a function of loading in (a) HS-FAU, (b) NaY, and (c) NaX. The values were obtained from GCMC simulation (dashed lines) and QE-TPDA (solid lines) data.

are for NaY and NaX. At low coverage, the values are about  $80\text{ kJ/mol}$  as for the

other systems. At intermediate loading, the curves show a minimum at about  $60 - 65 \text{ kJ/mol}$  and the adsorption enthalpy increases to  $70 - 75 \text{ kJ/mol}$  at high loading.

One of the main features of an adsorption heat storage device is its energy storage density or simply storage density. We calculated this quantity by integrating the adsorption enthalpy curves between fixed adsorption and desorption temperatures. The values shown in Figures 7a-c were obtained for a fixed adsorption temperature of  $315 \text{ K}$ . The figures show the storage density as a function of the desorption temperature. We select this temperature for being the lowest temperature measured in the QE-TPDA experiments for the three zeolites. From these figures it is possible to compare the values obtained with QE-TPDA and GCMC. These results show similar differences as in previous adsorption isobars (Figure 2) and adsorption enthalpy (Figure 5). However, the operating conditions play an important role here, making comparison more difficult. For example, Figure 7a shows the GCMC values for water in HS-FAU. Because of the high hydrophobicity of this zeolite, the adsorption obtained from QE-TPDA could not reach the saturation capacity of water in HS-FAU. This is because from the experimental side, establishing adsorption equilibrium in hydrophobic adsorbents takes long time. The driving force is very low, leading to condensation within the micropores. The inlet figure compares the storage density obtained from QE-TPDA and

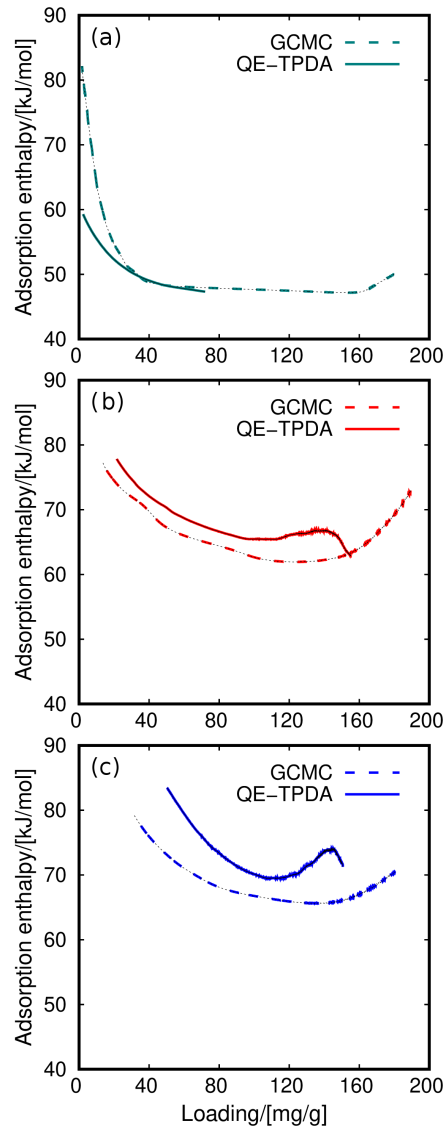


**Figure 6.** Adsorption enthalpy for methanol as a function of loading in (a) HS-FAU, (b) NaY, and (c) NaX. The values were obtained from GCMC simulation (dashed lines) and QE-TPDA (solid lines) data.

GCMC using adsorption temperatures of  $300 \text{ K}$  and  $324 \text{ K}$ , respectively. Using this approximation, the two curves show anal-

ogous abrupt increase, reaching similar storage density values. Extending the GCMC simulations to a wider range of temperature provides more detailed analysis of the storage density behavior. Therefore, it could lead to the optimization of the process based on the operational conditions for each working pair. To compare the maximum performance of the three adsorbents, we use the data from GCMC simulations and decrease the adsorption temperature to 300 K. This ensures that all systems reach saturation (Figure 7d). We found two trends; (i) HS-FAU shows an abrupt increase in the storage density. The maximum energy is released at relatively low temperatures compared to NaY and NaX because of the rapid desorption in this hydrophobic structure. For example, at a desorption temperature of 350 K, the storage density of HS-FAU surpasses 900 kJ/kg. At the same temperature, NaY and NaX do not even reach 600 kJ/kg. (ii) NaY and NaX have a moderate steep increase, reaching the maximum values at the higher tested desorption temperature, i.e., 500 K. NaY and NaX do not converge to the same storage density value because these zeolites have not released all the adsorbed water at 500 K (see Figure 2). In contrast, for HS-FAU, the curve is flat at temperature values above 350 K because the zeolite desorbs most of the molecules around this temperature. HS-FAU shows a maximum value of storage density lower than 1000 kJ/kg, while for NaY and NaX the value is be-

tween 1100 kJ/kg and 1200 kJ/kg. It is important to mention that the working pressure of water adsorption in HS-FAU was set circa 1 kPa lower than for NaY and NaX (1.98 kPa for HS-FAU, 2.8 kPa for NaY, and 3.1 kPa for NaX). However, the lower value of pressure does not explain the low storage density obtained for HS-FAU (compared to NaY and NaX), since for these values of pressure the three zeolites adsorb similar amount of water at room temperature (Figure 2). The maximum storage density depends on the maximum loading of water that the adsorbent can capture and release and the exchange adsorption enthalpy. This means that the differences in the maximum storage densities showed in Figure 7 d) are mainly due to the adsorption enthalpy of water (see Figure 5).

It is worth mentioning that the values analyzed above stand for energy per mass of adsorbent, however, the volumetric storage density is another common value analyzed in the literature. 1100 – 1200 kJ/kg corresponds to 1.7 – 1.8 GJ/m<sup>3</sup>, which is within the range of the top performing list of salt hydrates, another common type of thermochemical materials used for heat transfer applications. Donkers *et al.*<sup>91</sup> analyzed the thermodynamic data of almost 600 salt hydrates, selecting the 25 top performing candidates. The salt hydrates of this shortlist exhibit a storage density between 1.6 and 2.7 GJ/m<sup>3</sup>. Hence, water-NaY and water-NaX working pairs show comparable performance with the top per-

forming salt hydrates for energy storage applications.

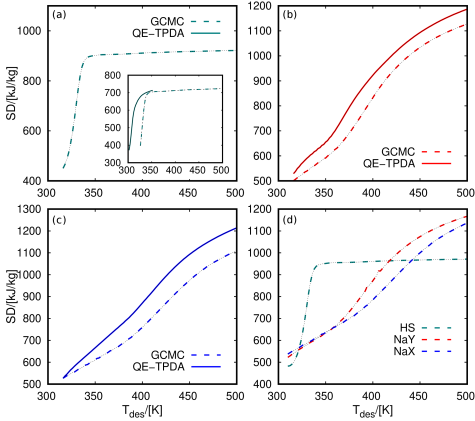


**Figure 7.** Storage density (SD) of water-zeolite pairs in (a) HS-FAU, (b) NaY, and (c) NaX at  $T_{ads} = 315\text{K}$  and  $P = 1.98\text{kPa}$  (HS-FAU),  $P = 2.8\text{kPa}$  (NaY), and  $P = 3.1\text{kPa}$  (NaX). The inset figure in (a) is for  $T_{ads} = 300\text{K}$  (QE-TPDA) and  $T_{ads} = 324\text{K}$  (GCMC). Figure (d) shows the storage density from GCMC simulation in three zeolites at  $T_{ads} = 300\text{K}$ .  $T_{des}$  stands for the temperature of the heat transfer device during the desorption cycles.

Previous results highlight the importance of the operating conditions in order to maximize the performance of each fluid-adsorbent working pair. Many works using process simulation or experimental measurements compare the values of several working pairs at single fixed operating conditions. However, the storage density values could change drastically by slightly changing the operating temperature. To compare our approach with reported data, we computed the storage density of water in NaY and NaX at the same conditions used in previous studies. Ristic *et al.*<sup>48</sup>

reported storage density of water in NaY of about  $675\text{kJ/kg}$  ( $187.5\text{Wh/kg}$ ) for fixed adsorption and desorption temperatures of  $313\text{K}$  and  $413\text{K}$ , respectively, and operating pressure of  $1.23\text{kPa}$ . Lehmann *et al.*<sup>43</sup> provided storage density values for water in NaX of about  $815\text{kJ/kg}$  ( $226.38\text{Wh/kg}$ ). However, in this case, the adsorption and desorption temperatures were extended to  $293\text{K}$  and  $453\text{K}$ , respectively. In principle, these two values cannot directly be compared, and one could think that NaX shows higher storage densities than NaY. However, extending the desorption temperature it is possible to analyze the performance of the two systems. In this regard, Figure 8 shows the computed storage density of water in NaY and NaX using reported adsorption conditions as a function of desorption temperature. For comparison, the figure also includes available experimental data. Our predictions are in agreement with the experiment and allow solid comparison between the performance of the two zeolites and water working pairs.

To check the effect of the operating pressure in the storage density, Figure A4.2 shows the results for water using values much lower than the saturation pressure of water. We can observe how the maximum storage density values for each working pair decreases at the pressure decreases up to  $0.1\text{kPa}$ . However, there are not significant differences when using  $0.5 - 1\text{kPa}$  with respect to the results shown in Figure 7.

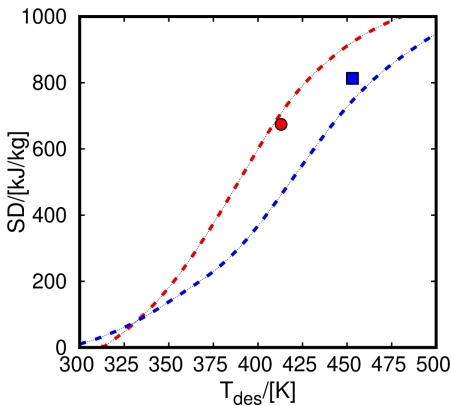


**Figure 8.** Storage density (SD) of water in NaY (red) and NaX (blue). The values taken from literature are indicated with symbols.<sup>43,48</sup> The values resulting from GCMC simulation are in dashed lines. The operational conditions are  $T_{ads} = 313K$  and  $P = 1.23kPa$  for NaY and  $T_{ads} = 293K$  and  $P = 3kPa$  for NaX.  $T_{des}$  stands for the temperature of the heat transfer device during the desorption cycles.

To compare the performance of the two working fluids, we calculated the storage density of methanol in the three zeolites using the data obtained with QE-TPDA and GCMC (Figure 9). As for water, differences between the two techniques are based on the differences found in the adsorption isobars (Figure 2) and the adsorption enthalpy (Figure 5).

The storage densities of methanol depicted in Figure 9 show the same trend than for water (Figure 7), but the maximum values are, on average, between 3 and 4 times lower. Despite the different trends on the adsorption enthalpy of water and methanol (Figures 5 and 6), the absolute values are similar. Another factor that

could influence the performance of storage densities when comparing distinct fluids is the vaporization enthalpy. At room temperature, this enthalpy is about  $10kJ/mol$  higher for water than for methanol. However, the limiting factor comparing the storage densities of the two fluids is the difference of adsorption loading. Figure 2 shows that the FAU zeolites adsorb between 3 and 4 times more water than methanol at low temperatures, which is in line with the trend observed in the storage densities.

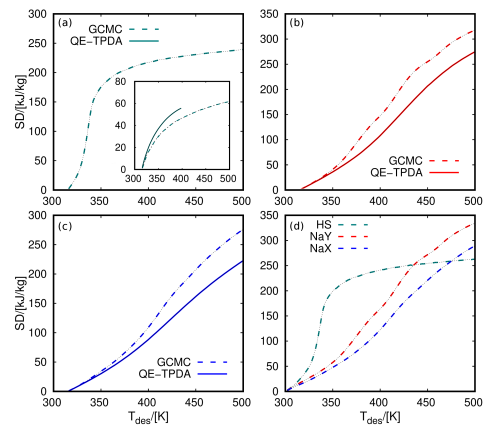


**Figure 9.** Storage density (SD) of methanol-zeolite pairs in (a) HS-FAU, (b) NaY, and (c) NaX at  $T_{ads} = 315K$  and  $P = 5kPa$  (HS-FAU) and  $P = 0.7kPa$  (NaY and NaX). The inset figure in (a) is for  $T_{ads} = 315K$  and  $P = 0.7kPa$ . Figure (d) shows the storage density from GCMC simulation at  $T_{ads} = 300K$  and  $P = 5kPa$  (HS-FAU) and  $P = 0.7kPa$  (NaY and NaX).  $T_{des}$  stands for the temperature of the heat transfer device during the desorption cycles.

## 6.4 CONCLUSIONS

The combination of QE-TPDA experiments with MC simulation gives detailed information on the use of FAU zeolites for heat storage application. The calculated adsorption isobars show strong influence of the hydrophobic degree of the adsorbent in the desorption temperatures. HS-FAU desorbs most water and methanol at much lower temperature than NaY and NaX. This large difference (circa 200 K) impacts the operating conditions of a heat storage device. Hydrophobic materials such as HS-FAU can be used at low-temperature conditions, e.g., in the 300 – 350 K range. Simultaneously, hydrophilic adsorbents can operate in high-temperature processes with desorption temperatures over 550 K. This suggests the possibility of tuning the Si/Al ratio to maximize the efficiency of adsorbate-fluid working pairs for given operational conditions.

We calculated characteristic curves, adsorption enthalpy, and storage densities of the working pairs using a thermodynamical model based on the theory of adsorption of Dubinin-Polanyi. The choice of the operating conditions for each adsorbent-fluid working pair is crucial. This is a limiting factor for the performance of materials or working fluids. The thermodynamical model provides insights on the performance of a heat storage device by only combining adsorption data with some physicochemical properties of the fluids. These are the density, the saturation pressure, and the enthalpy of vaporization in a range of

operational temperatures and pressures. These properties can be obtained from experiments, but also from molecular simulation. This could be useful for the screening of adsorbent-fluid working pairs oriented to energy storage applications.

The energy released upon heating and cooling a fluid is higher for water than for methanol. We found storage densities of the water-zeolite pairs higher than 1100 kJ/kg, while for methanol-zeolite pairs were about 350 kJ/kg. The water/methanol ratio of storage densities is related to the ratio of their adsorption loading. The highest values of water uptake are due to both, a strongest hydrogen bond network and the access of water to the sodalite cages of the FAU zeolites. The agreement found between experiments and simulation allows the use of GCMC simulation for other operational conditions and provides a comprehensive overview of the performance of the working pairs for energy storage.

## 6.5 BIBLIOGRAPHY

- [1] Hay, C. C.; Morrow, E.; Kopp, R. E.; Mitrovica, J. X. *Nature* **2015**, *517*, 481–484.
- [2] Liu, D.; Guo, X.; Xiao, B. *Science of the Total Environment* **2019**, *661*, 750–766.
- [3] Coumou, D.; Robinson, A.; Rahmstorf, S. *Climatic Change* **2013**, *118*, 771–782.
- [4] Jacobson, M. Z. Review of Solutions to Global Warming, Air Pollution, and Energy Security. 2009.
- [5] Arent, D. J.; Wise, A.; Gelman, R. *Energy Economics* **2011**, *33*, 584–593.
- [6] Mohamad, F.; Teh, J.; Lai, C. M.; Chen, L. R. Development of Energy Storage Systems for Power Network Reliability: A Review. 2018.
- [7] Mensah-Darkwa, K.; Zequine, C.; Kahol, P. K.;

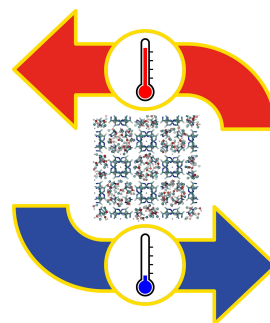
- Gupta, R. K. Supercapacitor Energy Storage Device Using Biowastes: A Sustainable Approach to Green Energy. 2019.
- [8] Ibrahim, H.; Ilinca, A.; Perron, J. Energy Storage Systems-Characteristics and Comparisons. 2008.
- [9] Rehman, S.; Al-hadhrami, L. M.; Alam, M. *Renewable and Sustainable Energy Reviews* **2015**, *44*, 586–598.
- [10] Anagnostopoulos, J. S.; Papantonis, D. E. *Energy Conversion and Management* **2007**, *48*, 3009–3017.
- [11] Oliveira, G. D.; Hendrick, P. *Applied Energy* **2016**, *179*, 1242–1250.
- [12] Lu, N.; Chow, J. H.; Desrochers, A. A. *IEEE TRANSACTIONS ON POWER SYSTEMS* **2004**, *19*, 834–841.
- [13] Ramos, H. M.; Amaral, M. P.; Covas, D. I. C. *Journal of Water Resource and Protection* **2014**, *06*, 1099–1111.
- [14] Jurasz, J.; Mikulik, J. *Bulletin of the Polish Academy of Sciences: Technical Sciences* **2017**, *65*, 859–869.
- [15] Jurasz, J.; Dąbek, P. B.; Kaźmierczak, B.; Kies, A.; Wdowikowski, M. *Energy* **2018**, *161*, 2–11.
- [16] Gleick, P. H. *Energy* **1992**, *17*, 735–747.
- [17] Greenblatt, J. B.; Succar, S.; Denkenberger, D. C.; Williams, R. H.; Socolow, R. H. *Energy Policy* **2007**, *35*, 1474–1492.
- [18] Hammann, E.; Madlener, R.; Hilgers, C. *Energy Procedia* **2017**, *105*, 3798–3805.
- [19] Liu, H.; Jiang, J. *Energy and Buildings* **2007**, *39*, 599–604.
- [20] Lund, H.; Salgi, G. *Energy Conversion and Management* **2009**, *50*, 1172–1179.
- [21] Swider, D. J. *IEEE Transactions on Energy Conversion* **2007**, *22*, 95–102.
- [22] Bolund, B.; Bernhoff, H.; Leijon, M. Flywheel Energy and Power Storage Systems. 2007.
- [23] Ribeiro, P. F.; Member, S.; Johnson, B. K.; Crow, M. L.; Member, S.; Arsoy, A.; Liu, Y.; Member, S. *Proceedings of the IEEE* **2001**, *89*, 1744–1756.
- [24] Wang, B.; Venkataramanan, G. *IEEE Transactions on Industry Applications* **2009**, *45*, 222–231.
- [25] Akagi, H.; Sato, H. *IEEE TRANSACTIONS ON POWER ELECTRONICS* **2002**, *17*, 109–116.
- [26] Ahrens, M.; Kucera, L.; Larssonneur, R. *IEEE Transactions on Control Systems Technology* **1996**, *4*, 494–502.
- [27] Duduta, M.; Ho, B.; Wood, V. C.; Limthongkul, P.; Brunini, V. E.; Carter, W. C.; Chiang, Y. M. *Advanced Energy Materials* **2011**, *1*, 511–516.
- [28] Wang, G.; Fu, L.; Zhao, N.; Yang, L.; Wu, Y.; Wu, H. *Angewandte Chemie* **2007**, *119*, 299–301.
- [29] Mauger, A.; Julien, C. M. *Ionics* **2019**, *23*, 1933–1947.
- [30] Cao, C.; Li, Z.-b.; Wang, X.-l.; Zhao, X.-b.; Han, W.-q. *frontiers in energy research* **2014**, *2*, 1–10.
- [31] Weiss, M.; Zerfass, A.; Helmers, E. *Journal of Cleaner Production* **2019**, *212*, 1478–1489.
- [32] dos Santos, C. S.; Alves, J. C.; Pires, S. d. S.; Sita, L. E.; Pires da Silva, S.; Evangelista Sita, L.; Catarini da Silva, P.; de Almeida, L. C.; Scarmínio, J. *Journal of Hazardous Materials* **2019**, *362*, 458–466.
- [33] Redondo-Iglesias, E.; Venet, P.; Pelissier, S. Measuring Reversible and Irreversible Capacity Losses on Lithium-Ion Batteries. 2016 IEEE Vehicle Power and Propulsion Conference (VPPC). 2016; pp 1–5.
- [34] Vasta, S.; Brancato, V.; La Rosa, D.; Palomba, V.; Restuccia, G.; Sapienza, A.; Frazzica, A. Adsorption Heat Storage: State-of-the-Art and Future Perspectives. 2018.
- [35] Solovyeva, M. V.; Gordeeva, L. G.; Krieger, T. A.; Aristov, Y. I. *Energy Conversion and Management* **2018**, *174*, 356–363.
- [36] Jenks, J. J.; Motkuri, R. K.; TeGrotenhuis, W.; Paul, B. K.; McGrail, B. P. *Heat Transfer Engineering* **2017**, *38*, 1305–1315.
- [37] Deshmukh, H.; Maiya, M. P.; Srinivasa Murthy, S. *Applied Thermal Engineering* **2017**, *111*, 1640–1646.
- [38] Sun, J.; Besant, R. W. *International Journal of Heat and Mass Transfer* **2005**, *48*, 4953–4962.
- [39] MebarkilĠ, B.; SolmuÅš, Å.; GomriĠ, R. *J. of Thermal Science and Technology* **2016**, *36*, 107–118.
- [40] Critoph, R. E.; Turner, L. *International Journal of Heat and Mass Transfer* **1995**, *38*, 1577–1585.
- [41] Critoph, R. E. *Carbon* **1989**, *27*, 63–70.
- [42] Xiao, J.; Tong, L.; Deng, C.; Bénard, P.; Chahine, R. *International Journal of Hydrogen Energy* **2010**, *35*, 8106–8116.
- [43] Lehmann, C.; Beckert, S.; Gläser, R.; Kolditz, O.; Nagel, T. *Applied Energy* **2017**, *185*, 1965–1970.
- [44] Tatsidjodoung, P.; Le Pierrès, N.; Heintz, J.; Lagre, D.; Luo, L.; Durier, F. *Energy Conversion and Management* **2016**, *108*, 488–500.
- [45] Du, S. W.; Li, X. H.; Yuan, Z. X.; Du, C. X.; Wang, W. C.; Liu, Z. B. *Solar Energy* **2016**, *138*, 98–104.
- [46] Wang, L.; Gandorfer, M.; Selvam, T.; Schwioger, W. *Materials Letters* **2018**, *221*, 322–325.
- [47] Jänchen, J.; Stach, H. *Energy Procedia* **2012**, *30*, 289–293.
- [48] Ristić, A.; Fischer, F.; Hauer, A.; Zabukovec Logar, N. *Journal of Materials Chemistry A* **2018**, *6*, 11521–11530.
- [49] Aristov, Y. *Applied Thermal Engineering* **2014**, *72*, 166–175.
- [50] De Lange, M. F.; Verouden, K. J.; Vlucht, T. J.; Gascon, J.; Kapteijn, F. *Chemical Reviews* **2015**, *115*, 12205–12250.
- [51] Kohler, T.; Müller, K. *Energy Science and Engineering* **2017**, *5*, 21–29.
- [52] Semprini, S.; Asenbeck, S.; Kerskes, H.; Drück, H. Experimental and Numerical Investigations of an Adsorption Water-Zeolite Heat Storage for Refrigeration Applications. *Energy Procedia*. 2017; pp 513–521.
- [53] Lehmann, C.; Beckert, S.; Nonnen, T.; Möllmer, J.; Gläser, R.; Kolditz, O.; Nagel, T. *Energy Procedia* **2017**, *105*, 4334–4339.
- [54] Stach, H.; Mugele, J.; Jänchen, J.; Weiler, E. *Adsorption* **2005**, *11*, 393–404.
- [55] Zhu, G.; Qiu, S.; Yu, J.; Sakamoto, Y.; Xiao, F.; Xu, R.;

- Terasaki, O. *Chem. Matter* **1998**, *10*, 1483–1486.
- [56] Azizi, S. N.; Ghasemi, S.; Kavian, S. *Biosensors and Bioelectronics* **2014**, *62*, 1–7.
- [57] Calero, S.; Gómez-Álvarez, P. *Journal of Physical Chemistry C* **2014**, *118*, 9056–9065.
- [58] Madero-Castro, R. M.; Vicent-Luna, J. M.; Peng, X.; Calero, S. *ACS Sustainable Chemistry & Engineering* **2022**, *10*, 6509–6520.
- [59] Slawek, A.; Vicent-Luna, J. M.; Ogorzały, K.; Valencia, S.; Rey, F.; Makowski, W.; Calero, S. *Journal of Physical Chemistry C* **2019**, *123*, 29665–29678.
- [60] Luna-Triguero, A.; Slawek, A.; Huinink, H. P.; Vlught, T. J. H.; Poursaeidesfahani, A.; Vicent-Luna, J. M.; Calero, S. *Enhancing the Water Capacity in Zr-Based Metal-Organic Framework for Heat Pump and Atmospheric Water Generator Applications*. 2019.
- [61] Makowski, W.; Ogorzały, Ł. *Thermochimica Acta* **2007**, *465*, 30–39.
- [62] Makowski, W. *Thermochimica Acta* **2007**, *454*, 26–32.
- [63] Slawek, A.; Vicent-Luna, J. M.; Marszałek, B.; Makowski, W.; Calero, S. *Journal of Physical Chemistry C* **2017**, *121*, 25292–25302.
- [64] Dubbeldam, D.; Calero, S.; Ellis, D. E.; Snurr, R. Q. *Molecular Simulation* **2016**, *42*, 81–101.
- [65] Darden, T.; York, D.; Pedersen, L. *The Journal of Chemical Physics* **1993**, *98*, 10089–10092.
- [66] Luna-Triguero, A.; Slawek, A.; Sánchez-de Armas, R.; Gutiérrez-Sevillano, J. J.; Ania, C. O.; Parra, J. B.; Vicent-Luna, J. M.; Calero, S. *Chemical Engineering Journal* **2020**, *380*, 122482.
- [67] González-Galán, C.; Luna-Triguero, A.; Vicent-Luna, J. M.; Zaderenko, A. P.; Slawek, A.; Sánchez-de Armas, R.; Calero, S. *Chemical Engineering Journal* **2020**, *398*, 125678.
- [68] Balestra, S. R.; Hamad, S.; Ruiz-Salvador, A. R.; Domínguez-García, V.; Merklung, P. J.; Dubbeldam, D.; Calero, S. *Chemistry of Materials* **2015**, *27*, 5657–5667.
- [69] Baker, J. *Journal of Computational Chemistry* **1986**, *7*, 385–395.
- [70] Sanders, M. J.; Leslie, M.; Catlow, C. R. *Journal of the Chemical Society, Chemical Communications* **1984**, 1271–1273.
- [71] Jackson, R.; Catlow, C. *Molecular Simulation* **1989**, *1*, 207–224.
- [72] Schmid, N.; Eichenberger, A. P.; Choutko, A.; Riniker, S.; Winger, M.; Mark, A. E.; Van Gunsteren, W. F. *European Biophysics Journal* **2011**, *40*, 843–856.
- [73] Mark, P.; Nilsson, L. *Journal of Physical Chemistry A* **2001**, *105*, 9954–9960.
- [74] Stubbs, J. M.; Potoff, J. J.; Siepmann, J. I. *Journal of Physical Chemistry B* **2004**, *108*, 17596–17605.
- [75] Di Lella, A.; Desbiens, N.; Boutin, A.; Demachy, I.; Ungerer, P.; Bellat, J. P.; Fuchs, A. H. *Physical Chemistry Chemical Physics* **2006**, *8*, 5396–5406.
- [76] Xiong, R.; Sandler, S. I.; Vlachos, D. G. *Journal of Physical Chemistry C* **2011**, *115*, 18659–18669.
- [77] Castillo, J. M.; Dubbeldam, D.; Vlught, T. J.; Smit, B.; Calero, S. *Molecular Simulation* **2009**, *35*, 1067–1076.
- [78] Castillo, J. M.; Silvestre-Albero, J.; Rodríguez-Reinoso, F.; Vlught, T. J.; Calero, S. *Physical Chemistry Chemical Physics* **2013**, *15*, 17374–17382.
- [79] Calero, S.; Dubbeldam, D.; Krishna, R.; Smit, B.; Vlught, T. J.; Denayer, J. F.; Martens, J. A.; Maesen, T. L. *Journal of the American Chemical Society* **2004**, *126*, 11377–11386.
- [80] Boda, D.; Henderson, D. *Molecular Physics* **2008**, *106*, 2367–2370.
- [81] Dubinin, M. M. *Russ Chem Bull* **1960**, *9*, 11072–1078.
- [82] Andersen, A. H. *Acta Pharmacologica et Toxicologica* **2009**, *3*, 199–218.
- [83] Bakaev, V. A.; Steele, W. A. *Adsorption Science Technology* **1993**, *10*.
- [84] Rastogi, A.; K., A.; Suresh, S. *Thermodynamics - Physical Chemistry of Aqueous Systems*; InTech, 2011.
- [85] JORGENSEN, W. L.; MADURA, J. D. *Molecular Physics* **1985**, *56*, 1381–1392.
- [86] Matsumoto, M.; Gubbins, K. E. *The Journal of Chemical Physics* **1990**, *93*, 1981–1994.
- [87] Narayana, M.; Kevan, L. *Journal of the American Chemical Society* **1981**, *103*, 5729–5733.
- [88] Ammouli, T.; Paillaud, J.-L.; Nouali, H.; Stephan, R.; Hanf, M.-C.; Sonnet, P.; Deroche, I. *The Journal of Physical Chemistry C* **2021**, *125*, 19405–19416.
- [89] Li, Z.; Rieg, C.; Beurer, A.-K.; Benz, M.; Bender, J.; Schnecko, C.; Traa, Y.; Dyballa, M.; Hunger, M. *Adsorption* **2020**, *27*, 49–68.
- [90] Li, Z.; Dittmann, D.; Rieg, C.; Benz, M.; Dyballa, M. *Catalysis Science & Technology* **2022**, *12*, 5189–5202.
- [91] Donkers, P.; Sögütöglü, L.; Huinink, H.; Fischer, H.; Adan, O. *Applied Energy* **2017**, *199*, 45–68.

## Alcohol-Based Adsorption Heat Pumps using Hydrophobic Metal-Organic Frameworks

Rafael María Madero-Castro, A. Luna-Triguero, C. González-Galán, José Manuel Vicent-Luna, and Sofía Calero

The building climate industry and its influence on energy consumption have consequences on the environment due to the emission of greenhouse gasses. Improving the efficiency of this sector is essential to reduce the effect on climate change. In recent years, the interest in porous materials in applications such as heat pumps has increased due to their promising performance. In this work, we propose a multistep approach based on the processing of adsorption data combined with a thermodynamic model to assess the performance of adsorption heat pumps and cooling systems. The process provides properties of interest, such as the coefficient of performance or the released heat upon adsorption and desorption cycles and has the advantage of identifying the optimal conditions for each adsorbent-fluid pair. We select several metal-organic frameworks with varying topologies, chemical composition, and pore sizes to test the proposed method, using methanol and ethanol as working fluids. We computed the adsorption equilibrium curves using Grand-Canonical Monte Carlo simulations to describe the adsorption mechanisms in the selected adsorbents. Then, we use a thermodynamic model to calculate the energetic properties combined with iterative algorithms that simultaneously vary all the required working conditions. We discuss the strong influence of operating temperatures on the performance of heat pump devices. Our findings point to the highly hydrophobic metal azolate framework MAF-6 as an outstanding candidate for heating and cooling applications based on its high working capacity and excellent energy efficiency.



## 7.1 INTRODUCTION

The building energy demand for energy efficiency has increased in the last two decades.<sup>1,2</sup> Forecasts manifest that this growth will continue rising due to global warming.<sup>2,3</sup> Consequently, the emission of greenhouse gasses into the atmosphere will be higher, producing a feedback process.<sup>4–6</sup> Improving efficiency in this sector and reducing greenhouse gasses emissions are critical aspects in mitigating the climate change.<sup>7–10</sup> Traditional heating systems such as electric or gas heaters offer low performance.<sup>11</sup> They are based on Joule effect or on the specific heat of the substances to be burned, respectively, so that the heat supplied for the heating system is equal to the energy used. It is essential to foster advanced heating devices that take advantage of outside heat to increase performance. For example, heating devices like solar collectors, which use solar energy to warm water or air, are eco-friendly options.<sup>12–14</sup> The main problem of solar systems is that weather acts as restrictive factor.<sup>15</sup>

Heat pumps are a promising alternative since they take heat from the surroundings, reducing the total energy consumption of the heating system.<sup>16</sup> These systems are efficient and a sustainable alternative to conventional methods, increasing the performance and decreasing greenhouse gasses released into the atmosphere. Traditional heat pumps are based on the compression/decompression of a working fluid, with hydrofluorocarbons

(like HFC-134a or HFC-125) being the most used at the industrial level.<sup>17,18</sup> The main problem with these devices is that they use greenhouse gasses<sup>19</sup> that need to be reduced according to the Montreal Protocol.<sup>19</sup> In this context adsorption-based Heat Pumps (AHP) and Adsorption Cooling Systems (ACS) using porous materials, are promising options. The operation mechanism of the AHP and ACS devices is based on adsorption and evaporation of a refrigerant. These devices follow the assumption that reversible adsorption (desorption) is an exothermic (endothermic) process.<sup>20</sup>

In recent years, AHP and ACS made with porous materials such as activated carbons,<sup>14,21–29</sup> zeolites,<sup>29–36</sup> and metal-organic frameworks (MOFs)<sup>29,37–42</sup> have shown promising performance, showing remarkable benefits as cost and versatility. Pal *et al.*<sup>43</sup> studied the production of highly porous carbons from vegetable waste for heat pump applications. Works reported by de Lange *et al.*<sup>44</sup>, Li *et al.*<sup>45</sup>, Erdos *et al.*<sup>46</sup>, or Jeremias *et al.*<sup>47</sup>, among others, studied a variety of MOFs with methanol and ethanol as working fluids for adsorption-driven heat pumps and chillers applications. Kayal *et al.*<sup>48</sup> studied the water-AQSOA zeolite working pair to create of adsorption chillers, concluding that these zeolites are also suitable for this purpose. One of the most challenging parts of designing AHPs is the selection of the working pair. It is desirable to work with environmentally friendly fluids with

high enthalpy of vaporization. However, the large amount of synthesized porous adsorbents makes it difficult to assess the performance of each working pair experimentally. Computationally, it is also very expensive to test several operating conditions for the selection of the optimal range for a given pair. The number of synthesized MOFs is large and continuously growing.<sup>49</sup> The high versatility in terms of composition and pore size makes them good candidates to operate in different conditions. In-depth knowledge of the adsorbent-fluid interactions makes it possible to choose the most suitable pair for given working conditions. In general, MOFs exhibit higher adsorption capacity than zeolites or other porous materials, a fundamental aspect of increasing the heat transfer between adsorption/desorption cycles. In this work, we have selected ZIF-8, ZIF-71, ZIF-90, MIL-140, and MAF-6, as adsorbents. Four of these MOFs exhibit a large pore size ( $> 11 \text{ \AA}$ ), which is desired for a stepwise isotherm. The exception is MIL-140 with a pore size lower than  $6 \text{ \AA}$  that we included for comparison. These MOFs have been successfully tested for the adsorption of methanol and ethanol<sup>44,50,51</sup>. We will use this experimental data to validate our models.

The selection of the refrigerant for an adsorption energy storage device is as important as the selection of the adsorbent, because the synergy between adsorbent and fluid working pairs is a critical aspect of achieving maximum performance.

As alternatives to conventional refrigerants, ammonia<sup>30,52</sup> and water<sup>52,53</sup> have been proposed as working fluids. Water is an excellent candidate due to the high enthalpy of vaporization and the zero toxicity to humans, but as a downside, water can affect MOFs stability.<sup>54</sup> Ammonia is also an excellent working fluid with a shallow melting point ( $-40^\circ\text{C}$ ) and slightly lower enthalpy of vaporization than water. However, ammonia is a toxic compound that should be used carefully. In the search for other working fluids for AHPs and ACSs, light alcohols have become a possible alternative.<sup>44,55</sup> Highly hydrophobic materials cannot adsorb/desorb water at realistic pressure/temperature conditions,<sup>56-59</sup> however, these adsorbent can capture and release methanol and ethanol within the range of operational conditions. de Lange *et al.*<sup>44</sup> summarized the main differences of replacing water (the most common working fluid in MOFs) by ethanol and methanol. These are, among others: 1) decrease of the onset pressure of methanol and ethanol compared to water, 2) lower hysteresis loop for large pore materials (below  $3.4 \text{ nm}$ ), 3) lower energy release per cycle, but heat and mass transfer may be improved, and 4) in general, MOFs seem to be more stable upon alcohol adsorption than upon water adsorption. These facts make light alcohols a promising alternative to water and other common refrigerants used in industry. Another important aspect is the reduced global warming potential (GWP)

of small alcohols compared to traditional working fluids. Ethanol GWP fluctuates between 0.31 – 5.55 depending on the production path<sup>60</sup> compared to the 1120–3500 GWP for HFC-based refrigerants, i.e. HFC-134a and HFC-125. Hence, in addition to previous discussion, the relatively low-cost, high heat capacities and low melting points make methanol and ethanol good candidates as working fluids for AHP/ACS applications.

The large amount of synthesized structures makes the assessment of the performance of each working pair challenging, from an experimental point of view. Several studies focused on strategies to analyze the performance of alcohol-adsorbent using computational screenings. Erdos *et al.*<sup>46</sup> designed a screening process for methanol and ethanol on almost 3000 adsorbents. The most promising structures were selected based on the maximum working capacity obtained in consecutive relative values of pressure defined by the authors. A computational screening and selection based on the coefficient of performance (COP) for cooling applications was reported by Li *et al.*<sup>45</sup> They systematically rejected structures that perform under below the imposed limit of 0.8. The significant number of samples made an in-depth study challenging in suitable operating conditions for each system, which lead to qualitative-based interpretations. To fasten the selection process, they performed relatively short GCMC simulations ( $4 \cdot 10^4$  cycles), only running more cycles for the

promising structures. This approach was aimed to obtain high-performance structures. However, short simulations in the first step can also lead to the rejection of viable materials. It has been previously demonstrated that materials with big pores and hydrophobic structures need more MC cycles to reach equilibrium.<sup>53</sup> Following a similar approach, another recent computational screening by the same authors<sup>61</sup> analyzed the performance of COF-ethanol working pairs for heating, cooling, and ice-making applications. As before, they performed short GCMC simulations that can disregard promising candidates. Each adsorbent-fluid pair and its range of operational conditions should be analysed carefully. This is because any small change could imply a considerable deviation on the predicted application of heating and cooling systems. In this regard, Xia *et al.*<sup>62</sup> went a step further by varying the working conditions and the effect on the cooling/heating performance of COF-5/ethanol and several MOF/ethanol working pairs.

Here we propose a novel approach to assess the coefficient of performance or other thermodynamic quantity, such as the heat released during the adsorption process. We apply this method to investigate MOFs-methanol/ethanol working pairs and rely on adsorption data and the consecutive application of mathematical and thermodynamic models. The advantage of this methodology is that it can be applied to either experimental or com-

putational data sets and is also extensible to other working fluids. Another benefit of the analysis proposed here is that we considered a wide range of operating conditions proving that fixing the operating temperatures could lead to a significant loss of information about the performance of the process. In short, an AHP cycle consists of four primary parts: an adsorber containing the adsorbent, a condenser, an evaporator, and an expansion valve. The heat pump operates by driving adsorbate between the adsorber, condenser, and evaporator. The cycle can be divided into two parts. In the first part, the evaporator vaporizes the fluid taking heat from a low-temperature source and releasing heat to an intermediate temperature source (adsorption). In the second part, during the condensation of the fluid, the condenser receives heat from a high-temperature source and releases heat to a second intermediate temperature source (desorption). During the cycle, the evaporator, condenser, desorption and intermediate temperatures play an important role on the performance of the process. In the analysis that we propose, we simultaneously screen all these temperatures providing detailed information of the operation of each MOF-fluid working pair.

The main objective of this work is to understand the mechanisms that govern the adsorbate-adsorbent pair, which enhances the efficiency of the thermodynamic cycle. With this in mind, we computed equilibrium adsorption isotherms

and isobars of ethanol and methanol in the MOFs. We analyzed the energetic and structural properties of the adsorbed molecules by evaluating the internal energy contributions and the hydrogen bonds, thus providing atomistic information on the adsorption behavior. We used the Dubinin-Polanyi thermodynamic model to calculate the characteristic curves discussing its applicability. To analyse the efficiency of the systems we calculated the coefficient of performance (COP) and the energy transferred to the condenser. We search for optimal conditions for each MOF-alcohol pair, discussing the limitations of fixing the values of operating temperatures. Our results show a high performance of the working pairs for cooling and heating, making them an alternative to conventional AHP/ACS.

## 7.2 METHODOLOGY

We propose a multistep process to methodically evaluate the performance of MOFs for heating and cooling applications and to find the optimal working conditions for each adsorbent-fluid working pairs. This method is tested using five MOFs for the adsorption of methanol and ethanol working fluids. The multistep process consists of a combination of molecular simulation, thermodynamical modelling, and in-house algorithms that iteratively analyze the performance of and AHP/ACS process.

### 7.2.1 Adsorbents

We study the prospects of ZIF-8, ZIF-40, ZIF-71, ZIF-90, and MIL-140C for

AHP and ACS applications. The first four are Zn-based Zeolitic Imidazolate Frameworks (ZIFs), and the last one is a previously reported Zr-based MOF for similar applications.<sup>44</sup> Table 1 summarizes the topology and structural properties, pore volume ( $V_p$ ), surface area ( $S_A$ ), framework density ( $\rho$ ), and helium void fraction (HvF) of the selected adsorbents. ZIF-8<sup>63</sup> and ZIF-90<sup>64</sup> exhibit SOD topology and are formed by Zn metal centers connected to 2-methylimidazole and 2-carboxydehyde organic linkers, respectively. The SOD topology is characterized for sodalite central cages interconnected through small windows. ZIF-8 and ZIF-90 possess pores in the range of 10.5 – 11 Å and apertures of 3.5 Å. ZIF-71<sup>65</sup> and MAF-6,<sup>59</sup> with RHO topology, are formed by Zn metal centers connected to Zn metal centres connected with 4,5-dichloroimidazole and 2-ethylimidazole organic linkers, re-

spectively. The RHO topology structures are constructed by large central cages interconnected through channels. These two MOFs have similar pore sizes, big cages of about 16.5 – 17.5 Å and cylindrical channels of 6.5 – 7 Å. The nature of the organic ligand exerts a strong influence in the available pore volume of ZIF-71 and makes MAF-6 the MOF with the largest pore volume under study. MIL-140C<sup>66</sup> is a five-coordinated Zr-based MOF with a biphenyl-4,4'-dicarboxylic acid linker. The structure has small triangular-shaped channels of about 6 Å that propagate along the c-axis. MIL-140C is the smallest structure under study in terms of available pore volume and surface area. Figure 1 displays the schematic framework connectivity, pore size distribution (PSD). The schematic representation of the ligands can be found in the Appendix 5, (Figure A5.1).

**Table 1.** Structural properties of the selected MOFs, density, pore volume, helium void fraction, surface area and pore size.

MOF	Topology	$\rho$ [ $kg\ m^{-3}$ ]	$V_p$ [ $cm^3\ g^{-1}$ ]	HvF	$S_A$ [ $m^2\ g^{-1}$ ]	Pore Size (Å)
ZIF-8	SOD	924.586	0.52	0.484	1732.483	10.855
ZIF-90	SOD	988.431	0.51	0.507	1661.356	10.715
ZIF-71	RHO	1154.904	0.42	0.496	1379.243	16.645
MAF-6	RHO	813.579	0.59	0.482	1664.484	17.435
MIL-140C	-	1173.139	0.34	0.400	1298.945	5.795

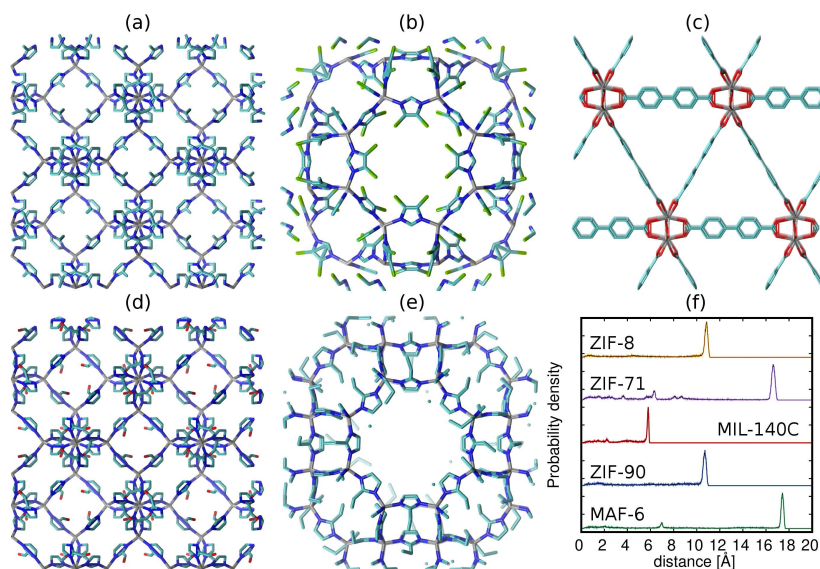


**Figure 1.** Schematic representation of the framework connectivity of (a) ZIF-8, (b) ZIF-71, (c) MIL-140C, (d) ZIF-90 and (e) MAF-6, and (f) Pore Size Distribution. Nitrogen atoms are coloured in blue, carbon atoms in cyan, oxygen atoms in red, chlorine atoms in green, and zirconium and zinc atoms in grey. Hydrogen atoms are omitted for clarity.

## 7.2.2 Simulation Details

We carried out Monte Carlo (MC) simulations in the Grand-Canonical ensemble (GCMC) using the RASPA simulation software,<sup>67,68</sup> to obtain the adsorption capacities as a function of temperature or external pressure. The MC production run cycles range between  $7 \cdot 10^5$  and  $2.2 \cdot 10^6$ . The number of cycles changes depending on the nature of the system working fluid-adsorbent to ensure that the results fluctuate around an equilibrium value.<sup>53</sup> The final data are averaged over the last  $5 \cdot 10^5$  MC cycles.

We used Lennard-Jones and Coulombic potentials to describe the interactions between adsorbates and adsor-

bents. We employed Lorentz-Berthelot mixing rules<sup>69</sup> to calculate Lennard-Jones crossed terms between different atoms. We fixed the length of the simulation box so that we always exceed twice the spherical cut off of 12 Å. Electrostatic contributions to the energy of the system have been obtained using Ewald summation.<sup>70</sup> We used TraPPE force field<sup>71</sup> to describe the models for the adsorbates. The structures are considered rigid during the simulations, placing the framework atoms in their crystallographic positions. We used the reported crystal structures of ZIF-8,<sup>63</sup> ZIF-71,<sup>72</sup> MIL-140C,<sup>66</sup> ZIF-90,<sup>73</sup> and MAF-6.<sup>74</sup> The Lennard-Jones parameters for the adsorbates are taken from DREID-

ING<sup>75</sup> except for the metal atoms, taken from UFF.<sup>76</sup> The partial charges of the adsorbents (see Figure A5.1 of the Appendix 5) are calculated using the EQeq method,<sup>77</sup> except for MAF-6, taken from the work of Gutierrez-Sevillano *et al.*<sup>78</sup> Since the interactions of molecules of alcohols via hydrogen bonds play an essential role in the adsorption mechanism,<sup>79</sup> we compute the average number of hydrogen bond per molecule using methodology described in previous work.<sup>79</sup>

### 7.2.3 Thermodynamic Model

The AHP cycle consists of two steps for adsorption (isobaric adsorption and isosteric heating) and two for desorption (isobaric desorption and isosteric cooling) as represented in Figure 2. The system has different operating conditions pairs  $(p, T)$  during the cycle, the temperature of the evaporator ( $T_{ev}$ ), temperature of the condenser ( $T_{con}$ ), temperature of desorption ( $T_{des}$ ), and intermediate temperatures ( $T_{ev} < T_{con} < T_1 < T_2 < T_3 < T_{des}$ ), and associated pressures.

The adsorption and desorption phases of an AHP are characterized for the energy in the different stages: heat taken from the evaporator ( $Q_{ev}$ ), the required energy for desorption or regeneration ( $Q_{reg}$ ), heat released by the condensed fluid ( $Q_{con}$ ), and the heat released during the adsorption ( $Q_{ads}$ ) at intermediate temperature. For practical reasons, it is common to assume that  $T_1$ , also called the minimum temperature of adsorption ( $T_{ads}$ ), is equal to  $T_{con}$ .

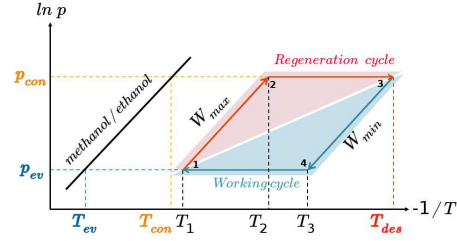


**Figure 2.** Isosteric cycle of an AHP, including vapor pressure of alcohol molecules (black line), temperature and pressure of the evaporator ( $T_{ev}, p_{ev}$ ), and the condenser ( $T_{con}, p_{con}$ ), desorption temperature ( $T_{des}$ ), and intermediate cycle temperatures ( $T_{1-3}$ ). Highlighted in blue, the working cycle (adsorption) and in red the regeneration cycle (desorption).

The coefficient of performance (COP), used to describe the energetic efficiency, is defined as the ratio between the obtained energy and the input energy. For heating, the COP is defined as

$$COP_H = \frac{-(Q_{con} + Q_{ads})}{Q_{reg}} \quad (7.1)$$

and for cooling

$$COP_C = \frac{-(Q_{ev})}{Q_{reg}} \quad (7.2)$$

$Q_{con}$  and  $Q_{ev}$  are proportional to the enthalpy of vaporization ( $\Delta H_{vap}$ ), the density of the working fluid ( $\rho^{wf}$ ) in confinement, and the working capacity ( $\Delta W$ ), which is the difference between the maximum and minimum isosteres ( $W_{max} - W_{min}$ ). The calculation of the energy needed for regeneration ( $Q_{reg}$ ) and the energy release during adsorption ( $Q_{ads}$ ) is more complex and involves the estimation of the enthalpy of adsorption,

$\Delta H_{vap}(W)$ . The equations that govern the AHP process from a thermodynamic perspective are detailed in the literature.<sup>44</sup>

The enthalpy of vaporization is taken from Majer *et al.*,<sup>80</sup> while the remaining parameters are calculated using models.

Based on the Dubinin-Polanyi (DP) theory,<sup>81,82</sup> any equilibrium adsorption curve where loadings is pressure and temperature dependent,  $q(p, T)$ , can be reduced to a characteristic curve. The characteristic curve is the relation between the potential of adsorption ( $A$ ) and the adsorbed specific volume ( $W$ ) defined as:

$$A = RT \left( \ln \frac{p_0(T)}{p} \right) \quad W = \frac{q(p, T)}{\rho^{wf}(T)} \quad (7.3)$$

where  $p_0$  is the vapor pressure of the working fluid,  $q$  is the mass adsorbed, and  $\rho^{wf}$  is the density of the working fluid in the adsorbed phase. We used the Peng-Robinson equation of state<sup>83</sup> to set the saturation pressure. The DP theory allows to calculate adsorption enthalpy from the characteristic curve using numerical techniques.

We calculated the adsorbate density using the Hauer model.<sup>84</sup> This model establishes linear relations between the bulk density and the density inside the pores of the structure. The model was initially developed for water, and has been modified to estimate the density of alcohols were  $\rho(T_0)$  is the free liquid density taken from experimental data at the reference temperature ( $T_0 = 283K$ ).<sup>85</sup>

$$\rho^{wf}(T) = \rho(T_0)[1 - \alpha_T(T - T_0)] \quad (7.4)$$

The coefficient of thermal expansion,  $\alpha_T$ , is considered constant for each working fluid.  $\alpha_T$  has been calculated using the equation

$$\alpha_T = -\frac{1}{\rho(T)} \left( \frac{\partial \rho(T)}{\partial T} \right)_p \quad (7.5)$$

using the density of the fluid at high pressure, 100 MPa. At  $T = 300K$ ,  $\alpha_T$  is  $8.026 \cdot 10^{-4} [1/K]$  for methanol and  $7.285 \cdot 10^{-4} [1/K]$  for ethanol.

#### 7.2.4 Multistep Process

The process is schematically represented in Figure 3. **Step 1** is to obtain the equilibrium adsorption curves, *e.g.*, adsorption isotherms and isobars. This can be done either experimentally or with GCMC simulations. In **Step 2** the input data is processed according to Dubinin-Polanyi theory. From there, we obtained a temperature invariant characteristic curve that allows i) to predict new adsorption curves at any conditions (step 1) and ii) proceed with the thermodynamic analysis of the system.

It is necessary to insert pre-processed functions into the algorithm to apply DP theory. The most significant variables are the density of the fluid in confinement ( $\rho^{wf}$ ), and the saturation pressure ( $p_0$ ). Once the characteristic curve is obtained, the process bifurcates. During **Step 3** we calculate the enthalpy of adsorption of the system, which depends on the enthalpy

of evaporation of the fluid, the adsorption potential, and the entropy's contribution. The entropy calculation is pre-processed due to its dependency on the thermal expansion coefficient of the fluid in confinement. In **Step 4** the isosteric cycle is calculated, estimating the maximum and minimum capacity isosteres for given conditions, *i.e.*, setting  $T_{ev}$  and  $T_{con}$  and the associate pressures. The calculation of COP for either heating or cooling can be done under different conditions (**Step 5**). Without optimization, the temperature of the evaporator and the condenser are fixed, and therefore the associated pressures. The COP is assessed as a function of the desorption temperature. **Step 6** is the optimization step. Here we scan the operat-

ing conditions and associated thermodynamic parameters in subsequence loops. The variation of  $T_{ev}$ ,  $T_{con}$  and  $T_{des}$  are made simultaneously, with the only condition of  $T_{ev} < T_{con} < T_{des}$ . After the massive data generation, the algorithm computes the COP by fixing only one temperature ( $T_{ev}$  or  $T_{con}$ ) and scanning for the optimal conditions. From this step, we obtain a 3D plot per fixed variable that allows the election of the operational conditions that provide maximum performance. Using the same procedure, we calculated other quantities of interest such as the heat released to the condenser ( $Q_{con}$ ), proving that it is useful to obtain properties that strongly depend on the operating conditions.

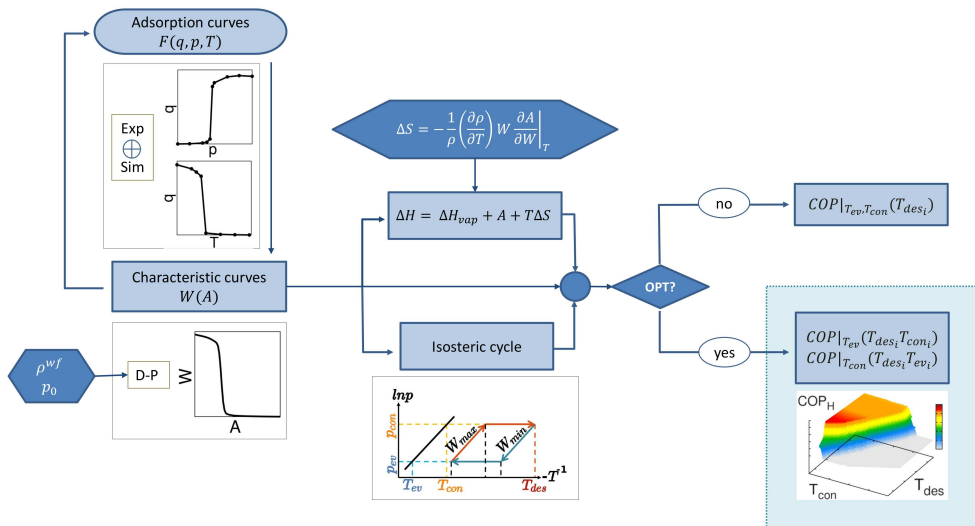


**Figure 3.** Schematic algorithm of the designed multistep process.

### 7.3 RESULTS AND DISCUSSION

The first set of calculations was used to test the suitability of the force field to reproduce the experimental adsorption of these polar molecules in the selected MOFs. We calculated the adsorption isotherms of methanol and ethanol to compare with reported experimental data for ZIF-8,<sup>44,50</sup> ZIF-71,<sup>50</sup> MIL-140C,<sup>44</sup> ZIF-90,<sup>50</sup> and MAF-6.<sup>51</sup> Figure 4 shows that the computed and experimental adsorption isotherms are in line. We found small discrepancies on the onset pressures of ZIF-90 and ZIF-71. This can be due to the

choice of a generic force field, which has not been refined for a particular adsorbent-adsorbate pair. We found larger deviations for the adsorption isotherms of the two alcohols in MIL-140C, overestimating the adsorption capacity of methanol and underestimating the adsorption capacity of ethanol. Regarding this mixing behaviour, we cannot rule out any flexibility effect of the MOF, neglected in the simulations. However, the general behaviour of all isotherms is well described by the selected force field, making it suitable for studying the adsorption of alcohols in zeolitic imidazolate frameworks.

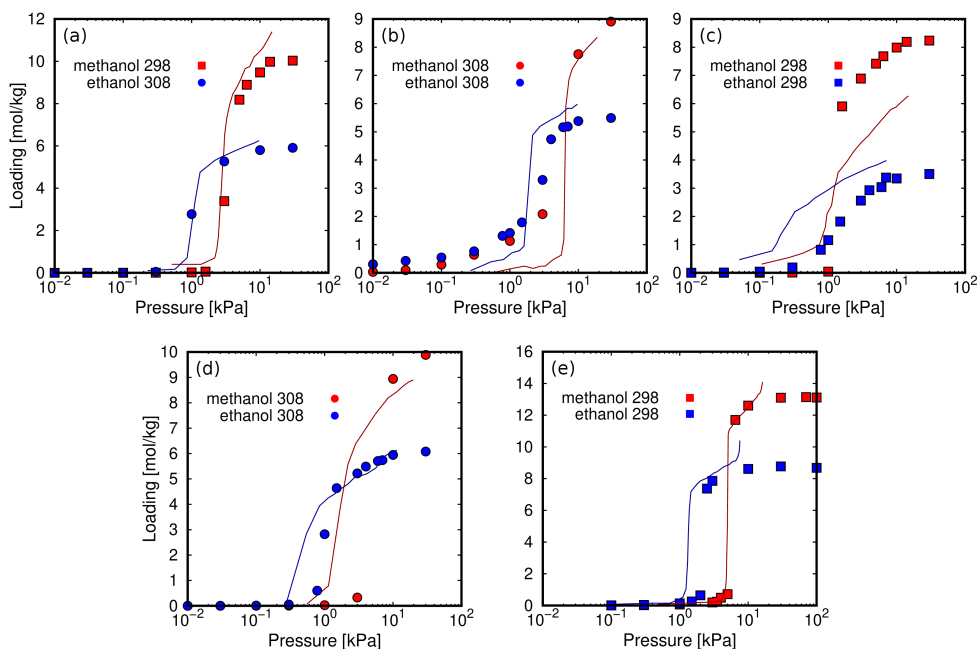


**Figure 4.** Computed adsorption isotherms (symbols) of methanol (red) and ethanol (blue) in (a) ZIF-8, (b) ZIF-71, (c) MIL-140C, (d) ZIF-90 and (e) MAF-6 at different temperatures, 298K (squares) and 308K (circles). The experimental values (solid lines) are taken from the literature.<sup>44,50,51</sup>

Figure 5 compares the adsorption isotherms at room temperature. The adsorption isotherms of methanol and ethanol in ZIF-8 and ZIF-90, which have SOD topology, show very similar behaviour. This can be explained in terms of similar structural properties and composition (see Table 1). The other pair of adsorbents that share the RHO topology are ZIF-71 and MAF-6. The presence of chlorine atoms in ZIF-71 have significant effects on the adsorption. Compared to MAF-6 we observe a decrease of the adsorption capacity and a slight attenuation of the abrupt step caused by the higher hydrophilic degree. In addition, the highly hydrophobic MAF-6 shows the highest adsorption capacity for both adsorbates among the studied structures. MIL-140C shows the lowest ethanol capacity while the adsorbed methanol is comparable to that obtained in the other MOFs. This is due to more effective packing of methanol than ethanol within the small channels of MIL-140C, directly related with the kinetic diameters,  $3.6\text{\AA}$  and  $4.3\text{\AA}$ , respectively.<sup>86</sup> The maximum adsorption capacity can be related to the pore volume ( $V_p$ ) of the adsorbent. Thus Figure 5c shows a clear hierarchy:  $MAF-6 > ZIF-8 \approx ZIF-90 > ZIF-71 > MIL-140C$ .

The adsorption isotherms calculated for ZIF-8, ZIF-90, and MAF-6 have a steeped behaviour, less prominent for ZIF-71 and MIL-140C. This is due to the strong guest-guest interactions of the adsorbates inside the pores, typical characteristic of

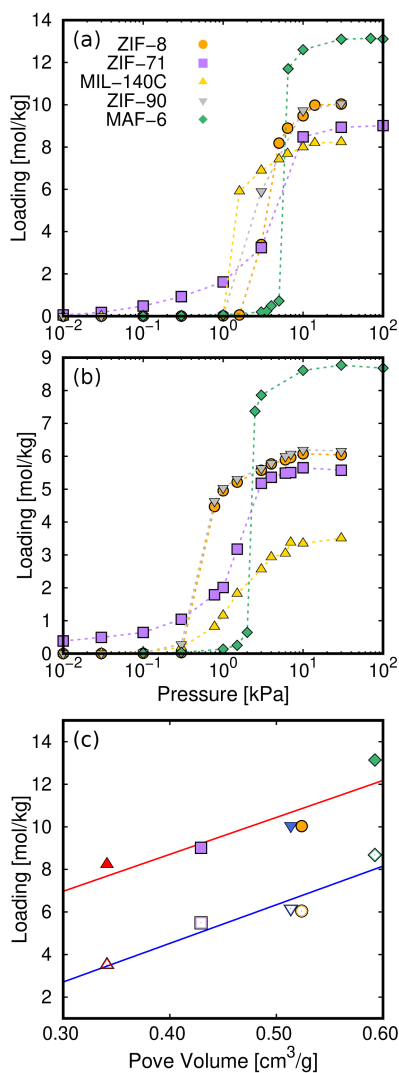


**Figure 5.** Computed adsorption isotherms of (a) methanol and (b) ethanol at 298 K. Saturation capacity (c) of methanol (closed symbols) and ethanol (open symbols) as a function of pore volume. The solid lines in (c) stands for the fitted values to a straight line showing the dependence of loading with the pore volume.

hydrophobic materials. These interactions are driven by hydrogen bonds (HB). Figures 6a and 6b show the average num-

ber of hydrogen bonds per molecule (nHB) as a function of pressure. In the onset pressure where the adsorption occurs we found an abrupt increase in nHB. At high loading the nHB is similar confinement to that in the bulk.<sup>79</sup> We found exceptions for methanol and ethanol in ZIF-71 and ethanol and in MIL-140C. In the case of ZIF-71, the reason is the type of organic ligand. The atoms of chlorine are partially placed in the large cage, and this reduces the hydrophobicity degree of the structure. This is reflected in the shape of the adsorption isotherm and in the reduction of the hydrogen bond network within the cavities. In the case of MIL-140C the reason is the shape and size of the framework. It is the only channel-shaped structure studied here. The other MOF are cage-shaped. The number of hydrogen bonds per ethanol molecule is lower in MIL-140C, while for methanol it is similar to the rest of the MOFs. In addition to the average number of hydrogen bonds, Figure A5.2 of the appendix 5 shows that the structure of these hydrogen bonds changes in confinement, with a competition between molecules of alcohol with one or two HBs. The effect of hydrogen bonds is reflected in the guest-guest potential energy ( $U_{GG}$ ) as a function of external pressure obtained from isotherms at 298 K (Figures 6c and 6d). The similarities in the adsorption isotherms, nHB, and guest-guest interaction energy confirms that the adsorption mechanism is driven by the nucleation of the polar molecules through hydrogen

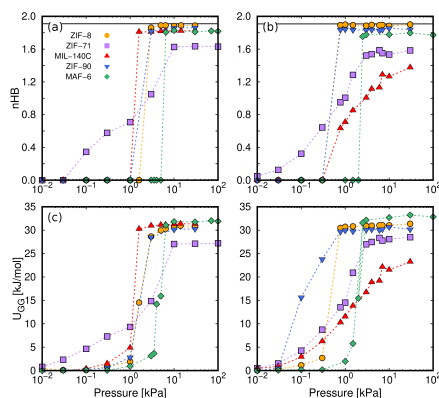


**Figure 6.** nHB (a,b) and guest-guest interactions (c,d) of methanol (left) and ethanol (right) as a function of external pressure. Non-depicted error bars denote fluctuations smaller than the symbol size. The black lines in (a,b) represent the nHB of methanol and ethanol in the bulk.

bond interactions. This behaviour is similar to that found in the adsorption of other polar compounds such as ammonia on adsorbents with large cavities.<sup>87</sup>

The remaining energy contribution is that corresponding to the interaction between guest molecules and adsorbents, as shown in Figure 7. The affinity between the adsorbates and the internal surface of the framework increases with the host-guest energy. Host-guest interactions generally weaken with loading as preferential adsorption sites fill up and guest-guest interactions become more important. Adsorption onset pressure is strongly related to host-guest interactions,<sup>88</sup> surface area of the structure and the kinetic diameter of the adsorbate. Pressure below the step in the adsorption isotherm (see Figures 4 and 5) represent the infinite dilu-

tion regime. We identify this regime with a reduction in host-guest energy of all the structures except MIL-140C. The host-guest energy of the two adsorbates is almost a constant value throughout the pressure range, because of the size and shape of the cavities of this MOF. MIL-140C has one-dimensional triangular-shaped channels of about 6 Å, (see Figure 1) that hinder the nucleation of the alcohol molecules, thus maintaining the same host-guest energy. The low coverage host-guest energy is approximately double for ZIF-71 and MAF-6 than for ZIF-8 and ZIF-90, due to the interaction of the first molecules entering the structures with specific binding sites. Methanol and ethanol first interact with the exposed chlorine atoms of the dichloroimidazole link of ZIF-71. As for MAF-6, the alcohol molecules interact with the aromatic rings of the ligand by electrostatic interactions, where the hydroxyl group aligns with the electrostatic field lines pointing towards the center of the ring.<sup>79</sup> After the step in the adsorption isotherm, the host-guest energy decreases to a constant minimum value, while the guest-guest energy reaches the maximum value in the same pressure interval (Figure 6c,d). This transition from host-guest to guest-guest interactions points to the nucleation of molecules in hydrophobic MOFs with large pores. Similarly, this energy exchange is the origin of the energy released during the adsorption process, which govern the AHP and ACS devices.

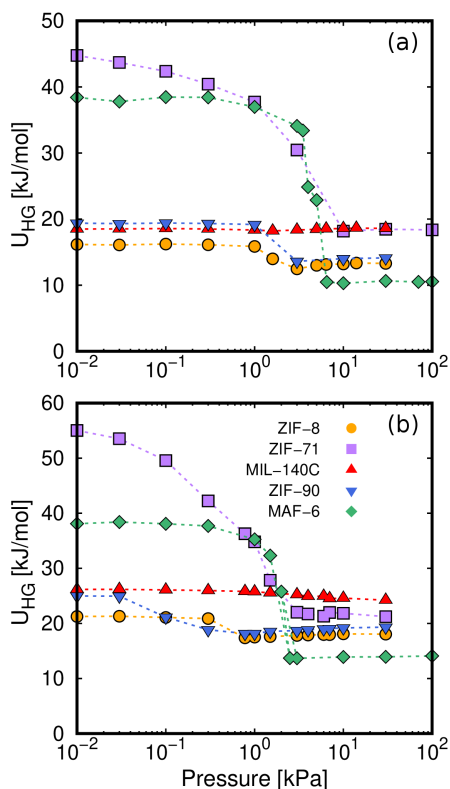


**Figure 7.** Host-guest interactions of methanol (a) and ethanol (b) as a function of external pressure in selected MOFs.

For realistic applications it is important to maximize the thermodynamic efficiency of the system.<sup>89</sup> One of the key aspects in the design of AHP and ACS devices is the choice of the operating conditions. The thermodynamic cycle (Figure 2) involves two isobaric and two isosteric steps, hence, it is convenient to analyze the adsorption isobars in addition to the adsorption isotherms described. It is desirable from an energetic point of view to have an adsorption isobar with a single and steep step. It is known that small vari-

ations in the regeneration conditions can lead to large changes in performance.<sup>45</sup> In this regard, we use pressure control as a mechanism to improve efficiency. The working pressure is based on the onset pressure of the adsorption isotherm at room temperature. The pressure is established for each working pair as the lowest value of pressure that ensures high uptake (immediately after the step in the adsorption isotherm at 298 K). We calculated the adsorption isobars of methanol and ethanol at the selected pressures (Figure 8). Table A5.1 (Appendix 5) summarizes the temperature and pressure conditions of the adsorption isotherms and isobars calculated in this work. Figure 8 shows the adsorption isobars of (a) methanol and (b) ethanol on selected MOFs. These isobars give an idea of the regeneration temperature for each working pair at the chosen operating conditions. The slope in the desorption isobar is a first indication of the efficiency and performance of a particular working pair. The temperature window for the desorption process is in the range of 300 – 340 K depending on the working pair. Above this temperature all structures have released most of the methanol and ethanol load.

The next stage of our multistep process is the post-processing of the adsorption data using the thermodynamic model. Here, the characteristic curve of adsorption is critical as we can extract a set of relevant quantities from this reduced representation of the adsorption data. As

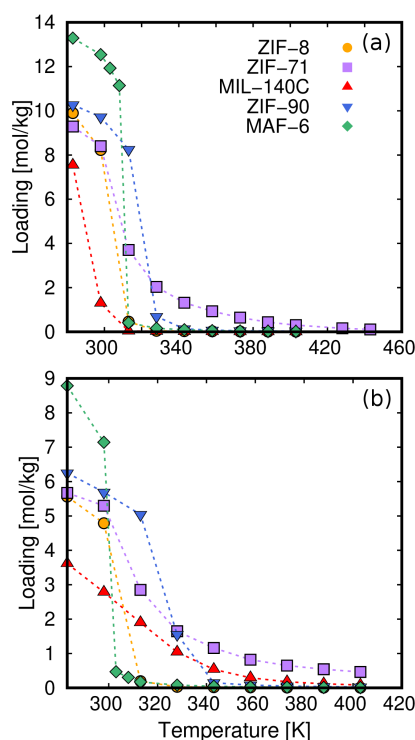


**Figure 8.** Calculated adsorption isobars of (a) methanol and (b) ethanol at the selected working pressures shown in Table A5.1. (Appendix 5)

described in the methodology section, the DP theory relates the adsorption potential ( $A$ ) and the amount of adsorbed volume ( $W$ ). One of the limitations, is the assumption of the temperature invariance of  $W$ . To ensure the applicability of the DP theory all calculated adsorption isotherms and isobars (see Table A5.1 of the Appendix 5) must converge to the same characteristic curve. Figure 9 shows the characteristic curves of the working pairs from all the calculated adsorption curves. The agreement of the different transforma-

tions indicates the suitability of the DP theory in the systems under study. We can then use the characteristic curve to calculate any adsorption equilibrium relation for a given operating conditions, since any combination of  $(p, T)$  is related via  $A$  to the working volume, and therefore to

the loading. We confirmed this interesting property of the characteristic curve by predicting adsorption isotherms at different temperatures (Figure A5.3, Appendix 5) and one adsorption isobar for each working pair (Figure A5.4, Appendix 5).

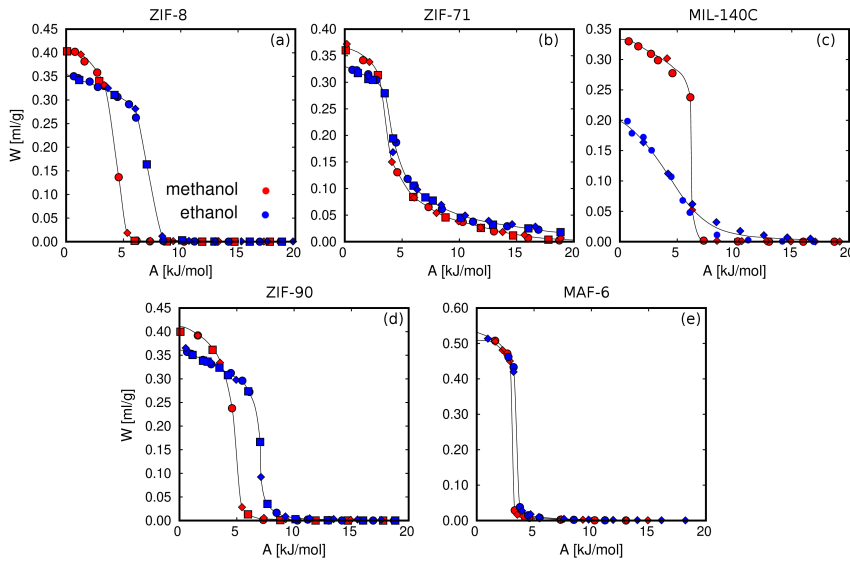


**Figure 9.** Characteristic curves determined from the calculated adsorption isotherms and isobars. The lines correspond to fit curves obtained by splines.

To verify the validity of our approach we compute relevant properties for the AHP and ACS devices. Figure 10 shows a comparison with the data from de Lange *et al.*<sup>44</sup> Figure 10a shows characteristic curves of methanol and ethanol in ZIF-8. It can be seen that for both working fluids, the characteristic curves are similar in shape and maximum capacity. The small differences are due to the choice of density,

taken as an approximation by de Lange *et al.*<sup>44</sup> and using Hauer's model. Figure 10b shows the enthalpy or heat of adsorption as a function of loading. The experimental  $\Delta H$  have been obtained using the Clausius Clapeyron method<sup>90,91</sup> while in this work we used the the Dubinin-Polanyi theory. Figure 10c shows the COPs for the two working fluids using the operating conditions specified by de Lange *et al.*,<sup>44</sup> That

is,  $T_{ev} = 278K$  and  $T_{con} = 303K$  for ACS and  $T_{ev} = 288K$  and  $T_{con} = 318K$  for AHP. The results agree very well, with only a small deviation due to density choices,  $\Delta H$  calculation method, or saturation pressure. Finally, Figure 10d shows the heat released in the condenser ( $Q_{con}$ ) with  $T_{con} = 298K$  and assuming maximum desorption. We found a reasonable agreement compared to the experimental values (circa 15% and 5% difference), considering the different methodology used in this work. We can then conclude that the choice of methodology is suitable to study the performance of porous materials for AHP and ACS applications.

The COP for the cooling and heating processes using methanol and ethanol allows to compare the performance of the adsorbents (Figure A5.5 of the Appendix 5). Similar to Figure 10c), The COP increases to a maximum value over a temperature range of about 320–340K, then decreases linearly as temperature increases. The optimal desorption temperature must be chosen to ensure complete regeneration of the material, avoiding unnecessary overheating and wasted energy. Methanol generally shows a slightly higher value than ethanol over the entire temperature range. An exception seems to be that of the COP (cooling) in MAF-6, where for methanol we find a maximum COP close to 0.9 and for ethanol it barely reaches 0.2. However, this low value is not an adequate indication of the performance of the material but rather a consequence of the setting

of the operating conditions. Figures 10c and 11 show a typical representation of the COP values, that is, varying the desorption temperature, but fixing the temperatures of the evaporator and condenser, respectively. To clarify this issue, Figure 11 shows the COP for cooling of ethanol in MAF-6, setting the temperature of the condenser to 288K, and for two nearby values of the temperature of the evaporator, 273 and 278K. We can see that variation of five degrees on the operating conditions drastically changes the performance of the working pair.

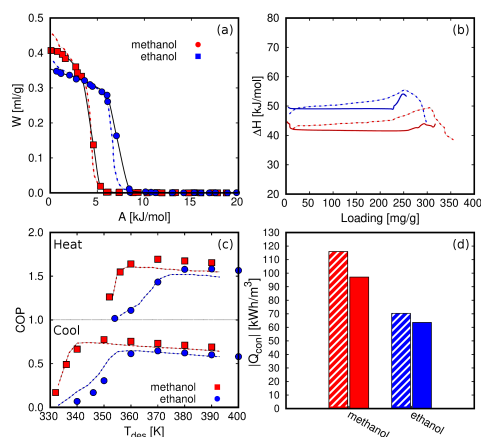


**Figure 10.** Characteristic curves of methanol and ethanol in ZIF-8. The points correspond to simulations and the black lines to the fit. (b) Heat of adsorption of methanol and ethanol in ZIF-8 using Dubinin-Polanyi. (c) COP of methanol and ethanol as a function of desorption temperature. (d)  $Q_{con}$  of methanol and ethanol in ZIF-8 at  $T_{con} = 298K$ . The red lines and symbols correspond to methanol and the blue lines and symbols to ethanol. The dashed lines are for values obtained from the literature<sup>44</sup> while the solid lines are for those calculated in this work.

The effect shown in Figure 11 is more noticeable for materials depicting steeped adsorption isotherms or isobars. However, steep adsorption is desired for these applications when complete regeneration of the thermodynamic cycle occurs in a small increase of temperature or pressure. To avoid misinterpretation of performance analysis, we suggest to deeply examine each working pair and reduce the number of fixed parameters. Using the proposed multistep process, we iteratively calculate the targeted properties for all the possible working temperatures. In this way, instead of having a single relationship between the COP and desorption temperature (Figure 11), we obtain a complex data set that shows the evolution of the COP. This is done by simultaneously varying all the operating temperatures of the thermodynamic cycle. Figure 12 represents the COP for cooling of ethanol in MAF-6 as a function of the temperature

of the condenser, evaporator, and desorption. From this data set, we can extract the values of the range of operating conditions that maximize the COP. In this case, the ethanol adsorption in MAF-6 shows a maximum COP of 0.84–0.86 at  $T_{ev} = 275 - 285\text{ K}$ ,  $T_{con} = 278 - 288\text{ K}$ , and  $T_{des} = 300 - 315\text{ K}$ .

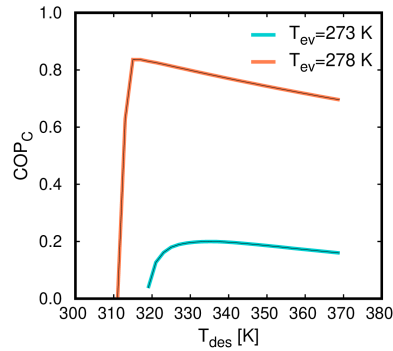


**Figure 11.** Coefficient of performance (cooling) of ethanol in MAF-6 as a function of desorption temperature, fixing the temperature of the evaporator at 273 K and 278 K, respectively. The temperature of the condenser is fixed at  $T_{con} = 288\text{ K}$ .

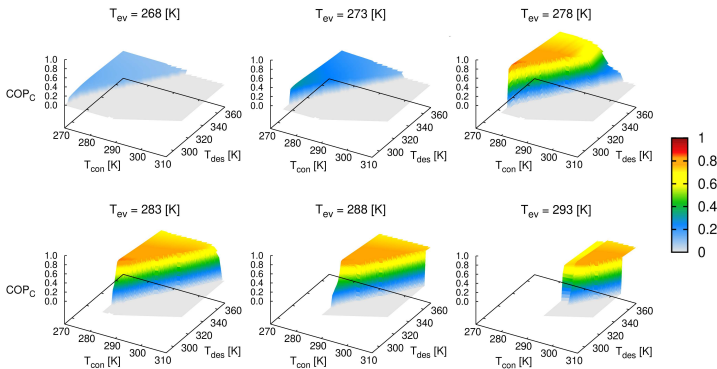


**Figure 12.** Evolution of the coefficient of performance (cooling) of ethanol in MAF-6 by varying the operating temperatures of the thermodynamic cycle (see Figure 2).

To compare the results obtained in the five MOFs, Figure 13 shows the COP for cooling, setting the temperature of the evaporator to  $278\text{K}$ . This temperature is within the range of operating conditions for cooling applications, and all working pairs reach the optimum level of COP values. As in Figure A5.5, methanol performs better than ethanol for cooling applications, which could be due to better molecular packaging leading to a higher adsorption capacity. The superior performance of MAF-6 compared to the other the adsorbents is remarkable. The high adsorption capacity and especially steeped adsorption behaviour make this MOF outperform the rest under study for AHP and ACS applications.

Another relevant property shown in Figure 10d) is the heat energy transferred to the condenser ( $Q_{con}$ ). Figures 14a) and b) compile the  $Q_{con}$  of methanol and ethanol for the five MOFs. It can be seen that methanol releases more energy than ethanol. The volumetric energy released in the condenser shows similar values for heating and cooling applications. Again, the exception to the rule is the value of ethanol in MAF-6 for cooling applications, for the same reasons as for COP. We obtained the  $Q_{con}$  assuming a complete regeneration of the cycle, *i.e.*, maximum desorption of the adsorbates. This means that the only temperatures that affect the calculation of  $Q_{con}$  are those of the evaporator and condenser. To get a broader overview of the variation of  $Q_{con}$  of metha-

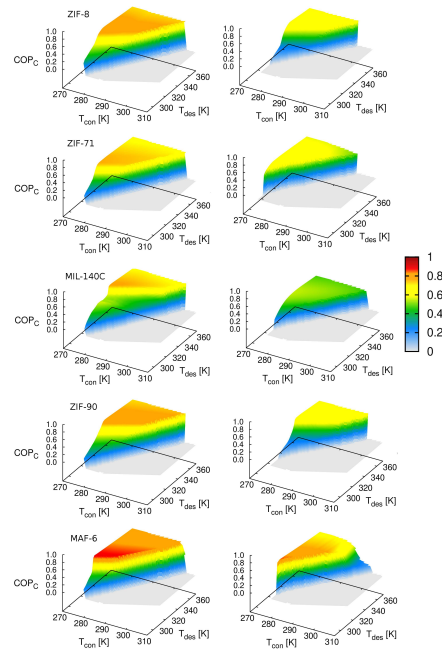


**Figure 13.** Coefficient of performance (cooling) of methanol (left column) and ethanol (right column) by varying the operating temperatures of the thermodynamic cycle (see Figure 2). The temperature of the evaporator is fixed at  $T_{ev} = 278\text{K}$ .

anol and ethanol with operating temperatures, we plot  $Q_{con}$  as a function of  $T_{con}$  and  $T_{ev}$  in Figures 14c) and d). We chose MAF-6 as the reference MOF due to its higher performance compared to the other MOFs studied here. In line with the adsorption isotherms and isobars, MAF-6 shows a pronounced  $Q_{con}$ , suggesting the importance of choosing the working conditions. After the step, all the curves converge to a similar maximum  $Q_{con}$  value, which is the optimal value for each working pair. In general, all the working pairs studied here show a good performance for

AHP and ACS applications. However, the best choice would be MAF-6, taking into account the energy release, the coefficient of performance, and the highest adsorption capacity.

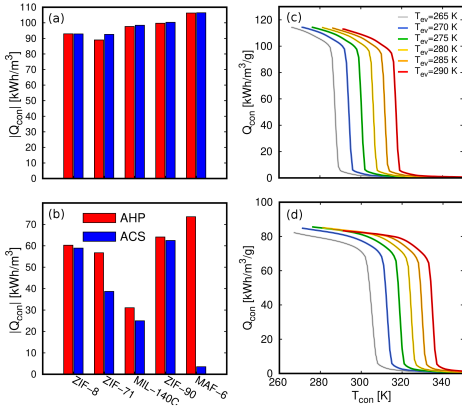


**Figure 14.** Volumetric heat energy transferred to the condenser per unit of volume of MOF using (a) methanol and (b) ethanol for AHP (red) with  $T_{ev} = 273\text{ K}$  and  $T_{con} = 288\text{ K}$  and ACS (blue)  $T_{ev} = 283\text{ K}$  and  $T_{con} = 298\text{ K}$ . Volumetric heat energy transferred to the condenser per unit of volume of MOF using (c) methanol and (d) ethanol in MAF-6 with variation of the temperature of the evaporator assuming full desorption

## 7.4 CONCLUSIONS

We shed light on the mechanisms that govern the adsorption-driven heat pumps for heating and cooling applications using MOFs and light alcohols. We examined and compared the performance of five MOFs using methanol and ethanol as working fluids. The adsorption isotherms and isobars, the energetic interactions between molecules and adsorbents, and

the nucleation of the fluids in confinement were calculated from GCMC simulation. Adsorption data was processed using mathematical modeling based on the Dubinin-Polanyi theory of adsorption and a thermodynamic model to describe relevant properties for heating and cooling applications. Finally, we proposed a multistep approach to analyze the relationships between performance and operating conditions, which allows describing the optimal working conditions for each adsorbent-fluid pair. All MOFs selected in this work, combined with methanol, show high performance for AHP and ACS applications. The performance coefficients were above 0.8 for cooling and 1.8 for heating. The energy released to the condenser was above  $90\text{ kWh/m}^3$ . The performance associated with ethanol adsorption is lower than for methanol but still significant for MAF-6. This MOF outperforms the other adsorbents studied here for AHP and ACS applications in a wide range of operating conditions. It exhibits COP above 0.9 and 1.9 for cooling and heating, respectively, and  $Q_{con} 115\text{ kWh/m}^3$  for methanol. With a pore size of about  $18\text{ \AA}$  and relatively low density, the hydrophobic MAF-6 exhibits large pore volume and surface area, resulting in a steeped isotherm and large adsorption capacity for light alcohols.

Overall, the multistep process proposed here seems to be an efficient tool for analyzing the performance of working pairs for heating and cooling applications. We have demonstrated the im-

portance of removing constraints for applying the thermodynamic model. Establishing or assuming fixed values of certain operating temperature could lead to misinterpretation of the performance of the working pairs. This is particularly remarkable for systems showing steeped isotherms, which at the same time are desired for these applications. An increase of temperature of a few degrees could decrease by 80% the performance of a working pair. Another advantage of the proposed approach is that it only needs an adsorption isobar or isotherm as input. This approach can be combined with simulation data or experimental measurements since we employed mathematical modeling to post-process the adsorption data. We have shown that we can simultaneously describe experimental results from the literature with high accuracy and predict various properties involved in heating and cooling applications.

## 7.5 BIBLIOGRAPHY

- [1] Sayadi, S.; Tsatsaronis, G.; Morosuk, T.; Baranski, M.; Sangi, R.; Muller, D. *Journal of Cleaner Production* **2019**, *241*, 118277.
- [2] Pérez-Lombard, L.; Ortiz, J.; Pout, C. *Energy and Buildings* **2008**, *40*, 394–398.
- [3] Isaac, M.; van Vuuren, D. P. *Energy Policy* **2009**, *37*, 507–521.
- [4] Hu, X.; Cai, M.; Yang, S.; Sejas, S. A. *Sci. China Earth Sci.* **2018**, *61*, 1491–1509.
- [5] Joos, F. *Nature* **2015**, *522*, 295.
- [6] Govindasamy, B.; Thompson, S.; MIRIN, A.; WICKETT, M.; CALDEIRA, K.; DELIRE, C. *Tellus B* **2005**, *57*, 153–163.
- [7] Hay, C. C.; Morrow, E.; Kopp, R. E.; Mitrovica, J. X. *Nature* **2015**, *517*, 481–484.
- [8] Liu, D.; Guo, X.; Xiao, B. *Sci. Total Environ.* **2019**, *661*, 750–766.
- [9] Coumou, D.; Robinson, A.; Rahmstorf, S. *Clim. Change* **2013**, *118*, 771–782.
- [10] Elsheikh, A.; Sharshir, S.; Mostafa, M. E.; Essa, F.; Ahmed Ali, M. K. *Renewable and Sustainable Energy Reviews* **2018**, *82*, 3483–3502.
- [11] Proszak-MiÅŁsik, D.; Rybak-Wilusz, E.; Rabczak, S. *Journal of Ecological Engineering* **2020**, *21*, 1–7.
- [12] Sharma, A.; Tyagi, V.; Chen, C.; Buddhi, D. *Renewable and Sustainable Energy Reviews* **2009**, *13*, 318–345.
- [13] Kumar, A.; Prakash, O.; Kaviti, A. K. *Renewable and Sustainable Energy Reviews* **2017**, *77*, 890–898.
- [14] Kannan, N.; Vakeesan, D. *Renewable and Sustainable Energy Reviews* **2016**, *62*, 1092–1105.
- [15] Wojdyga, K. *Energy and Buildings* **2008**, *40*, 2009–2014.
- [16] Chua, K.; Chou, S.; Yang, W. *Applied Energy* **2010**, *87*, 3611–3624.
- [17] Kuyper, B. et al. *Environmental Science & Technology* **2019**, *53*, 8967–8975, PMID: 31251602.
- [18] Wongwises, S.; Chimres, N. *Energy Conversion and Management* **2005**, *46*, 85–100.
- [19] Hu, L. et al. *Geophysical Research Letters* **2017**, *44*, 8075–8083.
- [20] Teker, M.; İmamođlu, M.; Saltabaş, Ö. *Turk. J. Chem.* **1999**, *23*, 185–192.
- [21] Cacciola, G.; Restuccia, G.; Mercadante, L. *Carbon* **1995**, *33*, 1205–1210.
- [22] Critoph, R. E. *Carbon* **1989**, *27*, 63–70.
- [23] Wang, L.; Wu, J.; Wang, R.; Xu, Y.; Wang, S.; Li, X. *Applied Thermal Engineering* **2003**, *23*, 1605–1617.
- [24] Kohler, T.; Muller, K. *Energy Science & Engineering* **2017**, *5*, 21–29.
- [25] Trager, L.; Glasel, J.; Scherle, M.; Hartmann, J.; Nieken, U.; Etzold, B. J. M. *Chemical Engineering & Technology* **2020**, *43*, 1876–1883.
- [26] Tamainot-Telto, Z.; Critoph, R. *Applied Thermal Engineering* **2001**, *21*, 37–52.
- [27] El-Sharkawy, I. I.; Pal, A.; Miyazaki, T.; Saha, B. B.; Koyama, S. *Applied Thermal Engineering* **2016**, *98*, 1214–1220.
- [28] Askalany, A. A.; Henninger, S. K.; Ghazy, M.; Saha, B. B. *Applied Thermal Engineering* **2017**, *110*, 695–702.
- [29] Capri, A.; Frazzica, A.; Calabrese, L. *Coatings* **2020**, *10*.
- [30] Critoph, R. E.; Zhong, Y. *Proceedings of the Institution of Mechanical Engineers, Part E: Journal of Process Mechanical Engineering* **2005**, *219*, 285–300.
- [31] Freni, A.; Maggio, G.; Sapienza, A.; Frazzica, A.; Restuccia, G.; Vasta, S. *Applied Thermal Engineering* **2016**, *104*, 85–95.
- [32] Calabrese, L.; Brancato, V.; Bonaccorsi, L.; Frazzica, A.; Capri, A.; Freni, A.; Proverbio, E. *Applied Thermal Engineering* **2017**, *116*, 364–371.
- [33] Zheng, X.; Wang, R.; Ge, T.; Hu, L. *Energy* **2015**, *93*,

88–94.

- [34] Freni, A.; Bonaccorsi, L.; Calabrese, L.; Capri, A.; Frazzica, A.; Sapienza, A. *Applied Thermal Engineering* **2015**, *82*, 1–7.
- [35] Atakan, A.; Fueeldner, G.; Munz, G.; Henninger, S.; Tatlier, M. *Applied Thermal Engineering* **2013**, *58*, 273–280.
- [36] Tatlier, M. *Heat Mass Transf.* **2021**, *57*, 975–984.
- [37] de Lange, M. F.; Verouden, K. J. F. M.; Vlugt, T. J. H.; Gascon, J.; Kapteijn, F. *Chemical Reviews* **2015**, *115*, 12205–12250, PMID: 26492978.
- [38] Henninger, S. K.; Ernst, S.-J.; Gordeeva, L.; Bendix, P.; Fröhlich, D.; Grekova, A. D.; Bonaccorsi, L.; Aristov, Y.; Jaenchen, J. *Renewable Energy* **2017**, *110*, 59–68, Increasing the renewable share for heating and cooling by the means of sorption heat pumps and chillers.
- [39] Kummer, H.; Jeremias, F.; Warlo, A.; Fuldner, G.; Fröhlich, D.; Janiak, C.; Gläser, R.; Henninger, S. K. *Industrial & Engineering Chemistry Research* **2017**, *56*, 8393–8398.
- [40] Jeremias, F.; Fröhlich, D.; Janiak, C.; Henninger, S. K. *RSC Adv.* **2014**, *4*, 24073–24082.
- [41] Steinert, D. M.; Ernst, S.-J.; Henninger, S. K.; Janiak, C. *European Journal of Inorganic Chemistry* **2020**, *2020*, 4502–4515.
- [42] Pinheiro, J. M.; Salústio, S.; Geraldes, V.; Valente, A. A.; Silva, C. M. *Applied Thermal Engineering* **2020**, *178*, 115498.
- [43] Pal, A.; Thu, K.; Mitra, S.; El-Sharkawy, I. I.; Saha, B. B.; Kil, H.-S.; Yoon, S.-H.; Miyawaki, J. *International Journal of Heat and Mass Transfer* **2017**, *110*, 7–19.
- [44] de Lange, M. F.; van Velzen, B. L.; Ottevanger, C. P.; Verouden, K. J. F. M.; Lin, L.-C.; Vlugt, T. J. H.; Gascon, J.; Kapteijn, F. *Langmuir* **2015**, *31*, 12783–12796, PMID: 26523608.
- [45] Li, W.; Xia, X.; Cao, M.; Li, S. *J. Mater. Chem. A* **2019**, *7*, 7470–7479.
- [46] Erdos, M.; de Lange, M. F.; Kapteijn, F.; Moulτος, O. A.; Vlugt, T. J. H. *ACS Applied Materials & Interfaces* **2018**, *10*, 27074–27087, PMID: 30024724.
- [47] Jeremias, F.; Fröhlich, D.; Janiak, C.; Henninger, S. K. *New J. Chem.* **2014**, *38*, 1846–1852.
- [48] Kayal, S.; Baichuan, S.; Saha, B. B. *International Journal of Heat and Mass Transfer* **2016**, *92*, 1120–1127.
- [49] Cambridge Crystallographic Data Centre.
- [50] Zhang, K.; Lively, R. P.; Dose, M. E.; Brown, A. J.; Zhang, C.; Chung, J.; Nair, S.; Koros, W. J.; Chance, R. R. *Chem. Commun.* **2013**, *49*, 3245–3247.
- [51] He, C.-T.; Jiang, L.; Ye, Z.-M.; Krishna, R.; Zhong, Z.-S.; Liao, P.-Q.; Xu, J.; Ouyang, G.; Zhang, J.-P.; Chen, X.-M. *Journal of the American Chemical Society* **2015**, *137*, 7217–7223, PMID: 25985194.
- [52] Keinath, C. M.; Garimella, S.; Garrabrant, M. A. *International Journal of Refrigeration* **2017**, *83*, 39–50.
- [53] Luna-Triguero, A.; Slawek, A.; Huinink, H. P.; Vlugt, T. J. H.; Poursaeidesfahani, A.; Vicent-Luna, J. M.; Calero, S. *ACS Applied Nano Materials* **2019**, *2*, 3050–3059.
- [54] Álvarez, J. R.; Sánchez-González, E.; Pérez, E.; Schneider-Revueltas, E.; Martínez, A.; Tejada-Cruz, A.; Islas-Jácome, A.; González-Zamora, E.; Ibarra, I. A. *Dalton Trans.* **2017**, *46*, 9192–9200.
- [55] Madero-Castro, R. M.; Vicent-Luna, J. M.; Peng, X.; Calero, S. *ACS Sustainable Chemistry & Engineering* **2022**, *10*, 6509–6520.
- [56] Sann, E. E.; Pan, Y.; Gao, Z.; Zhan, S.; Xia, F. *Separation and Purification Technology* **2018**, *206*, 186–191.
- [57] Calero, S.; Gómez-Álvarez, P. *The Journal of Physical Chemistry C* **2015**, *119*, 23774–23780.
- [58] Van deãVoorde, B.; DamascenoãBorges, D.; Vermoortele, F.; Wouters, R.; Bozbiyik, B.; Denayer, J.; Taulelle, F.; Martineau, C.; Serre, C.; Maurin, G.; DeãVos, D. *ChemSusChem* **2015**, *8*, 3159–3166.
- [59] He, C.-T.; Jiang, L.; Ye, Z.-M.; Krishna, R.; Zhong, Z.-S.; Liao, P.-Q.; Xu, J.; Ouyang, G.; Zhang, J.-P.; Chen, X.-M. *Journal of the American Chemical Society* **2015**, *137*, 7217–7223, PMID: 25985194.
- [60] Pacheco, R.; Silva, C. *Energies* **2019**, *12*.
- [61] Li, W.; Xia, X.; Li, S. *ACS Applied Materials & Interfaces* **2020**, *12*, 3265–3273, PMID: 31865693.
- [62] Xia, X.; Liu, Z.; Li, S. *Applied Thermal Engineering* **2020**, *176*, 115442.
- [63] Park, K. S.; Ni, Z.; Côté, A. P.; Choi, J. Y.; Huang, R.; Uribe-Romo, F. J.; Chae, H. K.; O’Keeffe, M.; Yaghi, O. M. *Proc. Natl. Acad. Sci. U. S. A.* **2006**, *103*, 10186–10191.
- [64] Shieh, F.-K.; Wang, S.-C.; Leo, S.-Y.; Wu, K. C. *Chemistry - A European Journal* **2013**, *19*, 11139–11142.
- [65] Liu, S.; Liu, G.; Zhao, X.; Jin, W. *Journal of Membrane Science* **2013**, *446*, 181–188.
- [66] Guillermin, V.; Ragon, F.; Dan-Hardi, M.; Devic, T.; Vishnuvarthan, M.; Campo, B.; Vimont, A.; Clet, G.; Yang, Q.; Maurin, G.; Férey, G.; Vittadini, A.; Gross, S.; Serre, C. *Angew. Chem. Int. Ed Engl.* **2012**, *51*, 9267–9271.
- [67] Dubbeldam, D.; Calero, S.; Ellis, D. E.; Snurr, R. Q. *Molecular Simulation* **2016**, *42*, 81–101.
- [68] Dubbeldam, D.; Torres-Knoop, A.; Walton, K. S. *Molecular Simulation* **2013**, *39*, 1253–1292.
- [69] Boda, D.; Henderson, D. *Molecular Physics* **2008**, *106*, 2367–2370.
- [70] Darden, T.; York, D.; Pedersen, L. *The Journal of Chemical Physics* **1993**, *98*, 10089–10092.
- [71] Stubbs, J. M.; Potoff, J. J.; Siepmann, J. I. *The Journal of Physical Chemistry B* **2004**, *108*, 17596–17605.
- [72] Banerjee, R.; Phan, A.; Wang, B.; Knobler, C.; Furukawa, H.; O’Keeffe, M.; Yaghi, O. M. *Science* **2008**, *319*, 939–943.
- [73] Morris, W.; Doonan, C. J.; Furukawa, H.; Banerjee, R.; Yaghi, O. M. *J. Am. Chem. Soc.* **2008**, *130*, 12626–12627.
- [74] Huang, X.-C.; Lin, Y.-Y.; Zhang, J.-P.; Chen, X.-M. *Angew. Chem. Int. Ed Engl.* **2006**, *45*, 1557–1559.
- [75] Mayo, S. L.; Olafson, B. D.; Goddard, W. A. *The Journal of Physical Chemistry* **1990**, *94*, 8897–8909.

- [76] Rappe, A. K.; Casewit, C. J.; Colwell, K. S.; Goddard, W. A. I.; Skiff, W. M. *Journal of the American Chemical Society* **1992**, *114*, 10024–10035.
- [77] Ongari, D.; Boyd, P. G.; Kadioglu, O.; Mace, A. K.; Keskis, S.; Smit, B. *Journal of Chemical Theory and Computation* **2019**, *15*, 382–401, PMID: 30419163.
- [78] Gutierrez-Sevillano, J. J.; Calero, S.; Ania, C. O.; Parra, J. B.; Kapteijn, F.; Gascon, J.; Hamad, S. *The Journal of Physical Chemistry C* **2013**, *117*, 466–471.
- [79] Madero-Castro, R. M.; Vicent-Luna, J. M.; Calero, S. *The Journal of Physical Chemistry C* **2019**, *123*, 23987–23994.
- [80] *Enthalpies of vaporization of organic compounds: a critical review and data compilation.*
- [81] Lehmann, C.; Beckert, S.; Gläser, R.; Kolditz, O.; Nagel, T. *Applied Energy* **2017**, *185*, 1965–1970, Clean, Efficient and Affordable Energy for a Sustainable Future.
- [82] Lehmann, C.; Beckert, S.; Nonnen, T.; Möllmer, J.; Gläser, R.; Kolditz, O.; Nagel, T. *Energy Procedia* **2017**, *105*, 4334–4339, 8th International Conference on Applied Energy, ICAE2016, 8-11 October 2016, Beijing, China.
- [83] Peng, D.-Y.; Robinson, D. B. *Industrial & Engineering Chemistry Fundamentals* **1976**, *15*, 59–64.
- [84] Nagel, T.; Beckert, S.; Böttcher, N.; Gläser, R.; Kolditz, O. *Energy Procedia* **2015**, *75*, 2106–2112, Clean, Efficient and Affordable Energy for a Sustainable Future: The 7th International Conference on Applied Energy (ICAE2015).
- [85] González, B.; Calvar, N.; Gómez, E.; Domínguez, A. *The Journal of Chemical Thermodynamics* **2007**, *39*, 1578–1588.
- [86] Tang, Y.; Dubbeldam, D.; Tanase, S. *ACS Applied Materials & Interfaces* **2019**, *11*, 41383–41393, PMID: 31600050.
- [87] Matito-Martos, I.; Martín-Calvo, A.; Ania, C.; Parra, J.; Vicent-Luna, J.; Calero, S. *Chemical Engineering Journal* **2020**, *387*, 124062.
- [88] Li, J.-R.; Kuppler, R. J.; Zhou, H.-C. *Chem. Soc. Rev.* **2009**, *38*, 1477–1504.
- [89] Aristov, Y. I. *Applied Thermal Engineering* **2013**, *50*, 1610–1618, Combined Special Issues: ECP 2011 and IMPRES 2010.
- [90] Pan, H.; Ritter, J. A.; Balbuena, P. B. *Langmuir* **1998**, *14*, 6323–6327.
- [91] Cimino, R. T.; Kowalczyk, P.; Ravikovitch, P. I.; Neimark, A. V. *Langmuir* **2017**, *33*, 1769–1779, PMID: 28135415.



## CONCLUSIONS

The main conclusions drawn from this thesis are:

1. The steep adsorption isotherms in MAF-6 make this MOF optimal for the capture of light alcohols by pressure swing adsorption as the structure does not require high pressure swings to adsorb and release adsorbates.
2. The clustering of molecules below the saturation pressure of each adsorbate is a key factor in the adsorption mechanism. Cluster formation requires a large energy exchange between the low concentration regime and the saturation loading.
3. The aromatic rings of 2-ethylimidazole organic linkers are specific binding sites for MAF-6. The hydroxyl groups of the alcohol molecules are oriented by the electrostatic field around the binding sites and point to the centre of the aromatic rings of the organic linker.
4. The self-diffusion coefficients of the molecules of alcohol in MAF-6 decrease with increasing chain length. The values are similar for all isomers.
5. MAF-6 exhibits high adsorption capacity and steep adsorption behaviour. The energy exchange during the adsorption process is also high and allows the adsorbates to diffuse. Based on these results, MAF-6 is a promising adsorbent for the capture of light alcohols.
6. The purification of bioalcohols using pervaporation membranes based on hydrophobic zeolites has several advantages over distillation, including a lower energy requirement.
7. The all-silica MFI zeolite allows diffusion of pure methanol and ethanol and prevents diffusion of pure water. This is due to the hydrophobic character of the zeolite. Pure water strongly interacts through hydrogen bonds with the silanol groups.
8. Hydrogen bonding of water to silanol groups is weaker when water is in a mixture with alcohol. The tendency of water to create hydrogen bonds with alcohols allows molecular permeability through the MFI-based membrane.
9. Strong hydrogen bonding between water and alcohol molecules reduces selectivity of alcohol over water in MFI-based membranes. To avoid this, a solution can be modified the surface with functional groups that overcome the interaction between water and alcohol molecules.

This can be used as a new strategy to fabricate membranes with improved separation performance for bioalcohol dehydration.

10. Activation of the adsorbent at high temperatures is an important step to ensure adequate porosity of activated carbons. The functional groups present on the inner surface regulate the degree of hydrophobicity/hydrophilicity of CS1000a.
11. Computational modelling of amorphous materials is challenging when the structure is not well defined crystallographically. The use of realistic models is necessary to adequately describe the adsorption properties of polar adsorbates. The simplified model can correctly predict the energy storage densities obtained from the adsorption of light alcohols. However, the simplified model fails to accurately describe the adsorption mechanisms due to its high hydrophobicity compared to real adsorbates. The knowledge presented in this thesis can assist in future materials modelling developments.
12. The combination of atomistic simulations with a mathematical analysis based on a thermodynamic adsorption model is a promising method to relate the performance of an energy storage process with physicochemical properties at the molecular level.
13. The interactions of the light alcohols with the structure dominate the low-coverage adsorption, while the mutual interactions are essential for the nucleation that fills the pore to saturation.
14. Steep isotherms coupled with a large amount of adsorbed mass make CS1000a outperform BPL-activated carbons. CS1000a carbon is an excellent candidate for light alcohol storage and thermal energy applications. The results derived from this thesis can serve as a guide for the future design of new and efficient adsorbents for storage applications with low energy cost.
15. The combination of the QE-TPDA experiments with the MC simulation provides detailed information on the use of FAU zeolites for thermal storage applications. The agreement between experiments and simulation ensures the use of GCMC simulations to extend the operating conditions and provide a comprehensive view of the performance of the working pairs for energy storage.
16. Adsorption isobars reflect the influence of the hydrophobic degree of the adsorbent on desorption temperatures. HS-FAU desorbs most of the water and methanol at a much lower temperature than NaY and NaX. This has an impact on the operating conditions of a heat storage device. Therefore, hydrophobic materials such as HS-FAU can be used in low-temperature conditions, and hydrophilic adsorbents can operate in high-temperature processes.
17. The adsorption isobars of methanol and water exhibit similar behaviour due to the polar nature of both adsorbates and their interaction with non-framework sodium cations. However, the amount of adsorbed water is more significant than that of methanol. The higher values of water adsorption are due to the stronger hydrogen bond network and the access

of water to the sodalite cages of the FAU zeolites. Therefore, the energy released by heating and cooling is higher for water than for methanol, and the ratio of storage densities is related to the ratio of adsorption loading.

18. Controlling the hydrophobicity of zeolites by adjusting the Si/Al ratio could maximize the efficiency of adsorbate-fluid working pairs for given operating conditions. The choice of such operating conditions is crucial because it is a limiting factor for the performance of materials or working fluids.
19. The use of the Dubinin-Polanyi thermodynamic model to process adsorption data is suitable for obtaining fundamental properties to evaluate the performance of heat storage devices. This model is based solely on adsorption data obtained from experiments or simulations and on a set of physicochemical properties of the fluids. In this sense, molecular simulation is a promising tool for identifying adsorbent-fluid working pairs oriented to energy storage applications.
20. The adsorption of methanol and ethanol in metal-organic frameworks is key for finding high-performing pairs in heating and cooling applications. In particular, the highly hydrophobic adsorbent MAF-6 outperforms other MOFs for adsorption-driven heat pump applications. The combination of large pore size, volume, and surface area with pronounced adsorption isobars and isotherms makes this material an excellent candidate for taking heat from the surroundings in a wide range of operating conditions.
21. The proposed multistep process to assess the performance of working pairs for energy storage applications has proven to be an excellent tool for describing properties relevant to heating and cooling applications. This iterative method screens all suitable combinations of operating conditions and avoids data loss due to the complexity and the number of variables of the thermodynamic model. It is suitable for post-processing adsorption data from experiments or simulations. This method can accurately describe the experimental results and also predict various properties related to heating and cooling applications.



## SUMMARY

This thesis deals with alcohols and water confined in porous materials for applications such as storage, separation or energy transfer. Alcohols can contain one or several hydroxyl groups ( $-OH$ ) simply linked by a covalent bond to a carbon atom. This carbon can be part of a chain of alkanes, alkenes or alkynes, or part of an aromatic ring. Possible configurations of existing alcohols are almost unlimited, which makes systematic studies costly. In this context, advanced simulation techniques can be useful. Monte Carlo simulations, molecular dynamics or energy minimizations provide relevant information on the physicochemical properties of alcohols and their behaviour in the pure state, in mixtures with other alcohols or with water and their interaction with porous materials.

Simulation techniques were used in this thesis to evaluate:

**Storage of alcohols in a highly hydrophobic MOF.** In this chapter, the adsorption of methanol, ethanol, propanol and butanol in the porous material MAF-6 has been studied. MAF-6 is a highly hydrophobic and stable adsorbent with high capacity. The results of this work indicate that nucleation by hydrogen bonding is the main mechanism governing the adsorption of alcohols on this hydrophobic adsorbent. This results in steep isotherms reaching high saturation capacity values. Nucleation takes place at values below the saturation pressure of each fluid and involves high energy exchange in the adsorption and desorption regimes. Further analysis revealed the existence of binding sites favouring the nucleation of alcohol molecules and the absence of diffusion limitations for light alcohols through the pores of this MOF.

**Dehydration of alcohols in equimolar mixtures using membranes composed of pure silica zeolites.** In this chapter, the separation of methanol and ethanol with water has been studied using pervaporation membranes composed of MFI zeolite. Liquid mixtures of alcohol and water have been investigated by concentration-guided molecular dynamics finding that the mutual interaction between the alcohol and water molecules makes the membrane unable to completely dehydrate the alcohol samples, although it achieves excellent separation.

**Use of activated carbons in combination with alcohols for energy storage.** This chapter explores the use of linear alcohols (methanol, ethanol, 1-propanol and 1-butanol) in combination with activated carbons derived from the pyrolysis of mineral coke to store thermal energy. The results suggest that the activated carbons studied can store a large amount of thermal energy. This is due to the synergy of the adsorbed molecules and their interaction with the internal

surface of the adsorbent. The selected activated carbon (CS1000a) improves the performance for energy storage applications compared to other commercial samples, being a promising alternative for industrial applications.

**Study of water and alcohol adsorption on zeolites with cations and their use for energy storage.** In this chapter, the adsorption of water and methanol on faujasites (FAU) has been studied by varying the cation concentration using quasi-equilibrium temperature programmed desorption and adsorption measurements and Grand Canonical Monte Carlo simulations. In addition, using the methodology proposed in the previous chapter, the energy density that the FAU-alcohol pair can store as a function of the number of cations has been calculated.

**Use of the alcohol-MOF pairs as heat pumps or refrigerators.** In this chapter, the possibility of using alcohols in different MOFs and ZIFs to transport heat from hot to cold environments is explored. By modifying the operating conditions of the adsorption and desorption cycles, a heat pump device can transport heat at convenience. All this is based on the principle that adsorption is an exothermic process. The high heat capacity of alcohols, their versatility and the ability to interact with both hydrophobic and hydrophilic structures make them great candidates for working fluids in devices such as heat pumps or refrigerators.

## RESUMEN

### (Summary in Spanish)

En esta tesis se han estudiado los alcoholes, tanto en estado puro como en mezclas con agua, en combinación con materiales porosos para aplicaciones como almacenamiento, separación o transferencias energéticas. Los alcoholes contienen uno o varios grupos hidroxilo ( $-OH$ ) unidos por un enlace covalente simple a un átomo de carbono. Este carbono puede pertenecer a una cadena de alcanos, alquenos o alquinos, o a un anillo aromático. Las posibles configuraciones de alcoholes son casi ilimitadas por lo que estudiarlos puede resultar una tarea complicada y costosa. El uso de técnicas avanzadas de simulación es una herramienta muy útil en este contexto. La simulación usando métodos como el de Monte Carlo, dinámica molecular o minimizaciones energéticas proporcionan información relevante sobre las propiedades fisicoquímicas de los alcoholes y su comportamiento en estado puro, en mezclas con otros alcoholes o agua y su interacción con materiales porosos. Utilizando estas técnicas hemos podido estudiar los siguientes sistemas:

**Adsorción de alcoholes en un MOF altamente hidrofóbico.** En este capítulo se ha estudiado la adsorción de metanol, etanol, propanol y butanol en el material poroso MAF-6. Este adsorbente es altamente hidrofóbico. Además es estable y tiene una gran capacidad de almacenaje molecular. Los resultados de este trabajo indican que la interacción a través de enlaces por puentes de hidrógeno es el principal mecanismo que gobierna la nucleación de alcoholes en el adsorbente. Esto da como resultado isotermas con una subida muy abrupta que alcanzan altos valores de capacidad en saturación. La nucleación tiene lugar a valores inferiores a la presión de saturación de cada fluido lo que implica un alto intercambio de energía en los regímenes de adsorción y desorción. Un análisis posterior reveló la existencia de sitios de adsorción que favorecen la nucleación de las moléculas de alcohol y que no limitan la difusión para los alcoholes ligeros a través de los poros de este MOF.

**Deshidratación de alcoholes en mezclas equimolares usando membranas compuestas de zeolitas pura sílica.** En este capítulo, hemos estudiado la separación de metanol y etanol de agua usando membranas de pervaporación compuestas por zeolita tipo MFI. Se han estudiado mezclas líquidas de alcohol y agua mediante técnicas avanzadas de dinámicas molecular, encontrando que la interacción mutua entre las moléculas de alcohol y agua hace que la membrana no sea capaz de deshidratar completamente las muestras de alcohol, aunque se logra una buena

separación.

**Uso de carbones activados en combinación con alcoholes para el almacenamiento de energía.** Este capítulo ha explorado el uso de alcoholes lineales (metanol, etanol, 1-propanol y 1-butanol) en combinación con carbones activados derivados de la pirólisis de coque mineral para almacenar energía térmica. Se ha visto que estos carbones son capaces de almacenar una gran cantidad de energía térmica ya que no sólo la interacción de las moléculas con la superficie interna del material juega un papel fundamental, sino que también es crucial la cantidad de moléculas adsorbidas. En este contexto, se ha visto que uno de los carbones aquí estudiados (CS1000a) muestra propiedades superiores a otros carbones comerciales utilizados a nivel industrial.

**Estudio de la adsorción de agua y alcohol en zeolitas con cationes y su uso para almacenar energía.** En este capítulo hemos estudiado la interacción a nivel molecular del metanol y el agua en faujasitas (FAU) con diferentes concentraciones de cationes, desarrollando un conjunto de parámetros que describen la adsorción con los elementos mencionados. Este estudio se ha desarrollado a través de un enfoque experimental y de simulación. Además, utilizando la metodología propuesta en el capítulo anterior, se ha calculado la densidad energética que puede almacenar el par FAU-alcohol en función del número de cationes.

**Uso de pares alcohol-MOF como bombas de calor o enfriadores.** Este capítulo ha explorado la posibilidad de usar alcoholes en diferentes MOFs y ZIFs para transportar calor de ambientes más cálidos a más fríos. Modificando las condiciones operacionales de los ciclos de adsorción y desorción se puede transportar el calor a conveniencia. Todo esto se basa en el principio de que la adsorción es un proceso exotérmico. La alta capacidad calorífica de los alcoholes, su versatilidad y la posibilidad de interactuar con estructuras tanto hidrofóbicas como hidrofílicas los convierten en excelentes candidatos para fluidos de trabajo en dispositivos como bombas de calor o enfriadores.

## **Appendix 1**

### **Adsorption of Light Alcohols in a High Hydrophobic Metal Azolate Framework**

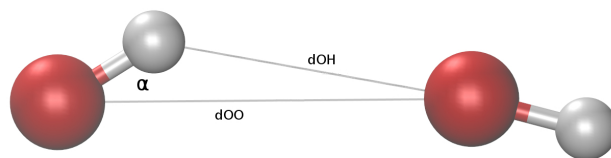


**Figure A1.1** Schematic representation of the HB criterion. Atoms of oxygen are represented by red spheres and hydrogen by white spheres.

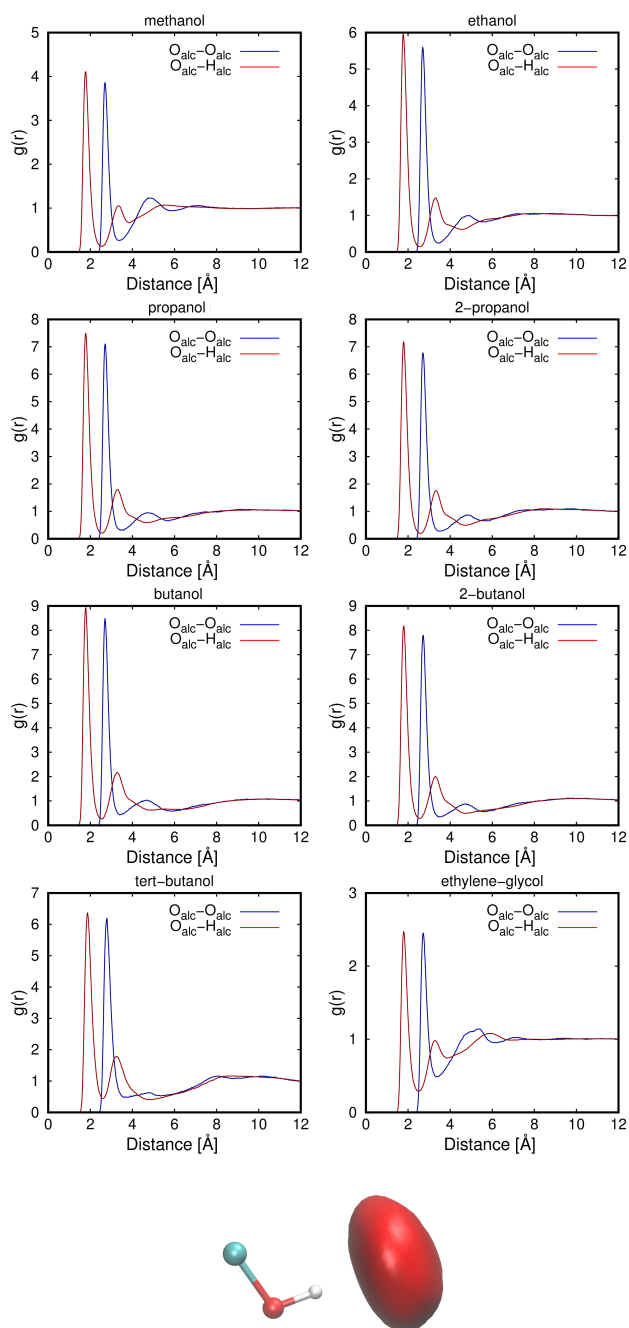


**Figure A1.2** Adsorbate-adsorbate radial distribution functions from MD simulation of each alcohol in the bulk and spatial distribution function of the oxygen atoms that can be connected via hydrogen bonds to a molecule of methanol.

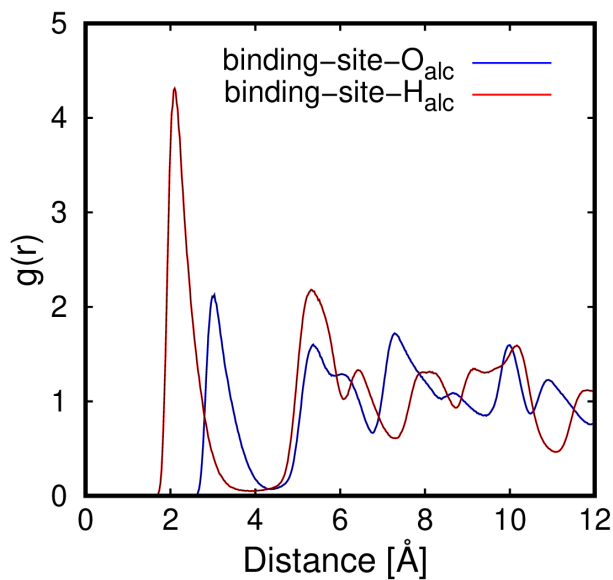


**Figure A1.3** Radial distribution functions of the atoms of oxygen and hydrogen of methanol with the binding-sites of MAF-6.

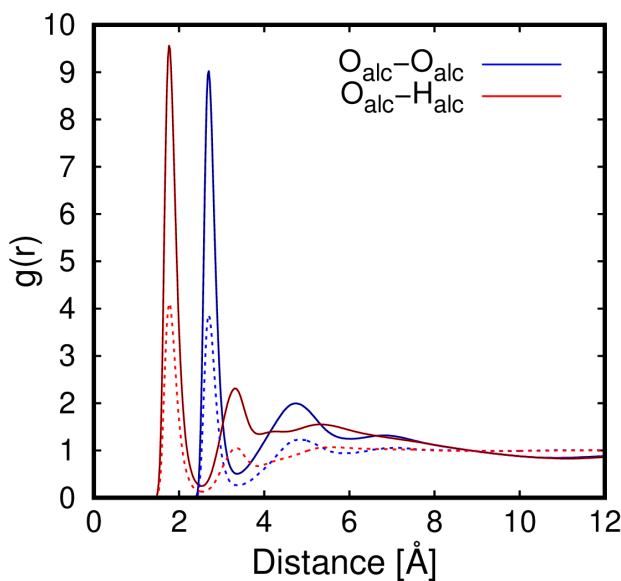


**Figure A1.4** Adsorbate-adsorbate radial distribution functions corresponding to the MD simulation of methanol in the bulk (dashed lines) and confined in the cavities of MAF-6 (solid lines).

**Table A1.1** Saturation pressure [kPa] of adsorbates calculated using Antoine equation and Peng-Robinson Equation of State.

Adsorbate	Antoine Eq.	Peng-Robinson EoS
methanol	16.78	15
ethanol	7.77	8
1-propanol	-	3
2-propanol	5.76	6
1-butanol	0.92	1.1
2-butanol	-	3.2
<i>tert</i> -butanol	5.51	7
ethylene-glycol	-	0.1

**Table A1.2** Average number of hydrogen bonds (nHB) of molecules of alcohol in the bulk.

Adsorbate	<i>n</i> HB in the bulk
methanol	1.91
ethanol	1.91
1-propanol	1.90
2-propanol	1.89
1-butanol	1.87
2-butanol	1.83
<i>tert</i> -butanol	1.68
ethylene-glycol	3.84



## **Appendix 2**

### **The Role of Hydrogen Bonding in the Dehydration of Bioalcohols in Hydrophobic Pervaporation Membranes**

## 2.1 Force field parameters for the MFI membrane atoms

**Table A2.1** Atom types (a) and parameters for the non-bonded Lennard-Jones potential (b), bonds (c), angles (d) and dihedrals.

### a) Atom types, and their corresponding masses and the partial charges

Atom	Mass[u]	Charge[e]
Si	28.0855	2.100
O1	15.999	-0.725
O2	15.999	-1.05
H1	1.008	0.200
CH3_MeOH	15.03452	0.265
CH3_EOH	15.03452	0
CH2_EOH	14.02658	0.265
O_alc	15.9994	-0.700
H_alc	1.008	0.435
O_wat	15.9994	-0.8476
H_wat	1.008	0.4238

### b) Non-Bonded potential

$$V_{ij} = 4\epsilon_{ij} \left( \left( \frac{\sigma_{ij}}{r_{ij}} \right)^{12} - \left( \frac{\sigma_{ij}}{r_{ij}} \right)^6 \right)$$

$A_i$	$A_j$	$\epsilon$ [kJ/mol]	$\sigma$ [nm]
Si	Si	$6.89057 \cdot 10^{-7}$	0.334478
O1	O1	0.7986	0.3107819
O2	O2	0.7986	0.3107819
H1	H1	0.0	0.0
Si	O1	0.10153396046	0.247105204426
Si	O2	0.00164729035	0.341646346144
CH3_MeOH	CH3_MeOH	0.815	0.375
CH3_EOH	CH3_EOH	0.815	0.375
CH2_EOH	CH2_EOH	0.382	0.375
O_alc	O_alc	0.773	0.302
H_alc	H_alc	-	-
O_wat	O_wat	0.650	0.3166
H_wat	H_wat	-	-

## c) Harmonic Bond Potential

$$V_{ij} = \frac{1}{2} k_b (r_{ij} - b_0)^2$$

$A_i$	$A_j$	$K_b$ [kJ/mol·nm <sup>-2</sup> ]	$b_0$ [nm]
O1	H1	4640.07	0.09476
CH3_MeOH	O_alc	502416.0	0.1430
CH3_EOH	CH2_EOH	502416.0	0.1540
CH2_EOH	O_alc	502416.0	0.1430
O_alc	H_alc	502416.0	0.0945
O_wat	H_wat	345168.134	0.1000

## d) Harmonic Angle Potential

$$V_{ijk} = \frac{1}{2} k_\theta (\theta_{ijk} - \theta_0)^2$$

$A_i$	$A_j$	$A_k$	$K_\theta$ [kJ/mol·rad <sup>-2</sup> ]	$\theta_0$ [°]
O1	Si	O2	144.1876	109.47
O2	Si	O2	144.1876	109.47
Si	O2	Si	149.6391	142.71
CH3_MeOH	O_alc	H_alc	460.61833	108.50
CH3_EOH	CH2_EOH	O_alc	419.04626	109.47
CH2_MeOH	O_alc	H_alc	460.61833	108.50
H_wat	O_wat	H_wat	383.18666	109.47

## e) Dihedral Potential

$$V_{RB} = \sum_{n=0}^5 C_n (\cos(\psi))^n, \text{ where } \psi = \theta_{ijkl} - 180^\circ$$

$A_i$	$A_j$	$A_k$	$A_l$	$C_0^*$	$C_1^*$	$C_2^*$	$C_3^*$	$C_4^*$	$C_5^*$
CH3_EOH	CH2_EOH	O_alc	H_alc	2.822	2.943	0.485	-6.25	0.0	0.0

\*All the coefficients are expressed in kJ/mol

## 2.2 GCMC methodology

To obtain the amount of molecules of alcohol and water inside the structure we performed  $2 \cdot 10^5$  equilibrate cycles, followed by  $10^6$  production run cycles in the grand-canonical ensemble (GCMC). In these simulations, we considered a rigid periodic crystal using the crystallographically determined position of the atoms, because the flexibility does not affect so much to adsorption. The MFI unit cell was replicated 2, 2 and 3 times in the x, y and z direction, respectively, to surpass twice the spherical cut-off used for non-bonded interactions; i.e. 12 Å. Translation, rotation and insertion/deletion moves were sampled with equal probabilities.

## 2.3 CGD-MD parameters

CGD-MD is a simulation method that provides regions in which the particle concentration is maintained at a target value. With this aim, a bi-directional bias force is applied on the particles to keep the concentration of the particles constant in the control regions. The expression for the bi-directional force is

$$F(z) = k_i (n_i^{CR} - n_{0i}) \cdot G(z, Z_F)$$

where  $k_i$  is a force constant,  $n_i^{CR}$  is the instantaneous density in the designated control regions (CR) while  $n_{0i}$  is the target density.  $G(z, Z_F)$  is a bell-shaped function whose value is equal to 1 for  $z = Z_F$  and it is null outside of a  $Z_F$ -centered  $w$  range, i.e.  $G(z, Z_F)$  delimits the region where forces are applied. Mathematical expression of this bell-shaped function is

$$G(z, Z_F) = \frac{1}{4w} \left[ 1 + \cosh\left(\frac{z - Z_F}{w}\right) \right]^{-1}$$

Instantaneous particle density is given by

$$n_i^{CR} = \frac{1}{V^{CR}} \sum_{j=1}^{N_i} \theta(Z_j) \quad \text{where } \theta(Z_j) \begin{cases} 1 & \text{if } Z_j \in CR \\ 0 & \text{otherwise} \end{cases}$$

where  $V^{CR}$  the volume of the CR.

**Table A2.2** Force constants and width of the control regions in the inlet and outlet of the membrane.

Side	$w[nm]$	$k_i[kJ \cdot nm^3/mol]$	$Z_F[nm]$	$V^{CR}[nm]/(L_x L_y)$
Inlet	0.25	500	4.107	2.5
Outlet	0.25	5000	24.690	2.5

## 2.4 Supplementary results from CGD-MD simulations

**Table A2.3** Target concentrations and computed average concentrations of methanol, ethanol and water in control regions in single component CGD-MD simulations.

	Feed control region (FCR)		Permeate control region (PCR)	
	Target concentration*	Average concentration*	Target concentration*	Average concentration*
Methanol	15.23	$14.99 \pm 0.06$	0	$0.004 \pm 0.007$
Ethanol	10.31	$10.16 \pm 0.05$	0	$0.028 \pm 0.007$
Water	33.46	$33.7 \pm 0.1$	0	0**

\*Expressed in [ $molecules/nm^3$ ] \*\*Water does not enter the MFI membrane in the single component simulation.

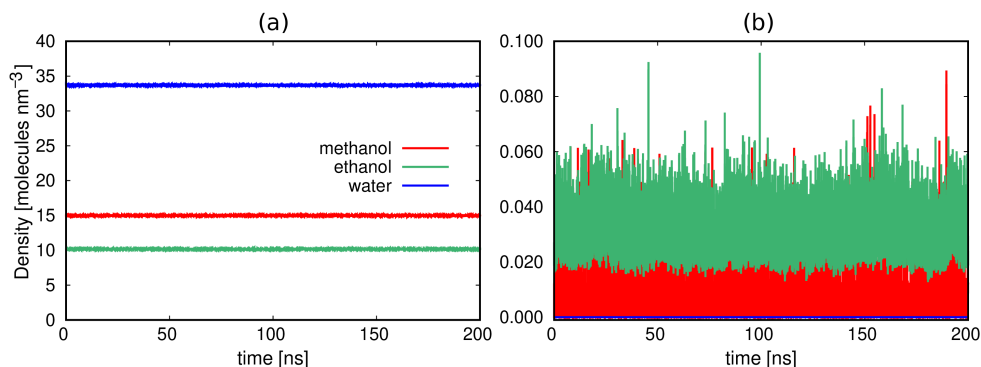


**Figure A2.1** Moving averages of the molecular density (calculated using preceding 100 data points) as a function of simulation time for methanol (red), ethanol (green) and water (blue) in the FCR (a) and PCR (b). Note that because pure water does not permeate through the MFI membrane, water density in PCR is effectively zero. For methanol and ethanol densities in PCR are noisy due to very low statistical probability of finding a particle in vacuum. Concentrations averaged over the 200ns production runs are given in Table A2.3.

**Table A2.4** Target concentrations and computed average concentrations of methanol, ethanol and water in control regions in alcohol-water mixture CGD-MD simulations.

	Feed control region (FCR)		Permeate control region (PCR)	
	Target concentration*	Average concentration*	Target concentration*	Average concentration*
Methanol-water	10.29	$10.43 \pm 0.07 / 10.39 \pm 0.09$	0	$0.0002 \pm 0.0008$
Ethanol-water	7.88	$7.92 \pm 0.06 / 7.89 \pm 0.09$	0	$0.003 \pm 0.004 / 0.0001 \pm 0.0006$

\*Expressed in [ $molecules/nm^3$ ]

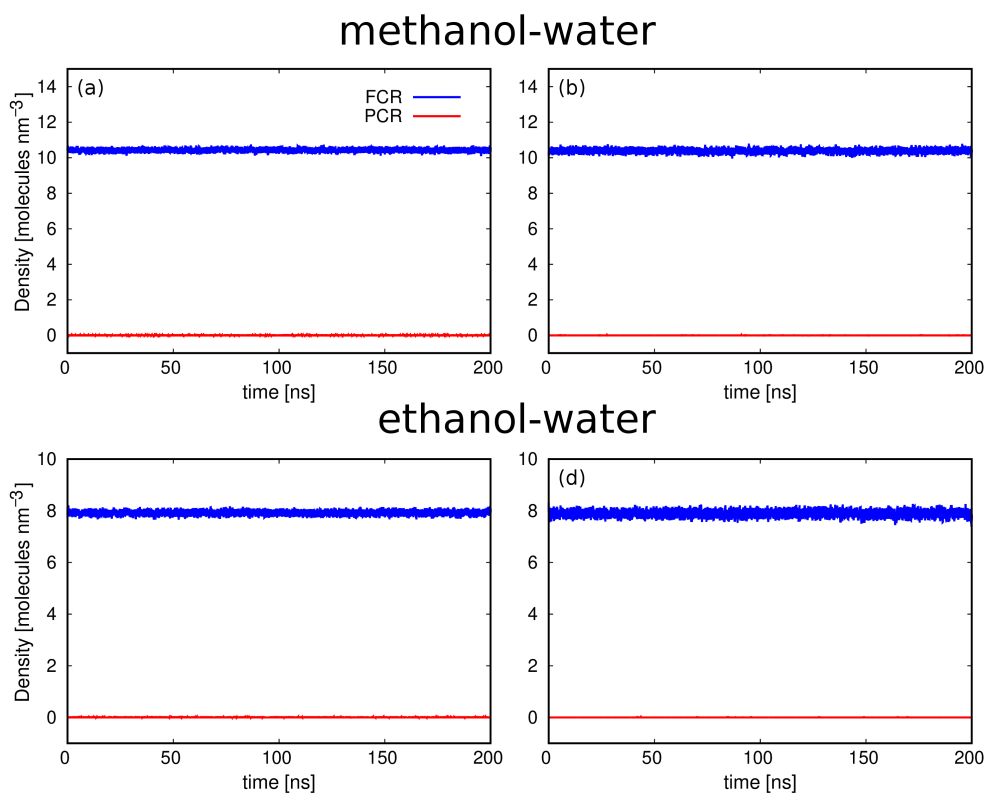


**Figure A2.2** Moving averages of the molecular density (calculated using preceding 100 data points) as a function of simulation time in the FCR (blue) and PCR (red) in the methanol-water (top) and ethanol-water (bottom) mixtures. The data for alcohols are shown on left side (methanol (a) and ethanol (c)) and water on right side ((b) and (d)). Concentrations averaged over the 200 ns production runs are given in Table S4.

**Table A2.5** Number of hydrogen bonds per alcohol molecules.

	Feed	Membrane	Membrane normalized*
Methanol	1.91	1.32	1.43(= $1.324 \times (14.99/3.713746463/0.292)$ )
Ethanol	1.91	1.27	1.32(= $1.273 \times (10.16/2.863494745/0.292)$ )

\*number of hydrogen bonds per alcohol molecule in the membrane  $\times$  molecular density of alcohol in the feed (Table A2.3)  $\div$  average molecular density of the alcohol in the membrane (data from Figure 3.3  $\div$  void fraction)

To speculate on the extent of the role that the hydrogen bonding plays in the diffusion of alcohol molecules, we calculated the number of hydrogen bonds per alcohol molecule in the feed and in the membrane from single component simulations. The data given in Table S5 shows that the number of hydrogen bonds between alcohol molecules decrease in MFI compared to the feed.

However, to be able to make a head-to-head comparison, the numbers for hydrogen bonding in the membrane should be normalized with respect to the molecular density of alcohols in accessible MFI pore volume; i.e. void fraction (predicted to be 0.292 from Monte Carlo simulations). The normalized number of hydrogen bonds between alcohols molecules are clearly smaller than those of in the bulk. Given that the hydrogen bonding is relatively weaker between alcohol molecules in the membrane, we can speculate that it does play an important role in the diffusion of alcohols in the membrane.



## **Appendix 3**

### **Adsorption of Linear Alcohols in Amorphous Activated Carbons: Implications for Energy Storage Applications**

**Table A3.1** Lennard-Jones parameters and point charges for (a) adsorbents and (b) adsorbates used in this work.

a)

Pseudo atom	$\epsilon/K_B [K]$	$\sigma [\text{\AA}]$	$q [e]$
$-\underline{\mathbf{C}}-H$	28.00	3.36	0.00
$-\underline{\mathbf{C}}-\underline{\mathbf{H}}$	15.08	2.42	0.00
$-\underline{\mathbf{C}}-OH$	X	X	0.20
$-\underline{\mathbf{C}}-\underline{\mathbf{O}}H$	78.20	3.07	-0.64
$-\underline{\mathbf{C}}-\underline{\mathbf{O}}\underline{\mathbf{H}}$	X	X	0.44
$-\underline{\mathbf{C}}-COOH$	X	X	0.08
$-\underline{\mathbf{C}}-\underline{\mathbf{C}}OOH$	52.00	3.75	0.55
$-\underline{\mathbf{C}}-\underline{\mathbf{C}}\underline{\mathbf{O}}OH$	105.7	2.96	-0.50
$-\underline{\mathbf{C}}-\underline{\mathbf{C}}\underline{\mathbf{O}}\underline{\mathbf{O}}H$	85.60	3.00	-0.58
$-\underline{\mathbf{C}}-\underline{\mathbf{C}}\underline{\mathbf{O}}\underline{\mathbf{O}}\underline{\mathbf{H}}$	X	X	0.45

\* "X" denotes that the atom does not interact through Van der Waals interactions.

\*\* The parameters are referred to atoms in bold and underlined.

b)

Pseudo atom	$\epsilon/K_B [K]$	$\sigma [\text{\AA}]$	$q [e]$
<b>methanol</b>			
<i>CH3_alc</i>	98.00	3.75	0.265
<i>O_alc</i>	93.00	3.02	-0.700
<i>H_alc</i>	X	X	0.435
<b>ethanol</b>			
<i>CH3_alc2</i>	98.00	3.75	0.000
<i>CH2_alc</i>	46.00	3.95	0.265
<i>O_alc</i>	93.00	3.02	-0.700
<i>H_alc</i>	X	X	0.435
<b>1-propanol</b>			
<i>CH3_alc2</i>	98.00	3.75	0.000
<i>CH2_alc3</i>	46.00	3.95	0.000
<i>CH2_alc</i>	46.00	3.95	0.265
<i>O_alc</i>	93.00	3.02	-0.700
<i>H_alc</i>	X	X	0.435
<b>1-butanol</b>			
<i>CH3_alc2</i>	98.00	3.75	0.000
<i>CH2_alc2</i>	46.00	3.95	0.000
<i>CH2_alc2</i>	46.00	3.95	0.000
<i>CH2_alc</i>	46.00	3.95	0.265
<i>O_alc</i>	93.00	3.02	-0.700
<i>H_alc</i>	X	X	0.435

\* "X" denotes that the atom does not interact through Van der Waals interactions.

\*\* The names of the pseudo atoms have been taken from TraPPE<sup>1</sup> nomenclature

**Table A3.2** Structural properties of ACs models.

	CS1000		CS400		CS1000a		without functional group sim.
	With functional groups exp.	sim.	with functional groups exp.	sim.	with functional group exp.	sim.	
$\rho$ [g/ml]	1.584 <sup>a</sup>	1.583 <sup>b</sup>	1.275 <sup>a</sup>	1.274 <sup>b</sup>	0.737 <sup>a</sup>	0.737 <sup>b</sup>	0.727 <sup>b</sup>
Porosity		0.14 <sup>b</sup>		0.15 <sup>b</sup>		0.60 <sup>b</sup>	0.60 <sup>b</sup>
O/C ratio	0.041 <sup>a</sup>	0.041 <sup>c</sup>	0.123 <sup>a</sup>	0.121 <sup>c</sup>	0.0087 <sup>a</sup>	0.0095 <sup>c</sup>	0
H/C ratio	0.15 <sup>a</sup>	0.17 <sup>c</sup>	0.53 <sup>a</sup>	0.54 <sup>c</sup>	0.091 <sup>a</sup>	0.097 <sup>c</sup>	~0
PV [ $cm^3/g$ ]		0.091 <sup>b</sup>		0.12 <sup>b</sup>		0.817 <sup>b</sup>	0.827 <sup>b</sup>
SA [ $m^2/g$ ]		60.91 <sup>b</sup>		130.9 <sup>b</sup>		2377.5 <sup>b</sup>	2409.6 <sup>b</sup>

<sup>a</sup> Jain, S. K.; Pellenq, R. J. M.; Pukuncic, J. P.; Gubbins, K. E. Molecular Modeling of Porous Carbons Using the Hybrid Reverse Monte Carlo Method. *Langmuir* 2006, 22 (24), 9942-9948.

<sup>b</sup> Peng, X.; Vicent-Luna, J. M.; Q. Jin. Separation of CF<sub>4</sub>/N<sub>2</sub>, C<sub>2</sub>F<sub>6</sub>/N<sub>2</sub>, and SF<sub>6</sub>/N<sub>2</sub> Mixtures in Amorphous Activated Carbons using Molecular Simulations. *ACS Appl. Mater. Interfaces*, 2020, (12), 20044-20055.

<sup>c</sup> This work.

**Table A3.3** Thermal expansion coefficients of the working fluids at room temperature and their corresponding pressure.

Fluid	$\alpha_T [K^{-1}] \cdot 10^{-4}$	Pressure [MPa]
methanol	8.026	100
ethanol	7.285	100-103.9
1-propanol	5.910	102-104.2
1-butanol	6.065	100-102.4

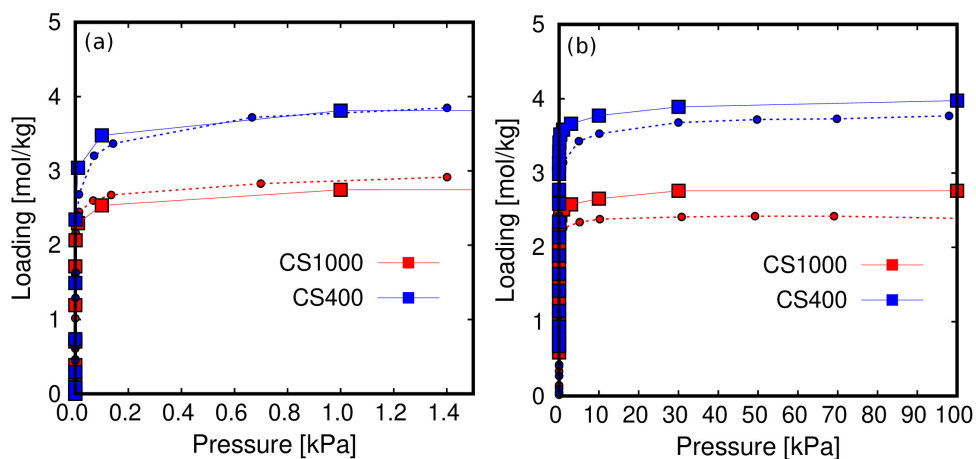


**Figure A3.1** Adsorption isotherms of Ar (a) and nitrogen (b), calculated by GCMC simulations (solid squares) and compared to experimental data<sup>2</sup> (solid circles) in CS400 and CS1000 at 77K. We used the force field for Ar and N<sub>2</sub> molecules reported by<sup>3,4</sup> to compute the adsorption isotherms.

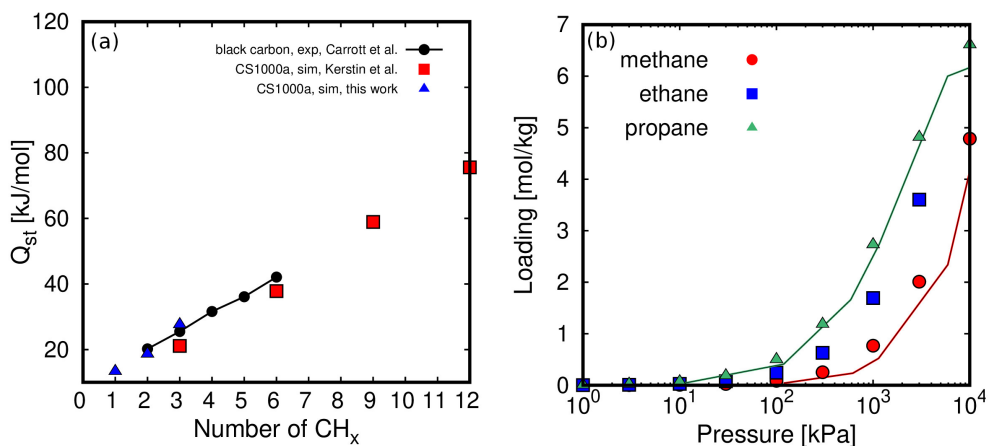


**Figure A3.2** Isothermic heat of adsorption of linear hydrocarbons (a) as a function of the chain length in CS1000a, calculated in this work and compared to the experimental data reported by Carrot *et al.*<sup>5</sup> and the simulated data provided by Falk *et al.*<sup>6</sup> (b) Computed adsorption isotherms at 423 K (points) compared to the simulation values (lines) reported by Falk *et al.*<sup>6</sup>

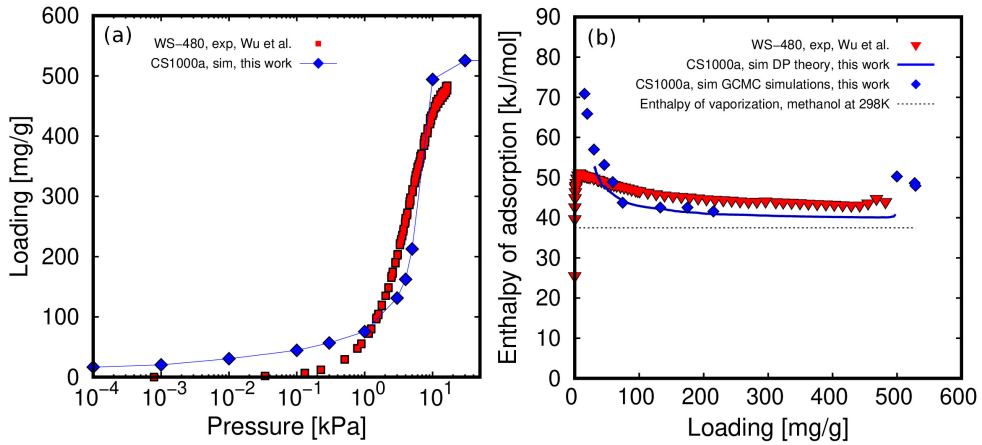


**Figure A3.3** Computed adsorption isotherms (a) of methanol in CS1000a compared to the experimental isotherm in WS-480 reported by Wu *et al.*<sup>7</sup> at 298K. Enthalpy of adsorption as a function of the adsorbed loading of methanol (b) in CS1000a calculated by GCMC simulations, using the Dubinin-Polanyi theory, and reported by Wu *et al.*<sup>7</sup> Enthalpy of vaporization of methanol at room temperature is presented as a baseline.

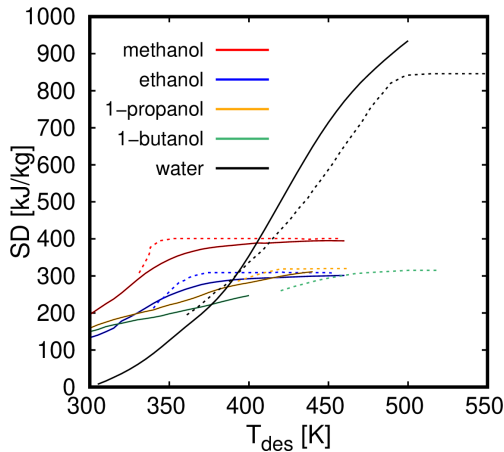


**Figure A3.4** Storage densities (SD) of n-alcohols in BPL and water in 13X zeolite reported by Kohler *et al.*<sup>8</sup> (dashed lines) and computed with the mathematical model (solid lines) used in this work. The loading of each working fluid to calculate the storages densities in BPL using the mathematical model (see Simulation Details section) has been estimated from their corresponding adsorption isobars at 5, 9, 2, and 0.9 kPa for methanol, ethanol, 1-propanol, 1-butanol, and water, respectively. The adsorption isobars have been computed from the characteristic curve generated using the experimental isotherms reported by Taqvi *et al.*<sup>9</sup>

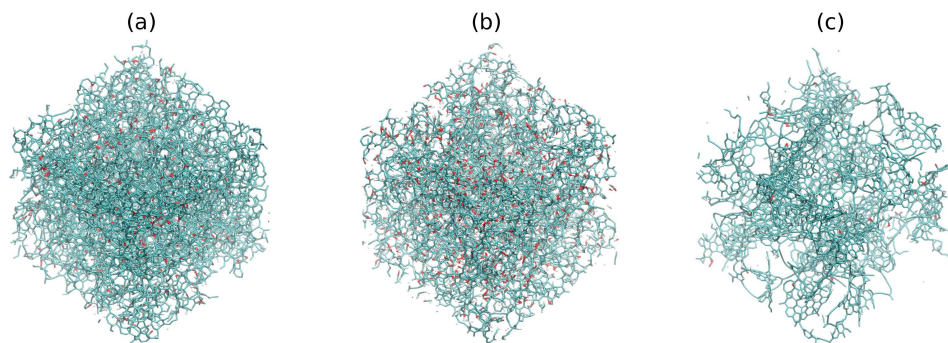


**Figure A3.5** Atomistic representation of (a) CS1000, (b) CS400 and (c) CS1000a AC models.

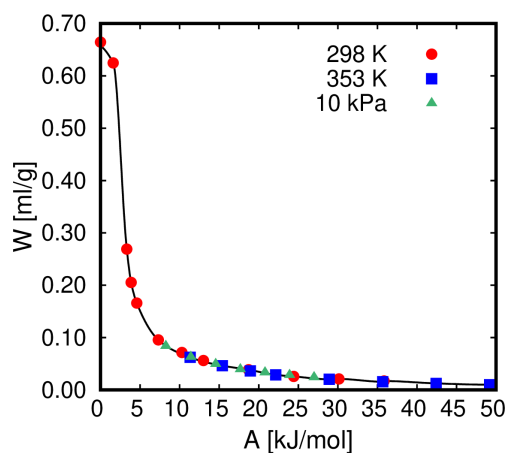


**Figure A3.6** Characteristic curve of methanol in CS1000a. The solid line represents the fitting using splines, and the point data are obtained from independent simulations; red circles, and blue squares from adsorption isotherms at 298 K and 353 K respectively and green triangles from an adsorption isobar at 10 kPa.

### 3.1 Bibliography

- [1] Stubbs, J.M.; Potoff, J.J.; Siepmann, J.I., *J. Phys. Chem. B*, **2004**, 108, 17596-17605
- [2] Pikunic, J., Llewellyn, P., Pellenq, R.; Gubbins, K.E., *Langmuir*, **2005**, 21, 4431-4440
- [3] Murthy, C.S., Singer, K., Klein, M.L.; McDonad, I.R., *Mol. Phys.*, **1980**, 240, 1387-1399
- [4] García-Pérez, E.; Parra, J. B.; Ania, C.O.; Dubbeldam, D.; Vlugt, T.J.H.; Castillo, J.M. ; Merklng, P.J. ; Calero, S., *J. Phys. Chem. C*, **2008**, 112, 9976-9979
- [5] Carrott, P.J.M.; Sing, K.S.W., in *Proceedings of the IUPAC Symposium (COPS I)* **1998** 77-87

- [6] Falk, K.; Pellenq, R.; Ulm, F. J.; Coasne, B., *Energy Fuels*, **2015**, 29, 7889-7896
- [7] Wu, J.W.; Madani, S.H.; Biggs, M.J.; Phillip, P.; Lei, C.; Hu, E.J., *J. Chem. Eng.*, **2015**, 60, 1727-1731
- [8] Kohler, T.; Muller, K. *Energy Sci. Eng.*, **2017**, 5, 21-29
- [9] Taqvi, S.M.; Appel, W.S.; LeVan, M.D., *Ind. Eng. Chem. Res.*, **1999**, 38, 240-250



## **Appendix 4**

### **On the use of Water and Methanol with Zeolites for Heat Transfer**

## 4.1 Structural model for zeolites

All zeolites were generated following the same procedure regardless the Si/Al ratio. The unit cell of the pure silica FAU contains 192 Si atoms. We substitute some Si atoms by Al atoms to reproduce the experimental chemical composition (Si/Al ratio of 100, 2.61, and 1.06, HS-FAU, NaY, and NaX, respectively). HS-FAU, NaY, and NaX contain 2, 56, and 88 Al atoms, respectively.

We generated the structures following the methodology described in previous works.<sup>1,2</sup> We started from the crystallographic positions of the pure silica zeolite from the International Zeolite Association (IZA) database<sup>3</sup> to construct the aluminosilicates. For each structure, we created a set of 50 configurations by randomly substituting some silicon atoms by aluminum atoms within the constraint of Lowenstein's rule and selected the most energetically favorable configuration. Then, we compensated the net negative charge of the adsorbents by placing sodium extra-framework cations in the most probable crystallographic positions reported in the literature. A detailed description of these extra-framework cations is given in references.<sup>4-6</sup> Once we added the extra-framework cations to their preferential location, we optimized the structures with energy minimization simulations using Baker's<sup>7</sup> method and a full-flexible core-shell potential.<sup>8,9</sup>

## 4.2 Parameterization of methanol-zeolite interactions

Interactions parameters between the molecules of water and the HS-FAU and NaX zeolites were developed in our previous work<sup>10</sup> using experimental adsorption isobars as reference data. In this work, we also computed the adsorption isobar of water in NaY, showing that the water-zeolite interactions are transferable in the whole range of Si/Al substitutions. Here we followed a similar procedure to obtain the methanol-zeolite interactions. Starting from the cross-term Lennard-Jones parameters for each pseudo atom of the methanol-zeolite pairs, we iteratively modify the  $\epsilon$  and  $\sigma$  parameters, creating a matrix of values smaller and larger than the initials. The partial charges for the adsorbates and zeolites are kept fixed and given in Table A4.1. For each set of parameters, we computed five values of an adsorption isobar from the low to the high coverage regime. We first compare with experimental data for NaX to narrow the search of adequate parameters to reproduce the adsorption in the zeolite with the highest content of extra-framework cations. Then, we compare with the measured data for HS-FAU and finally for NaY. We repeated the process until we found reasonable agreement between experiments and simulations using the same set of Lennard-Jones parameters regardless the Si/Al ratio. The optimal values are provided in Table A4.2 and the validation against experimental values is shown in Figure 2 of the manuscript.

**Table A4.1** Lennard-Jones parameters and charges of each pseudo-atom for the adsorbent and adsorbates.  $O_{zeo-Si}$  and  $O_{zeo-Al}$  are the oxygen atoms bridging to silicon and aluminum atoms, respectively.

$$V_{ij} = 4\epsilon_{ij} \left( \left( \frac{\sigma_{ij}}{r_{ij}} \right)^{12} - \left( \frac{\sigma_{ij}}{r_{ij}} \right)^6 \right) \quad (4.1)$$

Molecule	Atom	q[e]	$\epsilon/k_B$ [K]	$\sigma$ [Å]
water <sup>a</sup>	$O_w$	-0.8476	78.2878	3.165
	$H_w$	0.4238	0*	0*
	$CH_3$	0.265	98	3.75
methanol <sup>b</sup>	$O_{alc}$	-0.7	93	3.02
	$H_{alc}$	0.435	0*	0*
	$Si_{zeo}$	2.05	22	2.3
zeolite <sup>c</sup>	$O_{zeo-Si}$	-1.025	53	3.3
	$Al_{zeo}$	1.75	22	2.3
	$O_{zeo-Al}$	-1.2	53	3.3
	$Na$	1.0	0*	0*

\*“0” indicates this atom does not interact through van der Waals potential. [a] reported in reference,<sup>11</sup> [b] reported in reference,<sup>12</sup> and [c] reported in reference<sup>13</sup>

**Table A4.2** Lennard-Jones parameters to describe the interactions between the zeolite and the water and methanol molecules.

Molecule	Pair interaction	$\epsilon/k_B$ [K]	$\sigma$ [Å]
water <sup>a</sup>	$O_w - O_{zeo}$	80	3.3
	$O_w - Na^+$	50	3.3
	$CH_3 - O_{zeo}$	80	3.8
methanol <sup>b</sup>	$O_{alc} - O_{zeo}$	70	3.8
	$CH_3 - Na^+$	80	3.6
	$O_{alc} - Na^+$	80	3.2

[a] Taken from ref [b] This work.

**Table A4.3.** Intramolecular force field for water and methanol molecules.

a) Bonds

$$V_{ij} = \frac{1}{2}k_r(r - r_0)^2 \quad (4.2)$$

Molecule	Atom i	Atom j	$r_0$ [Å]	$k_r/k_B$ [K]
water <sup>a</sup>	$O_w$	$H_w$	1.0	415144.47
methanol	$CH_3$	$O_{alc}$	1.43	$\infty^*$
	$O_{alc}$	$H_{alc}$	0.945	$\infty^*$

\*“ $\infty$ ” indicates this atom does not interact through van der Waals potential.

b) Bends

Molecule	Atom i	Atom j	Atom k	$\theta_0$ [°]	$k_\theta/k_B$ [K]
water <sup>a</sup>	$H_w$	$O_w$	$H_w$	109.47	46087.0528
methanol <sup>b</sup>	$CH_3$	$O_{alc}$	$H_{alc}$	108.5	55400

[a] Bond and bend parameters reported in <sup>11</sup> (water) and [b] reported in reference <sup>12</sup> (methanol).

### 4.3 Thermodynamical model

We used the mathematical model based on the Dubinin-Polanyi theory <sup>14,15</sup> to obtain the energy storage properties of the zeolite-fluid working pairs. We first convert the adsorption isobars into their corresponding characteristic curves. The characteristic curve relates the volumetric uptake  $W$  (volume of fluid adsorbed in the micropores [ml/g]) and the adsorption potential  $A$  [kJ/mol].

$$A = RT \log\left(\frac{p_{sat}}{p}\right) \quad (4.3)$$

$$W = \frac{q(p, T)}{\rho(T)} \quad (4.4)$$

where  $p_{sat}$ , is the saturation pressure of the working fluid,  $q(p, T)$ , the loading of adsorbed fluid per mass of adsorbent, [g/g], and  $\rho(T)$ , the density of fluid confined within the micropores [g/ml]. We use the Peng Robinson equation of state to calculate the saturation pressure of each fluid. <sup>16</sup> We obtained the loading of fluid from QE-TPDA experiments and GCMC simulation. We used the model of Hauer to obtain the density of confined fluids within the micropores. <sup>17,18</sup> This model gives a linear relationship between the density of a fluid confined within the pores of an adsorbent and the operational temperature:

$$\rho(T) = \rho_0(T_0) \cdot [1 - \alpha_T(T - T_0)] \quad (4.5)$$

where  $\rho_0$  is the free liquid density at the reference  $T_0$  (283.15 K for water<sup>15</sup> and 298 K for methanol).<sup>19</sup>  $\alpha_T$  is the free liquid thermal expansion coefficient of each working fluid at the reference temperature and 100 MPa.<sup>18,19</sup> ( $3.871 \cdot 10^{-4} K^{-1}$  for water and  $8.026 \cdot 10^{-4} K^{-1}$  for methanol).

The Dubinin-Polanyi theory also allows determining the adsorption enthalpy, which is defined as:

$$\Delta H = \Delta H_{vap} + A - T\Delta S \quad (4.6)$$

where  $\Delta H_{vap}$  is the enthalpy of vaporization,  $A$  is the adsorption potential (Gibbs free energy) and  $\Delta S$  is the entropy variation,<sup>20</sup> calculated as:

$$\Delta S = \alpha_{Ads} W \left. \frac{\partial A}{\partial W} \right|_T \quad (4.7)$$

where  $\alpha_{Ads}$  is the thermal expansion coefficient of the fluid in the adsorbed phase, obtained from the density model. Finally, we calculated the thermochemical storage density by integrating the enthalpy curves within the selected adsorption and desorption temperatures:

$$SD = \int_{q(T_{ads})}^{q(T_{des})} \Delta H(q) dq \quad (4.8)$$

In summary, the mathematical model based on the Dubinin-Polanyi theory allows obtaining the storages densities of adsorbent-fluid working pairs, just from an adsorption isotherm or isobar and some physicochemical properties of the fluids. These properties are the enthalpy of vaporization, bulk liquid density, thermal expansion coefficient, and saturation pressure.

Another advantage of the characteristic curve is that it can be reverted to obtain the adsorption isobars or isotherms at different conditions. In addition to the adsorption isobars, we also computed the adsorption isotherms to check the validity of the Dubinin-Polanyi theory. Figure 4.1 shows the adsorption isotherms of both working fluids in the three zeolites.

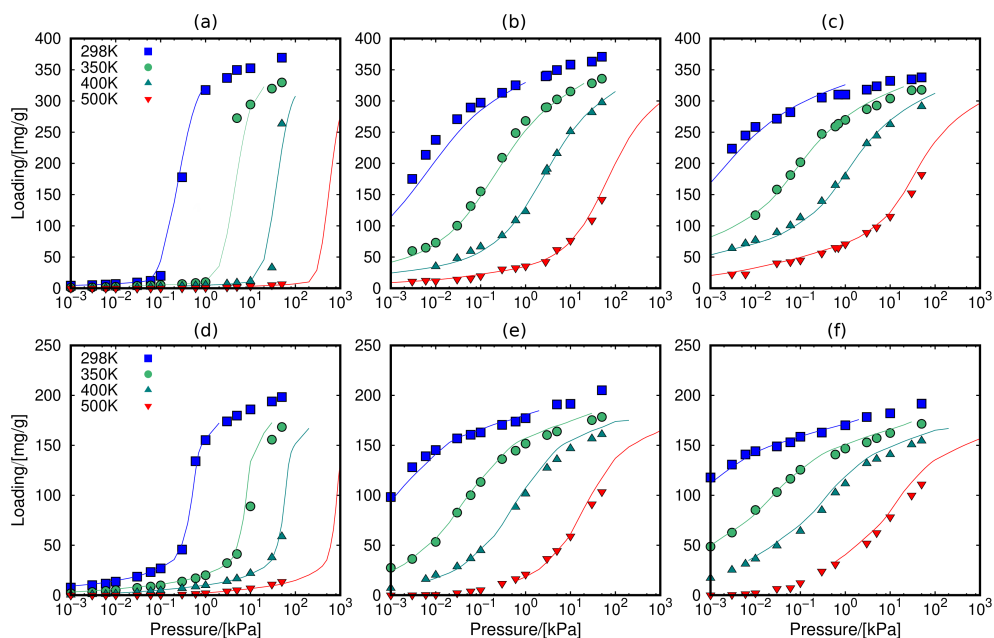


**Figure A4.1** Adsorption isotherms at 298, 350, 400, and 500 K of water (top) and methanol (bottom) in HS-FAU (a, d), NaY (b, e), and NaX (c, f), respectively. Closed symbols represent computed values with GCMC simulations and lines are predicted isotherms obtained from the characteristic curves using the thermodynamical model of Dubinin-Polanyi.

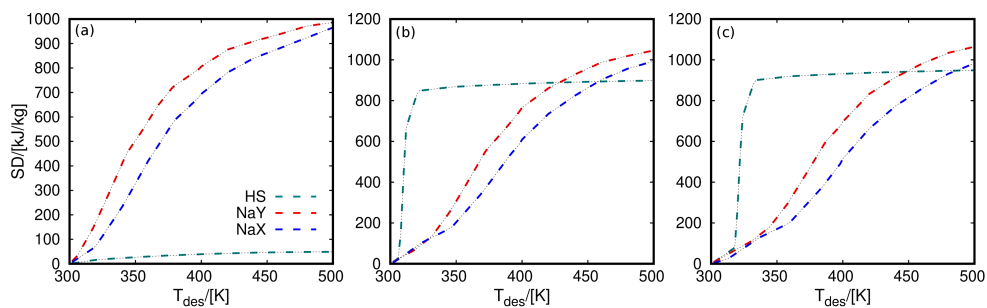


**Figure A4.2** Storage density (SD) of water-zeolite pairs in HS-FAU, NaY, and NaX at  $T_{ads} = 300\text{K}$  and  $P = 0.1\text{kPa}$  (a),  $P = 0.5\text{kPa}$  (b), and  $P = 1\text{kPa}$  (c).

## 4.4 Bibliography

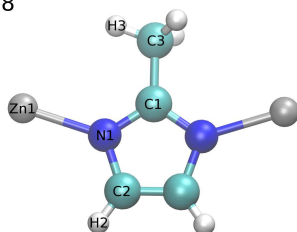
- [1] Balestra, S.R.G.; Hamad, S; Ruiz-Salvador; Domínguez-García, V.; Merklings, P.J.; Dubbeldam, D.; Calero, S., *Chem. Mater*, **2015**, 27, 5657-5667
- [2] Luna-Triguero, A.; Sławek, A.; Sánchez-de-Armas, R.; Gutiérrez-Sevillano, J.J.; Ania, C.O.; Parra, J.B.; Vicent-Luna, J.M.; Calero, S., *Chem. Eng. J.*, **2020**, 308, 122482
- [3] IZA Database <https://doi.org/10.1016/B978-0-444-53064-6.X5186-X>.
- [4] Olson, D.H., *Zeolites*, **1995**, 15, 439-443
- [5] Engelhardt, G., *Microporous Mater*, **1997**, 12, 369-373
- [6] Kaduk, A.J.; Faber, J., *Conference Paper*, **1995**,
- [7] Baker, J, *J. Comput. Chem.*, **1986**, 7, 385-395
- [8] Sanders, M. J.; Leslie, M.; Catlow, C. R. A., *J. Chem. Soc. Chem. Commun.*, **1984**, 1271-1273
- [9] Jackson, R.A.; Catlow, C.R.A., *Mol. Simul.*, **1987**, 1, 207-224
- [10] Luna-Triguero, A.; Sławek, A.; Huinink, H. P.; Vlugt, T. J. H.; Poursaeidesfahani, A.; Vicent-Luna, J. M.; Calero, S., *ACS Appl Nano Mater.*, **2019**, 2, 5, 3050-3059
- [11] Mark, P.; Nilsson, L., *J. Phys. Chem. A*, **2001**, 105, 43, 9954-9960
- [12] Stubbs, J.M.; Potoff, J.J.; Siepmann, J., *J. Phys. Chem. B*, **2004**, 108, 45, 17596-17605
- [13] Calero, S.; Dubbeldam, S.; Krishna, R.; Smit, B.; Vlugt, T.J.H.; Denayer, J.F.M.; Martens, J.A.; Maesen, T.L.M., *J. Am. Chem. Soc.*, **2004**, 126, 36, 11377-11386
- [14] Dubinin, M.M., *Russ. Chem. Bull.*, **1960**, 9, 1072-1078
- [15] Lehmann, C.; Beckert, S.; Glaser, R.; Kolditz, O.; Nagel, T., *Appl. Energy*, **2017**, 185, 1965-1970
- [16] Peng, D.; Robinson, D.B., *Ind. eng. Chem. Fundamen.*, **1976**, 15, 1, 59-64
- [17] Nagel, T.; Beckert, S.; Bottcher, N.; Glaser, R.; Kolditz, O., *Energy Procedia*, **2015**, 75, 2106-2112
- [18] Hauer, A.; Ziegler, F., *Doctoral Thesis*, **2002**
- [19] Madero-Castro, R.M., Vicent-Luna, J.M., Peng, X., Calero, S., *ACS Sustainable Chem. Eng.*, **2022**, 10, 20, 6509-6520
- [20] Bering, B.P.; Dubinin, M.M.; Serpinsky, V.V., *J. Colloid Interface Sci.*, **1966**, 21, 4, 378-393



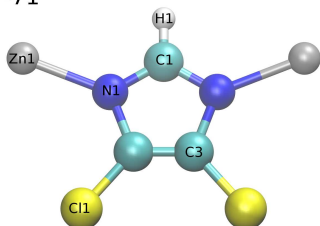
## **Appendix 5**

### **Alcohol-Based Adsorption Heat Pumps using Hydrophobic Metal-Organic Frameworks**

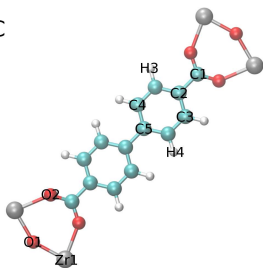
(a) ZIF-8



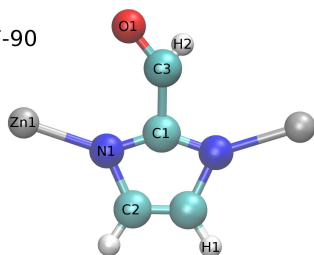
(b) ZIF-71



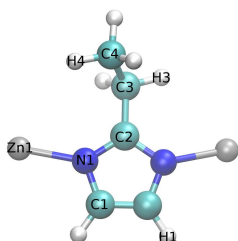
(c) MIL-140C



(d) ZIF-90



(e) MAF-6



MOF	Atom	Partial Charge [e]
-----	------	--------------------

**ZIF-8**

N1	-0.4973
Zn1	1.022
C1	0.4958
C2	-0.0672
C3	-0.272
H2	0.1023
H3	0.0632

**ZIF-71**

N1	-0.2873
Zn1	1.2054
Cl1	-0.24505
C1	0.14155
C3	0.16585
H1	-0.01125

**MIL-140C**

O1	-0.6152887
O2	-0.3996415
Zr	1.50139
C1	0.370644
C2	-0.107838
C3	0.023914
C4	0.0630835
C5	0.0203093
H3	0.0348988
H4	0.04140775

**ZIF-90**

C1	0.3078
C2	-0.0255
C3	-0.4335
H1	0.0321
H2	0.2944
N1	-0.3229
O1	-0.1371
Zn1	1.202

**MAF-6**

C1	-0.1872
C2	0.3068
C3	-0.4654
C4	-0.6812
H1	0.1768
H3	0.2185
H4	0.2202
N1	-0.7685
Zn1	2.6

**Figure A5.1.** Schematic representation of the organic linkers of (a) ZIF-8, (b) ZIF-71, (c) MIL-140C, (d) ZIF-90 and (e) MAF-6. Nitrogen atoms in blue, carbon atoms in cyan, oxygen atoms in red, chlorine in yellow, hydrogen in white and zirconium and zinc atoms in grey. Partial charges of the atoms of each MOF. MAF-6 charges are taken from the literature.<sup>1</sup>

**Table A5.1** Equilibrium adsorption conditions for methanol and ethanol.

MOF	Isotherm, Temperature [K]		Isobar, Pressure [kPa]	
	Methanol	Ethanol	Methanol	Ethanol
ZIF-8	298	298	5	0.8
	308	308		
ZIF-71	298	298	8	4
	308	308		
MIL-140C	298	298	1.5	4
	308	308		
ZIF-90	298	298	10	3
	308	308		
MAF-6	298	298	10	2.5
	308	308		

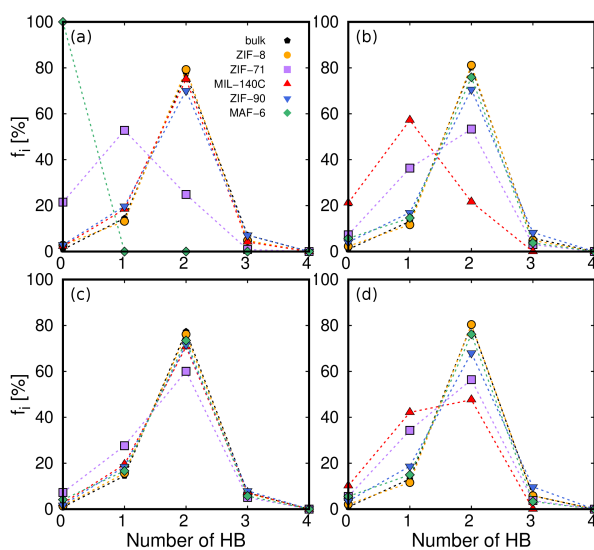


**Figure A5.2**  $f_i$  of methanol (left) and ethanol (right) at  $3kPa$  (a,b) and at saturation (c,d). Non-depicted error bars denote fluctuations smaller than the symbol size.

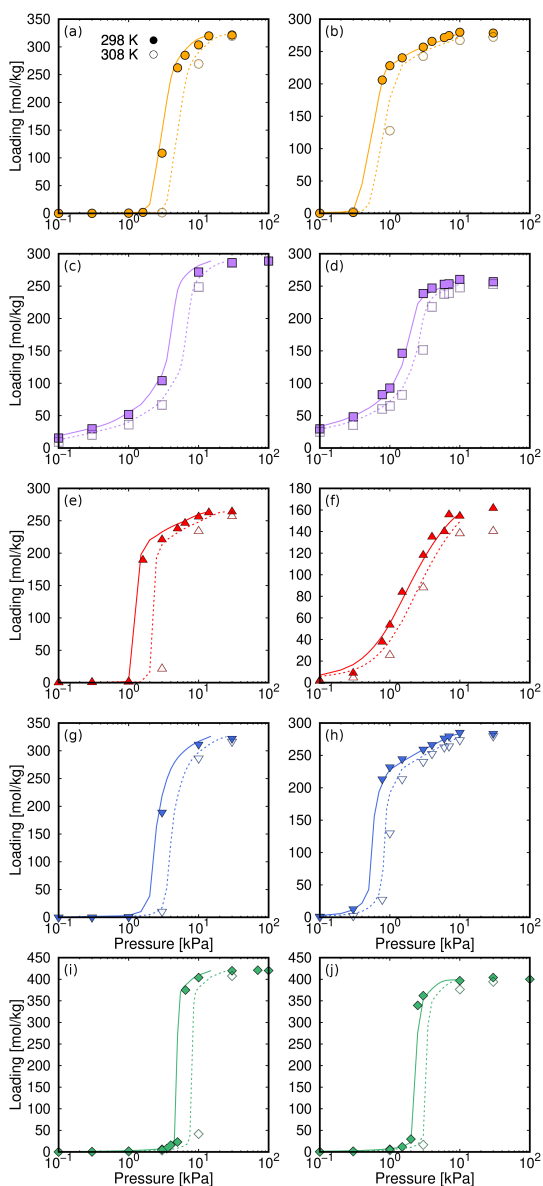


**Figure A5.3** Adsorption isotherms from Grand Canonical Monte Carlo simulation (symbols) and calculated from the characteristic curve (lines) of methanol (left column) and ethanol (right column) in (a,b) ZIF-8, (c,d) ZIF-71, (e,f) MIL-140C, (h,g) ZIF-90, and (i,j) MAF-6 at 298 K and 308 K.

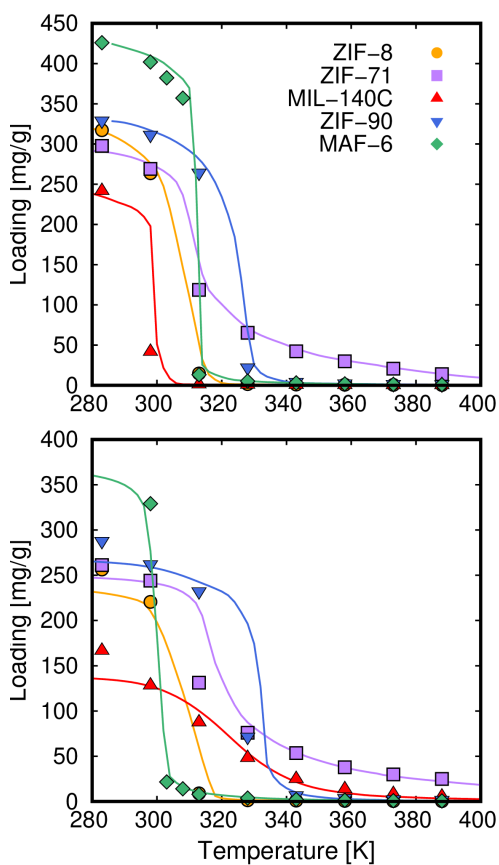


**Figure A5.4** Adsorption isobars from Grand Canonical Monte Carlo simulation (symbols) and calculated from the characteristic curve (lines) of methanol (top) and ethanol (bottom) in ZIF-8, ZIF-71, MIL-140C, ZIF-90, and MAF-6 at the selected working values of pressure shown in Table A5.1.

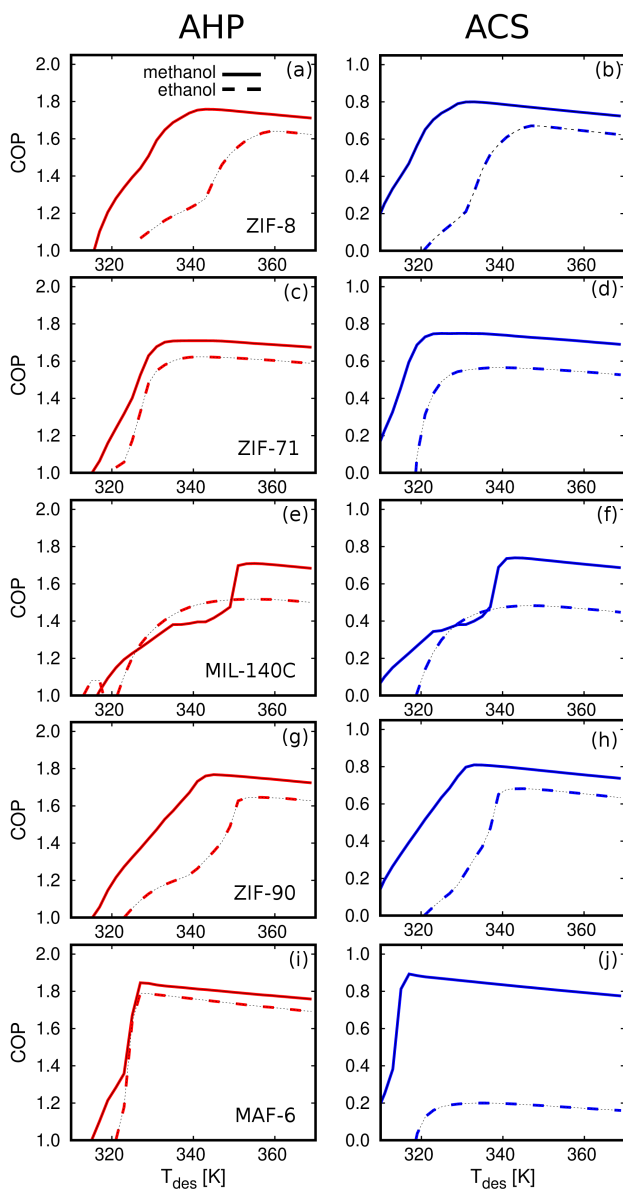


**Figure A5.5** Coefficient of performance as a function of the desorption temperature of methanol (solid lines) and ethanol (dashed lines) for AHP (red) and ACS (blue).

## 5.1 Bibliography

- [1] Gutierrez-Sevillano, J.J.; Calero, S.; Ania, C.O.; Parra, J.B.; Kapteijn, F.; Gascon, J.; Hamad, S., *J. Phys. Chem. C*, **2013**, 117, 1, 466-471

## List of publications

### Publications included in this thesis

#### ■ Chapter 3

R. M. Madero-Castro; J. M. Vicent-Luna and S. Calero. “Adsorption of Light Alcohols in a High Hydrophobic Metal Azolate Framework” *J. Phys. Chem. C*, 123(39), 23987-23994, **2019**.

#### ■ Chapter 4

R. M. Madero-Castro; S. Calero and O. Yazaydin. “The role of hydrogen bonding in the dehydration of bioalcohols in hydrophobic pervaporation membranes” *J. Mol. Liq.*, 340, 117297, **2021**.

#### ■ Chapter 5

R. M. Madero-Castro; J. M. Vicent-Luna, X. Peng and S. Calero. “Adsorption of Linear Alcohols in Amorphous Activated Carbons: Implications for Energy Storage Applications” *ACS Sustain. Chem. Eng.*, 10(20), 6509-6520, **2022**.

#### ■ Chapter 6

R. M. Madero-Castro; A. Luna-Triguero; J. M. Vicent-Luna; A. Sławek; and S. Calero. “On the use of Water and Methanol with Zeolites for Heat Transfer” **Submitted**, arXiv:2208.14235.

#### ■ Chapter 7

R.M. Madero-Castro, A. Luna-Triguero, C. González-Galán, J. M. Vicent-Luna, S. Calero “Alcohol-Based Adsorption Heat Pumps using Hydrophobic Metal-Organic Frameworks” *Manuscript in preparation*.

### Other Publications directly related to this thesis

■ A. Luna-Triguero; J. M. Vicent-Luna; R. M. Madero-Castro; P. Gómez-Álvarez; and S. Calero. “Acetylene Storage and Separation using Metal-Organic Frameworks with Open Metal Sites” *ACS Appl. Mater. Interfaces*, 11(34), 31499-31507, **2019**.

■ N. López-Salas, J. M. Vicent-Luna, S. Imberti, E. Posada, M. J. Roldán, J. A. Anta, S. R. G. Balestra, R. M. Madero-Castro, S. Calero, R. J. Jiménez-Rioboo, M.C. Gutiérrez, M. L. Ferrer, F. del Monte “Looking at the “water-in-deep-eutectic-solvent” system: A dilution range for high performance eutectics” *ACS Sustain. Chem. Eng.*, 7(21), 17565-17573, **2019**

- R.M. Madero-Castro “EosFiLiC: Cálculo de las líneas de campo electrostático en el interior de estructuras periódicas” *MoleQla: revista de Ciencias de la Universidad Pablo de Olavide*, 39, 10, **2020**
- N. López-Salas, J. M. Vicent-Luna, E. Posada, S. Imberti, R. M. Madero-Castro, S. Calero, C. O. Ania, R. J. Jiménez-Riobó, M. C. Gutierrez, M. L. Ferrer, F. del Monte “Further Extending the Dilution Range of the “Solvent-in-DES”Regime upon the Replacement of Water by an Organic Solvent with Hydrogen Bond Capabilities” *ACS Sustain. Chem. Eng.*, 8(32), 12120-12131, **2020**
- N. López-Salas, J. M. Vicent-Luna, E. Posada, S. Imberti, R. M. Madero-Castro, S. Calero, C. O. Ania, R. J. Jiméénez-Riobó, M. C. Gutierrez, M. L. Ferrer, F. del Monte “Further Extending the Dilution Range of the “Solvent-in-DES”Regime upon the Replacement of Water by an Organic Solvent with Hydrogen Bond Capabilities” *ACS Sustain. Chem. Eng.*, 8(32), 12120-12131, **2020**
- C. González-Galán, S. R. G. Balestra, A. Luna-Triguero, R. M. Madero-Castro, A. P. Zaderenko and S. Calero “Effect of diol isomer/water mixtures on the stability of Zn-MOF-74” *Dalton Trans.*, 50(5), 1808-1815, **2021**
- X. Lu, J. M. Vicent-Luna, S. Calero, R. M Madero-Castro, M. C. Gutiérrez, M. L. Ferrer, F. del Monte “EMIMBF<sub>4</sub> in ternary liquid mixtures of water, dimethyl sulfoxide and acetonitrile as “tri-solvent-in-salt”electrolytes for high-performance supercapacitors operating at  $-70^{\circ}\text{C}$ ” *Energy Storage Mater.*, 40, 368-385, **2021**
- J. A. Seijas-Bellido, B. Samanta, K. Valadez-Villalobos, J. J. Gallardo, J. Navas, S. R. G. Balestra, R. M. Madero-Castro, J. M. Vicent-Luna, S. Tao, M. C. Toroker, J. A. Anta “Transferable Classical Force Field for Pure and Mixed Metal Halide Perovskites Parameterized from First-Principles” *J. Chem. Inf. Model*, XX(X), XXXX-XXXX, **2022**
- R.M. Madero-Castro, O. Yazaydin, J.M. Vicent-Luna, S. Calero “Use of water with functionalized hydrophobic structure for Energy applications” *Manuscript in preparation*
- X. Lu, J.M. Vicent-Luna, L. González-Aguilera, B. Xu, S. Tao, S. Calero, R.M. Madero-Castro, M. C. Gutiérrez, M. Luisa Ferrer, F. del Monte “Co-solvent in double anion ionic liquids for expanding the electrochemical stability window of supercapacitors ” *Manuscript in preparation*

## Open access code developed in this thesis

- BondCalc, <https://github.com/rmmadcas/BondCalc>
- EosFiLiC, <https://github.com/rmmadcas/EosFiLiC>

## Acknowledgements/Agradecimientos

### Una parte del viaje es el final.

Viaje que culmina con esta Tesis. Parecía que este momento no iba a llegar nunca. Cuando comencé a realizar mi tesis doctoral hace unos cinco años.

En primer lugar debo agradecer, no sólo esta Tesis, si no todo lo que soy en la vida a mi **padre** y a mi **madre**. A mi madre y a mi padre. Unos padres que siempre estuvieron dispuestos a ayudarme, a sacrificarse por darme lo mejor. A llevarme por el buen camino. Y no siempre fue fácil, pero ellos siempre estuvieron ahí. No hay nadie en este mundo que se merezca estar aquí más que vosotros. Os quiero.

Junto a mis padres debo agradecer al resto de mi familia. Especialmente a mi hermana **Cristina**, por curtirme y evitar que me convirtiera en un pringado (aunque no terminé de conseguirlo), y por compartir una infancia conmigo en la que las mamis se escondían en bicis estáticas y en la que volaban cartas por la ventana. Gracias también por darme una **cuñada** tan guay y por una **sobrina** llena de bigotes que me muerde los tobillos. Por último, pero no por ello menos importante, al miembro más pequeño de nuestra familia. Por ahora **Luca** no hace demasiado, aparte de comer, dormir y escalar, pero eso es suficiente para que se haya ganado un hueco aquí y en el corazón de todos nosotros. Gracias a mi **Tata** y a mi **Tate**, porque siempre fuisteis mucho más que unos tíos para mí. A los **Mallorquines**, enanos incluidos. Y a los que ya no están... os echo de menos.

Académica y científicamente, hay mucha gente que ha influido a que yo esté hoy aquí. Pero me gustará hacer mencionar, por supuesto a mis directores, **Sofía** y **Vicent**. Gracias por todo lo que habéis contribuido a esta tesis con todo vuestro conocimiento y dedicación, pero sobre todo, porque es cierto que sois grandes científicos, pero sois mejores personas. Jamás encontraré mejores "jefes". Junto a mis directores quiero agradecer a **Azahara** por rescatarme de ese hotel donde aparcaba coches, a **Ali** (sí, Ali también es RASPA) por ser tan genial, a **Julio** e **Ismael** por la ingente cantidad de lagrimitas de pollo que me permitieron comer y en general a todos los demás miembros del grupo con los que tuve el placer de compartir espacio-tiempo (**Salva**, **Javi**, **Pilar**, **Juanjo**, **Ana**, **Carlos**, **Patrick**, **Jose Manuel**, **Rocío & Rocío**, **Isidro**, **Paco**, **Rabdel**, **Said**...)

Thanks to **Özgür**, **Ben**, **Kai** and **Selman** for hosting me in London for 3 months as another

member of the group. In those 3 months I learned much more than physics... and I ate things I never thought I would eat.

Muchas gracias a todos mis amigos de la universidad, a **Carmelo, Bea, Aza** (otra vez), **Luigi, Maridegui, Rafalito, José Ángel, Enrique, Pele...** porque sin esas tardes de biblioteca, quizás nunca habríamos acabado la carrera... o quizás sí, pero nos habríamos reído bastante menos.

A la **Superpandi (Jesús, Vicky, Sergio, Dani & Dani, María, Bruno, Ángel y los que están por venir,** porque aunque no os interesa demasiado cuando hablo de ciencia... en el fondo yo sé que me queréis. Y a **Miguel, Miriam, Soledad, Carlos, Carmen, Cris, Vicky, Rafa Lion, Mario, Jesús, Rafdaga e Isa** por la cantidad de fotos que me han regalado, fotos que ponen de manifiesto lo mucho que nos hemos divertido siempre.

Gracias a **Joaquín**, por todo lo que nos has enseñado aún siendo tan pequeño. Te queremos.

Gracias a **Javi y Noelia** por esas tardes de gimnasio que acababan en bares donde nos poníamos hasta arriba de agua con hielo y limón (es triste... pero es cierto) y por ayudar a llenar una ciudad que estaba vacía cuando llegué a ella.

Gracias a **Mojito**, a **Gala**, a **Khalessi**, a **Rave** y a **Nube** por enseñarme que no hay amor más puro que el que un animal siente por una persona. A todos os llevo en mi corazón, y a algunos en la piel. Siempre he pensado que os vais demasiado pronto. Pero volveremos a vernos.

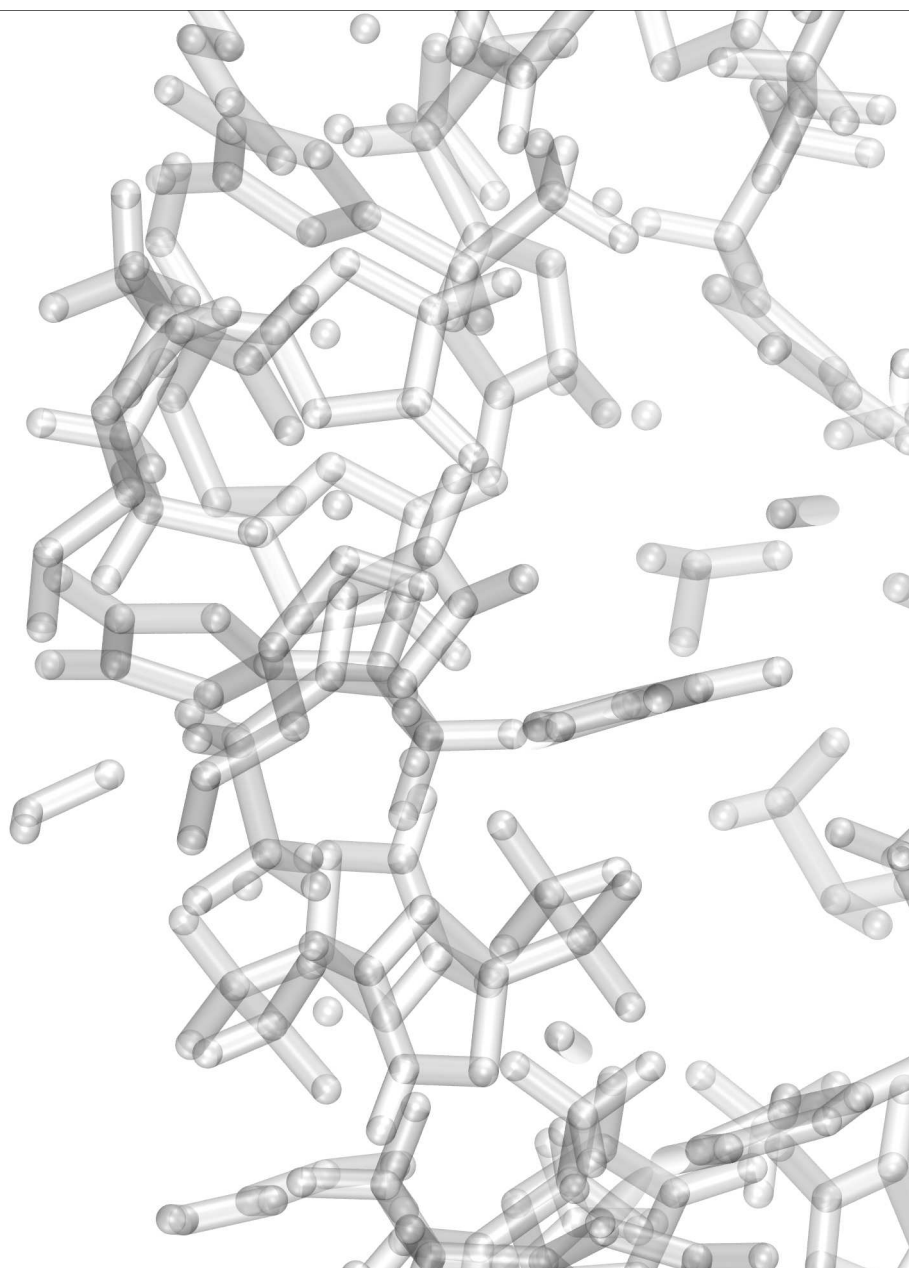
Y por último y por ello más importante, a mi **Carbunny**. Hace algo más de cuatro años nos conocimos en el mismo laboratorio donde hemos realizados nuestras tesis. Un dos de octubre de 2017. Desde entonces hemos ido creciendo juntos como científicos y como personas hasta formar lo que somos hoy día. Esta tesis es tan tuya como mía. Gracias por todo lo que has hecho por mí y por formar conmigo, con **Rave y Nube** una **familia**.

When the snows fall and the white winds blow the lone wolf dies but the pack survives.

**Eddard Stark**, Lord of Winterfell

May we meet again.

**Clarke Griffin**, one of the one hundred and two.



ISBN: 978-84-09-45592-8



UNIVERSIDAD  
**PABLO<sup>D</sup>  
OLAVIDE**  
SEVILLA

